

Quantitative Microstructural Imaging for Clinical Use

Présentée le 19 novembre 2021

Faculté des sciences et techniques de l'ingénieur
Laboratoire de traitement des signaux 5
Programme doctoral en génie électrique

pour l'obtention du grade de Docteur ès Sciences

par

Gian Franco PIREDDA

Acceptée sur proposition du jury

Prof. D. N. A. Van De Ville, président du jury
Prof. J.-Ph. Thiran, Dr T. Kober, directeurs de thèse
Dr J. Marques, rapporteur
Prof. D. Jones, rapporteur
Dr B. Lanz, rapporteur

A Giustina e Francesco...

Acknowledgements

At the end of this journey, I would like to express my sincere gratitude to all the people who supported and guided me through the realization of the thesis.

First, I would like to deeply thank my supervisors. Thank you, Jean-Philippe, for giving me the chance to pursue my PhD in your lab and supporting me with your help and precious suggestions. Thank you, Tobi, for the trust you placed in me since day one. I still have a very clear memory of how scared I was the first day we met for my interview, and how you made me feel at ease the moment you started talking. At that time, I did not know that it would have been the beginning of such an amazing journey together, but I am definitely glad it happened and that more is yet to come. You entrusted me to work on fascinating projects surrounded by stimulating people, and I will always be grateful to you for that. Your positive and problem-solving mindset, both in science and life, will always be an important source of inspiration. I also owe a great debt of gratitude to Tom, for sharing his knowledge with me and putting his expertise at my disposal every day. Whether I was struggling with complicated MR sequence code or crashing scanners during late evenings, you have always been there to help and support me in any way possible. Our cooperation and constant discussions were fundamental to complete this journey. Thank you for always believing in me, especially when I doubted the most.

I would like to thank the jury of my PhD defence, Prof. Derek Jones, Dr José Marques, Dr Bernard Lanz, and the committee president Prof. Dimitri Van De Ville, for having taken the time to carefully read my thesis and for the interesting discussions.

Already since the time of my master thesis, the Advanced Clinical Imaging Technology group welcomed me as a member of their family, making this journey a very enjoyable one. Many thanks to Arun, Gabri, Thomas, Marion, Emilie, Béné, Ricardo, Till, Jonathan, Chloé, Veronica, Mario, Davide, John, Ludovica, Jonas, Mezo, Ilaria, and all the people who have been part of the ACIT family during these years.

In these past four years I got to meet many new people whose friendship supported me along this journey. Thanks to the “Innovation Forum Lausanne” family, Bea, Cate, Claudia, Ele, Nicolas, Andrea, Davide, Daniel, Lorenzo, Alessia, Gianmarco, and all the others. The organization of many great events together always helped me distract from the struggles of the

Acknowledgements

PhD. Many thanks as well to the rest of the Italian gang, Francesco, Tommaso, Luca, Silvia, and Roberto. Thank you, Sammy and Soumya, for enriching this journey with your international culture. Most of you also contributed in practice to my PhD by helping with the scanning experiments in CHUV, so many thanks to you and all the volunteers who dedicated their time (and brain) to my research.

I would like to acknowledge all the people I met during my studies in Turin and whose friendship I treasure: Andrea, Gabriele, Ivan, Simone, Cristiana, Anna, Nicola, and all the others. A sincere thank you goes to Nicolò, for having eased with an incredible amount of laughs and hilarious moments the initial struggles of this adventure in Switzerland. Even though we both began new chapters of our lives in the last years, there will never be a distance that can diminish our friendship. Thank you for always being by my side and giving me reasons to cheer.

A special thank you to my best friends back home, Michelle, Jessica and Ginevra. Even though we are less frequently in touch, every time I come back to Sardinia, you make me feel like I never left. Also thank you for always supporting and joining me in the crusade to find the best place to stuff ourselves with good food.

During this journey, I have been fortunate enough to come in contact with people who eventually became my family and made Lausanne feel like home to me. When I started this experience, Mario was one of the first people with whom I immediately connected. Thank you, Mario, for having shared with me all the secrets and tips to face this adventure in the best way. You have always been an example to me, as human being and researcher, and I consider myself lucky to be among your friends. Even though Cipo joined this journey halfway, she certainly left a mark. Thank you, Cipo, for being my companion of many adventures and misfortunes over the past years. Thank you for the countless hours spent together discussing work-related things and other more enjoyable things such as food. You made me aware every day that I was certainly not alone in this. “Meglio pochi ma buoni”, as you always say, and I could not be happier to be in your “pochi”. Finally, thank you, RaC, for being the best friend I could have hoped to have at my side along this journey. I will be forever grateful for your advices and encouragement that always motivated me to move forward and do my best. During our “complaining Thursdays”, whether I was cracking a stupid joke or complaining about work and life, you were always there to hear me out. Thank you for being at the same moment the shoulder I could rely on and the friend with whom sharing a great deal of fun. Your friendship was a gift I received from this journey that I will always treasure. Gracias hermano.

My heartfelt gratitude goes out to the person who shared with me all the joys and fears of this journey and many others before, Adele. Thank you for your patience, your kindness, but before all for your love. Thank you for adding meaning to my life every day, for making the hard times a lot easier and the good times even better. I cannot wait to see the great things future holds for us and to share all of that with you. Thank you for never giving up on me. Ti amo.

Infine, vorrei dedicare questa tesi alla mia famiglia. A mio fratello, Antonio, per riuscire sempre a tirarmi su di morale e per rendermi ogni giorno un fratello orgoglioso. A mio padre, Bastianino, per i sacrifici fatti affinché potessi raggiungere questo traguardo, per avermi insegnato che se si ha la volontà di farlo ci si può rialzare anche dopo le cadute peggiori, per aver sempre appoggiato incondizionatamente ogni mia scelta. A mia madre, Antonella, per l'amore con cui mi ha cresciuto, per avere condiviso con me tutte le ansie degli ultimi anni, per essere la mia fan numero uno, perché senza di lei non sarei chi sono oggi. Ai miei nonni, Giustina e Francesco, per avermi cresciuto come un figlio, per avermi insegnato l'umiltà e il rispetto, perché siete stati e sempre sarete il mio esempio di vita. Grazie.

Lausanne, September 30, 2021

G. F. P.

Abstract

Today, Magnetic Resonance Imaging (MRI) is a well-established medical imaging modality thanks to its excellent soft tissue contrast. Conventional MR image contrasts can be weighted towards one or more physical properties that discriminate different tissues, which represents one of the main advantages of MRI compared to other imaging techniques. However, conventional contrasts always depend on the combination of different tissue properties, imaging parameters and employed hardware. Quantitative MRI (qMRI) techniques allow moving from such relative contrast information to a single, absolute measure of one or more separate tissue properties.

The measurement of water proton relaxation rates represents one major approach for quantitatively characterizing the human brain tissue microstructure with MRI. MR relaxation mechanisms depend on complex interactions among protons and between protons and their surrounding lattice. Hence, important determining factors of the physical parameters measured with qMRI are, for example, the concentration of water, macromolecules (for instance abundant in myelin) and paramagnetic atoms (e.g., iron). The exhibited sensitivity and specificity of qMRI acquisitions towards the microstructural properties of brain tissues drove an incremental investigation around qMRI metrics as biomarkers for alterations caused by disease. However, the practical use of qMRI in clinical settings is still hindered by difficulties in delivering precise quantification in an adequate resolution and within acquisition times comparable to conventional imaging. Moreover, to exploit the full potential of quantitative maps, normative values of physical parameters in healthy tissues are required, enabling the comparison of tissue properties from a single patient to normal values, potentially improving diagnosis and follow-up assessments.

With a focus on brain relaxometry and myelin water imaging, this thesis aims at bringing qMRI closer to clinical routine by tackling challenges ranging from the image acquisition to its practical application. More specifically, a validated T_2 relaxometry sequence for myelin imaging – the multi-echo gradient and spin echo sequence – has been implemented and subsequently accelerated by combining it with parallel imaging to achieve whole brain coverage in a clinical compatible acquisition time. The direct estimation of microstructural features from relaxometry data has been also investigated using a fast protocol for T_1 and T_2 mapping and a data-driven approach that takes advantage of recent advances in the machine learning domain. Finally, the clinical value of qMRI in conjunction with normative atlases of physical

Abstract

properties has been explored to detect personalized changes in tissue parameters that reflect the underlying pathology.

Keywords – Quantitative MRI, tissue microstructure, brain relaxometry, myelin water imaging, normative atlases.

Résumé

L'imagerie par résonance magnétique (IRM) est une modalité d'imagerie médicale largement répandue qui présente un excellent contraste entre les tissus mous. Les contrastes des images conventionnelles peuvent être pondérés en fonction d'une ou plusieurs propriétés physiques qui distinguent les différents tissus, ce qui représente l'un des principaux avantages de l'IRM par rapport aux autres techniques d'imagerie. Cependant, les contrastes conventionnels dépendent toujours d'une combinaison de différentes propriétés des tissus, de paramètres d'imagerie et de l'appareil IRM utilisé. Les techniques d'IRM quantitative permettent de passer de ces informations de contraste relatives à une mesure unique et absolue reflétant une ou plusieurs propriétés distinctes des tissus.

La mesure des temps de relaxation des protons représente la méthode la plus courante pour caractériser quantitativement la microstructure du tissu cérébral humain par IRM. Les mécanismes de relaxation de résonance magnétique dépendent des interactions complexes entre protons et entre les protons et leur milieu ambiant. Pour cette raison, les facteurs déterminants des paramètres physiques mesurés par IRM quantitative sont la concentration d'eau, de macromolécules (par exemple abondantes dans la myéline), d'atomes paramagnétiques (par exemple, le fer), entre autres. La sensibilité de l'IRM quantitative à l'égard de ces propriétés microstructurales a favorisé une augmentation continue de la recherche dans ce domaine dans le but d'identifier des biomarqueurs reflétant les altérations du tissu cérébral causées par les maladies neurologiques. Toutefois, l'utilisation pratique de l'IRM quantitative dans un contexte clinique est entravée par les difficultés à fournir une quantification précise dans une résolution adéquate et dans des temps d'acquisition comparables à ceux de l'imagerie conventionnelle. En outre, pour exploiter tout le potentiel des cartes quantitatives, il faut disposer des valeurs normales des paramètres physiologiques des tissus sains. Ainsi, les propriétés des tissus d'un patient peuvent être comparées aux valeurs normales dans le but d'améliorer potentiellement le diagnostic et le suivi médical.

Cette thèse vise à rapprocher l'IRM quantitative de la routine clinique en relevant des défis allant de l'acquisition de l'image à son application pratique. Plus précisément, une séquence validée pour la mesure du temps de relaxation T_2 a été implémentée et ensuite accélérée en la combinant avec l'imagerie parallèle pour obtenir une couverture du cerveau entier dans un temps d'acquisition compatible avec les temps cliniques. L'estimation directe des caractéristiques microstructurales à partir des données de relaxométrie a également été

Résumé

étudiée à l'aide d'un protocole rapide de cartographie T_1 et T_2 et d'une approche qui tire parti des progrès récents dans le domaine de l'apprentissage automatique. Enfin, la valeur clinique de l'IRM quantitative en conjonction avec des atlas de propriétés physiques normales a été explorée pour détecter des changements personnalisés dans les paramètres tissulaires qui reflètent la pathologie sous-jacente.

Mots-clés – IRM quantitative, microstructure du tissu, relaxométrie cérébrale, imagerie de l'eau de la myéline, atlas normatifs.

Sommario

La Risonanza Magnetica per Immagini (RMI) è una consolidata modalità di diagnostica che fornisce un eccellente contrasto tra tessuti molli. L'intensità relativa del segnale in immagini ottenute attraverso tecniche convenzionali di RMI è determinata (ovvero “pesata”) in funzione di una o più proprietà fisiche che caratterizzano i tessuti molli. Questa possibilità rappresenta certamente uno dei principali vantaggi della RMI rispetto ad altre tecniche di diagnostica per immagini. Tuttavia, il contrasto che si ottiene rimane sempre influenzato da tutte le diverse proprietà fisiche del tessuto, dai parametri dell'acquisizione e dal macchinario impiegato. Al contrario, le tecniche di RMI quantitativa consentono di passare da un'informazione relativa ad una misura assoluta di una o più proprietà fisiche che differenziano i tessuti.

La misurazione dei tempi di rilassamento dei protoni rappresenta uno dei principali approcci per caratterizzare in maniera quantitativa la microstruttura dei tessuti cerebrali umani con la RMI. Poiché tali meccanismi di rilassamento derivano da complicate interazioni che avvengono tra protoni e tra i protoni e il loro ambiente circostante, le proprietà fisiche misurate con la RMI quantitativa dipendono, ad esempio, dalla concentrazione d'acqua, di macromolecole (soprattutto abbondanti nella mielina) e di atomi paramagnetici (come il ferro). La sensibilità della RMI quantitativa rispetto a tali proprietà microstrutturali ha favorito un continuo incremento della ricerca in questo ambito per l'identificazione di biomarcatori delle alterazioni dei tessuti cerebrali causate da patologie neurologiche. Nonostante ciò, l'affermazione della RMI quantitativa in ambito clinico è ostacolata dalla difficoltà nel fornire una misura accurata con adeguata risoluzione ed entro tempi di acquisizione paragonabili alle tecniche convenzionali. Inoltre, in modo da poter sfruttare a pieno le potenzialità cliniche che tale tecnologia può offrire, sono richiesti dei database contenenti i valori considerati “normali” delle proprietà fisiche dei tessuti analizzati. Tali database, infatti, consentirebbero di operare un confronto diretto tra le proprietà fisiche dei tessuti di un nuovo paziente e l'intervallo di valori fisiologici stabilito per un tessuto in salute, migliorando la diagnosi e il follow-up di diverse patologie.

L'obiettivo di questa tesi è quello di rendere alcune tecniche di RMI quantitativa più accessibili in ambito clinico affrontando problemi che vanno dall'acquisizione delle immagini fino al loro utilizzo pratico. Più precisamente, una sequenza già consolidata per la misura del tempo di rilassamento T_2 è stata implementata e successivamente accelerata entro tempi compatibili con la pratica clinica grazie ad una tecnica di acquisizione parallela. In aggiunta, è stata studiata la possibilità di derivare proprietà microstrutturali, come il contenuto in acqua della

Sommario

guaina mielinica, direttamente dai tempi di rilassamento attraverso un approccio basato su metodi di apprendimento automatico. Infine, sono stati derivati atlanti contenenti gli intervalli fisiologici “normali” per i tempi di rilassamento T_1 and T_2 a partire da soggetti in salute e sono stati sviluppati dei metodi per comparare i tempi di rilassamento di un nuovo soggetto con tali valori di riferimento in modo da individuare e caratterizzare automaticamente l'eventuale presenza di tessuto patologico in pazienti.

Parole chiave – RMI quantitativa, microstruttura dei tessuti, rilassometria cerebrale, contenuto in acqua della guaina mielinica, atlanti di intervalli fisiologici.

Contents

Acknowledgements	i
Abstract (English/Français/Italiano)	v
List of figures	xv
List of tables	xix
1 Introduction	1
1.1 Thesis rationale and outline	3
2 Background	5
2.1 The Nuclear Magnetic Resonance phenomenon	5
2.1.1 Magnetization	5
2.1.2 Radio-frequency excitation	7
2.1.3 Relaxation	7
2.2 Magnetic Resonance Imaging	9
2.2.1 Spatial encoding and k-space	9
2.2.2 Pulse sequences and MR contrasts	11
2.3 Quantitative MRI	14
2.3.1 T_1 mapping	14
2.3.2 T_2 mapping	15
2.3.3 Simultaneous multi-parametric mapping	17
2.3.4 MR imaging specific to myelin content	18
2.3.5 On the clinical value of quantitative MRI in the brain	20
2.4 MRI acceleration techniques	21
2.4.1 Parallel imaging	21
2.4.2 Compressed sensing	24
2.4.3 Model-based reconstructions	25
2.5 Automatic image post-processing	25
2.5.1 Segmentation of brain tissues	26
2.5.2 Spatial registration of brain images	27
3 Probing myelin content of the human brain with MRI	29
3.1 Introduction	29

Contents

3.2	Probing myelin with relaxometry	30
3.2.1	T_2 relaxometry	30
3.2.2	T_2^* relaxometry	34
3.2.3	T_1 relaxometry	36
3.2.4	Simultaneous T_1 and T_2 relaxometry	37
3.2.5	Discussion	39
3.3	Targeting the brain macromolecular content	41
3.3.1	Magnetization transfer imaging	41
3.3.2	Ultrashort TE	46
3.3.3	Macromolecular tissue volume	47
3.3.4	Discussion	47
3.4	Other MR contrasts	48
3.4.1	Diffusivity and fractional anisotropy	48
3.4.2	Susceptibility imaging	49
3.4.3	Magnetic resonance elastography	50
3.4.4	Ratio of T_1 -weighted and T_2 -weighted images	50
3.4.5	Discussion	51
3.5	Conclusions	52
4	Fast and high-resolution myelin water imaging: Accelerating multi-echo GRASE with CAIPIRINHA	59
4.1	Introduction	59
4.2	Methods	60
4.2.1	Sequence design	60
4.2.2	Image acquisition and MR protocols	62
4.2.3	Image processing	64
4.2.4	MWF estimation	64
4.2.5	Statistical analysis	65
4.3	Results	65
4.3.1	Comparison of acceleration schemes	65
4.3.2	Multi-echo GRASE vs MESE	67
4.3.3	Multi-echo GRASE repeatability	69
4.3.4	Gradient-echo shifting	69
4.3.5	Influence of TR	70
4.4	Discussion	70
4.5	Conclusions	77
5	Data-driven myelin water imaging based on T_1 and T_2 relaxometry	79
5.1	Introduction	80
5.2	Materials and Methods	81
5.2.1	MR dataset	81
5.2.2	Image processing	82
5.2.3	Modeling of MWF maps from relaxometry	82

5.2.4	Statistical analysis	84
5.3	Results	84
5.4	Discussion	85
5.5	Conclusion	89
6	Quantitative brain relaxation atlases for personalized detection and characteriza- tion of brain pathology	91
6.1	Introduction	92
6.2	Methods	92
6.2.1	Study population	92
6.2.2	MR protocol	93
6.2.3	Image processing	93
6.2.4	Population-derived norms	95
6.2.5	Method of single-subject comparison	96
6.2.6	Norms validation	96
6.2.7	Detection of relaxometry alterations in example patient's cases	97
6.3	Results	97
6.4	Discussion	100
6.5	Conclusion	106
7	Normal volumetric and T_1 relaxation time values at 1.5 T in segmented pediatric brain MRI using a MP2RAGE acquisition	107
7.1	Introduction	108
7.2	Material and methods	109
7.2.1	Study population	109
7.2.2	Image acquisition	110
7.2.3	Image processing	110
7.2.4	Qualitative segmentation validation assessment	110
7.2.5	Normative data modeling	111
7.3	Results	111
7.3.1	Image processing	111
7.3.2	Development of brain volumes	111
7.3.3	Evolution of relaxation times	113
7.4	Discussion	114
7.5	Conclusion	121
8	Conclusions, scientific and clinical impact	123
8.1	Main contributions	123
8.1.1	Myelin water imaging	123
8.1.2	Learning tissue microstructure from relaxometry	124
8.1.3	Characterization of abnormal tissues	124
8.2	Scientific and clinical collaborations	124
8.2.1	Myelin water imaging	124

Contents

8.2.2	Characterization of abnormal tissues	125
8.3	Future research directions	127
8.3.1	Myelin water imaging	127
8.3.2	Learning tissue microstructure from relaxometry	128
8.3.3	Characterization of abnormal tissues	128
8.4	Final consideration	129
Bibliography		131
Curriculum Vitae		157
Publications		159
	Articles in peer-reviewed journals	159
	Articles in proceedings of international conferences	160
	Abstracts in proceedings of international conferences	160
	Patent applications	164
	Work-in-progress packages (MR sequences)	164

List of Figures

1.1	Example MR images	2
2.1	Magnetization in the presence of an external magnetic field	6
2.2	T_1 and T_2 relaxation mechanisms	8
2.3	T_1 and T_2 relaxation curves	9
2.4	k-space frequencies	10
2.5	Spin echo sequence timing diagram	11
2.6	Gradient echo sequence timing diagram	12
2.7	Examples of different MR contrasts	13
2.8	MP2RAGE sequence timing diagram and example images	16
2.9	Multi-echo spin echo sequence timing diagram	17
2.10	Organization of axonal myelination	19
2.11	GRAPPA reconstruction	23
2.12	Compressed sensing	24
2.13	T_2 mapping with GRAPPATINI	25
2.14	Brain tissue segmentation	27
3.1	Myelin water imaging from multi-echo T_2 data	32
3.2	Myelin water imaging from multi-echo T_2 data acquired with a gradient and spin echo and a T_2 -prep sequence	33
3.3	Myelin water imaging from multi echo T_2^* data	35
3.4	Myelin water imaging from T_1 relaxometry	37
3.5	Myelin water imaging from the multicomponent driven equilibrium single-pulse observation of T_1 and T_2	38
3.6	Myelin partial volume maps derived with QRAPMASTER	40
3.7	Generation of magnetization transfer contrast	42
3.8	Binary spin bath model for magnetization transfer	43
3.9	Macromolecular proton fraction mapping	45
3.10	Inhomogeneous magnetization transfer imaging	46
3.11	Inversion recovery prepared ultra short echo time imaging	47
3.12	Additional sources of MR contrast sensitive to myelin changes	51
4.1	Multi-echo GRASE pulse sequence diagram	61
4.2	Phantom data acquired with different CAIPIRINHA undersampling schemes	66

List of Figures

4.3	G-factor maps estimated for different CAIPIRINHA undersampling schemes . .	66
4.4	Brain images acquired with different CAIPIRINHA undersampling schemes . .	67
4.5	MWF maps resulting from the investigated CAIPIRINHA undersampling schemes	68
4.6	T ₂ -weighted axial slice, with estimated flip angle map and T ₂ spectra	69
4.7	MWF maps from single-slice MESE sequence and the proposed multi-echo GRASE	70
4.8	Comparison of MWF maps from the MESE and the multi-echo GRASE sequence	71
4.9	Comparison of MWF maps derived from the multi-echo GRASE in a scan-rescan scenario	72
4.10	Phantom multi-echo GRASE data acquired without and with echo shifting . . .	73
4.11	Brain multi-echo GRASE data acquired without and with echo shifting	74
4.12	MWF maps retrieved from multi-echo GRASE data acquired without and with echo shifting	75
4.13	Brain multi-echo GRASE data acquired with different repetition times	76
4.14	Comparison of MWF maps derived from multi-echo GRASE data acquired with different repetition times	77
5.1	Representative axial slices of the acquired images	85
5.2	MWF maps obtained from the investigated modeling strategies	86
5.3	Comparison of MWF values obtained from the investigated modeling strategies	88
6.1	Pre-processing pipeline for T ₁ and T ₂ z-score computation	94
6.2	Representative axial slices of the acquired images	97
6.3	Brain slices of the study-specific template, the white matter prior, and an exam- ple outcome of the spatial registration	98
6.4	Representative slice of the established normative T ₁ and T ₂ atlases	99
6.5	T ₁ and T ₂ correlation with age	100
6.6	Voxels with a normal distribution of T ₁ and T ₂ values	101
6.7	Results of the 10-fold cross-validation	102
6.8	Example z-score deviation maps in healthy subjects and in patients	103
6.9	Z-score deviation maps in a patient	104
7.1	Demographics of the healthy cohort	109
7.2	Building process of the T ₁ -weighted anatomical template	112
7.3	Example brain slices of MP2RAGE UNI, T ₁ maps, and corresponding segmenta- tion masks	113
7.4	Normal evolution with age of the total intracranial volume, cortical gray matter, whole gray matter, and white matter volumes	114
7.5	Normal evolution with age of the cortical gray matter and white matter volumes with respect to brain lobes	115
7.6	Normal evolution with age of the basal ganglia, thalamus, hippocampus, amyg- dala, cerebellum gray matter and white matter, corpus callosum, and brainstem volumes	116

7.7	Normal evolution with age of the cerebrospinal fluid, lateral ventricle, third ventricle, and fourth ventricle volumes	117
7.8	Normal evolution with age of the cortical gray matter and white matter T_1 relaxation times with respect to brain lobes	118
7.9	Normal evolution with age of the basal ganglia, thalamus, hippocampus, amygdala, cerebellum gray matter and white matter, corpus callosum, and brainstem T_1 relaxation times	119

List of Tables

3.1	Summary of reviewed methods for myelin imaging	53
3.2	Summary of studies investigating reproducibility of reviewed methods for myelin imaging	57
4.1	Relevant parameters of the acquired sequences	63
5.1	Relevant parameters of the acquired sequences	82
5.2	Measurements of agreement between estimated and reference myelin water fraction values	87
6.1	Relevant parameters of the acquired sequences	93

1 Introduction

Magnetic Resonance Imaging (MRI) is a well-established medical imaging modality exhibiting excellent soft tissue contrast that offers valuable information in a variety of clinical applications. MRI relies on the Nuclear Magnetic Resonance (NMR), a physical phenomenon involving the absorption of electromagnetic radiation oscillating at a specific frequency by nuclei subjected to a strong magnetic field. The history behind the NMR phenomenon dates back to the 1920's, when Stern and Gerlach discovered the spin nature of the proton [1]. Following up on this observation, in 1946 Purcell et al. [2] and Bloch [3] separately developed a method to measure the proton precession signal, building the foundation for the development of the MRI technology. For this achievement, the two scientists shared a Nobel prize in 1952. However, it was only in 1973 that Lauterbur [4] and Mansfield [5] introduced the use of spatially varying magnetic fields for image encoding, paving the way for the clinical application of MRI.

Since its introduction in clinical routine in the early 1980's, MRI is mostly used in neurology and muscular-skeletal applications due to its unique and valuable soft tissue contrast (see Figure 1.1). Compared to other imaging modalities, MRI offers great flexibility and sensitivity to many biophysical processes underpinning the recorded signal. In fact, MR image contrasts can be weighted towards one or more physical properties that discriminate soft tissues, such as proton density (PD), longitudinal (T_1), transverse (T_2) and apparent transverse (T_2^*) relaxation times, magnetization transfer (MT) or diffusion parameters ("apparent diffusion coefficient", fractional anisotropy, among others). The weighting is achieved through the chosen acquisition method – called "sequence" in MRI – and its corresponding parametrization. The versatility of the weighted contrast is the foundation of its ever-growing range of clinical applications. However, as the "weighting" is merely an increased sensitivity towards one of the above parameters (or a combination of them), it depends on many different factors, especially the acquisition method, the chosen imaging parameters and the employed hardware. Any comparison of image intensities among different subjects, MRI scanners or in longitudinal studies is thus difficult or even precluded.

In contrast, quantitative MRI (qMRI) techniques allow moving from such relative contrast information to a single, absolute measure of one or more separate tissue properties, thus providing

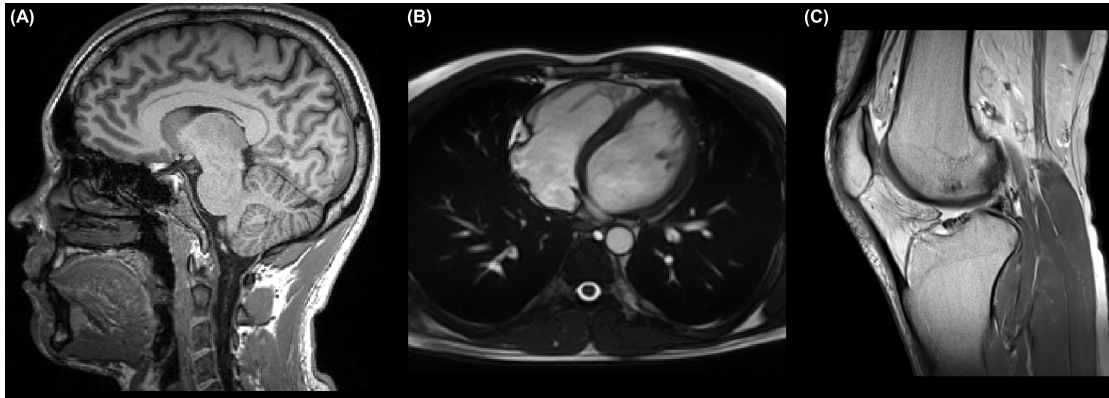


Figure 1.1 – Example MR images acquired in a brain (A), heart (B) and knee (C) of a healthy subject.

the means to quantitatively characterize tissues and gain further insight into microstructural alterations caused by diseases [6]. In neurological applications, the measurement of water proton relaxation rates (i.e., relaxometry) represents one major set of quantitative imaging methods sensitive to the brain tissue microstructure. Since MR relaxation mechanisms depend on complex interactions among protons and between protons and their surrounding lattice, relaxometry measurements reflect the biophysical environment of the tissue under investigation (e.g., concentration of water molecules, macromolecules, and paramagnetic atoms). For instance, a reduction in extra-cellular water content results in the shortening of T_1 and T_2 , whereas its accumulation prolongs both relaxation times. Degradation of myelin – the insulating sheath with the highest concentration of macromolecules in the brain that guarantees signal propagation among neurons [7] – results in increased relaxation times while reducing MT. On the contrary, the accumulation of paramagnetic atoms, with iron being the most abundant in brain tissues, shortens relaxation times. More challenging is, however, the reverse inference that relates changes in the measured MR signal to microstructural processes. For instance, myelination of brain tissues during early development shortens both T_1 and T_2 – yet these changes may as well be due to iron deposition. Complex models have been thus explored to ascribe the measured MR signal to the underlying microstructural composition – usually obtainable only with ex vivo histology – at the sub-voxel level. Here, a case of interest is the estimation of the brain myelin water content from the multicompartiment modeling of T_2 relaxation curves used in myelin water imaging (MWI) studies [8]. However, the larger amount of data points required in these cases usually entails longer acquisition times and the increased complexity of the employed models may hinder the inference and undermine the stability of the solution.

Nonetheless, during the past years, the exhibited sensitivity and specificity of qMRI acquisitions towards the microstructural properties of brain tissues drove the investigation of qMRI metrics as biomarkers for alterations caused by disease [9]. Despite these efforts, the practical use of qMRI in clinical settings today is still hindered by difficulties in delivering accurate quantification in acquisition times comparable to conventional imaging. Additionally, to exploit the better comparability of qMRI, normative values of physical parameters in healthy

tissue are required, enabling the comparison of tissue properties from a single patient to normal values and potentially improving diagnosis and follow-up assessments by correlating parameter variations with microstructural changes.

1.1 Thesis rationale and outline

With a focus on brain relaxometry and MWI, this thesis investigates novel methods to promote the practical utility and increase the value of qMRI in clinical settings. More specifically, this goal is first pursued by optimizing acquisition and reconstruction methods, shortening the required scan times for retrieving quantitative measurements of microstructural tissue composition. Furthermore, datasets of normal physical parameters in healthy tissues are collected and solutions for abnormal tissue detection and characterization on the single-patient level are proposed.

The content of the thesis is structured as follows:

- **Chapter 2** provides the relevant background on the topics discussed in this thesis, starting from an explanation of the physical principles related to MRI acquisitions and ending with a brief discussion on techniques developed for the automatic analysis of MR images.
- **Chapter 3** reviews acquisition strategies developed for myelin imaging with MRI. Advantages and pitfalls of the different approaches are compared and discussed.
- **Chapter 4** investigates the acceleration of a pulse sequence designed for MWI, the multi-echo gradient and spin echo sequence, with parallel imaging to improve resolution and brain coverage with respect to the state of the art and to further reduce the scan time. As a first validation step, the derived myelin water fraction (MWF) maps are compared to values derived from conventional multi-echo spin echo acquisitions.
- **Chapter 5** explores the direct estimation of MWF maps from single-compartment relaxometry data. Although the potential of deriving microstructural features from multivariate models of relaxometry data has been previously shown, prior studies relied on protocols with long acquisition times or used models whose complexity hinder their stability or generalizability. Here, a fast protocol for brain relaxometry is investigated in the data-driven estimation of MWF values derived from a conventional MWI analysis.
- **Chapter 6** focuses on developing a method for the clinical application of qMRI. More specifically, the clinical value of fast brain relaxometry acquisitions in combination with population-derived norms is explored. An acquisition protocol tailored towards clinical practice is proposed for whole brain T_1 and T_2 relaxometry. Norms are derived from a healthy cohort by modeling the relaxation times inter-subject variability with age and gender. The potential of the normative atlases in the detection of brain tissue alterations is tested in example patient case studies.
- **Chapter 7** introduces a tailored T_1 mapping technique for a comprehensive assessment of the normal maturing brain. Following the same rationale as in Chapter 6,

age-dependent models describing the normal brain maturation with respect to changes in volume and T_1 relaxation times are established.

- **Chapter 8** discusses the findings presented in this thesis with the aim of putting it in a more general perspective. Additional studies investigating preliminary clinical applications and outcomes are discussed, as well as future work needed to further improve and validate the developed methods.

2 Background

This chapter provides an overview of the physical principles and technical details related to MRI acquisitions. This overview starts by illustrating the NMR phenomenon and how it is exploited to generate MR images, followed by a description of qMRI techniques. The next section summarizes methods specifically designed to accelerate MRI scans; finally, the last section briefly discusses techniques developed for the automatic analysis of brain MR images.

Additional and more in depth details regarding the topics presented in this chapter can be found in Brown et al. [10], McRobbie et al. [11], Bernstein et al. [12], and Tofts [6].

2.1 The Nuclear Magnetic Resonance phenomenon

2.1.1 Magnetization

Atomic nuclei of chemical elements with an odd number of protons and/or neutrons exhibit an intrinsic spin angular momentum, a quantum property that can assume only a limited set of discrete values. In nuclei with a non-zero spin, a magnetic dipole moment is always associated with the angular momentum, to which it is directly proportional through the constant γ , an inherent characteristic of the considered nucleus defined as the *gyromagnetic ratio*. The magnetic moment is the reason why such nuclei can interact with an external magnetic field (\mathbf{B}_0). This interaction is at basis of the NMR phenomenon. It should be noted that, besides few references to quantum mechanics, the classical model (i.e., “rotating particles”) is used in the following to describe the basics of MRI.

The dominant nucleus in MRI applications is hydrogen, ^1H ($\gamma/2\pi = 42.58 \text{ MHz/T}$), a single, positively charged proton that is abundant in the human body due to its presence in water and organic molecules. In the absence of an external magnetic field, the magnetic moments of protons are randomly oriented in different directions, and thus a set of ^1H nuclei would show no bulk magnetization (Figure 2.1A). In the presence of a high external \mathbf{B}_0 , ^1H nuclei magnetic moments experience a force towards the direction of \mathbf{B}_0 . More specifically, the experienced

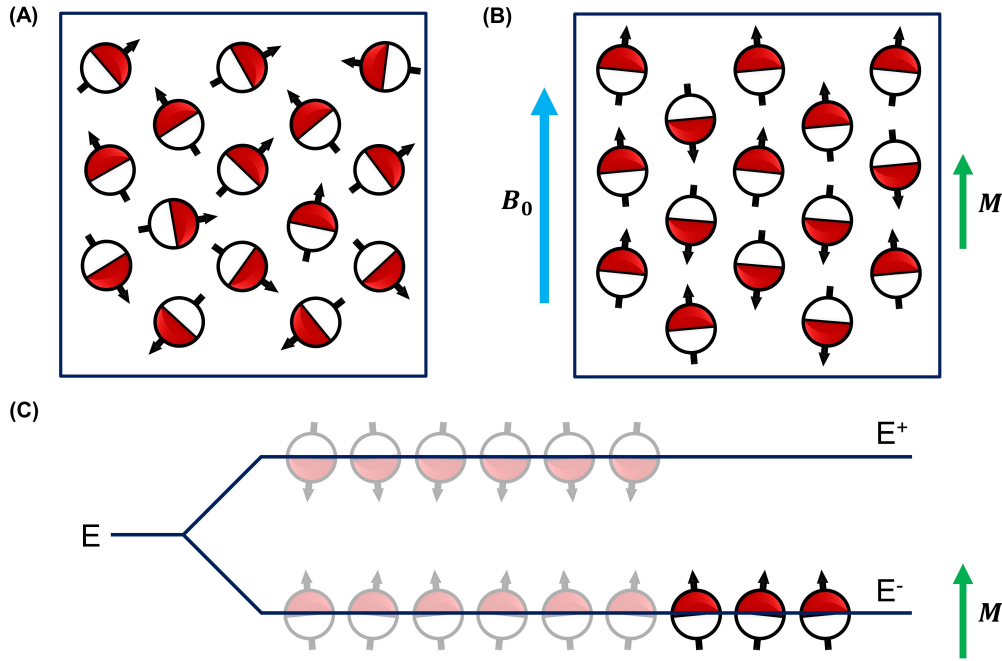


Figure 2.1 – (A) Protons and associated magnetic moments randomly distributed in the absence of an external magnetic field (B_0). (B) Magnetic moments aligned parallelly or anti-parallelly to an external B_0 . (C) An excess of protons in the parallel (i.e., lower energy) state generates a net magnetization (M).

torque causes the magnetic moments to precess around the direction of B_0 with an angular frequency (ω_L , called the Larmor frequency) that solely depends on B_0 :

$$\omega_L = \gamma B_0 . \quad (2.1)$$

Eq. (2.1) implies that all particles experiencing the same B_0 will precess with the same ω_L . Additionally, while some magnetic moments will align parallel to B_0 (lower energy state), others will retain an anti-parallel spin (higher energy state) (Figure 2.1B). The ratio between the number of spins in the two states follows the Boltzmann distribution:

$$N_{E^-} / N_{E^+} = e^{\left(\frac{\gamma h B_0}{k_B T}\right)} , \quad (2.2)$$

where h is the Planck's constant, k_B is the Boltzmann's constant, and T is the absolute temperature. At body temperature and assuming an external B_0 of 1.0 T, an excess of three spins in the parallel state is observed over a population of a million spins. Despite being small, this excess causes the rise of a net magnetization (M) within any sample with high ^1H content, as the human body, in the presence of an external magnetic field (Figure 2.1C).

In the following sections, the external magnetic field is always assumed to follow the z-direction ($B_0 = B_0 \hat{z}$) and the x-y plane will be thus referred to as the *transverse plane*. As for the magnetization M , its longitudinal component lies along the z-axis:

$$M_{\parallel} = M_z = M_z \hat{z} , \quad (2.3)$$

2.1. The Nuclear Magnetic Resonance phenomenon

whereas its transverse component lies in the x-y plane:

$$\mathbf{M}_{\perp} = \mathbf{M}_{xy} = M_x \hat{x} + M_y \hat{y} . \quad (2.4)$$

2.1.2 Radio-frequency excitation

The net magnetization that arises in the body resulting from the application of an external magnetic field is many orders of magnitude weaker than \mathbf{B}_0 and points in the same direction. These conditions impede to directly measure \mathbf{M} . Here is where the NMR phenomenon comes into play, enabling to probe the body magnetization based on the interaction between the proton spins and an electromagnetic radiation. More specifically, radio frequency (RF) pulses, whose magnetic field component (\mathbf{B}_1) points perpendicular to \mathbf{B}_0 , are employed to disturb the spins equilibrium state. Due to the resonance condition, a set of protons will absorb RF radiation oscillating at the same frequency. As a result, while applying an RF pulse, \mathbf{M} describes a spiral motion from the longitudinal direction to the transverse plane, resulting in a transversal magnetic component that can be measured. In the case of a single rectangular RF pulse of duration t_p , the angle by which \mathbf{M} is tilted into the transverse plane, referred to as *flip angle* (α), can be approximated as:

$$\alpha = \gamma B_1 t_p , \quad (2.5)$$

A 90° pulse turns \mathbf{M} fully into the transverse plane (i.e., $M_z(t_p) = 0$). By doubling B_1 or t_p , \mathbf{M} can be longitudinally inverted (i.e., $M_z(t_p) = -M_z(0)$) and this is referred to as a 180° or inversion pulse.

2.1.3 Relaxation

The precessing transverse component M_{xy} creates an electromagnetic field that can be measured using a receiving coil tuned to the resonance frequency. The produced signal is known as Free Induction Decay (FID), which decreases exponentially after the RF excitation. In fact, after experiencing an RF pulse, relaxation mechanisms occur, driving the spins towards their initial equilibrium condition. Such relaxation processes involve the recovery of the longitudinal magnetization and the decay of the transverse magnetization. These two mechanisms can be described separately and are characterized by two time constants, T_1 and T_2 , respectively.

The recovery of the longitudinal magnetization is due to the dissipation of the gained energy through the interaction between protons and the surrounding lattice. Assuming a complete recovery after an excitation with a 90° pulse, the longitudinal magnetization follows an exponential growth to the equilibrium value, M_0 :

$$M_z(t) = M_0(1 - e^{-t/T_1}) . \quad (2.6)$$

After a time interval of about five T_1 , the recovery of M_z can be considered complete (Figure 2.2B).

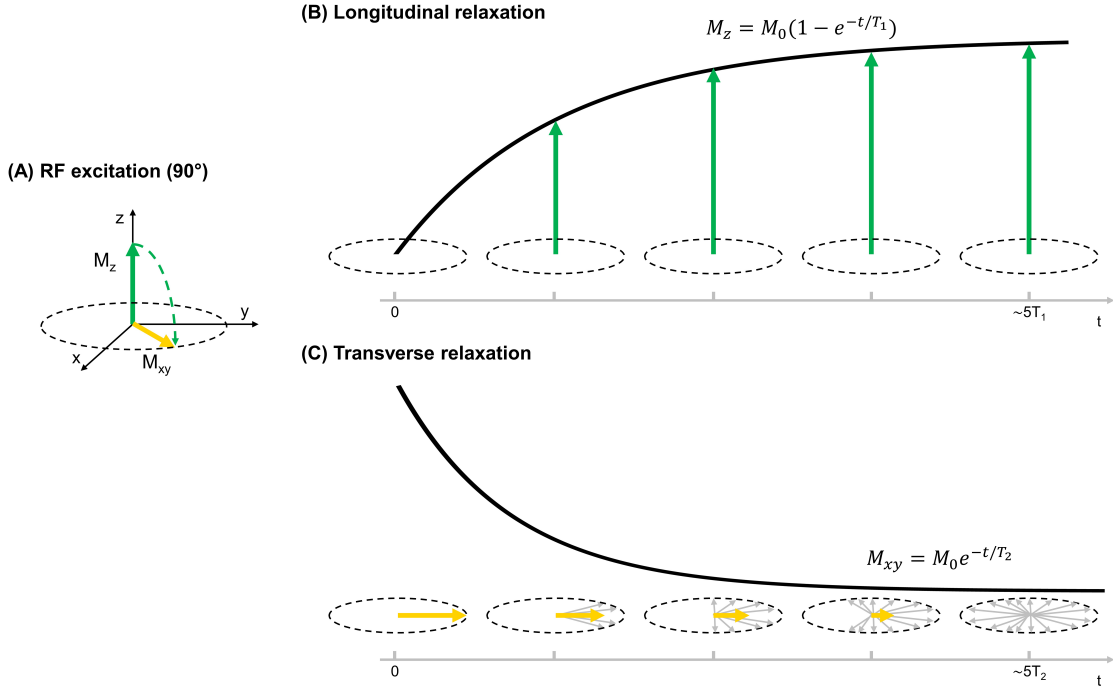


Figure 2.2 – (A) Spins excitation with an RF pulse flipping the magnetization of 90°. Relaxation of longitudinal (B) and transverse (C) magnetization after excitation. Time scales differ between (B) and (C).

The loss of phase coherence among spins after an RF excitation results in the decay of the transverse relaxation (Figure 2.2C). For instance, after applying a 90° pulse, the decay of the transverse magnetization follows an exponential curve described by the time constant T_2 :

$$M_{xy}(t) = M_0 e^{-t/T_2} . \quad (2.7)$$

In reality, B_0 inhomogeneities within the investigated sample cause an additional dephasing of spins, causing the FID signal to decay even faster and with the time constant T_2^* (“apparent T_2 ”) smaller than T_2 . To avoid this additional signal loss, a rephasing of this source of dispersion can be achieved by applying a 180° pulse in the transverse plane that inverts the phase of the spins. Since the spins now precess again in the same direction and with the same frequency, they will rephase and generate a recordable signal called spin echo. The amplitude of the measured NMR signal now depends only on T_2 and the time interval between the RF excitation and the echo generation, referred to as the echo time (TE):

$$M_{xy}(TE) = M_0 e^{-TE/T_2} . \quad (2.8)$$

Relaxation time constants T_1 and T_2 are determined by the chemical environment of the spins and are thus tissue-specific (Figure 2.3); the specific differences between these time constants seen in different biological tissues are the reason for the utility of MRI in medicine. How to create a tomographic image based on the NMR phenomenon is illustrated in the next section.

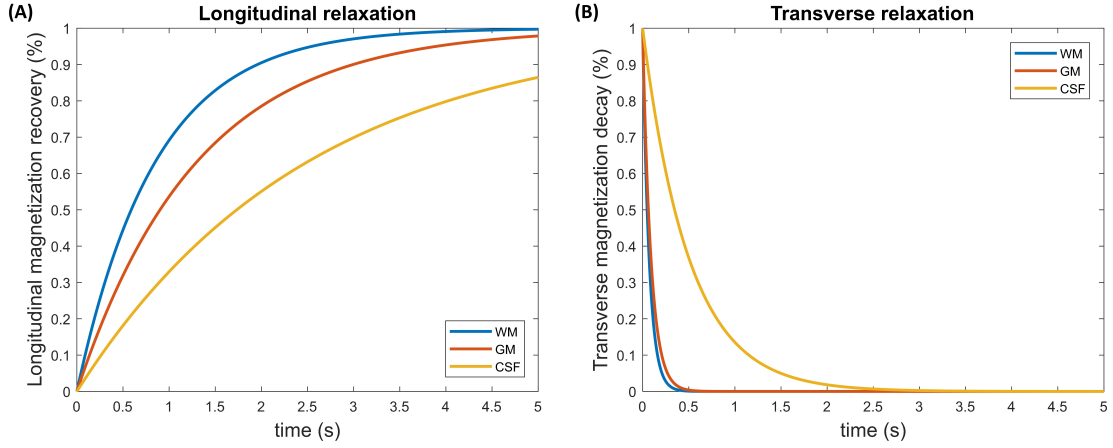


Figure 2.3 – Evolution of longitudinal (A) and transverse (B) relaxation curves in example brain tissues with different relaxation times ($T_{1,WM} = 850$ ms, $T_{1,GM} = 1300$ ms, $T_{1,CSF} = 2500$ ms; $T_{2,WM} = 70$ ms, $T_{2,GM} = 90$ ms, $T_{2,CSF} = 500$ ms). WM: white matter; GM: gray matter; CSF: cerebrospinal fluid.

2.2 Magnetic Resonance Imaging

2.2.1 Spatial encoding and k-space

The NMR signal recorded by a receiving coil close to a set of spins undergoing relaxation does not contain any information regarding the spatial location of the spins. To spatially localize the NMR signal during an MRI acquisition, the external magnetic field \mathbf{B}_0 is altered using additional magnetic fields generated by gradient coils. More specifically, a sequence of linear magnetic field gradients is applied to alter \mathbf{B}_0 across a spatial dimension, and, consequently, change the precession frequency of spins depending on their location. For instance, a linear gradient along the longitudinal direction (\mathbf{G}_z) changes the resonant frequency of spins as follows:

$$\omega_L(z) = \gamma(B_0 + zG_z) . \quad (2.9)$$

The alteration of the Larmor frequency will be thus spatial-dependent and specific locations can be selectively excited by employing RF pulses with a matching frequency to $\omega_L(z)$. Applying linear gradients also in the transverse plane (\mathbf{G}_x and \mathbf{G}_y) allows to spatially encode the NMR signal in all three dimensions of space.

In 2D imaging, first a slice-selective gradient \mathbf{G}_z is applied concurrently to the RF pulse to excite the plane of interest along the z-direction. The position of the excited slice depends on the RF pulse frequency, whereas its thickness can be varied by changing the RF pulse bandwidth or the amplitude of \mathbf{G}_z . A phase-encoding gradient (\mathbf{G}_y) and a frequency-encoding gradient (\mathbf{G}_x) are then employed to record the signal from each voxel in the selected slice. Prior to the recording of the NMR signal, the phase-encoding gradient \mathbf{G}_y is applied causing the spins to accumulate phase differences depending on their spatial location along the y-direction. \mathbf{G}_y needs to be repeated as many times as the number of lines in the phase-encoding direction. The signal readout is then performed by means of the frequency encoding gradient

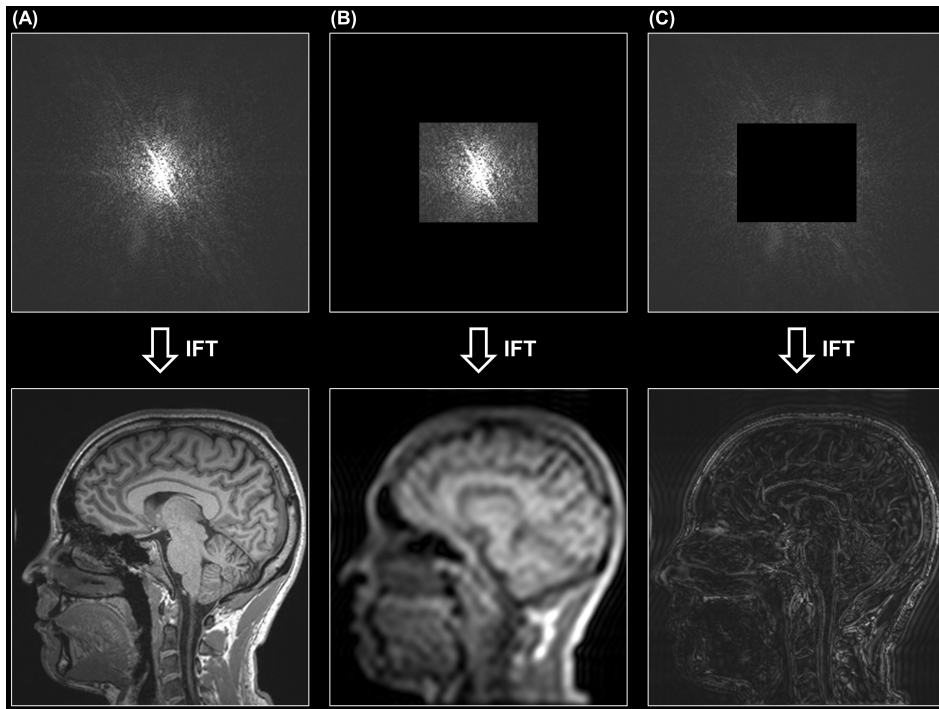


Figure 2.4 – MR brain images reconstructed from the whole k -space (A), only the k -space center (B), and only the k -space outer samples (C). IFT: Inverse Fourier Transform.

G_x , applied to encode the spatial frequency of each voxel in the last spatial dimension.

The slice-selective excitation performed in 2D imaging has one major drawback: the shape of the slice profile. In fact, an ideal rectangular profile could be generated only by an RF pulse whose waveform corresponds to a sinc-function of infinite duration (small flip angle regime). However, truncated sinc-functions need to be employed in practice, resulting in spins that experience different flip angles along the slice profile (i.e., the excitation profile is not perfectly rectangular). This limitation is overcome in 3D imaging, where a non-selective RF excitation of the entire volume is used. However, an additional dimension needs to be spatially encoded by playing a phase-encoding gradient also along the z -direction prior to frequency encoding. As more phase-encoding steps are required, 3D acquisitions usually entail longer scan times.

The encoded spatial frequencies for each location in the imaged sample are used to fill a raw data matrix, known as k -space. The Inverse Fourier Transform operator is applied to the k -space entries to evaluate the contribution of each frequency to the overall recorded signal resulting in a conventional MR image (see Figure 2.4). It should be noted that the k -space voxels represent spatial frequencies and do not have a one-to-one correspondence with the final image. Low spatial frequency information is encoded in the center of the k -space, which determines the overall contrast of the resulting image (Figure 2.4B). The outer k -space contains the high frequency information defining the edges and fine details of the resulting image (Figure 2.4C).

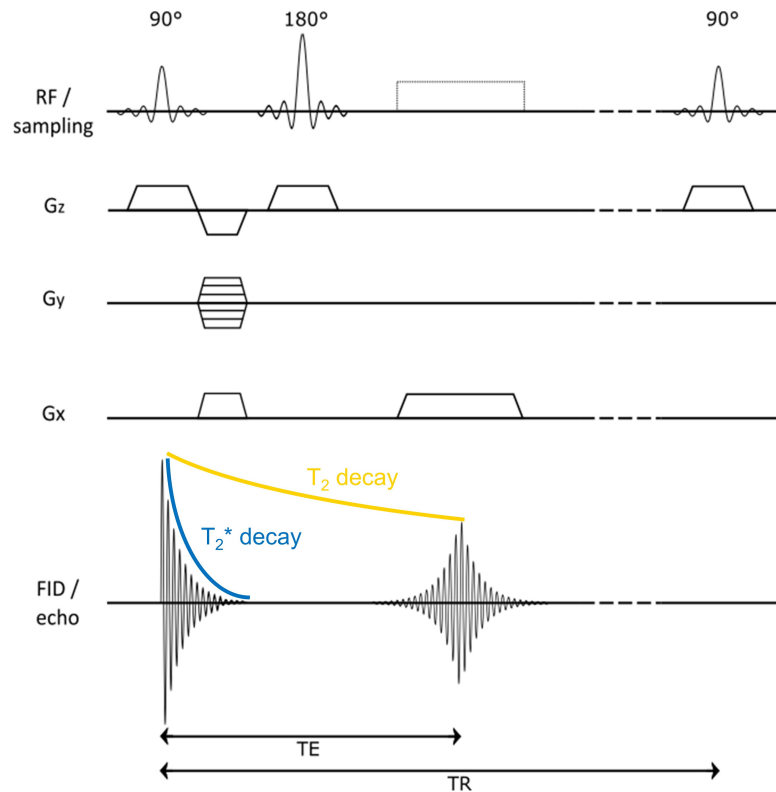


Figure 2.5 – Spin echo sequence timing diagram with corresponding generated FID and echo signals.

2.2.2 Pulse sequences and MR contrasts

An MR pulse sequence is defined as a series of RF pulses and gradients, which are played out with a precise timing in order to manipulate the magnetization and obtain an image with the desired contrast. This section provided an overview over the most basic MR pulse sequences.

Spin echo sequence

As already introduced in **Section 2.1.3**, a spin echo is formed after applying two consecutive RF pulses of 90° and 180° , respectively. The maximum amplitude of the echo is achieved after a time interval TE equal to twice the time delay between the two RF pulses. In a standard 2D single-echo spin echo experiment, to sample all phase-encoding directions and, if applicable, multiple slices, this pulse sequence is repeated at regular time intervals of duration known as the repetition time (TR). Since in one TR only a single phase-encoding line is acquired, the scan time of this sequence is usually quite long. The acquisition time could be reduced by interleaving the sampling of multiple slices within one TR. Figure 2.5 shows the timing diagram for a 2D single-echo spin echo experiment and the corresponding evolution of the FID and spin echo signals.

The main advantage of this sequence is that T_1 -, T_2 - or PD-weighted contrasts can be obtained simply by varying the TR and/or the TE. For instance, using a long TR and a short TE would

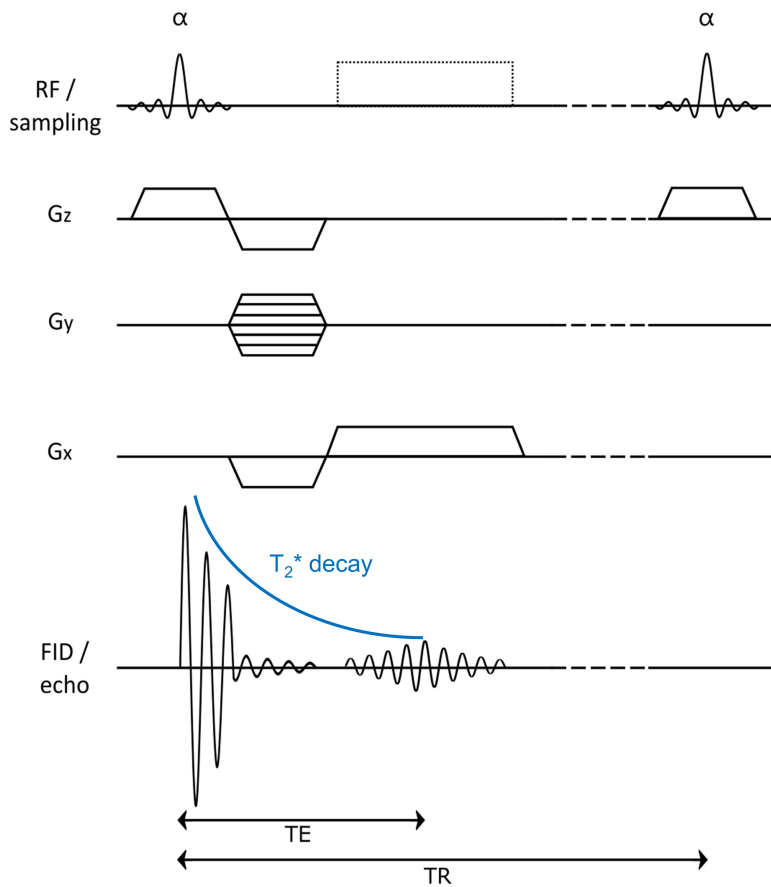


Figure 2.6 – Gradient echo sequence timing diagram with corresponding generated FID and echo signals.

result in an image contrast mostly PD-weighted (Figure 2.7A), whereas a long TE would determine a T_2 -weighted contrast (Figure 2.7B). T_1 -weighted images can be obtained employing short TR and TE.

Gradient echo sequences

Different to spin echo sequences, gradient echo (GRE) sequences do not employ a second RF pulse to generate an echo but use a gradient reversal in the frequency encoding direction to dephase and subsequently rephase the FID signal to form an echo. More specifically, after the RF excitation with a flip angle usually smaller than 90° , a pre-phasing gradient is applied to cause a phase dispersion of spins and, consequently, a faster decay of the FID signal. Spins are then quickly refocused by applying a reverse gradient. The maximum amplitude of the resulting echo occurs when the area under the reverse gradient lobe matches that of the pre-phasing gradient. Since only one RF pulse needs to be applied, GRE sequences allow for shorter TEs in comparison to spin echo sequences. The timing diagram of a GRE sequence is depicted in Figure 2.6 along with the corresponding evolution of the FID and echo signals.

GRE is usually the sequence of choice for fast 3D imaging. In fact, when small flip angles

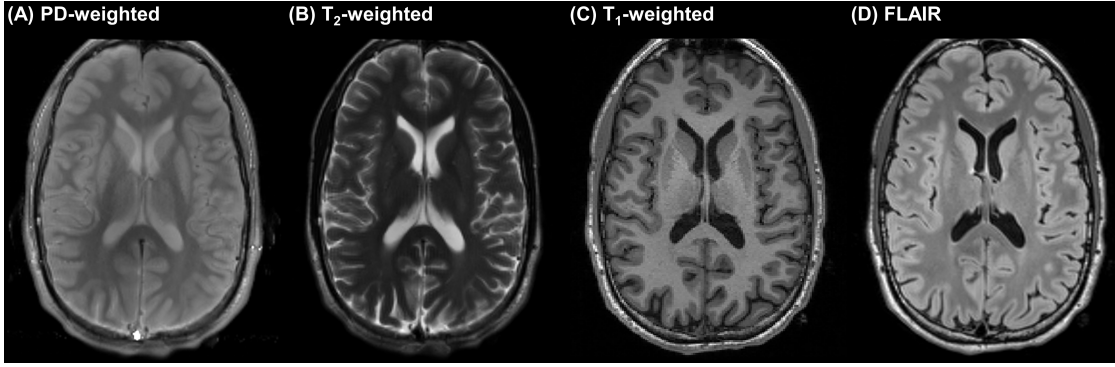


Figure 2.7 – Example brain MR contrasts acquired with the spin echo (A-B), Magnetization Prepared Rapid Acquisition Gradient Echo (MPRAGE) (C), and FLuid-Attenuated Inversion Recovery (FLAIR) (D) sequences.

are employed, the longitudinal magnetization is barely perturbed and fully recovers quickly, allowing for short TRs. However, with TRs shorter for example than five times T_2 , a transverse magnetization is retained before the next excitation. Therefore, when employing a GRE sequence to retrieve a T_1 -weighted contrast, the remaining transverse magnetization is usually dephased with a gradient (“crusher gradient”) or RF spoiling, in order to keep the TR short and, consequently, the scan time. This sequence variant is referred to as fast-low-angle-shot (FLASH) or spoiled gradient recalled echo (SPGR) sequence. The resulting contrast also depends on T_2^* , whose influence can be reduced by shortening the TE.

Inversion recovery sequences

Inversion recovery (IR) offers an additional way to manipulate image contrast according to T_1 variations among tissues. In an IR sequence, an inversion is applied to invert the longitudinal magnetization, which then recovers with the following time evolution:

$$M_z(t) = M_0(1 - 2e^{-t/T_1}) . \quad (2.10)$$

After a delay denoted as the inversion time (TI), the main pulse sequence is played out. As the magnetization of tissues with different T_1 values recovers with a different rate, T_1 -weighting is imprinted in the resulting contrast. An additional source of contrast can be introduced in the image depending on the chosen main pulse sequence. Two IR sequences of interest here are the Magnetization Prepared Rapid Acquisition Gradient Echo (MPRAGE) and the FLuid-Attenuated Inversion Recovery (FLAIR) sequences.

The MPRAGE is one of the most widely used sequences for 3D T_1 -weighted imaging of the human brain [13]. During an MPRAGE acquisition, an inversion pulse is followed by a series of spoiled GREs to rapidly sample multiple k-space lines within the same TR and generate a strong T_1 -weighted contrast between brain tissues (Figure 2.7C). The obtained T_1 -weighting depends on the chosen TI and flip angles of the GRE readout.

In the FLAIR sequence, the IR preparation module is used to selectively suppress the signal of spins with a given T_1 , specifically those of the cerebrospinal fluid (CSF) in brain applications [14]. In fact, in T_2 -weighted images of the brain, the hyperintense signal of CSF may cause problems in the detection of abnormalities as lesions, oedema, or tumours. However, since spins in the CSF have a considerably longer T_1 than the other brain tissues, an IR sequence can be used to specifically suppress the CSF signal. In the FLAIR sequence, this effect is achieved by employing an inversion pulse and a TI that coincides with the time when the CSF magnetization traverses the null line (around 0.69 times the T_1 of CSF). A spin echo sequence is then usually employed to fill the k-space and introduce a T_2 -weighted contrast into the acquired image (T_2 -FLAIR, Figure 2.7D).

2.3 Quantitative MRI

Although conventional MR image contrasts can be weighted in a certain way towards one or more physical properties that discriminate different tissues – which is one of the advantages of MRI – the obtained contrast still depends on the combination of the whole set of physical properties, as well as the chosen imaging parameters and the employed hardware. Any comparison of image intensities among different subjects, MRI scanners or in longitudinal studies is thus precluded. qMRI techniques allow moving from such relative contrast information to a single, absolute measure of one or more separate tissue properties, thus providing a mean to quantitatively characterize tissues and the potential to gain further insight into microstructural alterations caused by diseases. This chapter provides an insight into different qMRI methods, with a focus on T_1 and T_2 relaxometry, and it discusses the potential clinical applications of these measurements.

2.3.1 T_1 mapping

IR spin echo

The gold standard technique for measuring T_1 values is based on the IR spin echo sequence. The sequence is played out multiple times with different TIs to generate and record multiple spin echoes with different T_1 -weighting. The acquired spin echo amplitudes are then fitted to the signal evolution described in Eq. 2.10 to estimate T_1 . However, the need for multiple repetitions and a long TR – required to allow the longitudinal magnetization to fully recover before the next inversion – usually result in long acquisition times.

Look-Locker

The Look-Locker sequence represents a common alternative to the IR spin echo sequence [15]. In a Look-Locker acquisition, GRE readouts with small flip angles are applied at different TIs spaced by a fixed time interval (τ), allowing the acquisition of many samples of the longitudinal

recovery within the same TR. The longitudinal recovery is, however, altered by the applied flip angles, causing systematic biases when estimating the time constant (T_1^*). However, T_1^* only depends on the flip angle, τ , and T_1 :

$$T_1^* = \frac{\tau}{(\tau/T_1) - \log_e[\cos(\alpha)]}, \quad (2.11)$$

allowing for T_1 to be estimated from the acquired data. As all the samples needed to fit T_1 can be measured during a single recovery of the longitudinal magnetization, the Look-Locker sequence has a shorter acquisition time compared to the IR spin echo sequence.

MP2RAGE

Another T_1 mapping approach of interest is the Magnetization Prepared 2 Rapid Acquisition Gradient Echoes (MP2RAGE), a 3D sequence originally introduced to provide T_1 -weighted images with a reduced bias field in comparison to an MPRAGE acquisition [16]. Additionally, it provides the means to estimate T_1 parametric maps.

In the MP2RAGE sequence (Figure 2.8A), after an adiabatic inversion pulse, two GRE readout blocks are employed to sample two T_1 -weighted images at different TIs (GRE₁ and GRE₂, Figure 2.8B). The effective TI₁ and TI₂ of the two GRE blocks correspond to the time interval between the inversion pulse and the sampling of the respective k-space center. Subsequently, GRE₁ and GRE₂ are combined in a uniform T_1 -weighted image – hereafter referred to as UNI (Figure 2.8B) – as follows:

$$UNI = \text{real} \left(\frac{GRE_1^* GRE_2}{|GRE_1|^2 + |GRE_2|^2} \right), \quad (2.12)$$

with GRE_1^* being the complex conjugate of GRE_1 . The UNI shows a T_1 -weighted contrast with reduced B_1 field inhomogeneity as well as decreased T_2^* and PD contrast influence compared to an MPRAGE image. Since the contrast in the UNI image depends almost exclusively on T_1 , a T_1 map (Figure 2.8B) can be derived using Bloch simulations based on the employed sequence parameters [16].

2.3.2 T_2 mapping

Multiple single-echo spin echo

The reference approach for T_2 mapping is based on the spin echo sequence. As already introduced in **Section 2.1.3** and **Section 2.2.2**, the amplitude of a spin echo formed by consecutively applying a 90° and 180° RF pulse ideally only depends on M_0 , T_2 , and the chosen TE (see Eq. 2.8). Therefore, similarly to what is done in an IR spin echo experiment for T_1 mapping, the spin echo sequence is repeated multiple times with different TEs to generate and record multiple spin echoes with different T_2 -weighting. The signal evolution described

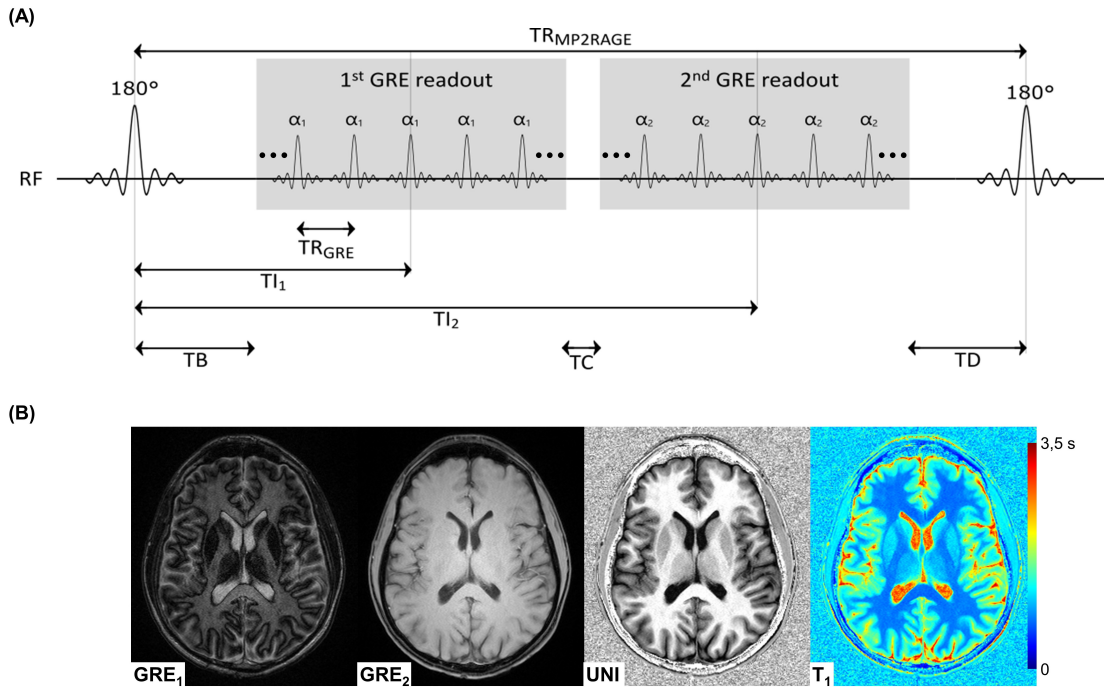


Figure 2.8 – (A) MP2RAGE pulse sequence timing diagram. (B) Representative brain axial slices obtained with the MP2RAGE sequence. Part (A) is adapted with permission from Marques et al. [16].

in Eq. 2.8 is then fitted to the acquired amplitudes to estimate T_2 . The used signal model assumes that the longitudinal magnetization is fully recovered within one TR, which is thus usually set to long values. Although achieving high accuracy in the estimation of T_2 , repeating the sequence to sample multiple TEs usually entails long acquisition times.

Multi-echo spin echo

The multi-echo spin echo (MESE) sequence is commonly employed for T_2 mapping as alternative to the single-echo spin echo. In a MESE acquisition, an entire train of multiple 180° pulses is applied after the 90° excitation in order to keep rephasing the spins and generate multiple echoes within the same TR [17]. Due to some irreversible dephasing of the protons, the amplitude of the acquired echoes still decreases exponentially over time with the time constant T_2 (see Figure 2.9). Since all the required samples to fit T_2 are measured during a single TR, the MESE sequence has a shorter acquisition time compared to the single-echo spin echo sequence.

Multi-echo gradient and spin echo

A faster way of acquiring T_2 decays compared to the MESE was proposed by Does et al. [18] and makes use of the gradient and spin echo (GRASE) sequence [19]. The multi-echo GRASE sequence shares the same RF pulse scheme with the MESE, but combines it with an echo-planar imaging (EPI) readout [20]. EPI pulse sequences employ a train of gradient readouts of

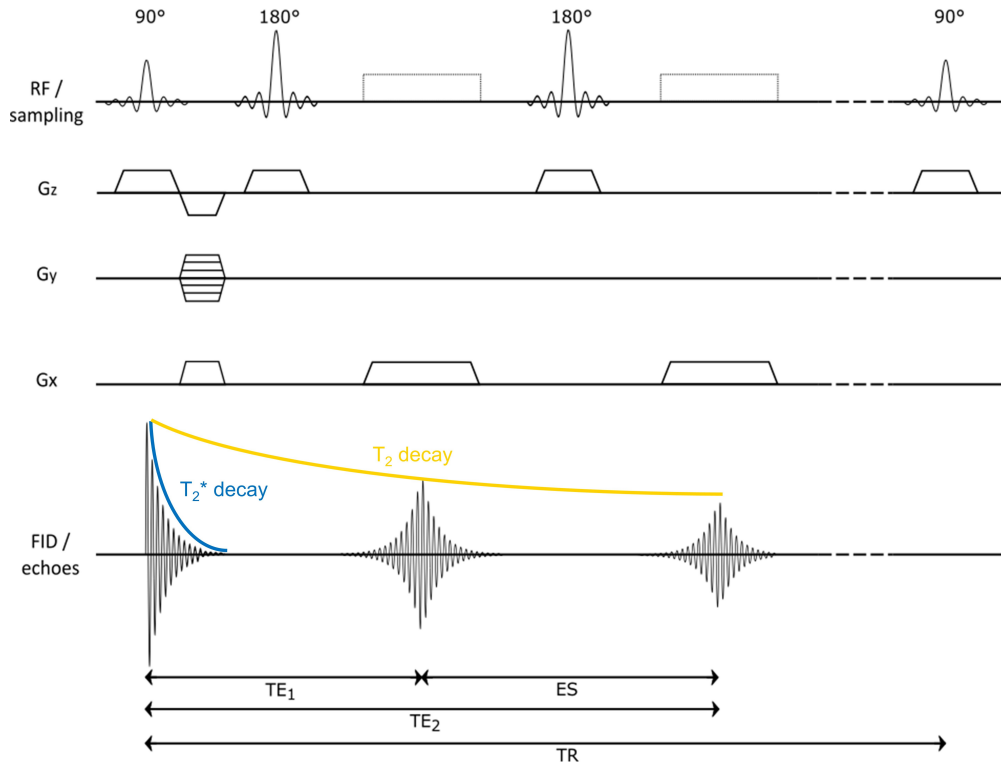


Figure 2.9 – Multi-echo spin echo sequence timing diagram with corresponding generated FID and multiple echo signals.

alternating polarities to rephase the FID signal multiple times (or RF spin echoes), enabling to sample multiple phase encoding lines from a single event. The multi-echo GRASE sequence centers an EPI readout around each spin echo to acquire more than one k-space line per echo. Compared to a MESE sequence, the acquisition time is shortened by a factor equal to the number of EPI readouts per spin echo. However, EPI acquisitions are more prone to image artifacts such as ghosting in the phase-encoding direction or blurring induced by the T_2^* modulation of k-space intensities.

2.3.3 Simultaneous multi-parametric mapping

DESPOT

The Driven Equilibrium Single Pulse Observation of T_1 and T_2 (DESPOT) was developed to measure the longitudinal and transverse relaxation times in a short scan time, at high resolution and covering the whole brain [21]. DESPOT involves the acquisition of a series of spoiled GREs over a range of different flip angles for T_1 relaxometry [22] and a similar GRE pulse sequence without spoiling (the balanced steady-state free precession sequence) for T_2 estimation [23]. Holding the TR constant throughout the acquisition, a linear regression can be used to estimate T_1 from the collected spoiled gradient recalled-echo images. Once T_1 is known, T_2 can be retrieved from the acquired balanced steady-state free precession data,

whose intensity varies linearly with both T_1 and T_2 . Since the relation between the acquired signals and T_1 and/or T_2 can be linearized, only two acquisitions with a different flip angle are needed to accurately estimate both relaxation times, making DESPOT a fast technique.

QRAPMASTER

Another approach for simultaneous T_1 and T_2 mapping is offered by the QRAPMASTER (Quantification of Relaxation times and Proton density by Multi-echo Acquisition of a Saturation-recovery using TSE Readout) framework, also referred to as *synthetic MRI* (SyMRI). QRAPMASTER simultaneously measures T_1 and T_2 relaxation times by combining a multi-echo GRASE sequence with a multi-delay saturation recovery preparation [24]. More specifically, the repetition block of the QRAPMASTER sequence is divided in two phases: a slice selective saturation pulse of 120° is first applied on a specific slice, and a slice-selective multi-echo GRASE acquisition is performed subsequently on a different slice to measure T_2 . A time delay (TD) is introduced between the saturation in each slice and the subsequent multi-echo GRASE sampling. Repeating the sequence with four different TDs and acquiring five echoes for each slice, 20 images are obtained for the subsequent fitting. The T_1 relaxation is thereby encoded through the different TDs; T_2 , in turn, is sampled over the different TEs. The use of a saturation pulse instead of an inversion pulse allows in addition to estimate the local B_1 field. Moreover, knowing T_1 , T_2 and B_1 , the unsaturated magnetization M_0 can be estimated, which is scaled to mimic PD maps.

Magnetic resonance fingerprinting

A distinct acquisition framework in qMRI is offered by Magnetic Resonance Fingerprinting (MRF) [25]. In MRF, the concept of repetitive fixed excitation and readout schemes for retrieving tissue property information is abandoned. In fact, MRF exploits pseudorandomized acquisition parameters that are changed during the scanning procedure. This results in different tissues producing a unique resonance signal (i.e., “fingerprint”) whose evolution strictly depends on the whole set of physical tissue properties and the MRF pulse sequence design. Prior to image reconstruction, a dictionary is built containing all the possible combination of tissue properties (i.e., T_1 and T_2 values in the most simple case) with the corresponding signal evolution. The reconstruction employs a pattern recognition strategy to find the combination of parameters in the dictionary that yields a fingerprint which matches best the acquired data. All the factors included in the model that was used to generate the dictionary will therefore be retrieved, such as the T_1 and/or T_2 relaxation times of the tissue under investigation.

2.3.4 MR imaging specific to myelin content

To guarantee a rapid transmission of information in the form of electric signals between neurons, axons of vertebrates are enwrapped in myelin [7]. In the central nervous system, the

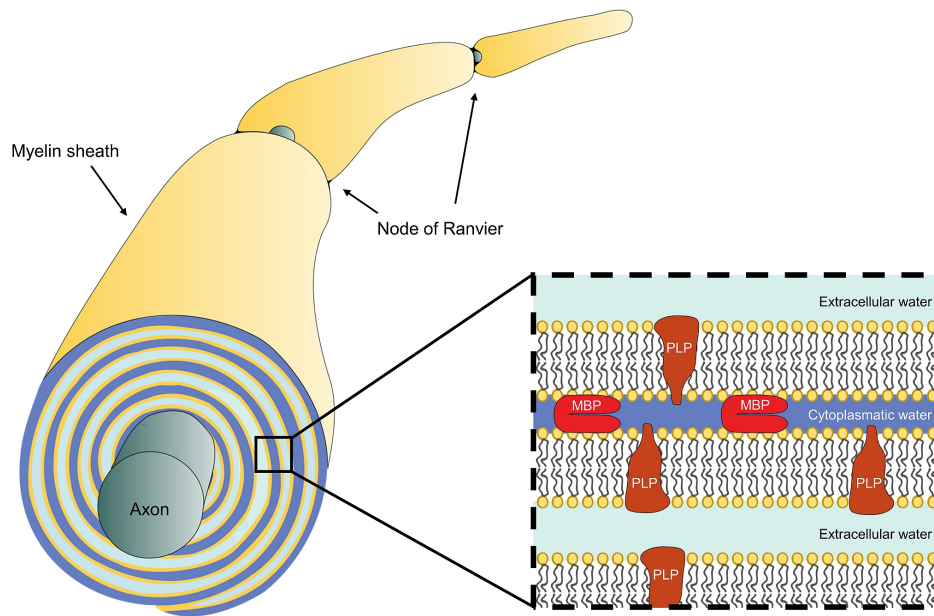


Figure 2.10 – The organization of axonal myelination. A myelin sheath surrounding an axon is shown along with the double bilayers structure composed of oligodendrocyte cell membranes. Gaps between adjacent bilayers are filled with water. Proteolipid Proteins (PLP) constitute about 50% of the protein content in myelin sheaths and Myelin Basic Protein (MBP) 20-30%. PLPs are fundamental to keep the extracellular space between bilayers, whereas the MBPs create adherence between the two bilayers facing the cytoplasmatic space. Adapted with permission from Min et al. [27] and Laule et al. [35].

myelin sheath is composed of repeating units of compacted oligodendrocyte cell membranes, which are organized in double bilayers separated by aqueous cytoplasmic and extracellular gaps of 3-4 nm (Figure 2.10). Contrary to membranes of other cell types which are typically characterized by a 50% weight content of lipids and proteins, myelin membranes are composed of 75–80% lipids and 20–25% proteins [26, 27]. Given this elevated lipid content, the multilayer sheath acts as an electrical insulator that limits the electrical flow through the axonal membrane and constrains the rise of action potentials to small unmyelinated segments called *Nodes of Ranvier* [28]. The resulting saltatory conduction is more energy-efficient and a prerequisite for the evolution of a neuronal network as complex and dense as the human nervous system. Because human cognition, sensation, and motor functions rely on the efficiency of the saltatory conduction [29], compromised myelin integrity often leads to severe cognitive and physical disabilities. Myelin degradation has been linked to many neurological conditions [29–33]; it represents, for example, one major trait of multiple sclerosis (MS), an inflammatory disease that mostly manifests itself as sclerotic plaques in the central nervous system [34].

The excellent soft tissue contrast provided by MRI revolutionized the way these pathologies are studied and monitored [11]. However, regarding myelin-specific acquisitions, the short T_2 (< 1 ms) of macromolecular protons abundant in the lipids and proteins that constitute myelin complicates the possibility to directly image myelin with conventional MRI techniques, (which usually target the signal of mobile water protons with relative long $T_2 > 10$ ms). Hence,

various methods have been and are currently being developed to indirectly probe the myelin content of the brain using quantitative MRI.

Given the vast body of literature around this topic, a comprehensive review on the different strategies developed for the non-invasive and in vivo assessment of brain myelin content is given in **Chapter 3**. The written review, titled “Probing myelin content of the human brain with MRI: A review”, was published in the journal “Magnetic Resonance in Medicine” [36].

2.3.5 On the clinical value of quantitative MRI in the brain

Since the relaxation processes described by the time constants T_1 and T_2 reflect proton-lattice and proton-proton interactions, T_1 and T_2 highly depend on biophysical tissue properties. Therefore, brain tissue alterations such as neuronal cell death, axonal loss and demyelinating processes are reflected by changes in the relaxation times. One target application for relaxometry is MS, a neurodegenerative condition characterized by white matter (WM) and gray matter (GM) focal lesions, as well as a diffuse inflammation of the normal-appearing white matter (NAWM) [34]. T_1 -weighted and T_2 -FLAIR images are the most commonly employed sequences to delineate lesions and formulate a diagnosis. However, such conventional contrasts show low sensitivity towards NAWM inflammation processes and cannot be exploited to quantify the degree of the alterations in lesions and other pathological tissue. MS lesions were found to exhibit prolonged T_1 and T_2 (due to tissue degeneration and myelin loss) and NAWM was reported to present prolonged T_2 (due to inflammation and microedema) [37,38]. Relaxation time variations were also assessed in other disorders such as Parkinson’s and Alzheimer’s diseases. Neuronal loss occurring in Parkinson’s disease was found to be associated with relaxation time alterations; degradation was found in the whole brain [32] or specifically in the brainstem [39], causing the typical motor disorders of the disease. T_2 was found to be prolonged in the WM of Alzheimer’s patients with reported memory loss [40]. T_1 and T_2 measurements may be of interest also in the diagnosis of epileptic patients. For instance, in temporal lobe epilepsy, T_1 and T_2 were found to increase in the WM of the temporal lobe and were suggested as imaging biomarkers for identifying seizure foci locations [41,42].

The aforementioned findings were, however, the result of neuroimaging studies that involved the comparison between groups of individuals, hence precluding any possible inference on the level of a single individual. To exploit the full potential of qMRI, normative values for relaxometry in healthy tissue are required, to which a single-patient can be compared [43,44]. The quantification of changes in physical parameters with respect to normative values will provide better insight to the underlying microstructural changes, promoting the definition of imaging biomarkers for the characterization of pathological tissue, and potentially facilitating the integration of qMRI techniques into the clinical realm.

2.4 MRI acceleration techniques

As described in the previous sections, the steps required to spatially manipulate and localize the NMR signal need to be repeated multiple times to sample the k-space. Therefore, MR acquisitions usually entail longer scan times than other imaging modalities (e.g., computer tomography). To increase patient comfort and the efficiency of MRI scans, many techniques were specifically developed to reduce acquisitions time both in conventional and quantitative MRI. An overview of the most important of these methodologies is presented in this section.

2.4.1 Parallel imaging

One of the simplest strategy to shorten MRI scan times involves reducing the number of k-space lines acquired in the phase-encoding direction, for instance by regularly skipping the sampling of some lines (e.g., every other line). The required acquisition time is then reduced by a factor equal to the ratio between the samples needed to fully cover the k-space (i.e., fully sampled according to the Nyquist-Shannon theorem) and those actually acquired – usually referred to as the *undersampling factor* R . However, as the acquired lines get more distant from one another, this sampling strategy effectively results in a smaller field of view. Hence, aliasing artifacts consisting of replicates of the imaged object in a number equal to R appear along the undersampled phase encoding direction.

Parallel imaging techniques aim at removing such aliasing artifacts by exploiting the redundant information shared among each element of a phased array coil used for the acquisition [45]. Phased arrays are frequently used in modern MRI scanners for that reason. They are made of multiple receiving coils that are more sensitive to MR signal close by and are usually spatially organized to uniformly cover the whole object imaged. In fact, different coil arrays, customized to image a specific body part, have been designed; as for the brain, coils with 20 to 64 receiving channels are conventionally used. In the case of fully sampled k-spaces, the final image is obtained by performing the inverse Fourier transform of the k-space sampled by each receiver followed by the combination of the retrieved images with the root-mean sum of squares. When the k-space is undersampled, parallel imaging methods resolve the aliasing and produce artifact free images by exploiting the redundant information among the receiving channels. This can be achieved either by separating the aliased voxels in the image domain (e.g., SENSE [46]) or by retrieving the missing lines in k-space (e.g., GRAPPA [47]).

SENSE

SENSitivity Encoding (SENSE) is a parallel imaging technique that resolves the aliasing artifacts in the image domain [46,48]. The first step of a SENSE reconstruction is the computation of the coil sensitivity maps, which quantify the signal weighting for each voxel within the receptive field of each coil channel. This is usually achieved by either acquiring a separate low-resolution reference scan or by fully sampling a certain radius around the k-space center. The redundant

information shared among coils is then used to remove the folding artifacts, for instance by formulating an inverse problem that models the transformation of undersampled data to the image space. This problem could be solved for example by minimizing the following cost function:

$$X = \underset{X}{\operatorname{argmin}} \frac{1}{2} \sum_{c=0}^N \|PF\{S_c X\} - Y_c\|_2^2, \quad (2.13)$$

where X represents the current image estimate, Y the acquired undersampled data, P the sampling mask, F the Fourier operator, S the coil sensitivities, and N the total number of available coils. Aliasing artifacts are then iteratively removed by minimizing the cost function with a conjugate gradient descent algorithm. This formulation is usually referred to as conjugate gradient SENSE (cg-SENSE) [48].

One drawback common to all parallel imaging methods is the noise amplification in the retrieved images. The extent of such amplification varies spatially in the image according to the coil geometry and is quantified as g-factor. The number of coils, their spatial distribution and the chosen undersampling pattern influence the g-factor. The signal-to-noise ratio in each voxel of the reconstructed image with parallel imaging ($\text{SNR}_{\text{parallel}}$) compared to a fully sampled one (SNR_{full}) is:

$$\text{SNR}_{\text{parallel}}(x, y) = \frac{\text{SNR}_{\text{full}}(x, y)}{g(x, y)\sqrt{R}}, \quad (2.14)$$

with the $\text{SNR}_{\text{parallel}}$ additionally decreasing with the square root of the acceleration factor R .

GRAPPA

Differently from SENSE, Generalized Autocalibrating Partially Parallel Acquisitions (GRAPPA) recovers the missing data points directly in k-space prior to image reconstruction [47]. GRAPPA assumes that missing k-space data points (i.e., target points) can be recovered as a linear combination of the acquired neighbouring k-space points (i.e., source points). The linear dependency between target and source points is encoded in the GRAPPA kernel (Figure 2.11). Notably, source points from all the available coils are used to reconstruct a single target point for one specific coil. The linear relationship between source and target points can be represented mathematically as:

$$S_{\text{targ}} = W \cdot S_{\text{src}}, \quad (2.15)$$

with S_{targ} being a vector of the same target point across coils, S_{src} a vector of source points for each coil, and W a matrix containing the GRAPPA weights. In Cartesian sampling schemes, weights are assumed to be identical throughout k-space. Therefore, in GRAPPA reconstructions, the GRAPPA kernel is simply slid throughout the k-space, and at each step source points are multiplied to the weights to reconstruct target points according to the kernel configuration (Figure 2.11). Prior to the reconstruction, weights are estimated from fully sampled auto-calibrating signal (ACS) lines, either acquired with an external reference scan with low

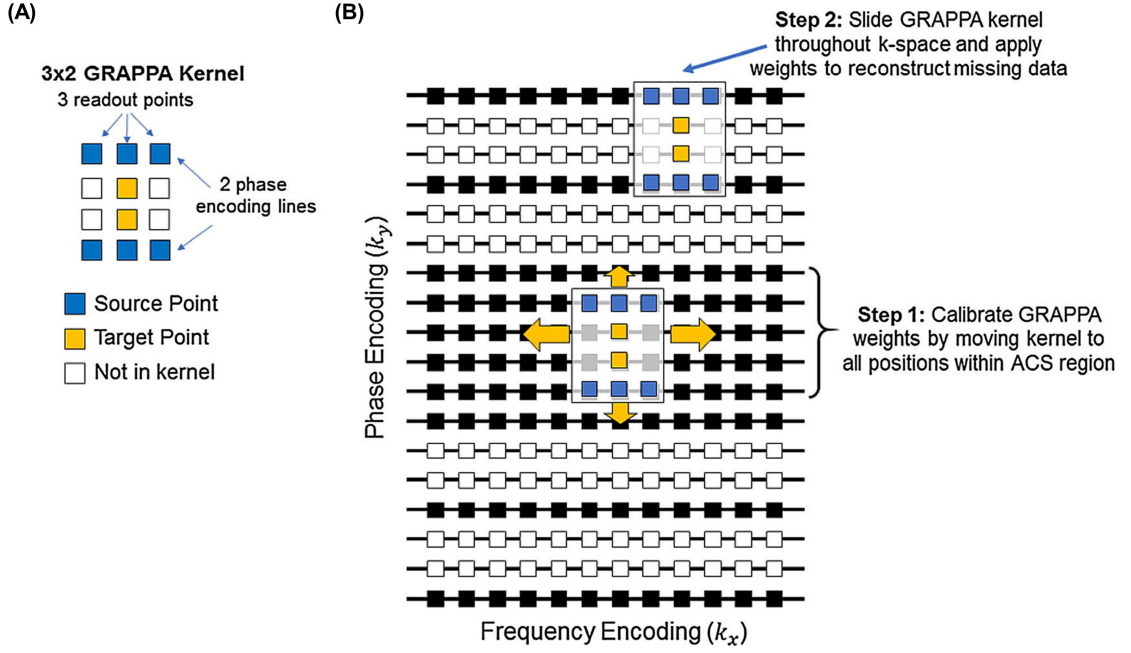


Figure 2.11 – (A) Example GRAPPA kernel for an acceleration $R = 3$ along the phase encoding direction k_y . (B) Schematic representation of GRAPPA reconstruction steps: weights calibration from the fully sampled k-space center (step 1), and reconstruction of missing target points in the outer k-space (step 2). Adapted with permission from Hamilton et al. [45].

resolution or by fully sampling the k-space center. The GRAPPA kernel is slid throughout the ACS lines accumulating the two vectors S_{tar} and S_{src} into matrices for all the available data points. Weights are then estimated by inverting Eq. 2.15 for W .

Like in SENSE reconstructions, GRAPPA results in a reduced image SNR that follows Eq. 2.14. Maps reporting the g-factor for each imaged voxel can be analytically estimated from the GRAPPA kernels.

CAIPIRINHA

Parallel imaging methods can be performed in 3D acquisitions by undersampling both phase encoding directions. However, when high acceleration factors are used, severe folding artifacts and noise amplifications are introduced in the acquired image. The Controlled Aliasing in Volumetric Parallel Imaging (CAIPIRINHA) method was developed to improve parallel imaging outcomes in 3D acquisitions [49]. In CAIPIRINHA, data points in one of the phase-encoding directions are shifted to reduce the minimum distance between aliased points. Although aliasing artifacts do not disappear, this sampling difference compared to conventional undersampling results in an improved aliasing condition as image replicates are pushed towards the corners of the image rather than being concentrated in the middle.

A recent variant of CAIPIRINHA is the wave-CAIPIRINHA strategy, where sinusoidal gradients are applied in the phase encoding directions during frequency encoding, spreading the aliasing

evenly in all three spatial dimensions [50]. This approach takes full advantage of the 3D coil distribution allowing for higher acceleration factors and reduced folding artifacts.

2.4.2 Compressed sensing

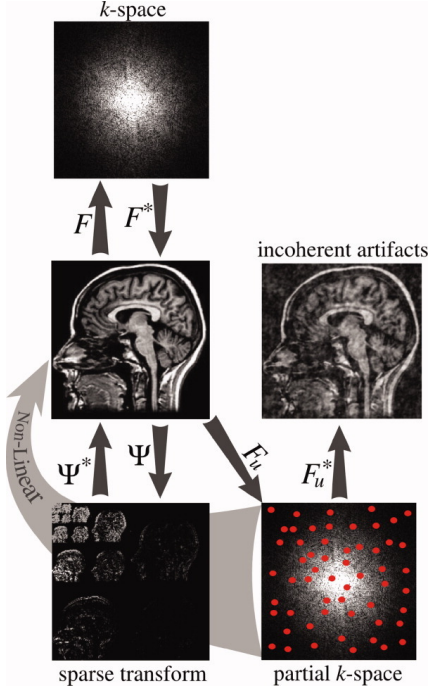


Figure 2.12 – Illustration of the main three requirements behind compressed sensing reconstructions: incoherent undersampling, sparse transform and non-linear reconstruction. Adapted with permission from Lustig et al. [51].

Compressed sensing (CS) represents a class of acceleration techniques based on the pseudo-random undersampling of k -space [51]. The main idea behind CS is that sparse MR images can be properly reconstructed by already applying a “compression” in the data acquisition process (i.e., acquiring only a subset of k -space). Three requirements are postulated for a successful CS implementation (Figure 2.12):

1. *Incoherent undersampling*: an undersampling scheme with a coherent and repeatable pattern, as those used in parallel imaging, create folding artifacts within the imaged field of view. Conversely, random k -space samplings do not yield folding artifacts but rather incoherent artifacts similar to noise, which are later removed in the CS reconstruction. As the frequency components in the k -space center are of essence in the determination of the image contrast, the sampling scheme can actually not be completely random. Hence, pseudo-random patterns with variable density are typically employed (e.g., Poisson disk with higher density in the center, among others);

2. *Sparsifying transform*: sparsity reflects the degree by which a matrix is filled with zeros. For instance, MRI angiograms are sparse images as most of the image exhibits close-to-zero intensities. However, most MR images are not naturally sparse but might be sparse in other domains. For example, brain images are sparse in the wavelet domain. This sparsity property of the image is used as prior information in the CS reconstruction;
3. *Non-linear iterative reconstruction*: images are reconstructed within an iterative optimization similar to cg-SENSE, with the addition of a regularization term that enforces sparsity by penalizing the low intensity coefficients associated to noise in the wavelet domain:

$$X = \arg \min_X \frac{1}{2} \sum_{c=0}^N \|PF\{S_c X\} - Y_c\|_2^2 + \lambda |\Psi\{X\}|_1, \quad (2.16)$$

where Ψ corresponds to the sparsifying wavelet transform and λ to the regularization weight.

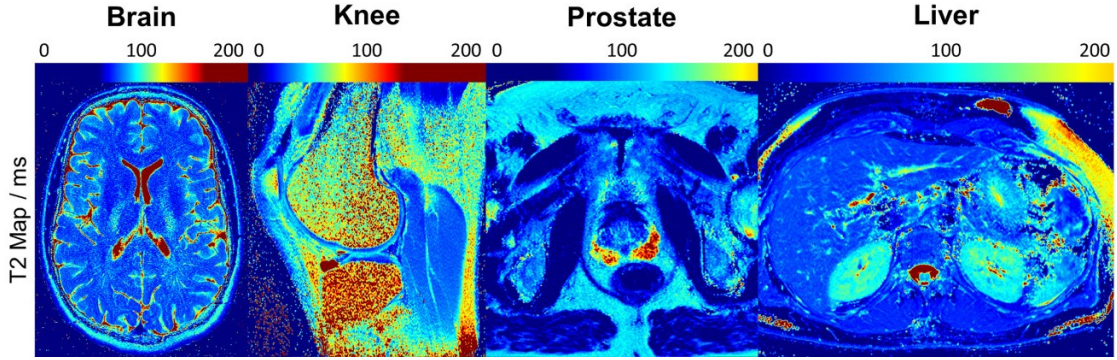


Figure 2.13 – Example T_2 maps obtained with GRAPPATINI in the brain, knee, prostate, and liver. Adapted with permission from Hilbert et al. [54].

Given the iterative nature of the optimization, CS reconstructions are computationally intense. Other limitations include the introduction of blurriness in the image and the required tuning of the regularization weight λ that highly impacts the solution.

2.4.3 Model-based reconstructions

As discussed in the previous sections, exploiting additional image information such as coil sensitivity maps or sparsity in a suitable domain allows accelerating data acquisition while reconstructing aliasing free images. In the context of qMRI, the acquisition of parametric maps can be accelerated by incorporating prior knowledge regarding the signal model behind the parameter under investigation within an iterative reconstruction [52, 53].

Using T_2 mapping as an example, undersampled MESE data can be used to directly estimate M_0 and T_2 (see Eq. 2.8) by minimizing the following cost function:

$$M_0, T_2 = \arg \min_{M_0, T_2} \frac{1}{2} \sum_{c=0}^N \| PF \{ S_c M_0 e^{-t/T_2} \} - Y_c \|_2^2. \quad (2.17)$$

This technique, referred to as “Model-based Accelerated Relaxometry by Iterative Non-linear Inversion” (MARTINI) [53], was recently combined with GRAPPA in the method GRAPPATINI [54], which is of interest for this thesis. In comparison with a fully sampled MESE scan, GRAPPATINI proved to robustly estimate T_2 values with undersampling factors up to 10. Example T_2 maps estimated with GRAPPATINI in different organs are shown in Figure 2.13.

2.5 Automatic image post-processing

Over the past years, the increased amount of high-quality MRI data and the development of advanced qMRI methods opened new frontiers for studying and analyzing anatomical and functional brain features. However, the manual computation and extraction of such features from large datasets is increasingly becoming a tedious task for clinicians. Therefore, several

automatic methods have been, and are currently being, developed for the computerized and automatic analysis of large volumes of data. With the focus on brain MRI, tools for tissue segmentation and spatial alignment are becoming of clinical use by providing quantitative information and helping with the qualitative assessment of MR images. This section provides a brief overview of these methods.

2.5.1 Segmentation of brain tissues

The segmentation of brain tissues into different types (e.g., WM, GM, CSF), lobes (frontal, parietal, temporal, occipital) or structures (e.g., hippocampus, amygdala, thalamus, among many others) is becoming important in many clinical applications. In fact, the parcellation of brain tissues into structures allows performing quantitative measurements of brain volumes (i.e., morphometry), which are instrumental for assessing the normal brain development or pathological effects, such as atrophy, in the adult brain. Additionally, brain MRI segmentation is often an indispensable step for other complex tasks, such as pathological lesion segmentation or image-guided surgical planning. In qMRI, brain segmentation offers the means to quantify and compare regional values of quantitative parameters, for instance among different subjects or in longitudinal studies. Given that manually performing such task is time-consuming and prone to human error, many methods were developed for the automatic segmentation of brain tissues. The review of the vast literature around this topic would fall out the scope of this thesis, hence the reader is referred to the following articles for more details [55–57].

A tool for automatic brain tissue parcellation that was extensively used in this thesis is the prototype software MorphoBox [58]. MorphoBox implements a variational expectation–maximization approach to derive a five-classes Gaussian-mixture model of T_1 -weighted image intensities for the main brain tissues (WM, GM, deep GM, ventricular and sulcal CSF). The five resulting brain maps represent the probability of each voxel to belong to a specific tissue. These maps are then summarized to WM, GM and CSF probability maps by adding together the two GM maps and the two CSF maps. A segmentation mask of WM, GM and CSF can then be derived by assigning each voxel to the tissue class with the highest probability. Finally, a T_1 -weighted template with manually segmented brain structures is spatially registered to the input image, resulting in the segmentation of several structures by combining the previously computed probability maps with the mask of the template. Although originally designed for MPAGE T_1 -weighted volumes, MorphoBox has been also optimized to operate with images from the MP2RAGE sequence. Even though the T_1 -weighted contrast offered by the MP2RAGE UNI image provides an excellent WM–GM contrast, the salt-and-pepper noise in the background around the head and in proximity of cortical GM structures complicates the automatic tissue segmentation in the UNI image. Therefore, a combined T_1 -weighted image is first computed by multiplying the GRE₂ and UNI as suggested by Fujimoto et al. [59]. The total intracranial volume is first extracted by matching the T_1 -weighted template onto the combined T_1 -weighted volume, and the variational expectation-maximization algorithm is then performed on the total intracranial volume of the UNI image (Figure 2.14).

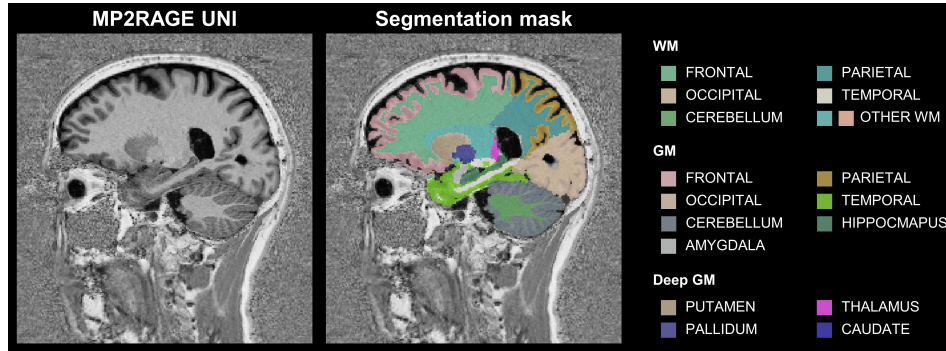


Figure 2.14 – Example brain segmentation obtained with MorphoBox on the MP2RAGE T_1 -weighted contrast (UNI), along with the corresponding label names.

2.5.2 Spatial registration of brain images

Image registration refers to estimating the spatial transformation between two images so that, after applying such transformation, every location in the two images corresponds to the same anatomy. The applications of registration techniques are many and include fusing data acquired with different imaging modalities (e.g., CT with MRI or PET with MRI), planning image-guided radiotherapy treatments and surgeries, studying and comparing anatomical and functional features between two cohorts (e.g., healthy subject vs. patients), performing a comparison of newly acquired images to previous time points in longitudinal analyses and correcting motion between different MR contrasts, among others [60–62].

In practice, given a reference fixed $I_F(x)$ and a moving $I_M(x)$ image, a spatial registration problem consists in finding the transformation $T(x)$ so that $I_M(T(x))$ is aligned to $I_F(x)$. The registration involves an iterative optimization, where at each iteration a similarity metric (S) between I_F and I_M is computed to minimize the cost function $C = S(T, I_F, I_M)$ with respect to T . In the example of a rigid registration, $T(x)$ only accounts for rotation and translation, thus $I_M(x)$ is treated as a rigid object that cannot be sheared or scaled. This is usually employed when I_F and I_M correspond to the same imaged object. When differences between the images involve also scaling and shearing, affine registration algorithms are used. More complex non-linear registrations are instead used when I_F and I_M correspond to two different imaged objects (e.g., two different subjects).

With regard to MR brain images, one of the main applications of spatial registration algorithms was already introduced in the previous section. A common coordinate system representing an average anatomical structure (i.e., anatomical template) is non-linearly registered to a single image aiming, for instance, at segmenting brain structures (see the example of the prototype software MorphoBox in **Section 2.5.1**). Another main application implies the opposite process, where images acquired in many subjects are spatially aligned to an anatomical template. In this common space, a voxel-based study can be carried out, for instance comparing anatomical and/or functional features between different cohorts (healthy vs patients). Many standardized

brain anatomical templates are publicly available^{1,2,3}, with most of them including a T_1 -weighted contrast that provides an excellent WM–GM contrast which is, thus, suitable for registration purposes. Finally, spatial registrations are also frequently performed when newly acquired images are compared to previous time points in longitudinal analyses.

Several algorithms exist for registering MR brain images [63]. Two open source software packages are of interest here, Elastix⁴ [64] and the Advanced Normalization Tools (ANTs)⁵ [65, 66]. Elastix is a modular software that offers several choices for each essential block of the registration problem (i.e., type of transformation, cost function, and optimization algorithm). A pair-wise non-linear registration of two whole brain images requires around 3 minutes on a desktop computer (Intel Core i7 CPU 3.06 GHz CPU and 24.0 GB of RAM). ANTs non-linear registration involves a more complex symmetric diffeomorphic transformation that is based on optimizing a time-varying velocity field [67]. Computational times for a pair-wise non-linear registration of two whole brain images are usually around one hour. Additionally, ANTs provides a framework for template creation that corrects for blurring introduced at each averaging step using shape adjustment and sharpening, resulting in good delineation of brain structures even in the averaged images [68]. This feature is instrumental when a study-specific template is preferred over publicly available templates.

¹MNI: <http://nist.mni.mcgill.ca/>.

²OASIS: <https://www.oasis-brains.org/>.

³IXI: <https://brain-development.org/ixi-dataset/>.

⁴Elastix: <http://elastix.isi.uu.nl/>.

⁵ANTs: <http://stnava.github.io/ANTs/>.

3 Probing myelin content of the human brain with MRI

*The content of the following chapter is adapted from the postprint version of the article: “Probing myelin content of the human brain with MRI: A review” published in Magnetic Resonance in Medicine [36]. DOI: [10.1002/mrm.28509](https://doi.org/10.1002/mrm.28509). The article was co-authored by Tom Hilbert, Jean-Philippe Thiran, and Tobias Kober. All co-authors contributed to this review article and revised the manuscript. It should be noted that some sections of the original article were shortened to reduce redundancy with **Chapter 2** “Background”.*

Abstract: Rapid and efficient transmission of electric signals among neurons of vertebrates is ensured by myelin-insulating sheaths surrounding axons. Human cognition, sensation, and motor functions rely on the integrity of these layers, and demyelinating diseases often entail serious cognitive and physical impairments. Magnetic resonance imaging radically transformed the way these disorders are monitored, offering an irreplaceable tool to non-invasively examine the brain structure. Several advanced techniques based on MRI have been developed to provide myelin-specific contrasts and a quantitative estimation of myelin density in vivo. Here, the vast offer of acquisition strategies developed to date for this task is reviewed. Advantages and pitfalls of the different approaches are compared and discussed.

3.1 Introduction

Fast-transmitting axons of vertebrates are surrounded by an insulating sheath that guarantees signal propagation among neurons: myelin [7]. Produced by glial cells, myelin is a multilayer plasma membrane dominated by lipids that restricts the rise of action potentials in small segments of the axons, thus contributing to the acceleration of the electrical conduction (see **Section 2.3.4** in Chapter 2). Human cognition, sensation, and motor functions rely on the integrity of these layers, and demyelinating diseases often entail serious cognitive and physical impairments [34]. Many advanced techniques based on MRI have been developed to provide myelin-specific contrasts and a quantitative estimation of myelin density in vivo. For instance, in 1994 MacKay et al. [8] suggested to exploit the shorter T_2 of water molecules trapped within the myelin sheaths to indirectly estimate the myelin content of brain tissues, paving the way

for in vivo MWI research [35, 69]. Another example for the indirect assessment of myelin is the probing of the MT occurring between macromolecular and free water protons [70].

This chapter provides a comprehensive review of the large spectrum of strategies developed to date for the non-invasive and in vivo assessment of brain myelin density based on MRI. The different imaging approaches were broadly grouped in the following three categories:

- **Probing myelin with relaxometry:** includes techniques that exploit the shorter relaxation rate of water molecules trapped in myelin sheaths to separate their contribution from the overall water signal, typically referred to as myelin water imaging [69];
- **Targeting the brain macromolecular content:** consists of approaches aimed at estimating the macromolecular content of the human brain following the assumption that myelin is the most abundant organic macromolecule in the brain [70, 71]; and
- **Other MR contrasts:** refers to additional sources of contrasts that have been explored as indirect measurements sensitive to myelin density.

3.2 Probing myelin with relaxometry

3.2.1 T_2 relaxometry

Multi-echo spin echo for multicomponent T_2 mapping

Following previous animal studies demonstrating the multicomponent nature of T_2 relaxation in myelinated axons [72–74], in 1994 Mackay et al. [8] investigated for the first time in vivo MWI of the human brain from multi-echo T_2 (MET_2) data acquired with the MESE sequence (see **Section 2.3.2** in Chapter 2). For MWI applications, amplitudes of each echo (y_i) are modelled as the sum of several exponential kernels [75]:

$$y_i = \sum_{j=1}^M s_j e^{-t_i/T_{2j}}, \quad i = 1, 2, \dots, N, \quad (3.1)$$

with N being the number of acquired echoes at echo time t_i , and M an arbitrary number of spectral components with different relaxation times T_{2j} and amplitudes s_j . Eq. (3.1) can be expressed in the form of a linear system as follows:

$$y_i = \sum_{j=1}^M A_{ij} s_j, \quad i = 1, 2, \dots, N, \quad (3.2)$$

by incorporating the exponential kernels into the matrix \mathbf{A} . A multicomponent decomposition of T_2 decays is then performed using a non-negative least square (NNLS) optimization [75], which minimizes the distance between the multi-exponential model and the actual acquired

signal (\bar{y}_i) using an L2-norm:

$$s = \arg \min_s \sum_{i=1}^N \left\| \sum_{j=1}^M A_{ij} s_j - \bar{y}_i \right\|_2^2. \quad (3.3)$$

If any a priori assumption is made on the number of T_2 components, M is usually chosen high enough to not influence the solution ($M \geq 40$). Since M is typically greater than N , the problem at hand is ill-posed and a regularization term is usually introduced to constrain the NNLS formulation.

Acquiring 2D single-slice MESE data (acquisition time around 25 minutes) from healthy subjects and using a NNLS optimization with Tikhonov regularization [76], Mackay et al. identified three main water compartments with different T_2 values in the human brain at 1.5 T [8]. The shortest T_2 component (between 10 and 55 ms) was ascribed to water trapped between myelin layers; a longer component (T_2 between 70 and 95 ms) was attributed to water molecules within cells and in the extracellular space; the component with the longest T_2 (longer than 1 s) was identified as free water (mainly CSF). For the first time, MWF maps were derived in vivo as the relative contribution of myelin water to the overall measured water content as follows:

$$MWF = \sum_{j=T_{2min}}^{T_{2max}} s(T_{2j}) / \sum_{z \in T_2} s(T_{2z}), \quad (3.4)$$

where the T_2 range for myelin was set to $T_{2min} = 10$ ms and $T_{2max} = 55$ ms. Average MWF across a cohort of five healthy subjects was found to be $15.6\% \pm 8.1\%$ in brain WM tissues. An overview of the method is depicted in Figure 3.1A-D. Follow-up studies proved the correlation of MWF measurements with post-mortem samples of MS patients stained for myelin content at 1.5 T ($R^2 = 0.67$) [77] and 7 T ($R^2 = 0.78$) [78] (Figure 3.1E-G). The sensitivity of MWF maps to myelin density reduction in demyelinated areas of the brain was also assessed (Figure 3.1H-J) [79], establishing this approach as the reference standard in the field.

Multi-echo gradient and spin echo sequence

The multi-echo GRASE sequence (see **Section 2.3.2** in Chapter 2) was first investigated by Prasloski et al. [80] for MWI by acquiring MET_2 data at 3 T in healthy volunteers. The MWF estimation was conducted while accounting for inhomogeneities in the transmit field (B_1^+), which cause the T_2 decays to deviate from the ideal exponential behaviour due to stimulated echoes [81]. The extended phase graph (EPG) model is used to model signals in the presence of stimulated echoes, provided that T_1 , T_2 , and the flip angle error δ (quantifying the B_1 deviation) are known for each voxel [81]. Eq. (3.1) is then modified by replacing exponential kernels with EPG simulations [82]:

$$y_i = \sum_{j=1}^M s_j EPG(T_1, T_{2j}, TE_i, \delta), \quad i = 1, 2, \dots, N. \quad (3.5)$$

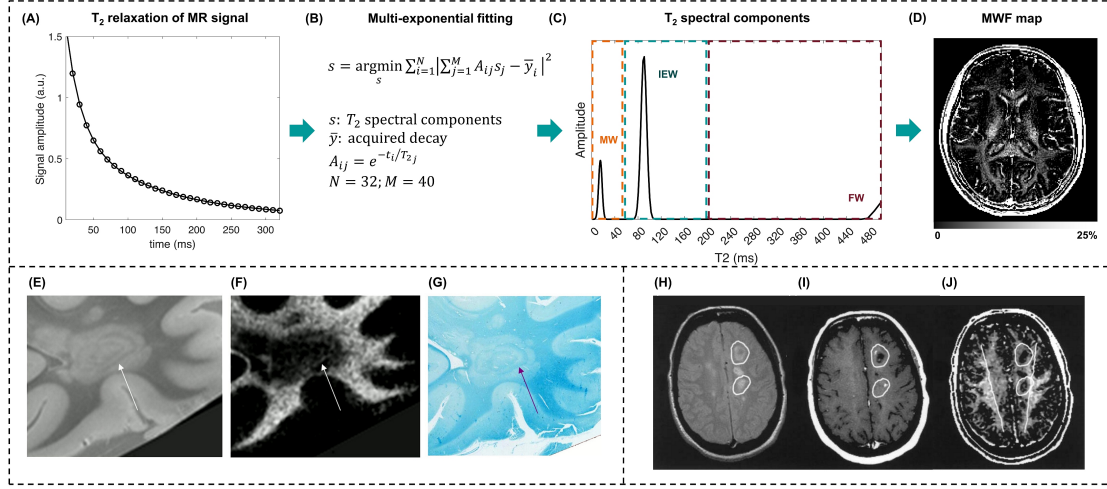


Figure 3.1 – Myelin water imaging from multi echo T₂ data. (A) T₂ decays in brain voxels are acquired, for instance with a multi echo spin echo sequence. (B) A multicompartiment decomposition of the measured decays is performed using a non negative least square optimization, which minimizes the distance between a multi-exponential model and the actual acquired signal. (C) T₂ spectral components are thus obtained and myelin water (MW) signal can be separated from intra- and extra-cellular water (IEW) and free water (FW) signals. (D) Myelin water fraction (MWF) maps are derived as the ratio of myelin water content to the overall measured water content. (E) T₂-weighted image, (F) MWF map and (G) luxol fast blue staining of a patient with multiple sclerosis (MS). Arrows indicate an area of preserved myelin within a demyelinated lesion. (H) Proton density weighted image, (I) post contrast T₁-weighted image, and (J) MWF map acquired in a patient with MS. Parts (E)-(G) are adapted with permission from Laule et al. [78]. Parts (H)-(J) are adapted with permission from Laule et al. [79].

The NNLS optimization is used in this case to estimate both s_j and δ :

$$s = \operatorname{argmin}_{s, \delta} \sum_{i=1}^N \left\| \sum_{j=1}^M A_{ij}^{EPG}(\delta) s_j - \bar{y}_i \right\|_2^2 + \mu \sum_{j=1}^M s_j^2, \quad (3.6)$$

with A^{EPG} representing the EPG-simulated T₂ decays. Of note, T₁ is usually set to a fixed value for the whole brain. Prasloski et al. [80] found MWF values in WM to be in the range 7-18% (Figure 3.2A). For validation, reference MWF maps were derived from a 3D MESE sequence and found to strongly correlate with the values obtained from the multi-echo GRASE ($R^2 = 0.95$). Subsequently, sensitivity of the multi-echo GRASE MWF maps to myelin loss was demonstrated using spinal cord data of MS patients [83].

Recent studies show that further acceleration of multi-echo GRASE acquisitions can be achieved with parallel imaging [84, 85].

T₂-prepared acquisitions

In T₂-prepared (T₂prep) acquisitions, a magnetisation preparation module is used to imprint T₂-weighting on the longitudinal magnetization, which is subsequently sampled as swiftly as possible, typically using a GRE readout [86]. The simplest T₂prep module resembles a classic

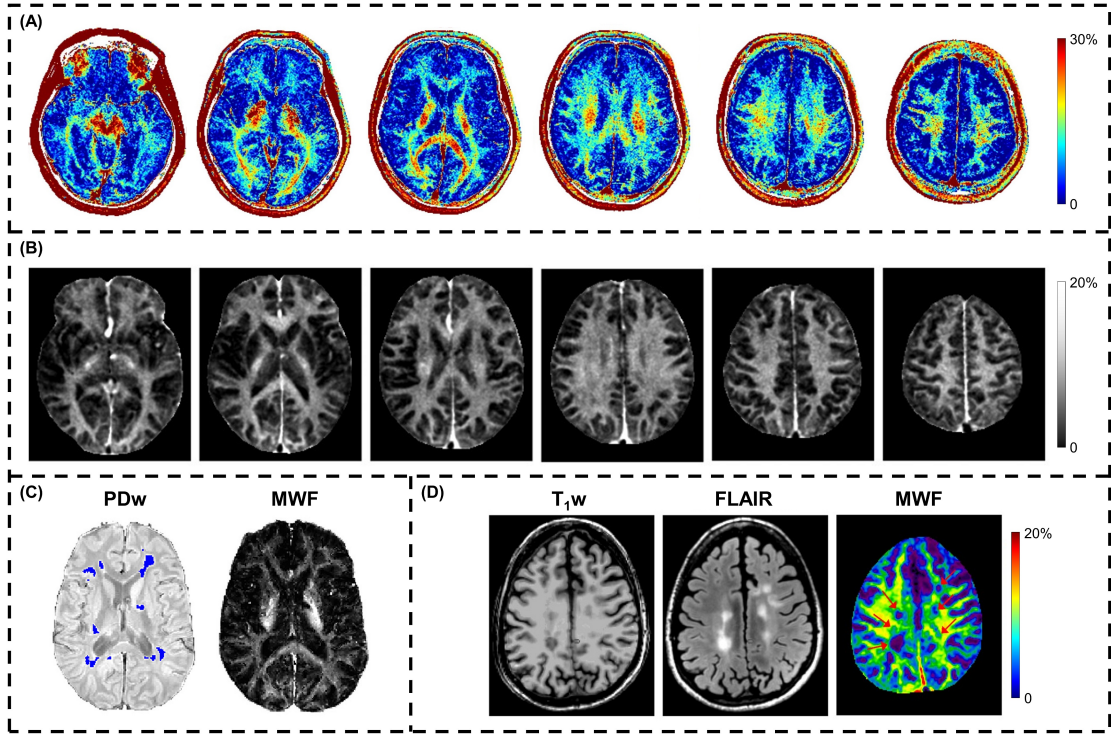


Figure 3.2 – Myelin water imaging from multi echo T_2 data acquired with a gradient and spin echo (GRASE) (A) and a T_2 prep sequence (B). (C) Proton density-weighted (PDw) image and myelin water fraction (MWF) map derived using a multi echo GRASE sequence acquired in a patient with multiple sclerosis (MS). Lesion mask is overlaid onto the PDw contrast. (D) T_1 -weighted (T_1 -w), fluid attenuated inversion recovery (FLAIR) and MWF derived using a T_2 prep sequence acquired in a patient with MS. Part (A) is adapted with permission from Prasloski et al. [80]. Part (B) is adapted with permission from Nguyen et al. [89]. Part (C) is adapted from O’Muircheartaigh et al. [90]. Part (D) is adapted with permission from Nguyen et al. [89]

spin echo experiment: a 90° “tip-down” excitation pulse flips the magnetization in the transverse plane followed by a refocusing pulse; at the time of the spin echo, the magnetization is flipped back using a 90° “tip-up” pulse. T_2 -weightings of varying strength can be imprinted on the longitudinal magnetisation by changing the delay between the tip-down and tip-up pulses (the “echo time” in the imaginary spin echo experiment) [86]. Oh et al. [87] investigated a 2D multi-echo T_2 prep sequence for deriving MWF maps both at 1.5 T and 3 T. Following a NNLS optimization, average MWF values in frontal WM tissue of healthy subjects were found to be $7.0\% \pm 0.4\%$ at 1.5 T and $10.1\% \pm 0.3\%$ at 3 T [87].

Aiming at increasing the SNR and brain coverage of the reconstructed maps, a 3D version of the multi-echo T_2 prep was later implemented and tested at 1.5 T [88] and 3 T [89]. By reducing the number of T_2 -weightings to six, MWF maps were acquired in 4 minutes and proved to be in agreement with acquisitions using 16 echoes (regional discrepancy smaller than 0.8%) [89]. Good sensitivity in detecting myelin content reduction was demonstrated in MS lesions (Figure 3.2D) [89].

3.2.2 T_2^* relaxometry

Multicompartment T_2^* mapping using gradient echoes

One limitation of both MESE and GRASE sequences is the rather long first echo time and echo spacing, yielding a limited number of acquired samples before the myelin water signal has decayed. To increase this number, Du et al. [91] were the first to propose the use of multi-gradient-echo (MGRE) sequences for MWF estimation from multi-echo T_2^* data [91]. In an MGRE sequence, after RF excitation and phase encoding, a train of GRE readouts with alternating polarity is employed to sample the T_2^* decay. To allow short TEs, echoes were acquired during both the positive and negative readout gradients. A three-pool model accounting for myelin (my), axonal (ma) and extracellular (mex) water was fitted to the acquired signal:

$$y(t) = A_{my}e^{-t/T_{2,my}^*} + A_{ma}e^{-t/T_{2,ma}^*} + A_{mex}e^{-t/T_{2,mex}^*} + A_{bl}, \quad (3.7)$$

where A_{my} , A_{ma} and A_{mex} are the relative signal amplitudes of the three water pools, and A_{bl} accounts for any residual signal from the acquired baseline. The root mean square error between the signal and the three-pool model in Eq. (3.7) was minimized with a quasi-Newton optimization [92] for multivariate analysis to retrieve the compartment's relative contribution and the associated T_2^* . Subsequently, MWF maps were derived as follows:

$$MWF = A_{my} / (A_{my} + A_{ma} + A_{mex}). \quad (3.8)$$

Average MWF values in post-mortem brains were found to be 11.0% in WM tissue. Comparison with histopathological samples of MS lesions stained for myelin confirmed the potential of the method in assessing demyelination processes [91].

As MGRE sequences are susceptible to field inhomogeneities, the analysis of multi-echo T_2^* data was later enhanced by introducing a correction for local B_0 inhomogeneities to the model [93]. A first order approximation of a sinc function was used as an estimate of the local field gradient to correct the acquired signal [93]. Applying the correction before the multicompartment fitting resulted in an improved MWF estimation in areas with high B_0 inhomogeneity [93].

The model was further refined to account for the relative frequency offsets between the water pools stemming from local field inhomogeneities generated by the different orientations of WM fibres. Van Gelderen et al. [94] extended the model to include these frequency offsets:

$$y(t) = A_{my}e^{-\left(\frac{1}{T_{2,my}^*} + i2\pi\Delta f_{my}\right)t} + A_{ma}e^{-\left(\frac{1}{T_{2,ma}^*} + i2\pi\Delta f_{ma}\right)t} + A_{mex}e^{-\left(\frac{1}{T_{2,mex}^*} + i2\pi\Delta f_{mex}\right)t}, \quad (3.9)$$

with Δf_{my} , Δf_{ma} , Δf_{mex} being the frequency offsets of the water pools evaluated with respect to the external water compartment (i.e., $\Delta f_{mex} = 0$). In following studies, macroscopic field inhomogeneities (i.e., non-local) were either suppressed during acquisition [95] or included

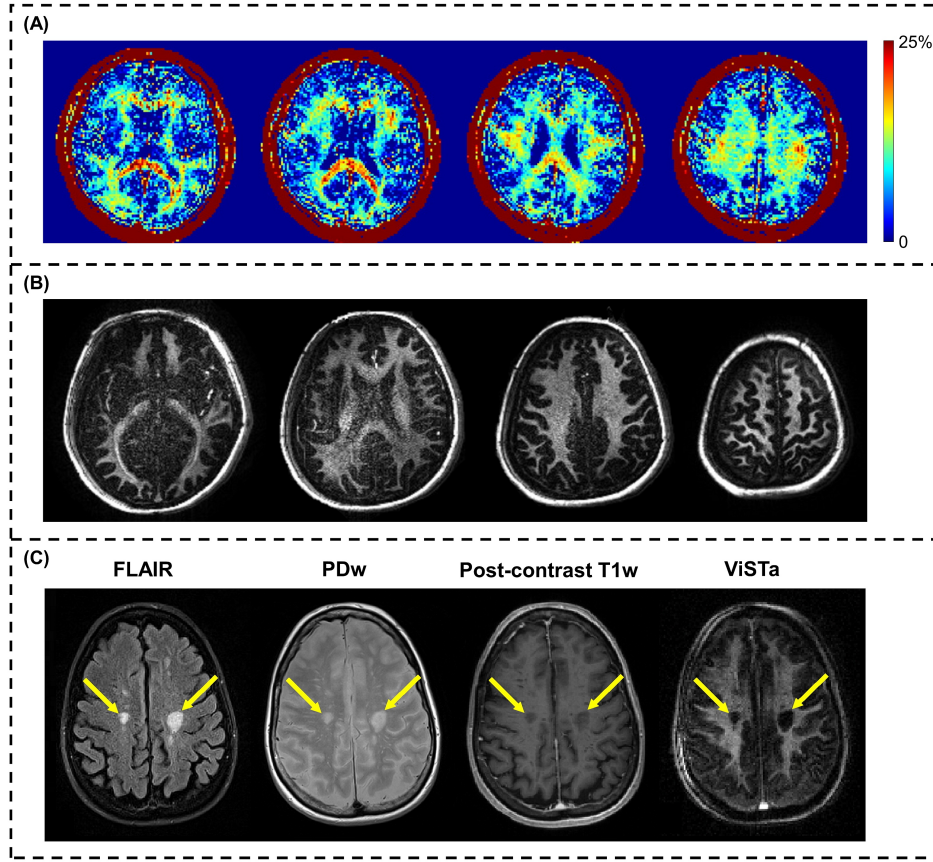


Figure 3.3 – Myelin water imaging from multi echo T_2^* data (A) and T_2^* data with tissue nulling (B) in healthy subjects. (C) Fluid attenuated inversion recovery (FLAIR), proton density-weighted (PDw), post-contrast T_1 -weighted (T_1w) and single echo ViSTa images acquired in a patient with multiple sclerosis (MS). Yellow arrows indicate a reduction of ViSTa signal in MS chronic lesions. Part (A) is adapted with permission from Nam et al. [96]. Part (B) is adapted with per mission from Wu et al. [97]. Part (C) is adapted with permission from Oh et al. [98].

in each pool model as a background frequency offset [96]:

$$y(t) = \left(A_{my} e^{-\left(\frac{1}{T_{2,my}^*} + i2\pi\Delta f_{my+bg}\right)t} + A_{ma} e^{-\left(\frac{1}{T_{2,ma}^*} + i2\pi\Delta f_{ma+bg}\right)t} + A_{mex} e^{-\left(\frac{1}{T_{2,mex}^*} + i2\pi\Delta f_{mex+bg}\right)t} \right) e^{-i\Phi_0}, \quad (3.10)$$

with Δf_{my+bg} , Δf_{ma+bg} , Δf_{mex+bg} being the sum of the pool and the background frequency offsets, and Φ_0 the initial B_1 phase offset. MWF maps reconstructed with the models in Eqs. (3.7), (3.9) and (3.10) were compared, showing more robust estimation of the unknown model parameters with the model of Eq. (3.10) (Figure 3.3A) [96].

Multicompartment T_2^* mapping with tissue nulling: ViSTa

Similarly to the findings for T_2 and T_2^* relaxation, ex vivo studies in myelinated axons suggest a multicomponent nature of the longitudinal relaxation time, with the shortest T_1 s originating

from water molecules trapped within myelin layers [99–101]. Oh et al. [98] exploited this property to achieve a direct visualization of short T_2^* components, a method referred to as ViSTa. In ViSTa, a pair of inversion RF pulses are employed to suppress T_1 values higher than those characteristic for myelin water ($T_1 > 750$ ms) [102, 103]. After the double inversion, an MGRE sequence is employed to sample the T_2^* decay, assuming that the short T_2^* components of myelin persist after the applied long- T_1 suppression. In a single-slice experiment at 3 T, Oh et al. [98] investigated the multicompartment decomposition of acquired T_2^* decays by modeling the signal as in Eq. (3.1), replacing T_2 with T_2^* and using a NNLS optimization. MWF in WM tissues of healthy volunteers was found to be $5.5\% \pm 0.4\%$, whereas values derived from an MGRE without T_1 suppression were found to be higher, $7.2\% \pm 1.2\%$ [98]. In addition, single-echo data ($TE = 6.36$ ms) were acquired after the double inversion to prove that the contrast information, once normalized, delivers clinical valuable information without the need of additional post-processing. The direct myelin visualization achieved with the single-echo ViSTa contrast revealed good sensitivity in detecting demyelinated chronic lesions in MS patients (Figure 3.3C) [98].

The acquisition time required for ViSTa was later reduced by including undersampling schemes based on wave-CAIPIRINHA for whole brain 3D volume reconstruction in single-echo experiments (Figure 3.3B) [50, 97].

3.2.3 T_1 relaxometry

Multicompartment Look-Locker

Following the same rationale as in ViSTa, i.e., that T_1 also has a multicompartment nature [99–101], a multicomponent analysis of phase-sensitive IR data was proposed to measure MWF [104]. After inversion of the magnetization with a nonselective adiabatic pulse, the signal is sampled using a classic Look-Locker scheme (see **Section 2.3.1** in Chapter 2). To decrease saturation effects, low flip angles are employed for the excitation and inversion times are sampled following a geometric distribution [104]. The signal intensity for each inversion time TI_i can be modelled as a sum of multiple T_1 recoveries:

$$y_i = \sum_{j=1}^M s_j \left[1 - 2 \left(\frac{\mu}{100} \right) e^{TI_i/T_{1j}} \right] + \varepsilon_i, \quad i = 1, 2, \dots, N. \quad (3.11)$$

where N is the number of different acquired inversion times, M is an arbitrary number of spectral components with different relaxation times T_{1j} and amplitude s_j , ε_i is normally distributed noise of the real part of the acquired signal and μ the effective inversion efficiency in percent. Labadie et al. [104] found T_1 values associated with myelin to be in the range 106–225 ms and MWF in WM tissue 8.3% at 3 T and 15% at 7 T [104] (Figure 3.4A), in agreement with multi-echo T_2 and T_2^* findings.

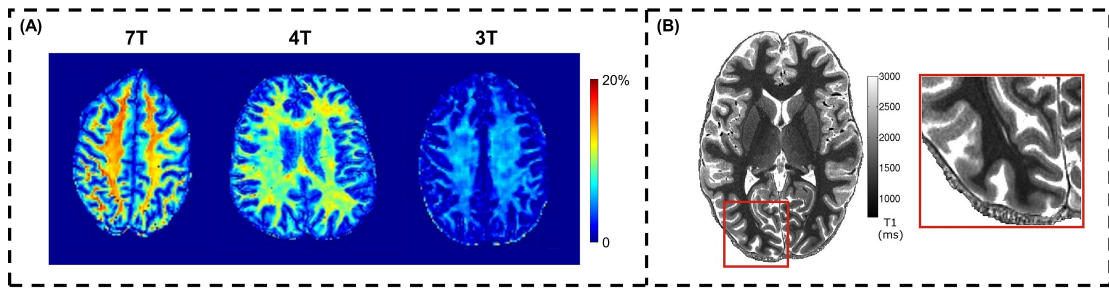


Figure 3.4 – (A) Myelin water imaging from T_1 relaxometry at different field strengths. (B) T_1 map acquired with an isotropic resolution of 0.5 mm^3 showing contrast differences among cortical regions and layers. The stria of Gennari is shown in the right zoom in as a band of low T_1 . Part (A) is adapted with permission from Labadie et al. [104]. Part (B) is adapted from Tardif et al. [105].

R_1 as biomarker of cortical myelination

When measuring the longitudinal relaxation, MT effects originating from the high power inversion pulses cannot be neglected [106–108] and may thus affect the multicomponent analysis of inversion-recovery time series in T_1 relaxometry [104]. However, the sensitivity of T_1 mapping schemes to this confounding effect highly dependent on myelin density drove the investigation of T_1 maps as a biomarker for myelin content [109]. T_1 relaxation is indeed sensitive to the presence of macromolecules, especially to those phospholipids that are abundant in the membrane of myelin sheaths [110, 111]. In vivo data demonstrated that T_1 is a good predictor of the macromolecular tissue volume of the brain throughout the whole lifespan [112]. In addition, the typical U-shape curves describing the change of T_1 with age were found to match the evolution of MT measurements [113]. On this basis, R_1 ($= 1/T_1$) mapping found application in mapping cortex myelination, where the differences between layers of the cortex require high resolution and low spatial bias [109], [114, 115]. The achievable spatial resolution nowadays in vivo, for instance with the MP2RAGE sequence [16], allows to visualize structures otherwise indiscernible with other methods, such as the stria of Gennari in the primary visual cortex [105] (Figure 3.4B).

3.2.4 Simultaneous T_1 and T_2 relaxometry

Multicomponent Driven Equilibrium Single Pulse Observation of T_1 and T_2

The Driven Equilibrium Single Pulse Observation of T_1 and T_2 (DESPOT) was developed for measuring simultaneously the longitudinal and transverse relaxation times in 3D, at high resolution and covering the whole brain [21] (see **Section 2.3.3** in Chapter 2). The DESPOT method was later extended to include a multicomponent fitting of the acquired signals (mcDESPOT) [101]. To obtain MWF maps, a two-pool model with intercompartment exchange is employed accounting for a fast and a slow relaxing component, associated with myelin and combined intra- and extra-cellular water, respectively. A local search method together with a stochastic genetic algorithm are used to fit the signal [116]. MWF values in healthy volunteers were found to be larger than 28% [101]. Derived MWF values in WM and

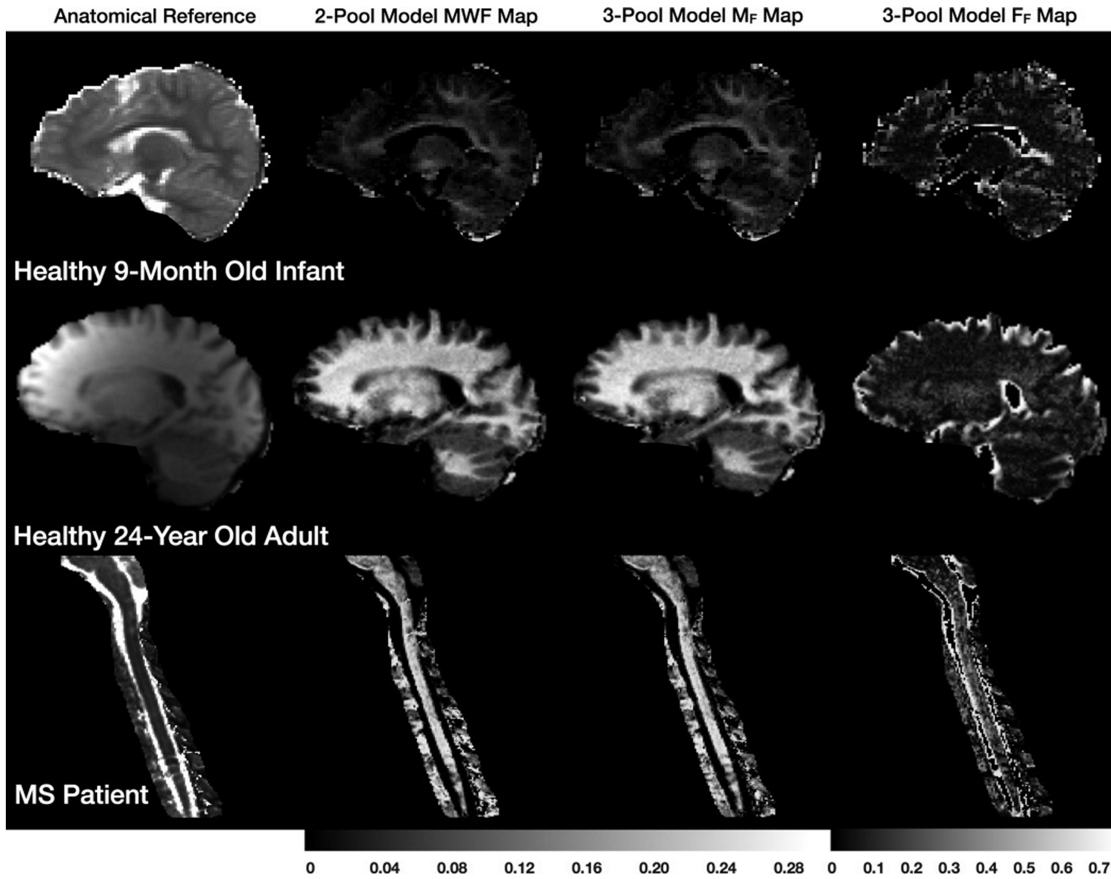


Figure 3.5 – Myelin water fraction (MWF) maps derived from a multicomponent driven equilibrium single pulse observation of T_1 and T_2 (mcDESPOT) acquisition in a 9 month old infant, a 24 year old adult, and a patient with multiple sclerosis (MS) using both a two-pool and a three-pool model. Adapted with permission from Deoni et al. [117].

lesions of MS patients were found to be significantly smaller than in healthy controls [101].

The model proposed in mcDESPOT was further extended to include a third non-exchanging pool accounting for the CSF and incorporating a model with 11 unknown parameters (relaxation times of the three pools, two independent fractions for the myelin and free water pools, exchange rate between myelin and intra/extra cellular water, an off-resonance value, B_1 inhomogeneities) [117]. MWF values resulting from this three-pool model were found to not deviate significantly from the two-pool model in WM and GM tissues, but improvements were assessed in voxels prone to partial volume effects, as those close to the ventricles (Figure 3.5).

QRAPMASTER

QRAPMASTER (Quantification of Relaxation times and Proton density by Multi-echo Acquisition of a Saturation-recovery using TSE Readout), also referred to as *synthetic MRI* (SyMRI), simultaneously measures T_1 and T_2 relaxation times by combining a multi-echo GRASE sequence with a multi-delay saturation recovery preparation [24] (see **Section 2.3.3** in Chapter 2).

Multicompartment 2D relaxometry was investigated using the QRAPMASTER framework [118]. A physical model was introduced, which considers four compartments for each voxel: myelin (V_{MY}), cells, free water and excess parenchymal water volumes. Each compartment has its own set of relaxation parameters T_1 , T_2 and PD. The model accounts for the exchange between myelin layers and the surrounding water, as well as the exchange between cellular water and oedema present in pathological brain parenchyma. The free water compartment is thereby considered a non-exchanging pool. To simplify the model, relaxation parameters for V_{MY} and parenchymal water are fixed using literature values for CSF and the same for the T_2 of myelin. Bloch equations were then used to simulate 141 combinations of the remaining six variable parameters and the relative volumes of the four pools. The resulting signal intensities were matched to the acquired T_1 , T_2 and PD maps in healthy subjects, and V_{MY} volumes were derived from the best matching simulated signal. V_{MY} volumes were found to be $23\% \pm 3\%$ for WM tissues [118]. Decreased V_{MY} was assessed in elderly subjects and in patients affected by MS [118, 119] (Figure 3.6).

Recently, the methodology has been extended to a 3D acquisition by replacing the multi-echo GRASE with a T_2 -prepared GRE sequence, and it has been further accelerated with compressed sensing [120].

3.2.5 Discussion

In this section, techniques targeting the shorter relaxation properties of water trapped in myelin sheaths have been reviewed. The MET_2 acquisitions based on the MESE sequence were the first to be explored for this application, and they are among the most validated methods in MWI. However, MESE experiments require long acquisition times. Acceleration of 2D acquisitions via interleaved slice sampling are critical as the obtained signal becomes prone to MT effects [121]. The need for higher resolution and extended brain coverage was addressed using 3D MESE acquisitions [122]; however, acquisition times become even longer.

Multi-echo GRASE enables whole brain 3D MET_2 imaging in less than 15 minutes [80, 85]. As it is usually acquired with a short TR of 1 s, it may, however, yield a biased estimation of long T_2 values. Similar maps with acquisition times comparable to the multi-echo GRASE were obtained using 3D T_2 prep sequences [89]. However, T_2 prep-derived MET_2 shows high sensitivity to field inhomogeneities and the reduced number of acquired echoes (to keep the acquisition time short) may result in a biased estimation of compartmental T_2 s.

The multicompartment analysis of T_2^* decays based on MGRE acquisitions has the advantage over T_2 decays that more echoes can be acquired before the myelin signal decays. Moreover, energy deposition restrictions are less limiting, and acquisitions can be performed at high magnetic field strengths [123]. MWF estimations from the MGRE sequence were compared and found to be in agreement with MET_2 analysis [124]. However, assuming a priori the presence of three water pools – to ensure convergence of the fitting when the frequency offset between the pools is considered – affects the solution and may lead to fitting errors in the

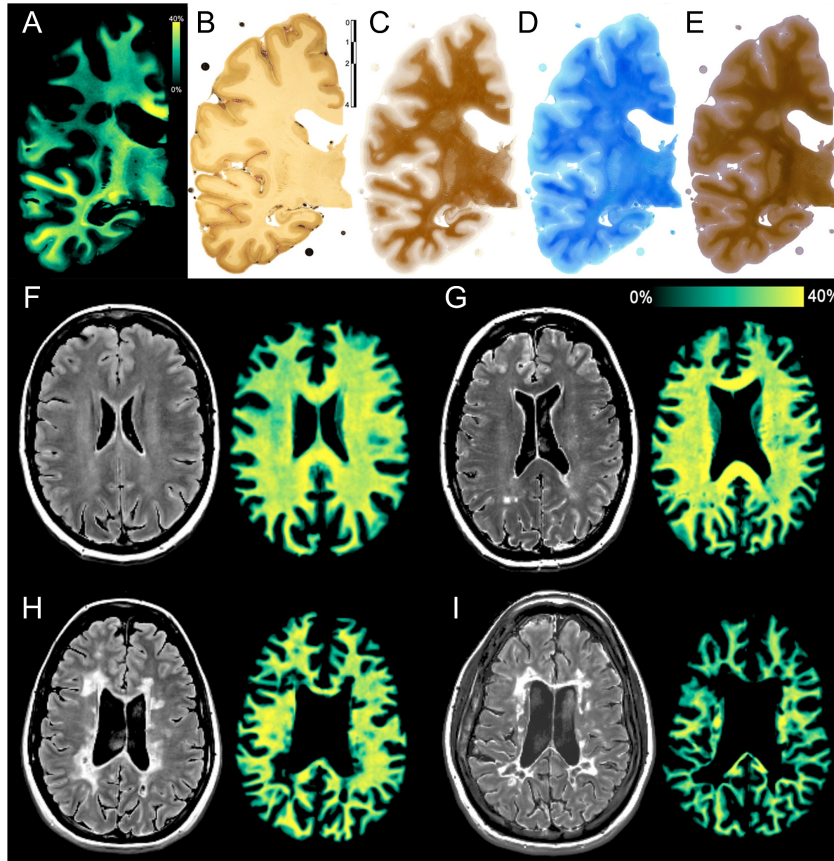


Figure 3.6 – (A-E) Ex vivo validation of myelin partial volume (V_{MY}) map derived with QRAPMASTER (synthetic MRI) in a post-mortem sample of a secondary progressive multiple sclerosis (MS) patient. (A) V_{MY} map, (B) post-mortem sample without histological processing, (C) proteolipid protein immunostaining, (D) luxol fast blue staining, (E) Bielschowsky silver staining. (F-I) Fluid attenuated inversion recovery (FLAIR) images and V_{MY} map in a healthy subject (F), a primary progressive MS patient (G), a relapsing remitting MS patient (H), a secondary progressive MS patient (I). Adapted from Ouellette et al. [119].

presence of pathological tissues with different T_2^* [79, 125, 126]. The possibility of acquiring a single T_2^* echo whose signal intensity is correlated to myelin content offered by the ViSta framework surely represents an advance in T_2^* based techniques. However, ViSta signals depend on an a priori estimate of the myelin T_1 to suppress the signal from compartments with longer T_1 , and the retained signal with short T_2^* after the double inversion may be affected by other confounding factors, such as exchange among water compartments or MT [97].

Although MWF obtained using the multicomponent analysis of IR time series were found in agreement with T_2 and T_2^* relaxometry studies, it remains a not well-spread or validated technique. The simpler mono-compartmental R_1 mapping is often preferred as it has the advantage of delivering bias-free contrast with a resolution that ensures the visualization of structures that are typically invisible in vivo with other methods [105]. This field of research is very active and several T_1 mapping strategies are available, even though a consensus among them is not always achieved [127]. Despite these advantages, T_1 relaxation is modulated by

iron depositions, which were found to account for 36% of the R_1 contrast in GM and 10% in WM [128]. Models of multiple physical parameters – including those more sensitive to iron, as T_2^* – have been explored in multimodal analyses to disentangle the iron contribution to the contrast and directly estimate myelin content [129, 130].

The reviewed methodologies based on simultaneous T_1 and T_2 relaxometry, mcDESPOT [101] and QRAPMASTER [118], guarantee improved brain coverage, resolution, SNR and acquisition time with respect to the multicomponent relaxometry approaches discussed before. Despite being sensitive to myelin changes in the presence of pathological tissues, derived MWF values from both mcDESPOT and QRAPMASTER are higher than conventional techniques (MWF > 20% versus ~10% in WM) [118], [131]. The complexity of the model which needs to be fit to the acquired data represents the main limitation of these methods. For example, in mcDESPOT, a three-pool model is used, which requires fitting bounds for all the estimated parameters. Although the derived myelin maps exhibit relatively low variance, numerical simulations revealed that MWF values estimated with mcDESPOT depend on the choice of these bounding conditions [132, 133]. To improve precision in the parameters estimation, Bouhrara et al. [30, 134, 135] proposed a Bayesian Monte Carlo (BMC) fitting, which is, however, computationally demanding. A four-pool model with water exchange is used instead in QRAPMASTER. To reduce the degrees of freedom and guarantee convergence in the fitting process, some relaxation parameters were fixed, such as the T_2 of myelin water. Biases in the results may be thus introduced as these fixed parameters may vary in the brain, especially in pathological tissue and between subjects.

3.3 Targeting the brain macromolecular content

3.3.1 Magnetization transfer imaging

MT refers to the exchange of magnetization that occurs between the pools of liquid (i.e., free water protons) and semi-solid (i.e., protons bound to macromolecules) spins [70, 136]. While at thermal equilibrium, the net MT between the two pools is null, any manipulation of their magnetization through RF irradiation generates a net MT that restores the initial equilibrium. The semi-solid spins thereby exhibit a broader RF absorption spectrum than the liquid protons. Therefore, in the simplest MT imaging experiment, an off-resonance RF pulse is employed to selectively saturate the semi-solid proton pool and generate a net MT, contributing to the recovery of the longitudinal magnetization of the semi-solid pool and causing a reduction of the magnetization of the liquid pool. As first demonstrated in vivo by Wolff and Balaban in 1989 [137], this effect can be exploited to generate a contrast that provides an indirect assessment of the macromolecular pool by measuring the decreased longitudinal magnetization of the liquid pool after saturation of the semi-solid pool (Figure 3.7). Considering myelin as the brain structure with the highest content of macromolecules, MT-related measurements have been exploited as an indirect marker for myelin content [70, 136, 137].

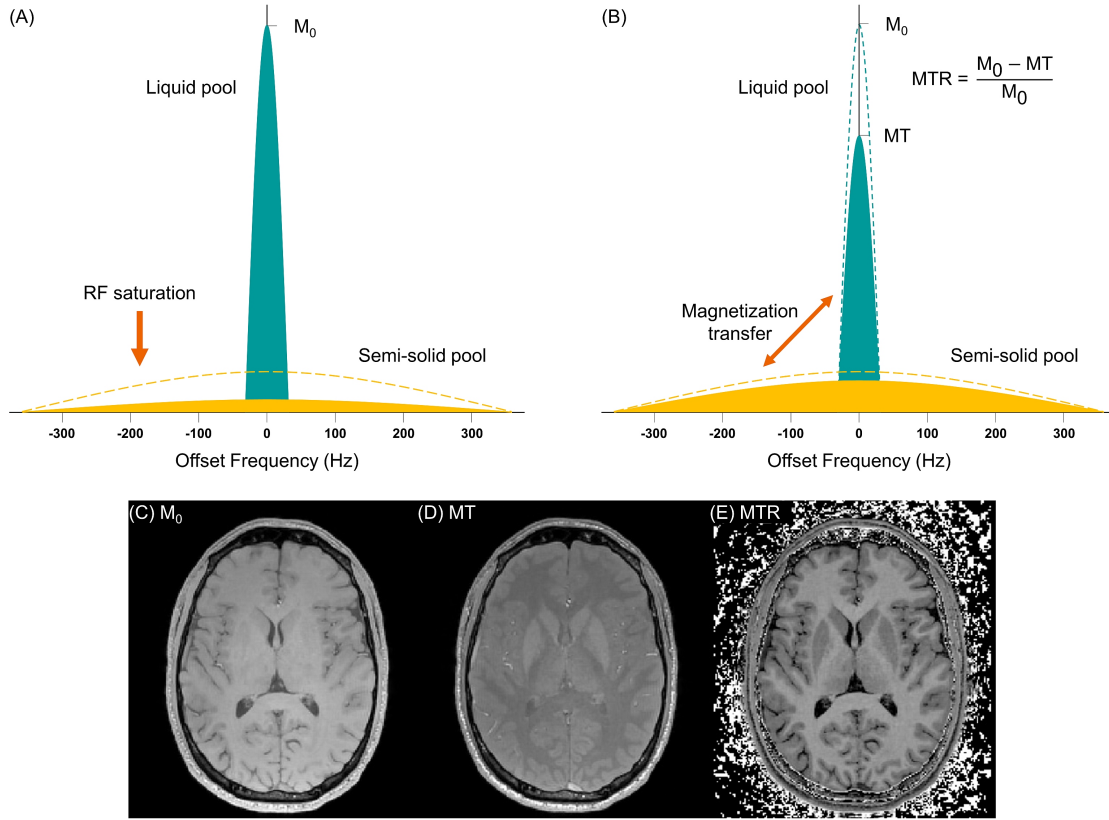


Figure 3.7 – Generation of magnetization transfer (MT) contrast. In the simplest MT imaging experiment, an off-resonance RF pulse is employed to selectively saturate the semi-solid proton pool (A) and provoke a net MT between the pools of liquid and semi solid protons (B), which brings the system back into equilibrium. The MT ratio (MTR) contrast is generated by probing the longitudinal magnetization of the liquid pool without (C) and with (D) saturation of the semi-solid pool and computing their normalized difference (E). The shown images were derived from an MT-prepared GRE sequence [138].

A binary spin bath model was later introduced to formalize the process of MT in biological tissues. According to the formulation of Henkelman et al. [108], the pool of liquid (A) and semi-solid (B) spins are modeled as reservoirs with their own longitudinal magnetization (M_z^A , M_z^B), relaxation rates ($R_A = 1/T_{1,A}$, $R_B = 1/T_{1,B}$) and RF absorption rate (R_{rfA} , R_{rfB}), with a rate of magnetization exchange (R) between pools (Figure 3.8). The RF absorption rates depend on the RF power (ω_1^2) and the RF absorption line shapes, which follow a Lorentzian function in liquids and a super-Lorentzian in semi-solids [139]: $R_{rfi}(2\pi\Delta f) = \omega_1^2 \pi g_i(2\pi\Delta f)$, with $g_i(2\pi\Delta f)$ being the line shape for the protons in the pool i and Δf the offset frequency of the RF irradiation. This model was extended to account for the dipolar relaxation of the semi-solid pool, which arises from the non-zero time averaging of residual dipolar coupling in solids and presumably in semi-solids [140, 141]. In biological tissues, this is most likely to happen between spins with highly constrained motion and low free diffusion, such as the ones found in the phospholipid chains forming the membrane of myelin sheaths. Hence, following the work of Protorov [140] and Goldman [141] on the theory of RF saturation in solids, Yeung et al. [142] extended the binary spin bath model including an additional reservoir related to

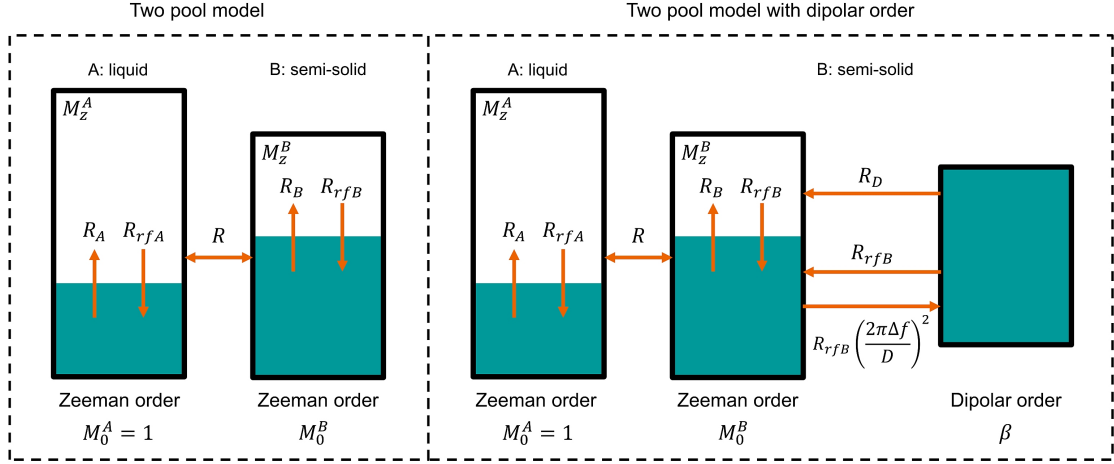


Figure 3.8 – Binary spin bath model for magnetization transfer without (left) and with (right) dipolar order. The coloured regions of each reservoir indicate the longitudinal magnetization. Adapted with permission from Morrison et al. [143].

the semi-solid protons to account both for the Zeeman order (polarization of the spins in the main magnetic field) and dipolar order (polarization of the spins in the local magnetic fields induced by dipolar-coupled protons) (Figure 3.8). Under RF irradiation, a magnetization exchange exists between the Zeeman and dipolar reservoirs that depend on R_{rfB} , with the dipolar relaxation time constant being $R_D = 1/T_{1,D}$. Following this formulation, the time evolution of the longitudinal magnetization of the pools under RF irradiation is computed as follows [143]:

$$\frac{dM_z^A}{dt} = R_A(M_0^A - M_z^A) - RM_0^B M_z^A + RM_0^A M_z^B - R_{rfA} M_z^A, \quad (3.12)$$

$$\frac{dM_z^B}{dt} = R_B(M_0^B - M_z^B) - RM_0^A M_z^B + RM_0^B M_z^A - R_{rfB} M_z^B + R_{rfB} \beta', \quad (3.13)$$

$$\frac{d\beta'}{dt} = R_{rfB} \left(\frac{2\pi\Delta f}{D} \right)^2 (M_z^B - \beta') - \frac{1}{T_D} \beta', \quad (3.14)$$

where β' is proportional to the inverse of the dipolar spin temperature ($\beta' = \beta \cdot 2\pi\Delta f$), and D corresponds to the local dipolar field expressed in angular frequency units and may be calculated from the second moment of g_B , the lineshape of the semi-solid pool.

One MT-derived metric of interest in this context is the MT ratio (MTR), evaluated as the difference in image intensities between an MT-prepared acquisition and a reference, unsaturated acquisition, normalized to the unsaturated image intensities. Notably, even though being a semi-quantitative measure, MTR was found to be sensitive to WM alterations [144, 145] and to correlate with myelin content in post-mortem studies of MS patients ($r = 0.84$) [146]. However, the MTR contrast depends heavily on the experimental conditions (e.g., sequence parameters and B_1 inhomogeneities) and tissue properties (e.g., relaxation times and exchange rate of the

two pools). Therefore, Helms et al. [147] proposed the acquisition of two reference images with predominant PD- and T_1 -weighting to evaluate an MT saturation (MT_{sat}) term decoupled from T_1 and B_1 dependencies. The MT_{sat} contrast was recently found to better correlate with disability metrics of MS patients than conventional MTR [148].

Quantitative MT

Quantitative measurements of the pools parameters have been developed to provide MT measurements independent from experimental conditions and more specific to tissue properties [108, 139]. Early quantitative MT (qMT) developments based on the binary spin bath theoretical model conducted on biological brain tissues suggested that dipolar order terms can be neglected in experiments performed with single-offset RF irradiations [149, 150]. Therefore, subsequent qMT studies typically employed the binary spin bath model without the dipolar order contribution and aimed at estimating the equilibrium magnetization and relaxation rate of the two pools of spins along with their exchange rate. To that end, a series of volumes with different MT-weightings is collected by varying the power and off-resonance frequency of the saturation pulses. The obtained signal evolution – referred to as the Z-spectrum – is fitted to Bloch equations describing the magnetization evolution in the spin bath model to estimate the parameters of interest [150]. Of note, the system of Bloch equations has a solution only for the steady-state condition and using approximations for the time-varying amplitude of the RF saturation pulses [149], [151–153]. The macromolecular proton fraction (MPF) – defined as the ratio between the equilibrium magnetization of the semi-solid pool and the total magnetization – was validated as a biomarker for myelin by showing its correlation with myelin density ($r = 0.99$) estimated in post-mortem samples of rat brains [154]. A strong correlation between MPF and myelin content (as well between MPF and axonal content) was also found in post-mortem samples of MS patients [155].

Single off-resonance saturation qMT

The long scan time required to sample the Z-spectra and the challenging fitting procedure are two drawbacks of qMT, limiting its clinical feasibility. As an alternative, fast whole brain MPF mapping was investigated by Yarnykh [156], proposing to combine a single off-resonance saturation prepared acquisition with T_1 , B_1 , and B_0 mapping and constrain the binary spin bath model. In this model, the R_1 of the two pools is assumed to be equal ($R_{1,A} = R_{1,B}$) and is measured with an additional variable flip-angle T_1 mapping sequence. For the other parameters, median values were extracted from healthy controls and MS patients and fixed in the model: $R = 19.0 \text{ s}^{-1}$, $T_{2,A} = 0.022/R_{1,A}$, and $T_{2,B} = 9.7 \mu\text{s}$. MPF values measured with a single MT-prepared GRE sequence were found to strongly correlate ($r = 0.995$) with MPF values estimated with conventional qMT both in healthy controls and MS patients (Figure 3.9) [156].

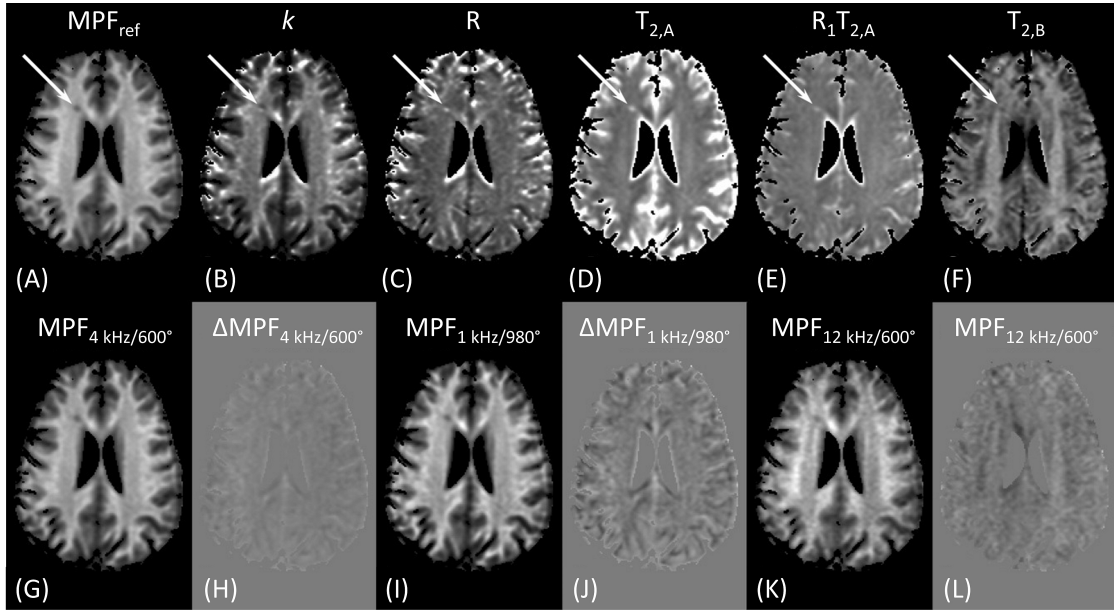


Figure 3.9 – (A F) Quantitative mapping of the macromolecular proton fraction (MPF) and the two-pool model parameters of magnetization transfer (MT) derived from four MT-prepared acquisitions in a patient with multiple sclerosis. (G-L) MPF maps and difference to the MPF_{ref} reconstructed by the single off-resonance saturation quantitative MT method for different offset frequencies and effective flip angles of the saturation pulse. Adapted with permission from Yarnykh [156].

Inhomogeneous MT

The inhomogeneous magnetization transfer (ihMT) has been recently proposed as a contrast mechanism with increased sensitivity to myelin [157–159]. Conventional MT experiments generally assume a two-pool model without any dipolar contribution. However, this assumption does not hold true in the presence of highly motion-restricted protons, such as methylene protons that constitute the myelin phospholipid bilayer structure [160]. Consequently, a nonnegligible dipolar order exists in myelin sheaths, and ihMT techniques aim at measuring its effect. A symmetric dual-offset RF saturation with equal power distributed on both positive and negative frequencies can be used to decouple the Zeeman from the dipolar order [158, 161]. Hence, the ihMT image defined by the difference between a MT image derived from a single offset RF saturation and a MT image derived from a dual-offset RF saturation, both with the same RF power, isolates the dipolar order contribution to RF saturation effects, thus providing a contrast specific to myelin content [157, 158]. The ihMT ratio (ihMTR) is usually computed as the ratio of this difference to the unsaturated reference M_0 .

In a recent publication, Duhamel et al. [162] systematically tested several possible combinations of ihMT preparations [157, 163, 164] and validated the sensitivity of ihMT to myelin by comparison with fluorescence microscopy analyses. Although every strategy showed high correlation to myelin content, the ihMT contrast obtained with “concentrated” RF power deposition and frequency-alternated pulses for dual-offset saturation [163, 164] was found to deliver the largest correlation ($R^2 = 0.96$) and sensitivity to myelin density measurements

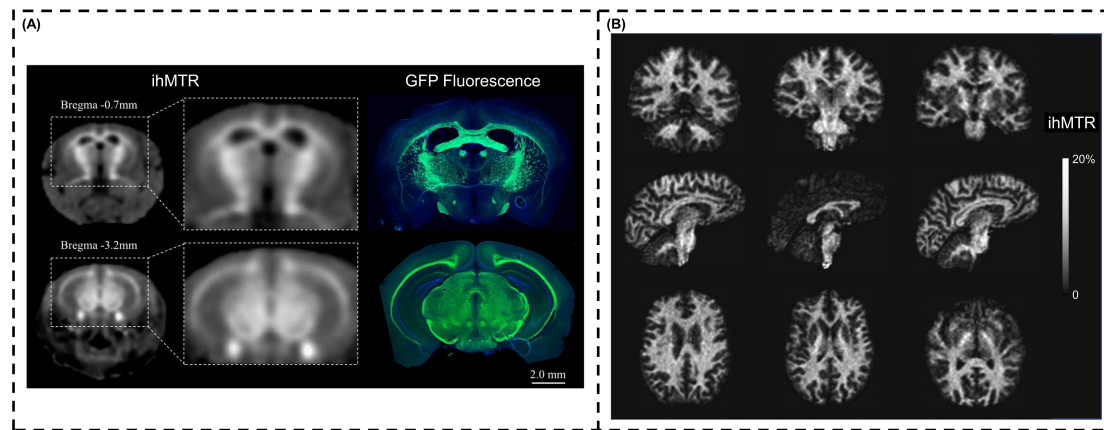


Figure 3.10 – (A) Comparison between inhomogeneous magnetization transfer ratio (ihMTR) images and green fluorescence protein (GFP) microscopy performed in a mouse. (B) Whole brain ihMTR acquisition in a healthy control. Part (A) is adapted with permission from Duhamel et al. [162]. Part (B) is adapted with permission from Mchinda et al. [165].

(Figure 3.10A). The same strategy was used to achieve whole brain in vivo ihMTR imaging in healthy subjects (Figure 3.10B) [165].

3.3.2 Ultrashort TE

While in MT imaging the semi-solid protons are indirectly assessed, ultrashort TE (UTE) techniques attempt to directly probe the signal of these protons with T_2 s shorter than 1 ms [166, 167]. In classical imaging methods that target free water protons, the relaxation of macromolecular spins is faster than the duration of the RF excitation and is thus negligible. Conversely, in UTE imaging, short RF pulses lasting hundreds of microseconds are followed as rapidly as possible by a fast gradient readout to sample the signal changes originating from the macromolecular pool of short T_2 s. Long T_2 components can be also selectively saturated, resulting in an additional contrast enhancement towards short T_2 s [168, 169].

To keep the nominal TE short (tens of microseconds or less), two main acquisition schemes are usually employed:

- 2D acquisitions with a half-pulse RF excitation in combination with slice-selective gradients [170, 171]; and
- 3D radial center-out spatial encoding in conjunction with a short, non-selective 3D hard pulse [172].

Ex vivo studies in myelinated nerves demonstrated that UTE contrast arises from those phospholipid chain that characterized myelin sheaths [71, 173], suggesting UTE sequences as a valid tool for the direct visualization of myelin. In vivo, single-slice scans were conducted with a 2D UTE sequence prepared with an adiabatic IR (AIR) pulse to saturate the long T_2 pools in WM, demonstrating the presence of short T_2 components in WM tissues [170] and expected hypo-intensities in damaged brain areas of MS patients (Figure 3.11) [171].

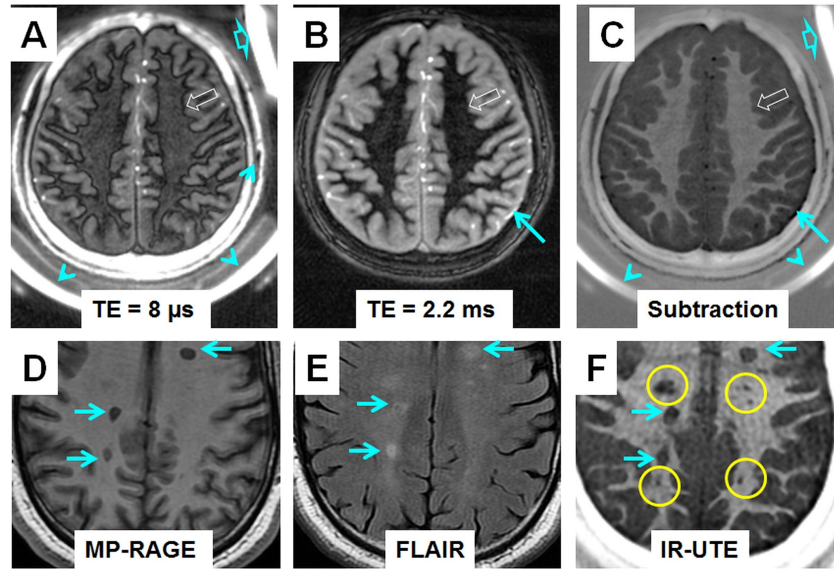


Figure 3.11 – Inversion recovery prepared ultra short echo time (IR-UTE) imaging in a healthy subject with an echo time of 8 μ s (A) and 2.2 ms (B). (C) Images obtained as subtraction of the IR-UTE images acquired at different echo times, showing white matter integrity in the healthy subject. Magnetization Prepared Rapid Gradient Echo (MPRAGE) (D), Fluid attenuated inversion recovery (FLAIR) (E) and IR-UTE (F) imaging of a patient with multiple sclerosis (MS). The MS lesions that are visible in all contrasts are indicated by arrows, whereas lesions that are more visible in the IR-UTE image are circled in yellow. Adapted with permission from Sheth et al. [171].

Following the same idea behind the multicomponent decomposition of T_2^* signals arising from free water molecules, maps reporting the fraction of semi-solid protons with short T_2^* were derived from data acquired by repeating a 3D whole brain UTE sampling for different TEs and fitting a bi-exponential decay [172].

3.3.3 Macromolecular tissue volume

The macromolecular tissue volume (MTV) has been proposed for myelin density quantification [174]. Whole brain PD and T_1 maps were derived from a spoiled GRE sequence [175] acquired with different flip angles. PD values in each voxel are considered proportional to water content and water volume fractions (WVF) were derived as the ratio between PD values in brain tissue and in CSF, assuming the latter to be filled with free water. The MTV fraction can then be computed as 1-WVF. Analysis of post-mortem samples of MS patients demonstrated a decreased MTV fraction correlated with changes in tissue properties [174].

3.3.4 Discussion

The simplicity of MT-weighted imaging, especially MTR, is attractive for clinical practice. However, MTR contrast strongly depends on the experimental conditions and was proven to be sensitive to other tissue alterations rather than being specific to myelin degradation,

such as inflammation, oedema and axonal loss [176–178]. Quantitative MT experiments have the advantage of being more independent from experimental conditions [150]. However, more data are required due to the complex modeling, increasing the acquisition time. Single off-resonance saturation qMT experiments hold a great promise for qMT studies with reduced acquisition time [156]. The enhanced sensitivity towards dipolar relaxation mechanism makes ihMTR an interesting approach for the monitoring of brain development [179] and demyelination [180, 181]. IhMTR benefits from a straightforward processing consisting of a combination of the different contrasts obtained. However, ihMTR remains still a semi-quantitative approach. Therefore, recent efforts focused on achieving quantitative ihMT [182, 183].

Although being a promising approach, technical challenges still hinder the widespread use of UTE techniques. First, when imaging short T_2 s ($\ll 1$ ms), protons in the RF coil housing generate background signals folding into the imaged field of view [184]. In addition, performant gradients are needed to guarantee short TEs, which are only available in recently deployed and more costly scanners [171, 172]. Finally, in a recent study, single AIR-prepared UTE acquisitions were compared to multiple AIR (MAIR)-prepared scans to directly image the short T_2^* of myelin by suppressing the MR signal related to either a single long T_1 or a range of T_1 s, respectively [185]. While AIR-UTE scans showed contrast in WM, no signal was detected in the WM and GM by the MAIR-UTE scans (only bones and hardware components were observed), raising the question of whether the signal related to the macromolecular protons of myelin may decay too fast to be detected with UTE techniques [185].

With respect to MTV fraction, while MTV fraction maps correlated in WM tracks with qMT ($r = 0.9$) and with MWF values ($r = 0.79$) [174], further validation of this contrast is needed.

3.4 Other MR contrasts

3.4.1 Diffusivity and fractional anisotropy

Diffusion refers to the irreversible and constant Brownian motion of small molecules [186], whose mean squared displacement is a function of the diffusion time and the diffusion coefficient (D , mm^2s^{-1}), a substrate specific constant [187]. In diffusion-weighted imaging (DWI), the self-displacement of water molecules is targeted [188, 189], which is of interest in the detection and/or characterization of neurological disorders that cause changes in water diffusion [190, 191]. The simplest experiment to acquire diffusion-weighted signals performs a pulsed gradient spin echo acquisition, in which a pair of diffusion-sensitizing gradients (DSGs) is added to a spin echo sequence on either side of the refocusing pulse [192]. The application of the DSGs causes phase dispersion of the diffusive spins, resulting in an attenuation of the overall MR signal (S_b):

$$S_b = S_0 e^{-bD}, \quad (3.15)$$

with S_0 being the signal acquired without DSGs, and b a value depending on the parameters describing the DSGs (duration, amplitude and delay between DSGs). Provided that two acquisitions, without ($b = 0$) and with DSGs, are acquired, D can be derived as follows:

$$D = -\ln(S_b/S_0)/b, \quad (3.16)$$

In in vivo DWI, D is usually referred to as the apparent diffusion coefficient (ADC), as the measured diffusion includes other sources of water mobility (e.g., active transport) that cannot be separated from Brownian diffusion [193].

While the estimation of ADC maps assumes an isotropic diffusion within the investigated medium, in biological tissues, the presence of ordered structures (e.g., axons) creates preferential directions of diffusion. Such anisotropic diffusion is usually described by a diffusion tensor and more advanced measurements have been developed to characterize the diffusion tensor in vivo by performing multiple acquisitions while DSGs are applied in different directions [194, 195]. One metric of interest derived from diffusion tensor imaging (DTI) experiments is the fractional anisotropy (FA), which corresponds to the amount of expected diffusional anisotropy within each voxel.

In the context of myelin imaging, studies on animal models showed that DTI measurements of the components parallel and perpendicular to the axon allow to detect demyelination even in the absence of axonal damage, enabling to discriminate between axonal and myelin damage [196, 197]. In ex vivo samples of human MS brain tissues, correlation was found between FA and both myelin content ($r = -0.79$) and axonal count ($r = 0.70$), with FA exhibiting lower values in MS lesions compared to NAWM (Figure 3.12A) [198]. In vivo DTI data acquired in MS patients showed an increased mean diffusivity and reduced FA in lesions [199–201].

Although mean diffusivity and FA are probably the most commonly used metric in clinical studies, a vast body of literature exists around more complex microstructural modeling of the diffusion signal (e.g., NODDI [202], CHARMED [203], among others), whose review would fall out of the scope of this work. The reader is thus referred to Cercignani and Gandini [204] and Alexander et al. [205] for additional details.

3.4.2 Susceptibility imaging

Magnetic susceptibility represents the degree to which a given material or tissue becomes magnetized in the presence of an external magnetic field, generating an internal polarization that either opposes (diamagnetism) or augments (paramagnetism) the magnetic field. More specifically, spins close to diamagnetic compounds precess with a frequency lower than the resonance frequency, whereas spins close to paramagnetic compounds precess with a higher frequency. In susceptibility-weighted imaging (SWI), the MR signal sensitivity towards these differences is captured using a GRE acquisition, in which the signal arising from spins dephased by the local field inhomogeneities results in spatial differences in the phase im-

ages. SW images are then derived by filtering the raw phase image and combining it with the magnitude [206, 207]. The SW contrast in the brain is mainly driven by nonheme iron (paramagnetic) [208, 209] and myelin, whose elevated content in lipids and proteins renders its sheaths more diamagnetic than water [210–212]. While relative differences in susceptibility are assessed by SWI, quantitative susceptibility mapping (QSM) methods have been developed to retrieve the bulk susceptibility of the investigated tissue by acquiring multi-echo GRE data [213, 214]. Nowadays, whole brain QSM maps with high resolution can be achieved in short acquisition times [50].

The use of susceptibility as biomarker for myelin has been investigated in a number of studies [215–217]. Notably, QSM changes were found to correlate with histological samples stained for myelin [216], and the depletion of myelin in MS active lesions was observed to result in increased QSM measurements (Figure 3.12B) [217].

3.4.3 Magnetic resonance elastography

Magnetic resonance elastography (MRE) comprises methods to non-invasively assess the stiffness of biological tissues using MRI [218, 219]. In order to perform MRE measurements, the organ under investigation is first exposed to an external vibration that induces a harmonic motion of the organ itself. For example, in the brain, shear waves can be induced with a soft pillow-like mechanical system [220]. Once the motion reaches steady-state, the induced displacement is measured with a phase-contrast image using a sequence that employs motion encoding gradients [220, 221]. The acquired displacement field is typically formulated as an inverse problem to quantify the stiffness of the tissue and its shear mechanical properties [222, 223]. In the brain, these mechanical properties have been related to tissue characteristics on different scales, from the cellular architecture up to the neuronal organization [224–226]. With regards to myelin, the stiffness was found to be sensitive to demyelination in studies conducted on animal models of MS [227, 228]. Brain global stiffness was found to be reduced in MS patients compared to matched healthy controls (Figure 3.12C) [229, 230].

3.4.4 Ratio of T_1 -weighted and T_2 -weighted images

Based on previous findings suggesting a correlation between T_1 -weighted and T_2 -weighted image intensities in human cortex with myelin content [231, 232], Glasser et al. [233] proposed the use of the T_1 -weighted/ T_2 -weighted ratio for high-resolution segmentation of cortical areas. Originally introduced for this purpose, the ratio was later explored as a marker for myelin content [234–236]. T_1 -weighted/ T_2 -weighted measurements were correlated with the variability in performance across the human lifespan [237] and tissue damage in the NAWM of MS patients (Figure 3.12D) [238].

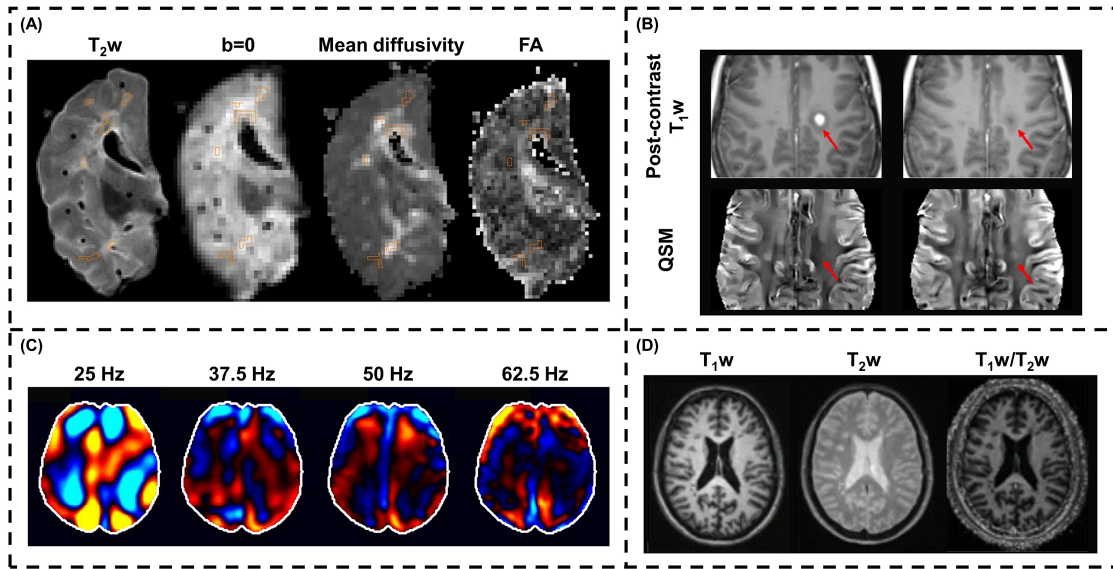


Figure 3.12 – (A) Brain T_2 -weighted (T_2w) MRI, mean diffusivity (MD) and fractional anisotropy (FA) maps acquired in post-mortem samples of a patient with multiple sclerosis (MS). (B) Post contrast T_1 -weighted (T_1w) images and corresponding quantitative susceptibility maps (QSM) of an active MS lesion acquired during enhancing (left) and after 19 days (right). The increased susceptibility between the two acquisitions suggested myelin digestion by macrophages. (C) Brain magnetic resonance elastography (MRE) images resolved for different experiment vibrational frequencies. (D) T_1w , T_2w and corresponding ratio in a MS patient. Part (A) is adapted from Schmierer et al. [198]. Part (B) is adapted with permission from Deh et al. [217]. Part (C) is adapted from Streitberger et al. [230]. Part (D) is adapted with permission from Beer et al. [238].

3.4.5 Discussion

Other sources of MR contrast that have been shown to be sensitive to myelin changes have been reviewed in this section.

Given the peculiar sensitivity towards cellular architecture, a vast literature exists around the use of diffusion imaging for investigating the integrity of WM microstructure [205]. Nonetheless, commonly used DTI measurements, such as FA, were found to be affected by other tissue characteristics at the microstructural scale that characterized the axonal fibre geometry [239].

The capability of capturing the diamagnetic properties of myelin sheaths with QSM acquisitions represents another alternative for myelin imaging. The major drawback of QSM in the context of myelin imaging are confounding effects such as iron deposition and varying myelin density. However, it was shown that the combined analysis of QSM with R_1 and R_2^* maps may separate iron and myelin contributions [128]. In addition, complex modeling is required to distinguish global from local field inhomogeneities in order to derive QSM maps. Hence, a large variety of post-processing techniques exist for QSM [214, 240, 241].

Despite promising findings, additional research is needed in the field of MRE to clarify the biophysically processes behind the measured changes in stiffness, as well as to improve the resolution that currently hinders the investigation of focal pathologies.

Finally, conventionally weighted contrasts have been investigated in retrieving metrics sensitive to myelin, such as the ratio of T_1 -weighted to T_2 -weighted images [234]. Although these acquisitions rely on more common clinical images and can be performed with high resolution, these measurements are highly affected by the experimental conditions and provide a source of contrast for targeting myelin that is not quantitative, as it depends on various experimental and physiological influences and does not have any physical basis. T_1 -weighted/ T_2 -weighted images were originally introduced to produce a contrast that allows better parcellation of brain cortex [233]. In fact, only a weak correlation was reported between T_1 -weighted/ T_2 -weighted images and MWF values derived from the multi-echo GRASE ($r = 0.029$) [235], and with MT in WM regions ($r = 0.38$) and QRAPMASTER ($r = 0.45$) [242].

3.5 Conclusions

This chapter intends to give an overview of a wide range of MRI-based approaches for myelin imaging in the human brain. A summary of the reviewed methods is offered in Table 3.1, where example acquisition parameters, along with the main pros and cons of each method, are listed. Table 3.2 provides a list of studies investigating the reproducibility of the reviewed methods [89, 97, 165, 243–257].

Although the “true” content of myelin in the brain – this being the myelin weight or volume fraction within a voxel – should be independent from the specific acquisition, reconstruction or field strength, the findings reported here show a high dependency of myelin-related measurements on the used methodology. Despite requiring longer acquisition times, quantitative techniques involving complex modeling that relates the measured MR signal to measures of myelin density have more potential to overcome this limitation by mitigating confounding effects. Of interest, West et al. [258] recently proposed to convert MWF values from MET_2 experiments and MPF measurements from qMT acquisitions into metrics of myelin volume fractions (MVF) using a volumetric WM model, which was calibrated with histological data for MPF. The converted measurements of MVF showed not only higher correlation but also higher accuracy in estimating “true” MVF computed from histological samples [258]. Future work towards this line of research is important to overcome the current limitations of myelin imaging, and it may benefit from recent developments in the field of MRF [25, 259–261] and machine learning [262–264].

Table 3.1 – Summary of reviewed methods reporting relevant sequence parameters along with advantages and disadvantages of each method.

Method	Type	Resolution (mm ³)	Acquisition matrix	TA (min)	Pros	Cons
Relaxometry	MESE	2D [8] 3D [122]	0.86×1.72×5 —	256×128×1 256×128×12	25 12	Most commonly used and validated method for myelin imaging; proved correlation with myelin density measurements in postmortem samples [77, 78].
	GRASE [80]	3D	1×1×5	232×192×20	14.4	Whole-brain coverage in less than 15 minutes; proved correlation with MESE-based maps [80].
	T ₂ prep	2D [87] 3D [89]	2×2×10 1.25×1.25×5	128×128×1 192×192×32	16 10	Whole-brain coverage with higher SNR than other T ₂ -based methods.
	MGRE [91]	2D	0.78×0.78×5	256×256×5	8.7	Larger number of samples are acquired before the myelin signal has decayed due to shorter TEs; proved correlation with MESE-based maps [124]; suitable for application at high field strengths (e.g., 7 T).
	ViSTa [97]	3D	1.15×1.15×3	192×192×32	14.9	Direct visualization of short T ₂ * components in a single-echo experiment enabled by the suppression of long T ₁ s; complex postprocessing and/or signal modeling is not required.
	IR time series [104]	2D	1.5×1.5×5	128×112×1	33.6	Based on relaxation mechanism that can be easily measured.
						Long TA for in vivo whole brain imaging; low SNR and noise-sensitive MWF computation.
						Generally used short TR (1 second) may result in wrong estimation of long T ₂ s; image blurring due to EPI readouts.
						Reduced number of echoes acquired to keep the TA short, which may result in the wrong estimation of compartmental T ₂ s; high sensitivity to B ₀ and B ₁ inhomogeneities.
						High sensitivity to field inhomogeneities that requires correction of signal decays and thus constrained modeling; introduction of a priori information into modeling may bias the parameters estimation.
						Single-echo experiments do not deliver quantitative maps; a priori estimate of the T ₁ of myelin is needed, which may change within different brain regions and with pathology.
						Not a well-spread technique.

Table 3.1 continued from previous page

Method	Type	Resolution (mm ³)	Acquisition matrix	TA (min)	Pros	Cons
R ₁ [105]	3D	0.5×0.5×0.5	(whole brain)	11	Bias-free contrast and high resolution in short TA that ensure the visualization of structures not discernible in vivo with other methods [105]; complex postprocessing is not required.	Contrast notably influenced by changes in iron content [113].
mcDESPOT [117]	3D	1.7×1.7×1.7	128×128×98	—	Whole-brain coverage with high resolution and SNR in acceptable TA.	Complex simultaneous modeling of the multicompartamental nature of relaxation times; fitting precision is improved considering a priori information that was proved to bias the estimated parameters and reduce specificity [132, 133]; higher myelin density estimates than 1-dimensional relaxation methods [131].
QRAPMASTER [118]	2D	1×1×4	(whole brain)	8.4	Whole-brain coverage with high resolution and SNR in acceptable TA.	Based on a biophysical model with fixed T ₂ of myelin; possible introduction of biases in the results; higher myelin density estimates than 1-dimensional relaxation methods [118].
Macromolecular content	MTR [144]	2D	—	10	Straightforward acquisition and postprocessing involving only the combination of different contrasts.	Only semi-quantitative; strongly depends on experimental conditions; sensitive to other tissue alterations rather than myelin degradation (e.g., inflammation, oedema, and axonal loss) [176, 177].
	qMT [155]	2D	1×1.3×5	240×180×1	—	An MT experiment that delivers quantitative maps more independent from experimental conditions.

Table 3.1 continued from previous page

Method	Type	Resolution (mm ³)	Acquisition matrix	TA (min)	Pros	Cons	
ihMTR [165]	3D	2.5×2.5×2.5	128×80×64	15.4	Straightforward postprocessing consisting of a combination of different contrasts; increased specificity to myelin compared with other MT-based contrasts.	Semi-quantitative signal; complex model accounting for physical phenomena behind ihMT [158] are needed to achieve quantitative ihMT effect measurements [182, 183].	
UTE	2D [170]	0.94×0.94×5	256×256×1	4.4	Direct visualization of short T ₂ components (<<1 ms) in a single-echo experiment; multicompartiment analysis of short T ₂ s is also possible.	Highly performant gradients are required to guarantee short TEs (few tens of microseconds); technical challenges still to be overcome before the wide-spread use of this approach [184, 265]; a question still remains whether the signal related to the macromolecular protons of myelin decay too fast to be detected with UTE techniques [185].	
	3D [172]	2.2×2.2×2.2	(whole brain)	45		Sensitivity to field inhomogeneities.	
MTV [174]	3D	1×1×1	(whole brain)	25	Based on simple contrast mechanism; complex postprocessing and/or signal modeling is thus not required; proved to correlate with MWF values in WM tracks.		
Others	DTI-based FA [200]	3D	2×2×2	10	Sensitivity to changes in cellular architecture; established and validated technique in the assessment of WM microstructural integrity [205].	Affected by other tissue characteristics at the microstructural scale, which characterized the axonal fiber geometry [239].	
	QSM [50]	3D	1×1×1	240×240×220	2.3	Whole brain high resolution with short TA.	Interpretation of maps may be complicated in the case of simultaneous changes in iron and myelin density; reconstruction requires complex modeling [214, 240, 241].
	MRE [229]	2D	1.5×1.5×6	128×128×3	15	Provides a quantitative measurement of brain tissue stiffness that has been shown to be sensitive to demyelination [227, 228].	Biophysical processes behind the measured changes in stiffness are still not clear; currently achievable resolution hinders the investigation of focal pathologies.

Table 3.1 continued from previous page

Method	Type	Resolution (mm ³)	Acquisition matrix	TA (min)	Pros	Cons
T ₁ w/T ₂ w [233]	3D	1 × 1 × 1	256 × 256 × 176	13	Based on conventional MR contrasts routinely scanned in clinics; high resolution and SNR; high contrast-to-noise ratio between regions with different myelin content in the cortex.	Not quantitative and without physical bases; weak correlation with relaxometry-based maps [235, 242]; originally introduced to obtain contrast for better parcellation of brain cortex regions and not as myelin density measurement.

Note: The reported sequence parameters were retrieved from the reference publications listed in the first two columns.

Table 3.2 – Summary of studies conducted to investigate the reproducibility of the reviewed methodologies for myelin imaging.

	Method	Reproducibility studies
Relaxometry	MESE	WM scan–rescan MWF COV of 3.99% (range 0.15%-25.11%) and ICC of 0.76 (range 0.49-0.92), averaged among 5 healthy subjects [251]. WM intersite MWF COV of 4.68% (range 2.86%-8.13%) and ICC of 0.69, averaged among 5 healthy subjects [251].
	GRASE	Scan–rescan MWF ICC (range of 0.83-0.96) in different brain regions of 11 healthy subjects [252]. Intersite MWF COV of 2.77% (range 0.03%-8.00%) averaged among 10 healthy subjects [253].
	T ₂ prep	Scan–rescan MWF correlation of 0.99 and COV (range of 1.3%-2.4%) in different brain regions of 11 healthy subjects [89].
	MGRE	Scan–rescan MWF correlation (range of 0.61 ± 0.14 to 0.72 ± 0.07 , depending on compensation for flowing blood and respiration) averaged among 8 healthy subjects [254].
	ViSTa	Scan–rescan ViSTa COV of 13.8% as median value among three scans of the same healthy subject [97].
	R ₁	Scan–rescan MP2RAGE T ₁ COVs (range of 2.08%-2.89%) in different brain regions of 20 healthy subjects [255].
	mcDESPOT	Intrasite MWF COV of 7% averaged over brain regions of 9 healthy subjects [256]. Intersite MWF COV of 8% averaged over brain regions of 7 healthy subjects [256].
	QRAPMASTER	Scan–rescan V _{MY} COV (range of $0.64\% \pm 0.30\%$ to $1.11\% \pm 1.07\%$), averaged among WM brain regions of 10 healthy subjects [257]. Intersite V _{MY} COV of $4.46\% \pm 0.82\%$ averaged among WM brain regions of 10 healthy subjects [257].
Macromolecular content	MTR	Median scan–rescan MTR COV of 1.2% among 7 healthy subjects [243].
	qMT	Scan–rescan MPF relative difference of 0.3% (range 0.06%-6.3%), averaged among 6 healthy subjects [244].
	ihMTR	Scan–rescan ihMTR intra-individual error < 2% in all brain regions of 3 healthy subjects [165]. Intrasite ihMTR ICC ranging from 0.747 to 0.949 in different brain regions of 5 healthy subjects [245]. Intersite ihMTR ICC ranging from 0.711 to 0.937 in different brain regions of 5 healthy subjects [245].
	MTVF	Scan–rescan MTVF correlation > 0.74 evaluated voxel-wise in 8 healthy subjects [246].
Others	DTI-based FA	Intrasite FA COV ranging from 0.8% to 3.0% averaged among 9 healthy subjects [247]. Intersite FA COV ranging from 1.0% to 4.1% averaged among 9 healthy subjects [247].

Table 3.2 continued from previous page

Method	Reproducibility studies
QSM	Intrasite whole-brain QSM ICC of 0.914, averaged among 8 healthy subjects [248].
MRE	Scan–rescan stiffness differences ranging from -0.05 kPa to 0.06 kPa for different imposed frequencies in WM, averaged among 10 healthy subjects [249].
T ₁ w/T ₂ w	Scan–rescan T ₁ w/T ₂ w ICC > 0.80 in different brain regions of 20 healthy subjects [250].

Note: Scan–rescan reproducibility refers to acquisitions performed during the same session (with or without repositioning). Intrasite reproducibility refers to acquisitions performed using the same scanner but in a separate session (time difference > 1 day). Intersite reproducibility refers to acquisitions performed on different scanners and/or in different centers. **Abbreviations:** COV, coefficient of variation; ICC, intraclass correlation coefficient.

4 Fast and high-resolution myelin water imaging: Accelerating multi-echo GRASE with CAIPIRINHA

The content of the following chapter is based on the postprint version of the article: “Fast and high-resolution myelin water imaging: Accelerating multi-echo GRASE with CAIPIRINHA” published in Magnetic Resonance in Medicine [85]. DOI: [10.1002/mrm.28427](https://doi.org/10.1002/mrm.28427). The article was co-authored by Tom Hilbert, Erick Jorge Canales-Rodríguez, Marco Pizzolato, Constantin von Deuster, Reto Meuli, Josef Pfeuffer, Alessandro Daducci, Jean-Philippe Thiran, and Tobias Kober. All co-authors contributed to the idea and reviewed the manuscript.

Abstract: Although several MRI methods have been explored to achieve in vivo myelin quantification, imaging the whole brain in clinically acceptable times and sufficiently high resolution remains challenging. To address this problem, this chapter investigates the acceleration of multi-echo T_2 acquisitions based on the multi-echo GRASE sequence using CAIPIRINHA undersampling and adapted k-space reordering patterns. To that end, a prototype multi-echo GRASE sequence supporting CAIPIRINHA parallel imaging was implemented. Multi-echo T_2 data were acquired from 12 volunteers using the implemented sequence ($1.6 \times 1.6 \times 1.6 \text{ mm}^3$, 84 slices, $TA = 10:30 \text{ min}$) and a MESE sequence as reference ($1.6 \times 1.6 \times 3.2 \text{ mm}^3$, single-slice, $TA = 5:41 \text{ min}$). In addition, scan-rescan datasets were acquired to evaluate the repeatability of the derived maps. Resulting MWF maps from the MESE and multi-echo GRASE sequences were found to be correlated ($r = 0.83$). A Bland-Altman analysis revealed a mean bias of -0.2% ($P = .24$) with the limits of agreement ranging from -3.7% to 3.3% . The Pearson’s correlation coefficient among MWF values obtained from the scan-rescan datasets was found to be 0.95 and the mean bias equal to 0.11% ($P = .32$), indicating good repeatability of the retrieved maps.

4.1 Introduction

Fast-transmitting axons of vertebrates are usually surrounded by a myelin sheath that speeds the signal propagation along the axon and among neurons (see **Section 2.3.4** in Chapter 2). Since eventual myelin impairment or degradation can severely compromise the activity of the

Chapter 4. Fast and high-resolution myelin water imaging: Accelerating multi-echo GRASE with CAIPIRINHA

central nervous system, several research efforts focused on the development of methodologies for non-invasive and in vivo quantification of brain myelin (see **Chapter 3**).

Of interest here are MRI-based techniques for myelin water imaging (MWI). Since the MR signal mostly originates from protons contained in water molecules, in 1994 MacKay et al. proposed to exploit the short transverse relaxation time T_2 of compartmentalized water in myelin sheaths to measure myelin density in vivo (see **Section 3.2.1** in Chapter 3). A single-slice MESE experiment was employed to acquire T_2 decays in brain voxels and derive MWF maps of the human brain [8]. However, the long acquisition time required to image even a limited portion of the brain with the MESE sequence impeded the use of this technique in clinical routine. In the attempt of overcoming this drawback, several alternative approaches were developed.

An alternative solution to obtain a series of images with different T_2 -weighting is offered by the multi-echo GRASE sequence, where an EPI readout is centered on each spin echo (see **Section 2.3.2** in Chapter 2). Compared to a MESE sequence, the acquisition time is shortened by a factor equal to the number of EPI readouts per spin echo. The multi-echo GRASE sequence was validated as an alternative to conventional MESE in the application of MWF mapping (see **Section 3.2.1** in Chapter 3). Using an image-based parallel imaging method (SENSE factor of 2), 20 brain slices of 5 mm thickness were acquired in 14.4 min [80].

This work aims at investigating the feasibility of further accelerating 3D multi-echo GRASE acquisitions with a k-space-based parallel imaging method, CAIPIRINHA (see **Section 2.4.1** in Chapter 2), to achieve increased resolution and brain coverage in a reduced scan time. Additionally, to mitigate possible T_2^* -related B_0 inhomogeneity dependent phase errors that contribute to image artifacts in EPI-based acquisition schemes, this study investigates the impact of including the gradient-echo shifting technique [266, 267] in the developed multi-echo GRASE sequence.

4.2 Methods

4.2.1 Sequence design

The sequence diagram of the implemented prototype 3D multi-echo GRASE sequence is shown in Figure 4.1. After the excitation of the image slab, a train of slab-selective refocusing pulses is used to acquire a series of T_2 -weighted volumes at different TEs. Multiple lines in the readout direction (k_x) are acquired in each spin echo using EPI. Since the T_2 values of compartmentalized water in myelin sheaths range from 10 to 40 ms [8], the EPI factor was fixed to three to maintain small echo spacing. Given that the coverage and order of k-space trajectories over the echo train strongly affects the image contrasts in GRASE-based acquisitions, the employed trajectories were optimized to guarantee the T_2 -weighting of the acquired contrasts while reducing T_2^* modulations and chemical shift artifacts. To that end, refocusing pulses are surrounded by spoiler gradients of equal size; after a gradient lobe of

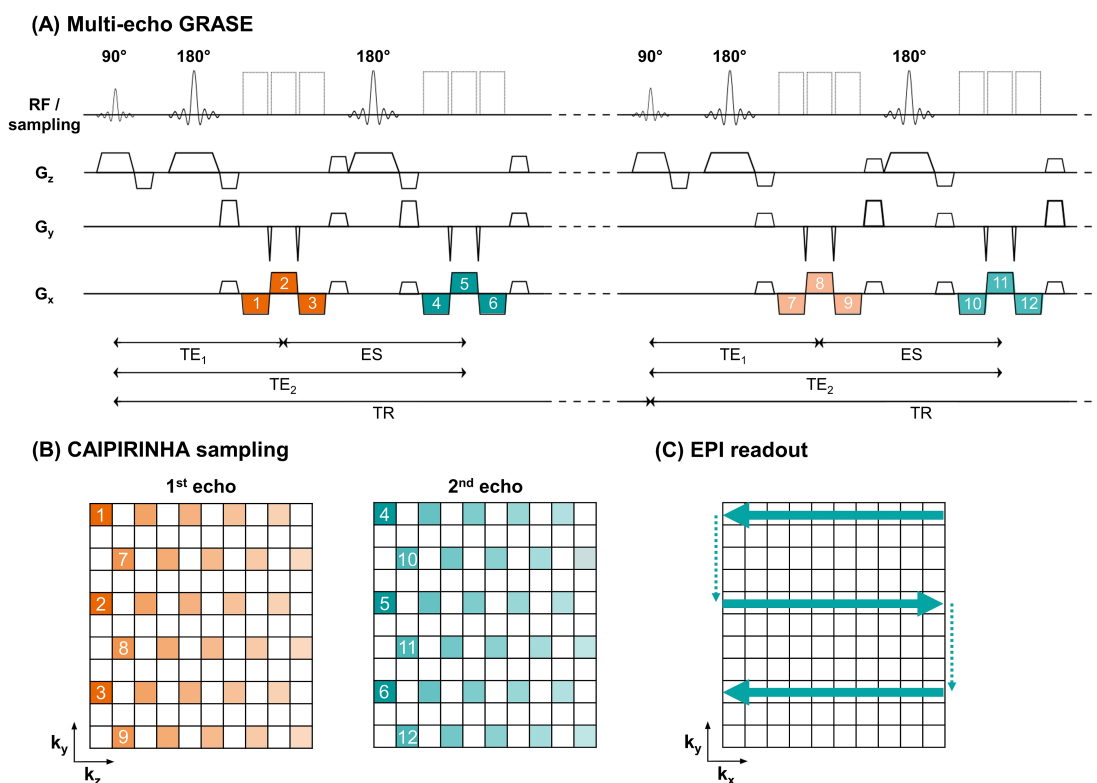


Figure 4.1 – (A) Multi-echo GRASE pulse sequence diagram for two example TRs and the first two echoes. (B) Sampling pattern for an acceleration factor of 4 ($R_y \times R_z^{(\Delta k_z)} = 2 \times 2^{(1)}$) in an example k -space. The shown TRs are employed to sample the first two k_z lines. Transparency increases with time during the acquisition. (C) A segmented interleaved EPI readout is performed in each k_x - k_y plane.

a single EPI readout, a phase gradient blip is used to increment the k -space trajectory in a segmented interleaved EPI manner (as shown in Figure 4.1C). This mitigates T_2^* modulation in k -space caused by the EPI readout. Furthermore, to guarantee the same reducing T_2^* modulation in each volume, within one TR, the image encoding is returned to the same coordinate at the beginning of the previous spin echo acquisition (i.e., image encoding in all directions is kept identical among different echoes throughout the whole acquisition). To promote T_2 -weighting in the acquired contrasts, the central gradient lobe of the EPI is always used to sample the central segment of k -space. Finally, to compensate phase inconsistencies between odd and even echoes, or, more specifically, between readout directions that are mainly due to gradient imperfections accumulated during the switching of gradients in the EPI readout, the central line of the k -space is acquired multiple times (i.e., performing an EPI readout without phase encoding gradients) at the end of each echo train. These lines are then used to perform the phase correction in the image reconstruction.

Parallel imaging acceleration was implemented for both phase encoding directions (k_y and k_z). In contrast to GRAPPA, every other line in the k_y direction is shifted by Δk_z in CAIPIRINHA undersampling schemes, resulting in an improved aliasing condition. Here, Δk_z shifts are applied between samples of subsequent TR, i.e., samples acquired within the same EPI readout

will have the same Δk_z shift. A reference FLASH scan with the same field of view as the main acquisition is used as calibration data for the CAIPIRINHA reconstruction kernels and each T_2 -weighted volume is separately reconstructed online, i.e., directly on the scanner.

Additionally, to mitigate T_2^* -related phase discontinuities through k-space, the developed prototype multi-echo GRASE sequence was adapted to accommodate gradient-echo shifting of the EPI readout according to Feinberg et al. [266, 267]. More specifically, a delay can be introduced between the refocusing pulses and the EPI readout, which is then incremented for each excitation cycle. This reduces the phase differences at the interfaces between k-space segments and, in turn, the resulting ghosting artifacts in image space. The use of echo shifting increases the minimum obtainable TE to accommodate the required shifts of the EPI readout between two consecutive refocusing pulse.

4.2.2 Image acquisition and MR protocols

All MR acquisitions were performed at 3 T (MAGNETOM Prisma, Siemens Healthcare, Erlangen, Germany) using a commercially available 64-channel head/neck coil. In all the in vivo acquisitions, written informed consent was obtained prior to each examination and an MPRAGE image was always acquired as anatomical reference (see Table 4.1C for sequence parameters). The study was approved by the local Institutional Review Board.

Comparison of acceleration schemes

To study the impact of different undersampling strategies on the T_2 decay, data using the prototype multi-echo GRASE sequence were first acquired on a multipurpose phantom (five compartments with different concentrations of $MnCl_2 \cdot 4H_2O$, Siemens E-38-19-195-K2130). Sequence parameters are listed in Table 4.1A; the following sampling schemes were tested:

- Fully sampled (TA = 62:27 min);
- GRAPPA ($R_y \times R_z$) and CAIPIRINHA ($R_y \times R_z^{(\Delta k_z)}$) schemes:
 - a. 1×2 , $1 \times 2^{(1)}$ (TA = 31:18 min each);
 - b. 2×2 , $2 \times 2^{(1)}$, $1 \times 4^{(2)}$ (TA = 15:42 min each);
 - c. 2×3 , $2 \times 3^{(1)}$, $2 \times 3^{(2)}$, 3×2 , $3 \times 2^{(1)}$, $1 \times 6^{(2)}$, $1 \times 6^{(4)}$ (TA = 10:30 min each);
 - d. 2×4 , $2 \times 4^{(2)}$, 4×2 (TA = 8:46 min each).

The total acquisition time of the session was 4 h and 32 min.

To study the same effect on the reconstructed MWF maps in vivo, the following sampling schemes were tested ($R_y \times R_z^{(\Delta k_z)}$) by acquiring multi-echo GRASE data on a healthy volunteer (male, 30 y/o): a) $2 \times 2^{(1)}$ (TA = 15:42 min); b) $2 \times 3^{(1)}$, $3 \times 2^{(1)}$, $1 \times 6^{(2)}$ (TA = 10:30 min each); c) $2 \times 4^{(2)}$ (TA = 8:46 min). All volumes were acquired with the same field of view (resolution 1.6 mm³ isotropic, 84 slices). The other relevant sequence parameters are listed in Table 4.1A. The total scan time was 62:23 min.

Table 4.1 – Relevant parameters of the sequences employed in this study.

Parameter	(A) 3D multi-echo GRASE	(B) 2D MESE	(C) 3D MPRAGE
Resolution	1.6×1.6×1.6 mm ³	1.6×1.6×3.2 mm ³	1×1×1.2 mm ³
Slices	84	1	176
Orientation	Transversal	Transversal	Sagittal
Field of View	230×202×134 mm ³	230×202 mm ²	240×212×256 mm ³
TI	-	-	900 ms
ΔTE/N-Echoes	10.7 ms / 32	10 ms / 32	-
Flip angle	180°	180°	9°
EPI factor/echo spacing	3 / 1.13 ms	-	-
Bandwidth	1240 Hz/Px	219 Hz/Px	490 Hz/Px
TR	1 s	3 s	2.3 s
Undersampling	CAIPI 3×2 ⁽¹⁾	-	GRAPPA ×2
TA	10:30 min	5:41 min	5:12 min

Multi-echo GRASE vs MESE and multi-echo GRASE repeatability

The CAIPIRINHA sampling $R_y \times R_z^{(\Delta k_z)} = 3 \times 2^{(1)}$ was found to deliver a good compromise between agreement with the base $R_y \times R_z^{(\Delta k_z)} = 2 \times 2^{(1)}$ scheme and acquisition time; it was therefore subsequently used to acquire data from twelve volunteers (six men, age range = [23-33] y/o). In this experimental protocol, a reference MESE sequence was added for validation, which was configured as a single-slice acquisition to avoid magnetization transfer contamination of the T_2 decays across different slices [121]. Moreover, to guarantee a homogeneous profile of the refocusing pulse throughout the acquired slice, the width of the slice-selective refocusing pulse was set to be four times the effective slice thickness [268, 269]. A second multi-echo GRASE acquisition was also added to evaluate the repeatability of the sequence. To that end, the multi-echo GRASE was scanned after repositioning each subject in a scan-rescan scenario. Relevant parameters of all sequences are listed in Table 4.1.

Gradient-echo shifting

To understand the influence of the gradient-echo shifting on the resulting T_2 -weighted volumes and MWF maps, multi-echo GRASE data were acquired on the multipurpose phantom (employing the protocol parameters reported in Table 4.1A) and performing an acquisition without and with echo shifting enabled. The latter resulted in an increased minimum TE of 11.8 ms (compared to 10.7 ms) to accommodate for the gradient-echo shifting. In addition, multi-echo GRASE data were acquired in a healthy volunteer (male, 34 y/o) with the same protocol parameters. Three acquisitions were performed in this case: 1) without echo shifting (TE = 10.7 ms); 2) with echo shifting and thus increased minimum TE of 11.8 ms; 3) without echo shifting but keeping the increased minimum TE of 11.8ms (i.e., the TE is kept elongated but the EPI readouts are always centered in the middle of two refocusing pulses). The last

acquisition was performed to differentiate if potential changes in the MWF maps originated from the introduction of the gradient-echo shifting or from the elongated TE.

Influence of TR

Finally, to evaluate the effect of the used short TR on the MWF maps, multi-echo GRASE data were acquired in a healthy volunteer (female, 26 y/o) using three different TRs: 1 s, 2 s, 3 s. The number of acquired slices was reduced to 42 and the remaining sequence parameters are detailed in Table 4.1A. The acquisition times were 5:18 min, 10:36 min and 15:54 min for the three TRs, respectively.

4.2.3 Image processing

G-factors maps were derived from phantom acquisitions according to Breuer et al. [270] to evaluate the benefit that CAIPIRINHA shifts introduce compared to GRAPPA sampling schemes in combination with a multi-echo GRASE acquisition.

In data acquired in vivo, brain tissues were classified applying the in-house prototype software Morphobox on the MPAGE contrast [58] (see **Section 2.5.1** in Chapter 2). Resulting masks were eroded by removing the outer layer of voxels to ensure that regions of interest (ROIs) were within the considered brain structure and to neglect voxels containing multiple tissues (i.e., partial volume effects). The MPAGE volume was then spatially aligned to the volumes corresponding to the first echo of the MESE and multi-echo GRASE [64], allowing the segmentation of brain tissues based on the acquired T_2 -weighted volumes. Finally, a local principal component analysis was employed to denoise T_2 decays [271].

4.2.4 MWF estimation

After brain extraction, MWF maps were derived from the MESE (MWF_{MESE}) and multi-echo GRASE (MWF_{GRASE}) datasets using a reconstruction toolbox freely available online at <https://github.com/ejcanalesr/multicomponent-T2-toolbox> [272, 273]. EPG simulations [81] were employed to account for stimulated echoes contamination on the acquired T_2 decays. The estimation of the spectral components was conducted via NNLS regression and flip angle optimization [82]. Specifically, the corresponding system of linear equations was built by generating T_2 -weighted synthetic signals using the EPG model for forty T_2 values logarithmically spaced between 10 ms and 2 s. Since B_1 inhomogeneities can alter the refocusing flip angle, the actual flip angle for each voxel was determined by solving the NNLS for a fixed range of flip angles between 90° and 180° equally spaced by 1° . The estimated flip angle was the one with the smallest chi-square χ^2 misfit measure [82]. Considering that B_1 inhomogeneities are expected to be smooth and not dependent on brain anatomy, the acquired T_2 -weighted images were smoothed with a Gaussian kernel with a FWHM of 4.8 mm prior to the computation of the flip angle errors [84]. Finally, a spectrum of T_2 values was estimated for each voxel by using

a regularized NNLS algorithm. Regularization was introduced with a second-order Tikhonov term [272] and the regularization weight was chosen so that the χ^2 misfit was $k = 1.025$ higher than the original misfit without regularization [274]. As usual, MWF values were computed as the ratio of the area under the curve enclosed in the range 10-40 ms to the total area of the spectrum.

4.2.5 Statistical analysis

To investigate the effect of the different acceleration schemes on the quality of each T_2 -weighted volume, images were visually compared, and root mean squared errors (RMSEs) were evaluated for each undersampled acquisition with respect to fully sampled in the phantom experiment and the $R_y \times R_z^{(\Delta k_z)} = 2 \times 2^{(1)}$ scheme in the in vivo experiment. Furthermore, average MWF values in brain ROIs were quantitatively compared through a Bland-Altman analysis. Biases were tested to be significantly different from zero with a one-sample t -test.

To validate the proposed acquisition scheme in comparison to the reference MESE, agreement among average MWF in brain ROIs of each volunteer was evaluated with correlation and Bland-Altman analyses. The same statistical analysis was performed between the scan-rescan MWF_{GRASE} maps to evaluate repeatability and to compare MWF_{GRASE} maps resulting from acquisitions with different TRs.

4.3 Results

4.3.1 Comparison of acceleration schemes

Axial slices of a phantom with five compartments are reported in Figure 4.2, and the corresponding estimated g-factor maps for each undersampling scheme are reported in Figure 4.3.

Visually, a decrease in image quality and increasing ghosting artifacts in the T_2 -weighted volumes can be observed with higher acceleration factors. In agreement with this visual assessment, the RMSE computed between the fully sampled acquisition and each undersampled dataset was found to increase with the acceleration factor (Figure 4.2). Given a certain acceleration $R_y \times R_z$, the introduction of CAIPIRINHA shifts always resulted in the reduction of the corresponding g-factors with respect to the same acquisition using a conventional GRAPPA scheme (Figure 4.3). Among the schemes with an acceleration factor of 6, the CAIPIRINHA $R_y \times R_z^{(\Delta k_z)} = 3 \times 2^{(1)}$ shows the lowest RMSE with respect to the fully sampled acquisition as well as lower g-factors.

Representative axial slices acquired in vivo with the prototype multi-echo GRASE sequence are shown in Figure 4.4A for the tested CAIPIRINHA undersampling schemes. Among the patterns providing a six-fold acceleration, the CAIPIRINHA scheme with $R_y \times R_z^{(\Delta k_z)} = 3 \times 2^{(1)}$ yielded the smallest RMSE in comparison to the acquisition with the lowest acceleration,

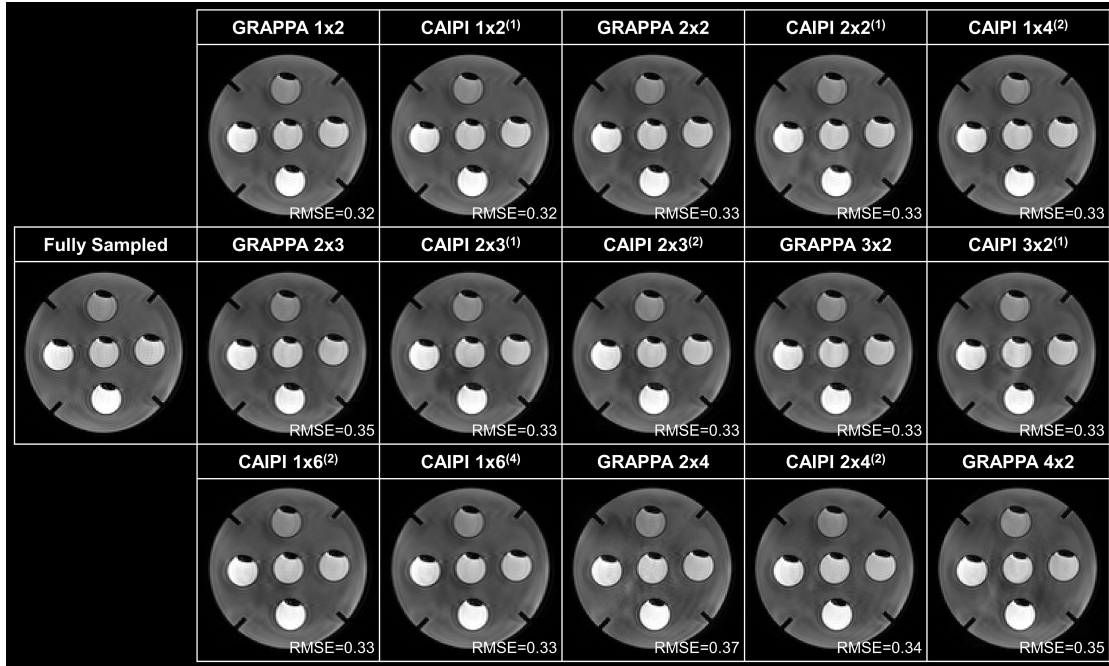


Figure 4.2 – Axial slice of the phantom acquired at the first echo time for different undersampling schemes. Root mean squared errors (RMSEs) with respect to the fully sampled acquisition are reported.

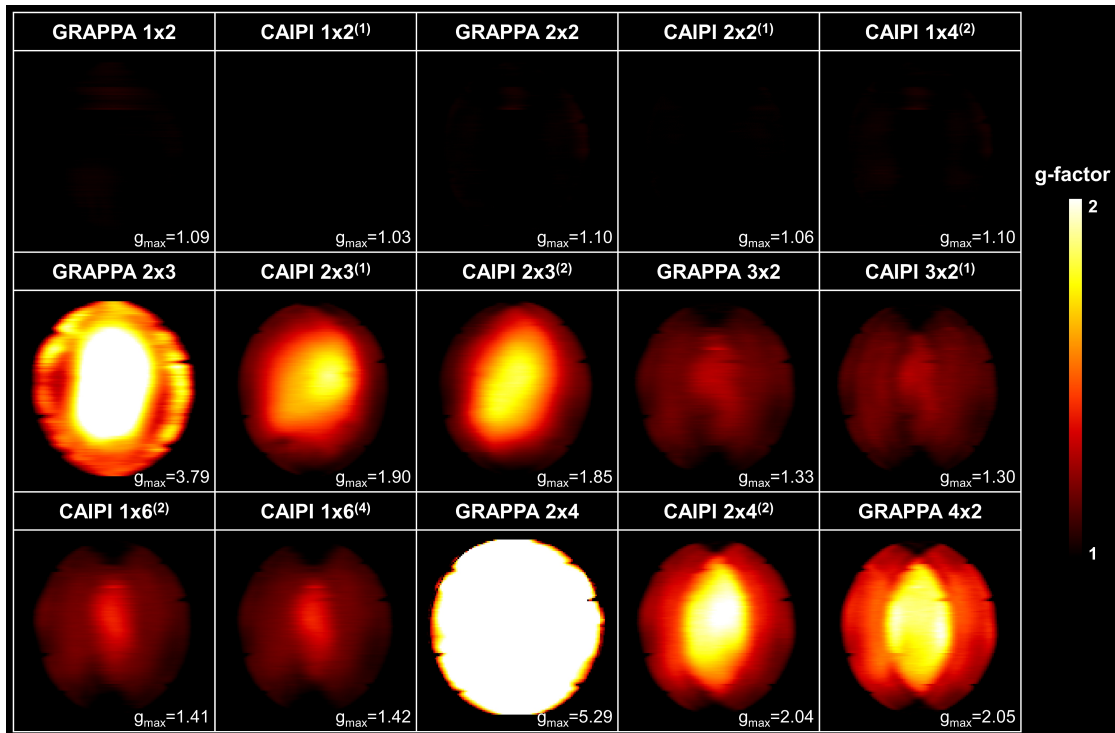


Figure 4.3 – G-factor maps estimated for each undersampling scheme in a phantom experiment. Corresponding axial slices of the phantom acquired at the first echo time are shown in Figure 4.2.

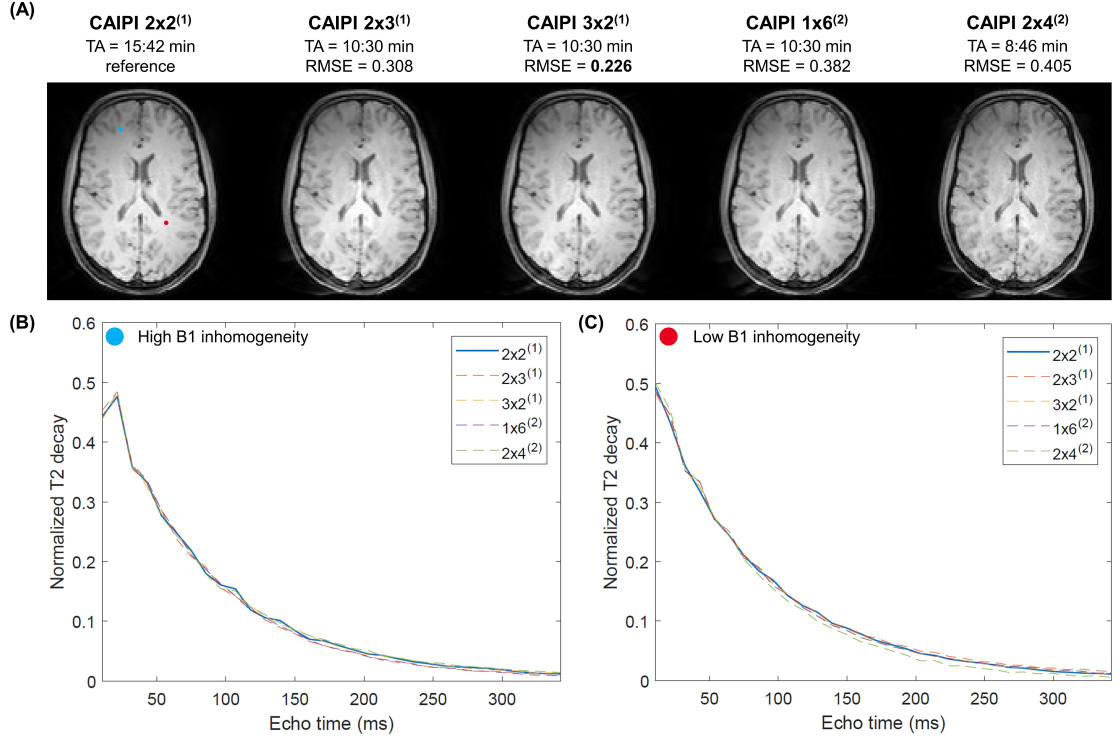


Figure 4.4 – (A) Axial brain slice acquired at the first echo time for different undersampling CAIPIRINHA schemes along with the root mean squared errors (RMSEs) between the T_2 decays acquired with the $R_y \times R_z^{(\Delta k_z)} = 2 \times 2^{(1)}$ scheme and every other undersampled acquisition. (B,C) Representative T_2 decays in voxels located in areas with high (B) and low (C) B_1 inhomogeneity, positioned respectively in the frontal lobe (blue dot) and parietal lobe (red dot).

$R_y \times R_z^{(\Delta k_z)} = 2 \times 2^{(1)}$ (Figure 4.4A). Two example T_2 decays in areas of the brain with differing B_1 fields are shown in Figure 4.4B-C, depicting the effect of stimulated echoes on the decay and the differences between the undersampling schemes. MWF_{GRASE} maps resulting from the investigated CAIPIRINHA undersampling schemes are shown in Figure 4.5, along with Bland-Altman plots comparing the maps obtained from the different undersampling schemes against the baseline $R_y \times R_z^{(\Delta k_z)} = 2 \times 2^{(1)}$ acquisition. Among the acceleration strategies, the $R_y \times R_z^{(\Delta k_z)} = 3 \times 2^{(1)}$ had the lowest bias with respect to the baseline, equal to -0.11% ($P = 0.75$), and limits of agreement ranging from -2.7% to 2.4%. The CAIPIRINHA scheme with $R_y \times R_z^{(\Delta k_z)} = 3 \times 2^{(1)}$ was thus selected as the best compromise between image quality and TA for the following experiments. Examples of the estimated B_1 map and T_2 spectrums are reported in Figure 4.6.

4.3.2 Multi-echo GRASE vs MESE

Example slices of MWF_{MESE} and MWF_{GRASE} maps obtained from two volunteers are shown in Figure 4.7. The whole-brain coverage of the multi-echo GRASE acquisition is illustrated by two additional reformats. Although the two maps appear visually comparable, MWF_{GRASE} maps are more blurred than MWF_{MESE} maps. In addition, MWF values in WM regions with high

Chapter 4. Fast and high-resolution myelin water imaging: Accelerating multi-echo GRASE with CAIPIRINHA

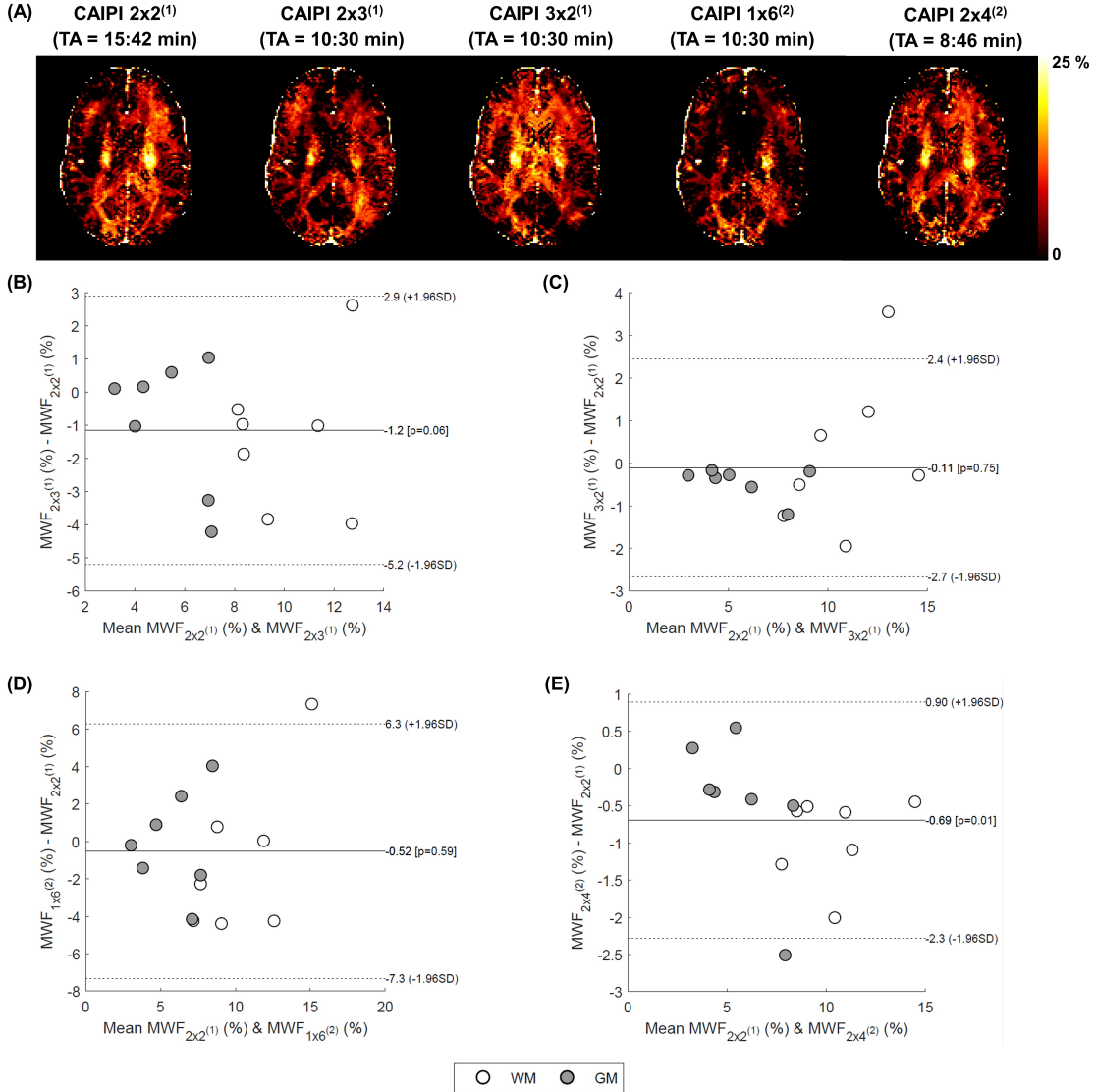


Figure 4.5 – (A) MWF maps resulting from the investigated CAIPIRINHA undersampling schemes. (B,C,D,E) Bland-Altman plots resulting from the comparison of the MWF maps obtained from the different undersampling schemes and the baseline $R_y \times R_z^{(\Delta k_z)} = 2 \times 2^{(1)}$ acquisition.

myelin content, such as the corpus callosum and the internal capsule, are slightly increased in MWF_{GRASE} . Lower MWF values in the frontal lobe can be also observed.

Results from the quantitative comparison of MWF values extracted from brain ROIs are shown in Figure 4.8. MWF_{MESE} and MWF_{GRASE} values were found to be linearly correlated ($r = 0.83$). In addition, the Bland-Altman agreement analysis revealed a non-significant mean difference of -0.2% ($P = 0.24$) with the limits of agreement ranging from -3.7% to 3.3%. These results indicate a good agreement between the maps derived from the two sequences.

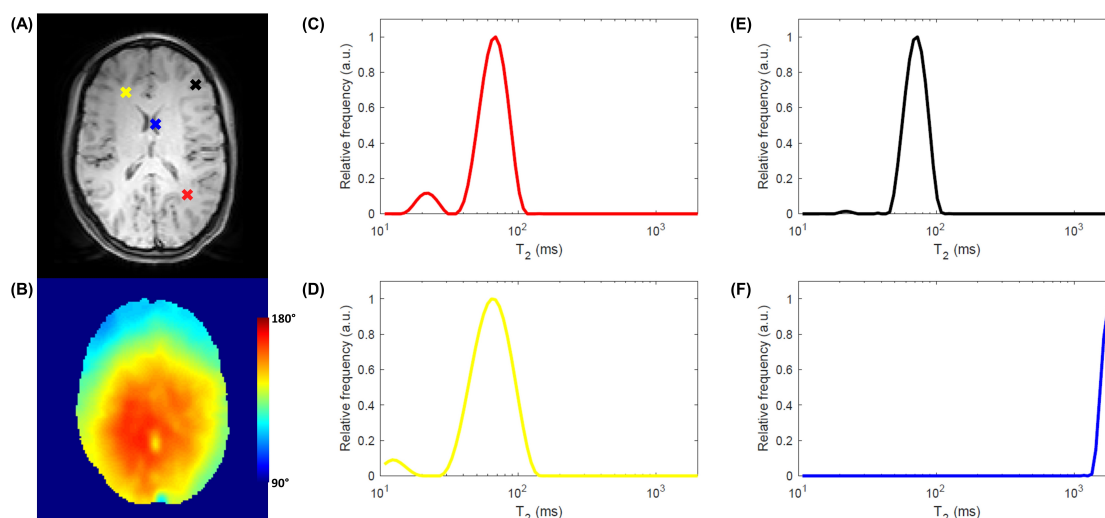


Figure 4.6 – T_2 -weighted axial slice (A) together with corresponding estimated flip angles map (B) and four estimated voxel-wise T_2 spectra in occipital lobe white matter (C), frontal lobe white matter (D), frontal lobe gray matter (E), and cerebrospinal fluid (F). The presence of two separate lobes with different T_2 s is identifiable in white matter voxels. All spectra were normalized to their maximum value.

4.3.3 Multi-echo GRASE repeatability

Example MWF maps resulting from a scan-rescan dataset are shown for a healthy volunteer in Figure 4.9. The Pearson's correlation coefficient among ROIs averaged MWF values was found to be 0.95 and a bias of 0.11% ($P = 0.32$) was assessed via the Bland-Altman analysis (Figure 4.9).

4.3.4 Gradient-echo shifting

Images acquired in the phantom without and with echo shifting are shown in Figure 4.10. Although visible changes in the image sharpness were not found between the two acquisitions, a reduction of Gibbs Ringing artifacts at the edges of regions with high intensities could be observed in the echo shifted data.

In the in vivo data, no differences in image sharpness were visible (Figure 4.11), which agrees with the phantom experiment. However, some ringing and ghosting artifacts present in the acquisition without echo shifting disappeared in the acquisition with echo shifting, although other artifacts were found only in the echo shifted acquisition but may be due to motion (Figure 4.11).

MWF maps derived from the acquired data are shown in Figure 4.12. Although small ringing artifacts are visible in the non-shifted data, no differences in terms of blurring can be observed. The maps differ in estimated MWF values of the WM, which were found to be $9.0\% \pm 2.6\%$ in the non-shifted acquisition, $12.1\% \pm 2.9\%$ in the echo-shifted acquisition with longer ΔTE and $11.8\% \pm 3.4\%$ in the non-shifted acquisition with the longer ΔTE . These numbers

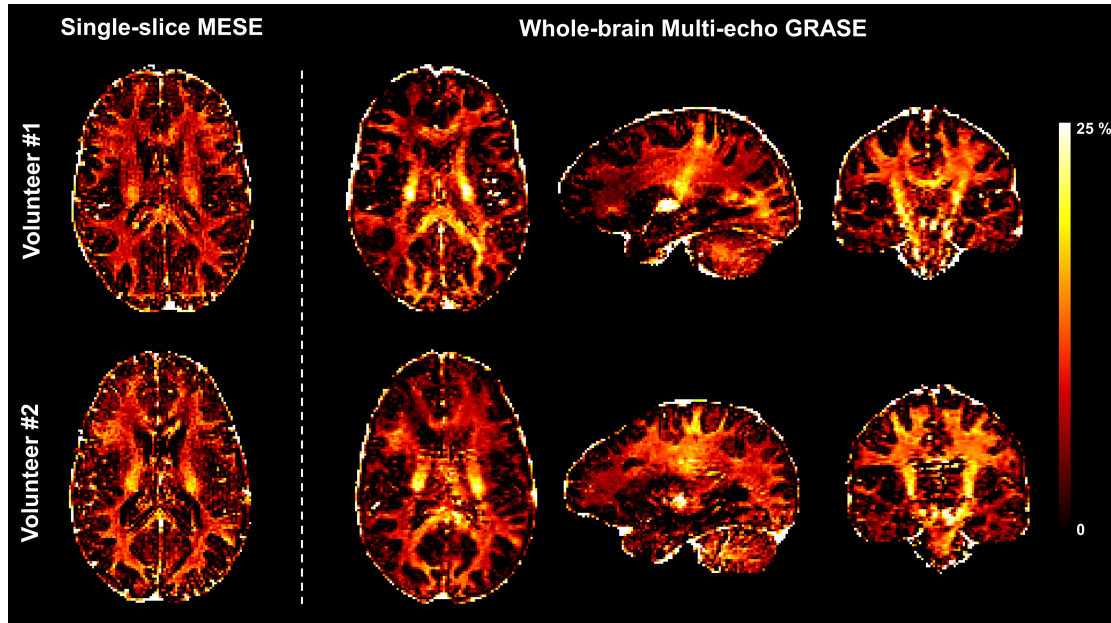


Figure 4.7 – Representative slices of MWF maps obtained with the reference single-slice MESE sequence and the proposed multi-echo GRASE from two volunteers.

suggest that the increase in MWF is due to the elongated ΔTE and not the echo shifting, whose different sampling of the spin echo does not change the contrast information.

4.3.5 Influence of TR

Representative axial slices of multi-echo GRASE data acquired with different TRs are shown in Figure 4.13 and resulting MWF maps are depicted in Figure 4.14. High correlation was found among all acquisition pairs ($r > 0.97$). A bias of 0.06% was found between MWF acquired with a TR of 1 s and 2 s, 0.60% between maps acquired with a TR of 1 s and 3 s, and 0.54% between maps acquired with a TR of 2 s and 3 s.

4.4 Discussion

This chapter investigated the acquisition of T_2 decays through the combination of a multi-echo GRASE sequence with CAIPIRINHA undersampling patterns. In vivo experiments showed that the proposed sequence yields MWF maps comparable with those derived from a reference MESE sequence ($r = 0.83$, mean bias = -0.20%), while providing increased brain coverage (multi-echo GRASE: $1.6 \times 1.6 \times 1.6 \text{ mm}^3$, 84 slices; MESE: $1 \times 1 \times 3 \text{ mm}^3$, single-slice) in an acquisition time of 10:30 min. The MESE sequence could be further accelerated with parallel imaging and the brain coverage extended using simultaneous multi-slice schemes – however at the expense of introducing magnetization transfer contamination of the T_2 decays across slices [121,275], imperfect slice profiles [268] and increased SAR. Conversely, the 3D nature of the proposed multi-echo GRASE sequence allows to reduce the slice thickness to achieve isotropic

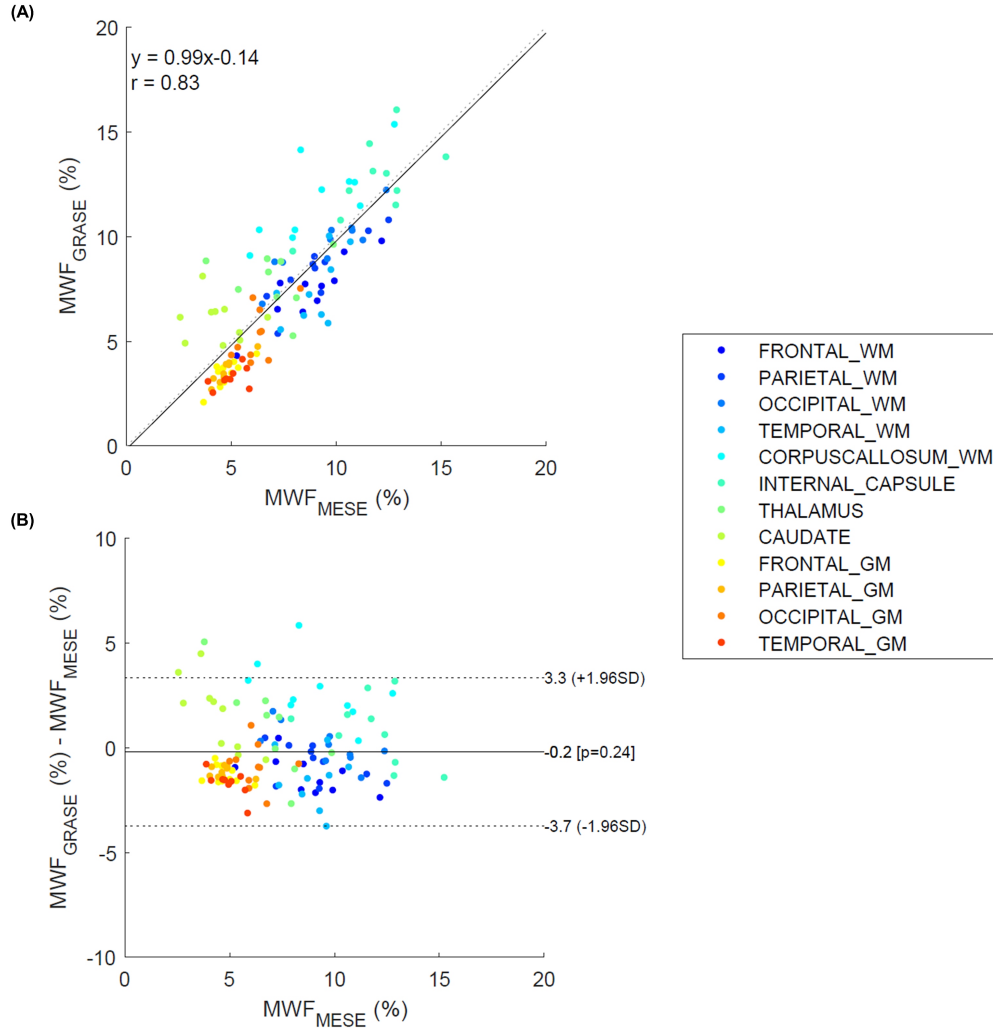


Figure 4.8 – (A) Correlation plot between MWF_{MESE} and MWF_{GRASE} considering brain ROIs extracted from the healthy volunteers. (B) Bland-Altman plot reporting the difference between MWF_{MESE} and MWF_{GRASE} values in the extracted brain ROIs against the reference MWF_{MESE} .

resolution while simplifying the fitting procedure because a slice profile correction is not needed. Compared to the state-of-art 3D multi-echo GRASE acquisition for MWI [80] ($1 \times 1 \times 5$ mm³, 20 slices, TA = 14.4 min), this study demonstrated the feasibility of obtaining MWF with higher resolution and brain coverage but reduced acquisition time when employing a $3 \times 2^{(1)}$ CAIPIRINHA undersampling pattern. MWF values in WM tissues ($9.6\% \pm 1.4\%$) were indeed found to be comparable with the ones obtained by Prasloski et al. [80] (reported MWF values from $\sim 7\%$ in the minor forceps up to $\sim 17\%$ in the internal capsule). Furthermore, a multi-slice 2D GRASE ($1.5 \times 1.5 \times 4$ mm³, 26 slices, TA = 7:30 min) was recently proposed for fast MWI [84]. Although yielding similar MWF values, the 2D nature of the acquisition impedes isotropic resolution, which is however desirable when studying WM microstructure. Moreover, the slice profile of the refocusing pulse needs to be corrected for, and its approximation may lead to estimation errors [268].

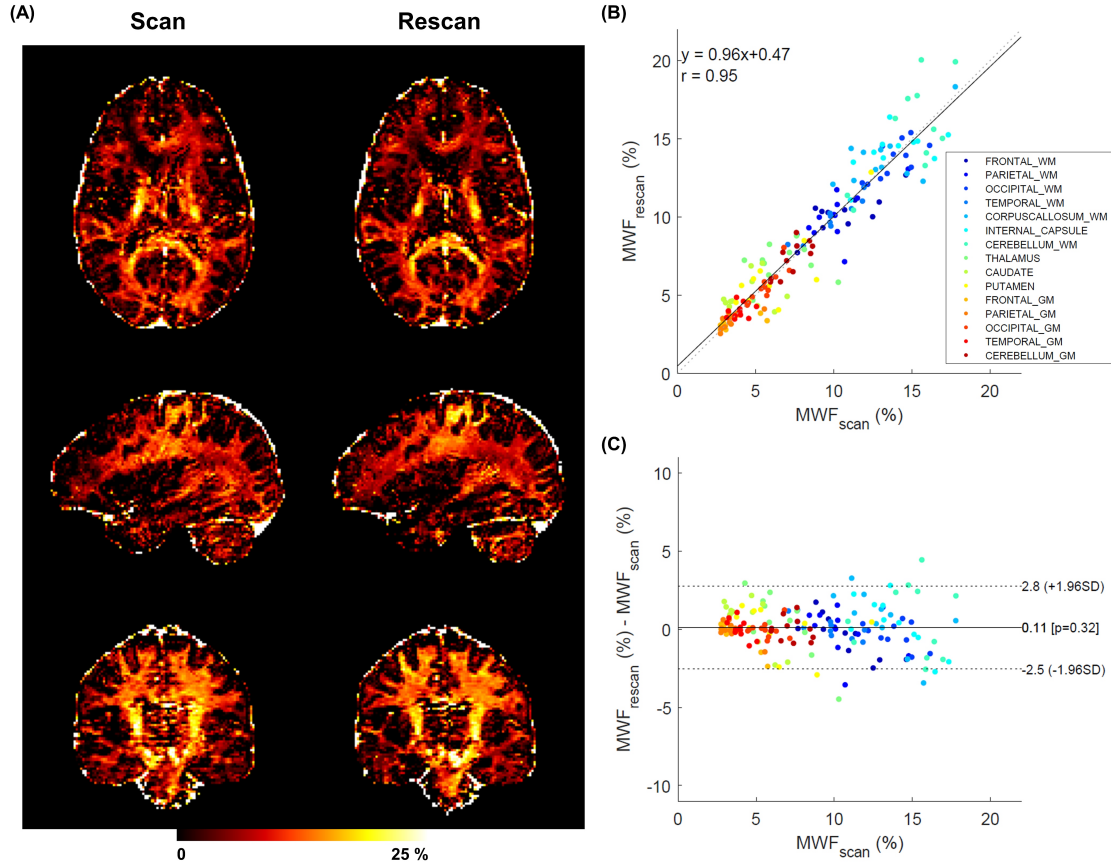


Figure 4.9 – Comparison of MWF maps derived from the multi-echo GRASE in a scan-rescan scenario. (A) MWF maps acquired from the same subject after repositioning. Correlation (B) and Bland-Altman analysis (C) considering average values from extracted brain ROIs.

To test the effect on T_2 decays of different undersampling schemes, experiments were conducted acquiring data in a multi-purpose phantom and one healthy subject. While a fully sampled acquisition and several undersampling schemes with and without CAIPIRINHA shifts were tested in the phantom, only few of them were tested in vivo due to the required long acquisition times. CAIPIRINHA shifts were shown to result in an improved aliasing condition compared to the same acquisition following conventional GRAPPA. Furthermore, the chosen $3 \times 2^{(1)}$ scheme showed lower g-maps, RMSE and best agreement with the baseline among the schemes with the targeted six-fold acceleration.

In comparison to other studies at 3 T based on multi-echo T_2 techniques, such as multi-echo T2prep acquisitions [88], the proposed sequence provides similar MWF values in comparable acquisition times. However, the reduced number of T_2 contrasts acquired in T2prep experiments to keep the acquisition time short [88] may affect MWF quantification, especially in the presence of pathological tissues [79, 125].

The proposed framework and the conducted study setup have limitations. The undersampling introduces a slight blurring of the images, as shown in the comparison of MWF_{MESE} and

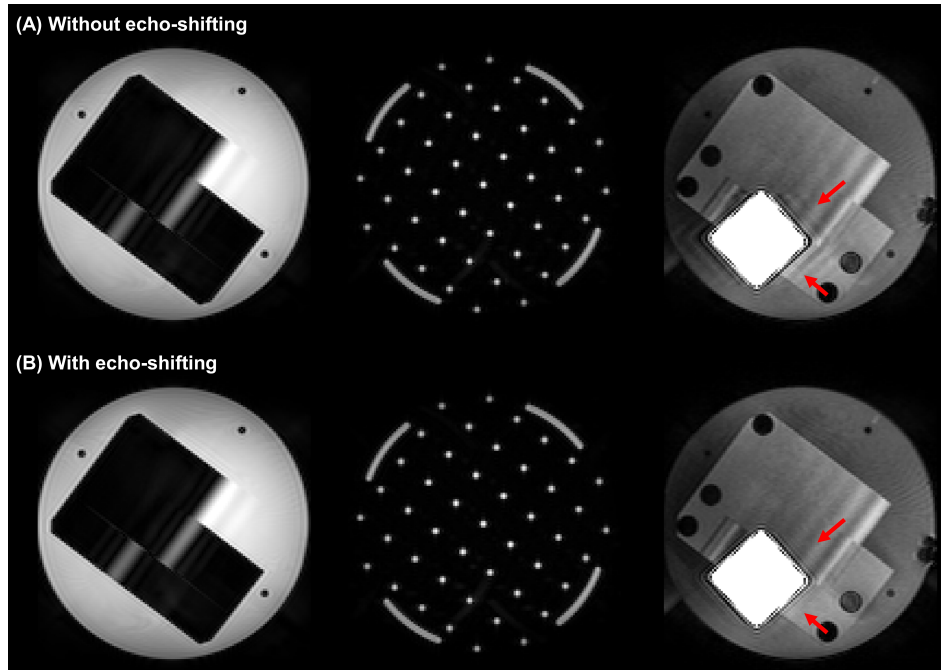


Figure 4.10 – Representative slices of the acquired phantom data without (A) and with (B) echo shifting. Reduction in ringing artifacts resulting from the shifted echoes are indicated by red arrows. Image intensities in the third column were magnified by a factor of $\sim 50\times$ to highlight the differences in the artifact behavior.

MWF_{GRASE} maps. It should be noted that for a conventional single-echo 3D GRASE the major blurring originates from the T_2 decay. However, in this study, this source of blurring can be ruled out as the employed multi-echo scheme does not mix k-space lines of different spin echo times in a single k-space. The CAIPIRINHA undersampling was also found to generate ghosting artifacts whose severity increases with the acceleration factor and whose position within the field-of-view changes according to the specific sampling scheme. Notably, these artifacts may affect the subsequent myelin quantification. Different undersampling schemes were thus compared acquiring data from one subject and assuming an acceleration of factor of two in both phase encoding directions as a baseline. Although proving the comparability between the $3 \times 2^{(1)}$ with $2 \times 2^{(1)}$ schemes, the analysis was conducted only with one subject due to the very long acquisition time (62:23 min) and thus cannot be considered fully conclusive. In addition, the inclusion of echo-shifted EPI readouts was investigated in the reduction of ghosting artifacts according to Feinberg et al. [266, 267]. Furthermore, residual dependency on B_1 inhomogeneities is shown by the acquired contrasts, which - together with the ill-posed NNLS reconstruction that is more affected by the lower SNR of multi-echo GRASE data in comparison to MESE acquisitions - may influence the reconstruction of the quantitative values and are probably the reason of the MWF decrease observed in frontal WM regions. This motivated the study part on the repeatability of the reconstructed maps, which were found to agree in a scan-rescan scenario (bias = 0.11%, $P = 0.32$). Reproducibility among different time points and centers remains to be investigated.

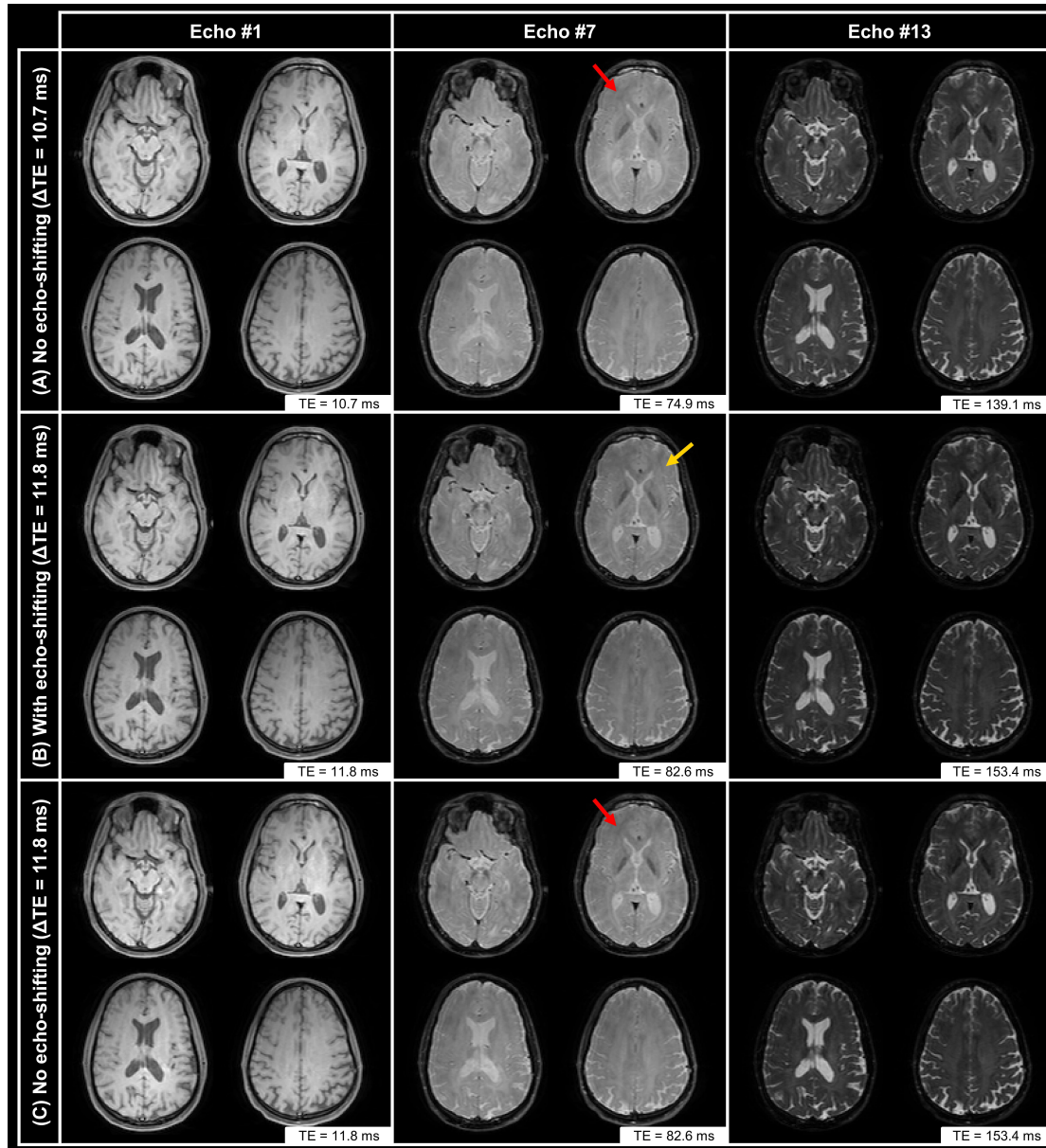


Figure 4.11 – Representative axial slices of the acquired multi-echo GRASE data in the same healthy volunteer without echo shifting (A), with echo shifting (B) and without echo shifting but keeping the same ΔTE as with the echo shifting (C). Ghosting artifacts present only in the acquisition without echo shifting are highlighted by the red arrows. Ringing artifacts visible only in the echo-shifted acquisition are marked with a yellow arrow.

Although some benefits resulting from performing echo shifted acquisitions were observed in phantom and brain scans, the increased minimum TE to accommodate the echo shifting resulted in an overestimation of the MWF values. Thus, maps obtained using the echo shifting technique should be interpreted carefully. Nevertheless, although brain acquisitions may not benefit too much from the echo shifting technique, this additional feature might be helpful for applications targeting other organs (e.g., luminal water fraction in the prostate) and/or

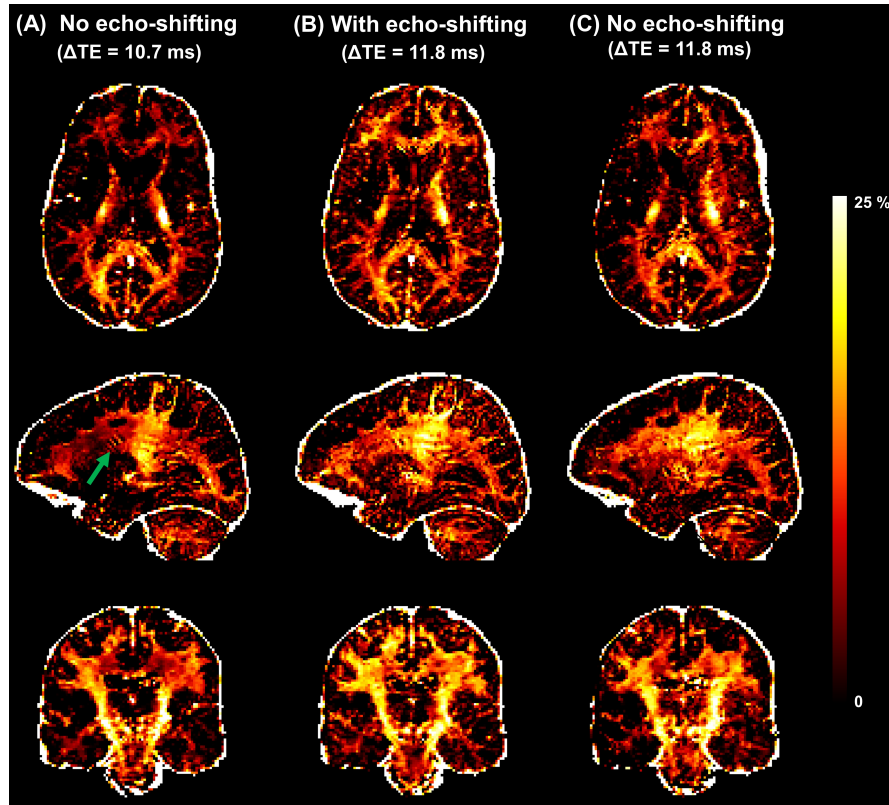


Figure 4.12 – MWF maps retrieved from the multi-echo GRASE data acquired in a healthy volunteer without echo shifting (A), with echo shifting (B) and without echo shifting but keeping the same ΔTE as with the echo shifting (C). Example ringing artifact present in the data acquired without echo shifting are marked by a green arrow in first column.

more conventional T_2 mapping techniques where the restrictions on the TE are less strong and larger EPI readouts can be employed [276–278]. In addition, to exclude the possibility that the chosen TR of 1 s biased the comparison, an additional experiment was conducted to compare MWF values resulting from multi-echo GRASE data acquired with different TRs. However, the MWF maps derived from multi-echo GRASE data acquired with a TR of 1 s, 2 s and 3 s were found to be comparable, showing that the reduction in scan time obtained by shortening the TR to 1s may be suitable for myelin imaging.

Future work is planned to further reduce the acquisition time while maintaining or improving image quality. Joint reconstruction of multi-contrast data [279] reduced parallel imaging artifacts with respect to the reconstruction of each echo separately and may be employed to further decrease the scan time. Moreover, a recent study with retrospective undersampling of fully sampled acquisitions and compressed sensing reconstruction showed promising results for MWF quantification [280]. The impact of the EPI sampling within the incoherent acquisition required by compressed sensing on the multicompartiment fitting should be first investigated, even though promising results were shown in single-contrast experiments [281].

Given the very broad realm of techniques existing nowadays to probe the myelin content of

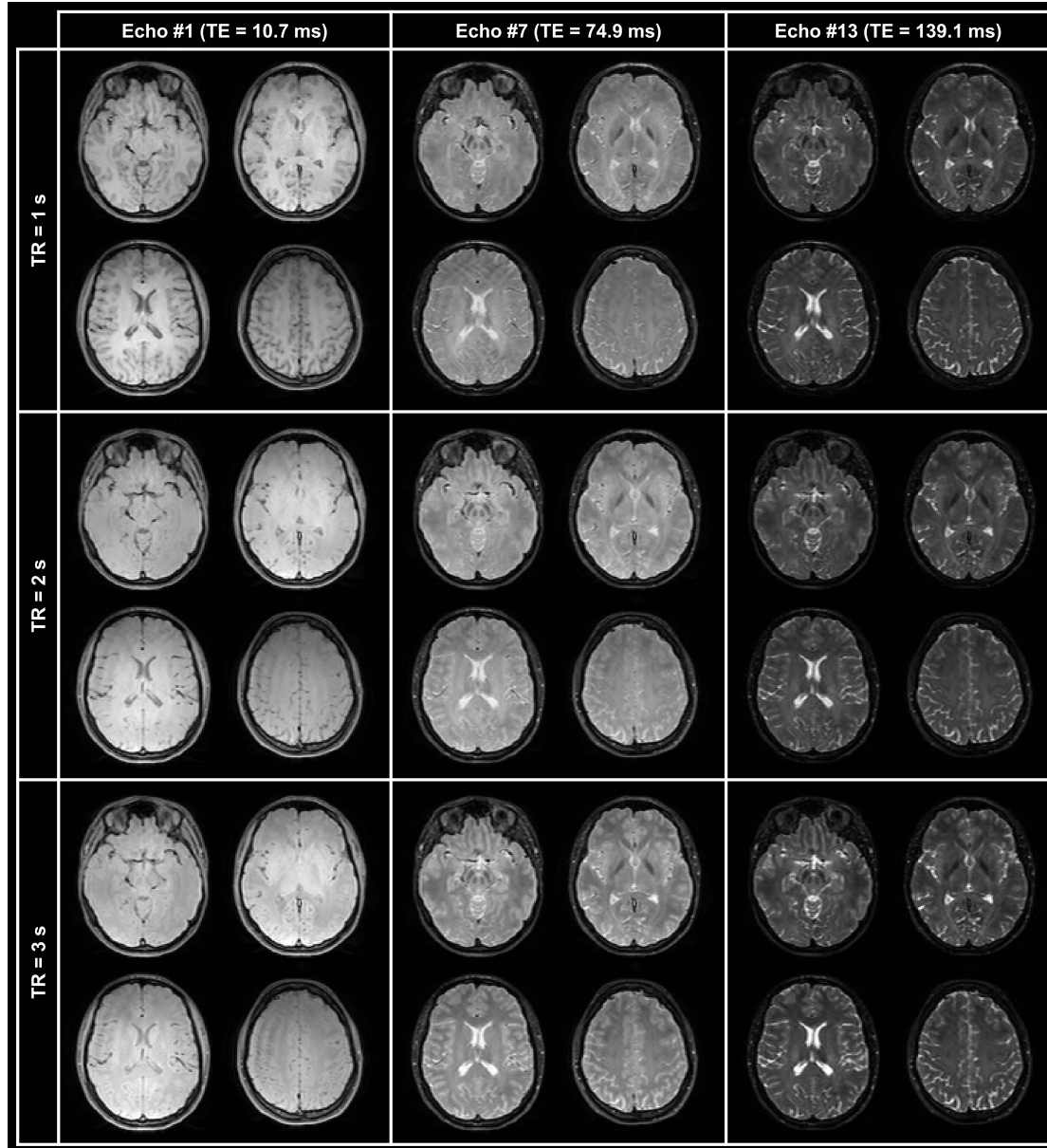


Figure 4.13 – Representative axial slice of the acquired multi-echo GRASE data on the same healthy volunteer for different TEs and different TRs. T_1 -weighting effects due to the short TR are visible in the images acquired with $TR = 1s$, especially in the shorter TEs.

the brain, validation of estimated MWF maps surely represent an important aspect. Since a true measure of myelin density in vivo is not yet available, validation is usually performed either by comparison with reference MWF_{MESE} or, since the main application of MWI goes in the direction of monitoring changes in brain tissue microstructure, looking for correlation with histological samples of pathological tissue [282]. Future work should be carried out to investigate the sensitivity of the proposed methodology to myelin depletion in post-mortem samples of pathological tissues.

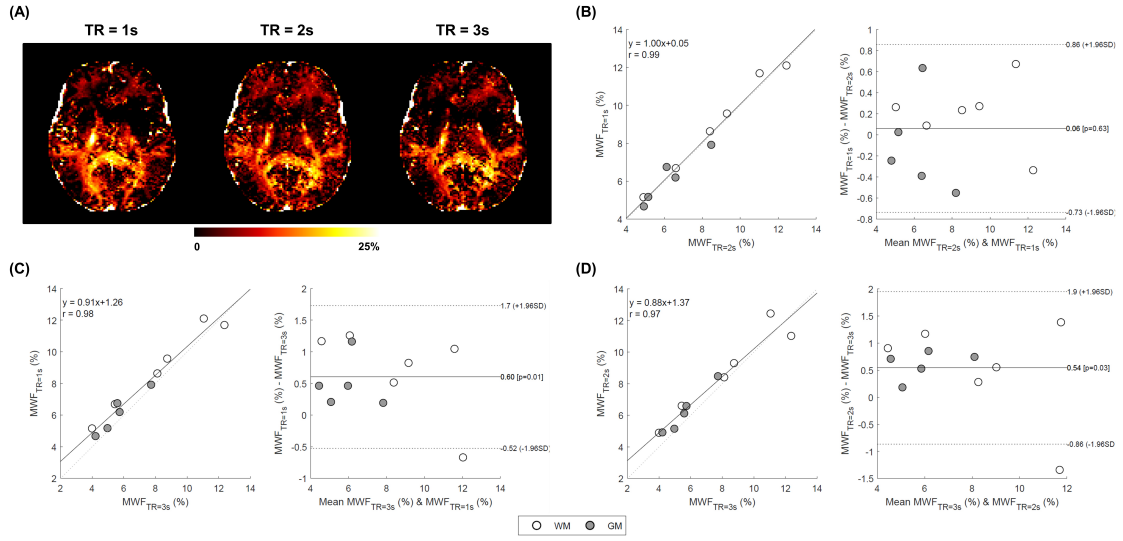


Figure 4.14 – Comparison of MWF maps (A) derived from the multi-echo GRASE sequence with different TRs. (B,C,D) Correlation and Bland-Altman analysis comparing maps resulting from acquisitions with TR = 1 s and TR = 2 s (B), TR = 1 s and TR = 3 s (C), and TR = 2 s and TR = 3 s (D).

4.5 Conclusions

Whole-brain MWI was achieved with a 3D multi-echo GRASE sequence (1.6 mm³ isotropic resolution, 84 slices) in 10:30 min by employing a CAIPIRINHA undersampling scheme. Resulting MWF values were found to correlate with conventional MESE-based maps. The increased resolution and shortened scan time may help to widen the use of MWI in clinical research and render the proposed sequence a promising and practical alternative to time-consuming MESE acquisitions.

5 Data-driven myelin water imaging based on T_1 and T_2 relaxometry

The content of the following chapter is based on the draft of the article: “Data-driven myelin water imaging based on T_1 and T_2 relaxometry” currently under revision in NMR in Biomedicine. The article was co-authored by Tom Hilbert, Veronica Ravano, Erick Jorge Canales-Rodríguez, Marco Pizzolato, Reto Meuli, Jean-Philippe Thiran, Jonas Richiardi, and Tobias Kober. All co-authors contributed to the idea and reviewed the manuscript.

Abstract: Long acquisition times preclude the application of MESE sequences for MWF mapping in clinical practice. In search of alternative methods, previous studies of interest explored the biophysical modeling of MWF from measurements of different tissue properties that can be obtained in scan times shorter than those required for the MESE. In this chapter, a novel data-driven estimation of MWF maps from fast single-component relaxometry measurements is proposed and investigated. T_1 and T_2 relaxometry maps were acquired in a cohort of twenty healthy subjects along with a conventional MESE sequence. Whole brain quantitative mapping was achieved with a fast protocol in 6:24 minutes. Reference MWF maps were derived from the MESE sequence (TA = 11:17 min) and their data-driven estimation from relaxometry measurements was investigated using three different modeling strategies: two general linear models (GLMs) with linear and quadratic regressors, a random forest regression model, and two deep neural network architectures, a U-Net and a conditional generative adversarial network (cGAN). Models were validated using a ten-fold cross validation. Resulting maps were visually and quantitatively compared by computing the RMSE between the estimated and reference MWF maps, the intraclass correlation coefficients (ICC) between corresponding MWF values in different brain regions, and by performing a Bland-Altman analysis. Qualitatively, the estimated maps appear to generally provide a similar, yet more blurred MWF contrast in comparison to the reference, with the cGAN model best capturing MWF variabilities in small structures. By estimating the average adjusted coefficient of determination of the GLM with quadratic regressors, we showed that 87% of the variability in the MWF values can be explained by relaxation times alone. Further quantitative analysis showed an average RMSE smaller than 0.1% for all methods. The ICC was greater than 0.81 for all methods, and the bias smaller than 2.19%. In conclusion, this work confirms the notion that relaxometry parameters

contain a large part of the information on myelin water and that MWF maps can be generated from T_1/T_2 data with only little error. Among the investigated modeling approaches, the cGAN provided maps with the best trade-off between accuracy and blurriness. Fast relaxometry like the 6:24 minutes whole brain protocol used in this work in conjunction with machine learning may thus have the potential to replace time-consuming MESE acquisitions.

5.1 Introduction

The sensitivity of qMRI acquisitions to microstructural properties of brain tissues stimulated the exploration of qMRI metrics as biomarkers for disease-induced alterations (see **Section 2.3.5** in Chapter 2). In particular, as brain relaxometry measurements depend on complex interactions among protons and between protons and their surrounding lattice, T_1 and T_2 measurements are affected by the composition of the tissue's biophysical environment, such as the concentration of water molecules, macromolecules and paramagnetic atoms. Therefore, microstructural biological features – usually only obtainable with ex vivo histology – can be inferred in vivo at the resolution provided by qMRI acquisitions with the help of biophysical models [283–285].

The myelin content of the brain represents one microstructural property of interest (see **Section 2.3.4** in Chapter 2). The most established and extensively validated method for brain myelin quantification using MR is based on the multicomponent modeling of T_2 relaxation decays to ascribe the measured signal to multiple water compartments having specific tissue properties at the sub-voxel level (see **Section 3.2.1** in Chapter 3). The reference acquisition scheme used in T_2 relaxation studies is the MESE sequence, which, however, requires long acquisition times (~ 10 min for a fully sampled single slice at 1 mm^2 in-plane resolution without interleaved slice sampling) that impede its practical use in a clinical setting. Various alternative solutions were developed to address these challenges (see **Chapter 3**), as well as the one proposed in **Chapter 4**. Additional prior work of particular interest to this chapter explored models using measurements of more than one different physical tissue property as input [101, 118, 128, 130]. A linear relation was found to exist between single-component relaxometry measurements and myelin content estimated in post-mortem samples [128]. Myelin partial volumes were also derived from single-component relaxometry measurements using a complex model based on Bloch simulations [118]. Recently, Drenthen et al. [286] derived MWF from conventional T_1 -weighted, T_2 -weighted and diffusion-weighted imaging using a machine learning based method. Additionally, Khattar et al. [287] proposed to replace computational expensive BMC-mcDESPOT reconstructions (~ 30 hours per dataset) with a neural network to derive MWF maps from single-component T_1 and T_2 measurements and PD maps. All these findings suggest that myelin content information is somehow encoded in single-component relaxometry measurements, whose clinical applicability is, however, still hindered by the difficulty in rapidly and accurately estimating relaxation times. In addition, the increased complexity of the employed biophysical models usually entails assumptions which undermine their capability to generalize when tissue characteristics exhibit pathological

alterations.

Following the rationale that single-compartment relaxometry maps contain sufficient information to estimate brain myelin water content, this work proposes a novel data-driven and model-free estimation of MWF from a fast relaxometry protocol exploiting recent advances in machine learning. To that end, a fast protocol is used for single-compartment relaxometry [288], consisting of the MP2RAGE sequence for T_1 mapping [16] (**Section 2.3.1** in Chapter 2) and the GRAPPATINI method for T_2 mapping [54] (see **Section 2.4.3** in Chapter 2). This protocol requires 6:24 minutes for a whole brain scan ($0.7 \times 0.7 \times 3 \text{ mm}^3$ at 3 T) and proved to deliver maps sensitive to pathological changes in brain tissues [44, 288] (see **Chapter 6**). Three different strategies with increasing level of model complexity were investigated in the multi-contrast derivation of MWF maps, and compared to maps estimated from a conventional MESE acquisition:

1. General Linear Model (GLM): conversely to studies based on weighted images [286], the quantitative nature of the data allows the investigation of a simple GLM for the data-driven estimation of MWF maps from relaxometry data; hence, based on prior work [118, 128], it was first hypothesized that a GLM would suffice to describe the relation between relaxation times and MWF;
2. Random Forest regression model (RFRM): the capability of an ensemble learning method to account for non-linearities in regression-based modeling is investigated as it offers the possibility to represent a larger space of functions compared to GLMs;
3. Deep neural network architectures: as demonstrated by recent studies in computer vision [289] and on conventional weighted MR imaging [290], deep learning architectures are reliable tools in image-to-image translation tasks. The conventional U-Net [291] and a conditional generative adversarial network (cGAN) [292] architectures are explored here.

This work investigates whether MWF maps can be accurately derived from single-compartment relaxometry data and how accuracy depends on the employed machine learning method.

5.2 Materials and Methods

5.2.1 MR dataset

After obtaining written informed consent, whole brain relaxometry data were acquired with the MP2RAGE and GRAPPATINI sequences from twenty healthy volunteers (8 male, age range = [23-33] y/o) at 3 T (MAGNETOM Skyra, Siemens Healthcare, Erlangen, Germany) using a commercially available 64-channel head/neck coil in 6:24 minutes total. Volunteer scanning was covered by a general investigational IRB approval. Along with the relaxometry protocol, conventional MESE data were acquired for each subject in 11:17 minutes (notably with a different resolution due to time restrictions). Parameters of the scanned sequences are summarized in Table 5.1.

Table 5.1 – Parameters of the acquired sequences. The distance factor is intended as the gap between acquired slices.

Parameter	T_1 mapping (MP2RAGE)	T_2 mapping (GRAPPATINI)	MESE
Resolution	$0.7 \times 0.7 \times 3 \text{ mm}^3$		$1 \times 1 \times 3 \text{ mm}^3$
Slices	44		9
Distance factor	0%		300 % (9 mm)
Field of View	$230 \times 215 \times 132 \text{ mm}^3$		$230 \times 202 \times 108 \text{ mm}^3$
TI_1/TI_2	700/2500 ms	–	–
$\Delta TE/N$ -Echoes	–	10 ms / 16	10 ms / 32
Flip angles	4-5°	180°	
TR	5 s	4 s	3 s
Undersampling	2x GRAPPA	2x GRAPPA and 5x MARTINI	–
TA	3:02 min	3:22 min	11:17 min

5.2.2 Image processing

Brain tissues were segmented on the MP2RAGE contrast using the in-house prototype software MorphoBox [58, 59] (see **Section 2.5.1** in Chapter 2). A total of forty-five brain ROIs were derived for each subject. ROIs were eroded by removing the outer layer of voxels to reduce partial volume effects. ROIs corresponding to CSF and non-parenchymal regions were discarded.

After brain extraction, a multicomponent decomposition of the T_2 curves sampled with the MESE sequence was performed voxel-wise with a regularized NNLS optimization, as implemented in the reconstruction toolbox freely available online at <https://github.com/ejcanalesr/multicomponent-T2-toolbox> [272, 273]. T_2 decays were modeled with EPG simulations to correct for stimulated echoes contamination of the acquired T_2 decays [82]. The actual flip angle for each voxel was computed by solving the NNLS for a fixed range of flip angles values between 90° and 180° equally spaced by 1°. A distribution of forty logarithmically spaced T_2 values between 10 and 1000 ms was assumed, and the cut-off time for myelin water was set to 40 ms.

Finally, for each subject, the T_2 map from GRAPPATINI was rigidly registered using Elastix [64] to the MP2RAGE contrast. Similarly, the first echo of the MESE was registered to the MP2RAGE contrast, and the resulting transformation was subsequently applied to the MWF map to match the same spatial alignment and in-plane resolution of the input T_1 and T_2 maps.

5.2.3 Modeling of MWF maps from relaxometry

Based on prior work [118, 128], it was first hypothesized that a GLM would be accurate enough to model the relation between MWF and relaxation times. For each segmented brain ROI, both

a linear (Eq. 5.1) and a quadratic (Eq. 5.2) version of a GLM were trained using the mean MWF, $R_1 (=1/T_1)$, and $R_2 (=1/T_2)$ values within the ROIs:

$$\mathbb{E}\{MWF\} = \beta_0 + \beta_{R_1} R_1 + \beta_{R_2} R_2, \quad (5.1)$$

$$\mathbb{E}\{MWF\} = \beta_0 + \beta_{R_1} R_1 + \beta_{R_2} R_2 + \beta_{R_1 R_2} R_1 R_2 + \beta_{R_1^2} R_1^2 + \beta_{R_2^2} R_2^2. \quad (5.2)$$

where β_0 is the model intercept and β_{R_1} , β_{R_2} , $\beta_{R_1 R_2}$, $\beta_{R_1^2}$, $\beta_{R_2^2}$ are the remaining regression coefficients to be estimated. A ten-fold cross-validation was performed by first partitioning the available dataset in $k = 10$ subsets, and then training the GLMs with $k-1$ subgroups and evaluating their performance on the remaining subset by reconstructing MWF maps voxel-wise. The procedure was iteratively repeated k times, so that each subset was used as a test sample once.

In addition, RFRM was explored for the task at hand to exploit its capability to account for non-linearities and thus represent a larger space of functions. An ensemble of 501 decision trees were employed to estimate a nonlinear regression between the relaxometry inputs of Eq. 5.2 (i.e., R_1 , R_2 , $R_1 R_2$, R_1^2 , R_2^2) and the reference MWF values. As for the GLMs, the RF model was trained considering the mean MWF, R_1 and R_2 values within the segmented brain ROIs. Random samples were drawn with replacement (i.e., bootstrapping) from the input data points to train each tree. The model was trained, and subsequently tested, within a ten-fold cross-validation as for the GLMs.

Lastly, two deep neural network architectures were explored. A 2D multi-channel cGAN [292] was designed to derive the reference MWF from the two input relaxometry maps. Conditional GANs are composed of two networks, the generator (G) that tries to capture the nonlinear function from a random noise vector (z) and the input image data (x) to the target image data (y) and a discriminator (D) that estimates the probability that a given image comes from the training data or G. The two networks are trained together in an adversarial manner where G tries to minimize $\log[1 - D(x, G(x, z))]$ and D to maximize $\log[D(x, y)]$. The final loss function (J) was obtained by also including a voxel-wise L_1 regularization between the target and the output of the network $G(x, z)$:

$$J_{cGAN}(G, D) = \arg \min_G \max_D \mathbb{E}_{x,y} \{\log[D(x, y)]\} + \mathbb{E}_{x,z} \{\log[1 - D(x, G(x, z))]\} + \lambda \mathbb{E}_{x,y,z} \{|y - G(x, z)|\}, \quad (5.3)$$

with λ being the weighting term of the voxel-wise loss. The employed architecture for G and D were the same as in [289], with the generator following the general shape of a U-Net with skip connections [291]. In our case, training was performed by providing to the network brain axial slices of the two relaxometry maps as two input channels. Training was performed over 400 epochs using the Adam optimizer (learning rate = 0.0002, $\beta_1 = 0.5$ and $\beta_2 = 0.999$, $\lambda = 500$, batch size of 1). The employed convolutional neural network comprised about 57 million trainable parameters (i.e., weights and biases) that were updated during training process. The network was implemented in TensorFlow 2.0 on Python 3.6 and the total training time was about 70 minutes on a GPU (NVIDIA Tesla V100-32GB).

In addition, a network consisting of the generator only (i.e., a conventional U-Net) was trained without adversarial loss to compare the two approaches. Both network architectures were tested on the healthy cohort using a ten-fold cross-validation.

5.2.4 Statistical analysis

To understand to what extent relaxation times can explain the variability in the MWF values, the adjusted coefficient of determination (adj-R^2) was evaluated for each GLM and averaged across the iterations of the cross-validation. An average pseudo- adj-R^2 was also evaluated for the RFRM.

For evaluating the accuracy of the different modeling approaches, the root mean squared error (RMSE) of the entire volume of estimated MWF maps (i.e., voxel-wise) with respect to the MESE reference was calculated. The intraclass correlation coefficients (ICCs) were also computed considering the mean MWF values in all brain ROIs using a two-way random model, i.e., $\text{ICC}(2,1)$.

Finally, correlation and Bland-Altman plots were computed to study the agreement between the derived mean MWF values from all brain ROIs of the investigated methods with the target values. The bias between the target and estimated MWF map was estimated for each method, along with the limits of agreement at a 95% level of confidence. A one-sample t -test was carried out to test if biases were significantly different from zero.

5.3 Results

Representative slices of the acquired images in two healthy volunteers are shown in Figure 5.1 along with the reference MWF map reconstructed from the MESE data.

Reference and estimated MWF maps with the proposed modeling strategies are shown in Figure 5.2. Under visual inspection, all estimated maps show similar regional MWF patterns to the reference, with the maps estimated from the deep learning methods resembling the most the reference. The introduction of the quadratic terms in the GLM results in maps with contrast information closer to the reference compared to the linear GLM. The nonlinear modeling achieved with RFRM provides maps similar to the quadratic GLM. The U-Net MWF maps exhibit increased blurriness, which is reduced in images derived from the cGAN where anatomical boundaries are sharper.

Quantitatively, the mean adj-R^2 of the GLMs across the iterations of the ten-fold cross-validation was 0.66 ± 0.01 for the linear, and 0.87 ± 0.01 for the quadratic model. In other words, the quadratic model can explain 87% of the variability in the MWF maps, 21 percentage points more than the linear model. The average pseudo- adj-R^2 of the RFRM was found to be 0.90 ± 0.01 . The other measurements of agreement between the estimated and reference MWF maps are reported in Table 5.2. In the voxel-wise comparison between the whole volume

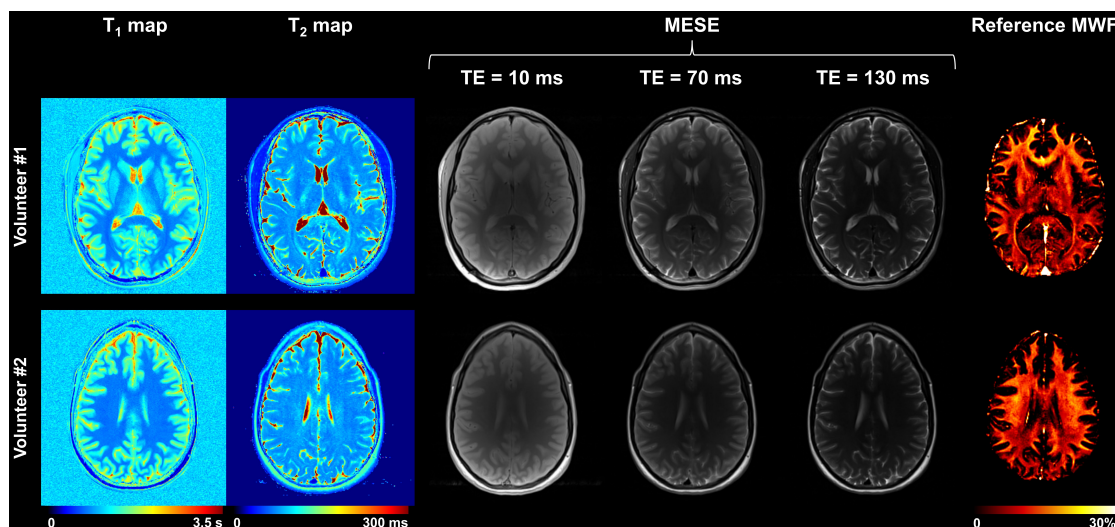


Figure 5.1 – Representative axial slices of the acquired volumes in two volunteers. Three contrasts acquired with the multi-echo spin echo (MESE) sequence out of the 32 acquired echoes are shown. Reference myelin water fraction (MWF) maps reconstructed from the MESE data after skull-stripping are also displayed in the last column.

of estimated MWF maps and the reference, an average RMSE smaller than 0.1% was observed for all methods. The lowest RMSE was observed in the maps estimated by the U-Net, while the maps with the highest ICC and smallest bias were obtained with the cGAN. The ICC among average values in brain ROIs was found to be greater than 0.81 and the bias smaller than 2.1% for all the investigated strategies. Resulting maps from the RFRM were comparable to the GLM with quadratic terms. Results of the correlation and Bland-Altman analysis are also shown in Figure 5.3 for the GLM with quadratic terms, RFRM, U-Net and the cGAN.

5.4 Discussion

In this work, different approaches for a data-driven estimation of in vivo brain myelin water content from single-compartment relaxometry measurements were proposed and compared. The feasibility to estimate MWF was demonstrated within a dataset of healthy volunteers. These findings confirm the initial hypothesis at the base of this work that brain myelin water content information is indeed encoded in relaxometry maps. Among the different modeling strategies that were investigated, deep neural networks produced MWF maps with the best agreement to reference values. The data suggest that, with an acquisition time of 6:24 minutes, the employed protocol for brain relaxometry may provide whole brain MWF maps along with T_1 and T_2 maps.

Three approaches with the capability of modeling a different space of mapping functions were investigated in the multi-contrast derivation of MWF maps – GLMs, RFRM and deep neural networks. The fact that most of the variability in the MWF maps can already be explained with a linear or quadratic polynomial model may be the reason why the modeling of non-linearities

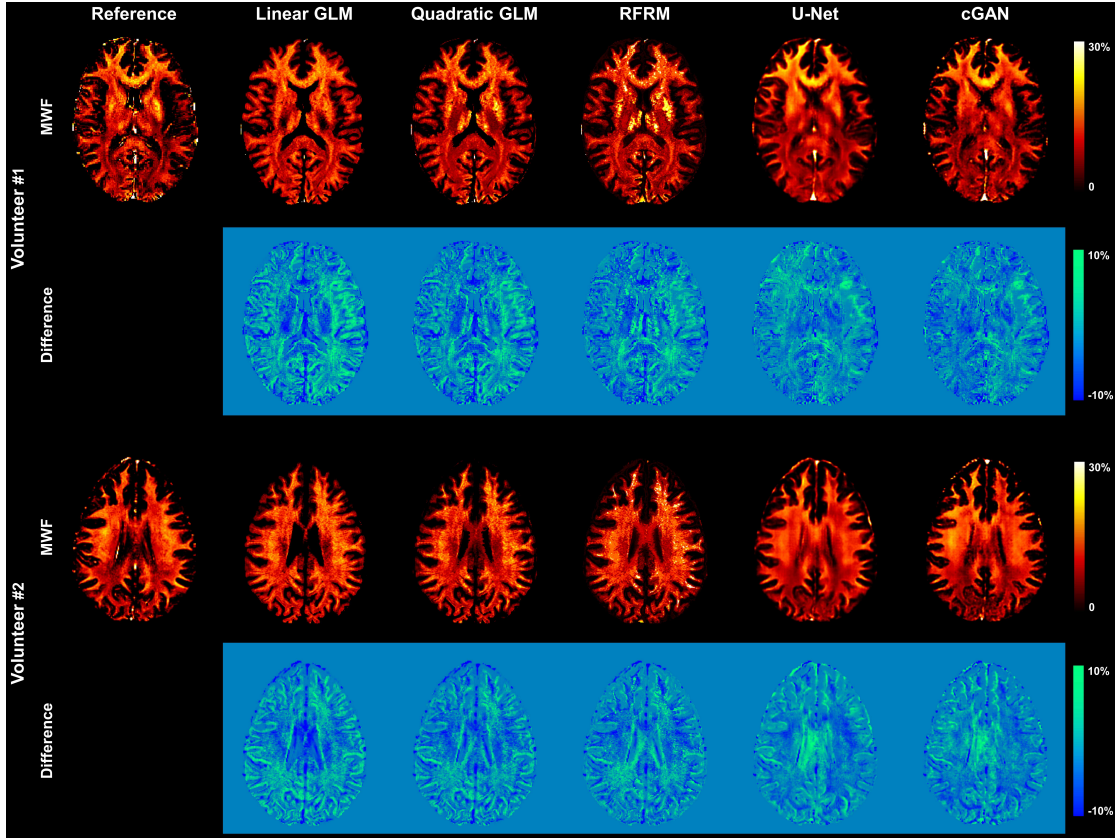


Figure 5.2 – Myelin water fraction maps in two example subjects obtained with the proposed general linear model (GLM) with its linear or quadratic terms, the random forest regression modeling (RFRM), the U-Net and the conditional generative adversarial network (cGAN). Signed differences between estimated and reference maps are shown.

with RFRM did not improve the estimation. The spatial awareness of the cGAN, whose input is conditioned to the entire slice of the two input relaxometry maps, and its capability to represent a larger space of functions to map the relaxometry values to MWF contribute to its improved accuracy. Training only the generator (i.e., U-Net) and removing the adversarial loss was found to deliver MWF maps in agreement with the reference, yet more blurred. Methods based on deep learning architectures were thus observed to be the best fit for the task at hand, with the cGAN providing a good trade-off between accuracy in the estimation and the refinement of anatomical boundaries in the resulting images.

Contrary to multivariate relaxometry models introduced for the estimation of myelin water maps [101, 118], the data-driven estimation proposed here does not require a priori biophysical model of the relationship between relaxation times and MWF maps. In fact, the relation between MWF values and relaxation times is not assumed to follow any biophysical model, but only a linear function or a non-linear arbitrary function estimated purely based on the available data. The complexity of previously employed models showed to limit their stability [133] or required a reduction of the degrees of freedom to guarantee convergence in the fitting process (e.g., fixing relaxation times of tissue compartments to predefined values) that may bias results.

Table 5.2 – Measurements of agreement between estimated and reference myelin water fraction (MWF) values. The root mean squared error (RMSE) was assessed for the entire brain volume voxel-wise; the intraclass correlation coefficients (ICC) was computed considering mean MWF values within ROIs using a two-way random model, i.e., ICC(2,1); the bias between the reference and estimated MWF is shown for each method, along with the 95% limits of agreement (LoA). Bold font indicates the method with best performance according to each metric.

Method	RMSE (%)	ICC(2,1)	Bias (%)	LoA (%)
GLM Linear	0.079 ± 0.0086	0.81	2.19*	[-1.88; 6.27]
GLM Quadratic	0.079 ± 0.010	0.94	1.21*	[-3.16; 5.57]
RFRM	0.072 ± 0.0080	0.94	0.89*	[-3.36; 5.15]
U-Net	0.056 ± 0.0064	0.96	0.18	[-3.08; 3.45]
cGAN	0.059 ± 0.0063	0.97	0.01	[-3.13; 3.16]

* $P < 0.05$ after correction for multiple comparisons.

In addition, biases in the relaxation maps (e.g., originating from MT or diffusion effects) would invalidate a priori biophysical models that assume accurate and uncompromised relaxation values. Data-driven approaches are more robust in this sense since these biases will be learnt during the training process. However, they are strongly dependent on the reference data used for training, which need to be carefully selected.

Image-to-image translation using deep learning networks was never investigated on quantitative MR data, to the best of the authors' knowledge. So far, these approaches have been used in studies with weighted imaging [286, 290, 293]. However, the introduced approach might be further improved in several ways. The amount of training data is one of the crucial concerns while training deep neural networks. While the results presented are promising especially given the small size of the training set, current work is focused on expanding its size. Of note, the training here was performed using spatially registered volumes to have a fair comparison across methods. However, the capability of dealing with unpaired data would enlarge the spectrum of suitable images for the training. To that end, cycleGANs have been developed that can cope with unregistered data [294]. In a cycleGAN, a second generator is used to learn the inverse transformation from the target to the input domain. The two generators are trained simultaneously, and a cycle consistency loss is introduced to guarantee data fidelity between the input of the first generator and the output of the second. The combination of these architectures with the adversarial training has shown value in the image-to-image translation of unpaired datasets [294, 295].

The conducted study and the proposed data-driven estimation of MWF maps have certain limitations. The main drawback of the suggested approach is that it will suffer from the same limitations (e.g., bias, noise, among others) as the MWF maps retrieved with the MESE sequence. Usually scanned in 2D and accelerated with interleaved slice sampling, MESE acquisitions are sensitive to B_1 inhomogeneities and MT contamination on the acquired

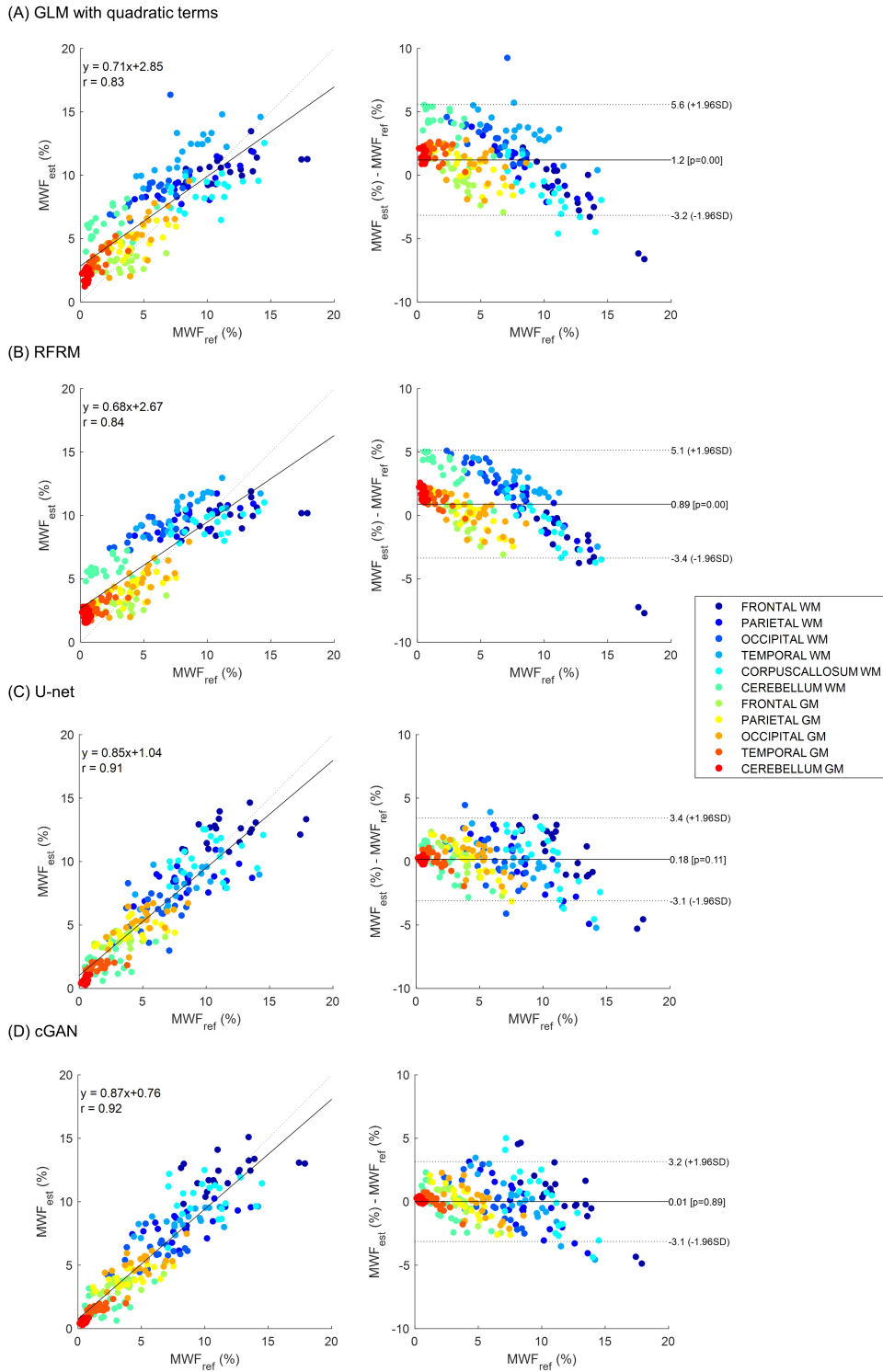


Figure 5.3 – Correlation analysis (left) and Bland Altman plots (right) comparing reference myelin water fraction (MWF_{ref}) values with those estimated (MWF_{est}) by the general linear model (GLM) with quadratic terms (A), the random forest regression modeling (RFRM) (B), the U-Net (C) and the conditional generative adversarial network (cGAN) (D).

decays [121]. Nonetheless, MWI achieved with the MESE sequence represents the most common and validated method in the field (see **Section 3.2.1** in Chapter 3). Hence, replacing this long acquisition with a fast protocol would be beneficial for clinical practice. The proposed protocol requires 6:24 minutes to image the whole brain and is thus more suitable for clinical practice. However, the 2D nature of the proposed acquisition limits the resolution in the slice direction and the required spatial registration of the MESE data to the T_1 map to match the field of view and spatial resolution might impact the accuracy of the estimation. A 3D version of the proposed protocol is thus currently under development [296]. Achieving higher resolutions would be also certainly beneficial in studying and characterizing brain focal abnormalities (e.g., MS lesions). On the other hand, for applications focused on studying global changes in brain tissues, as for instance the normal evolution of MWF values in brain regions, coarser resolutions could be even applied resulting in a further decreased acquisition time. Additionally, the robustness of the proposed approaches to different level of SNR of the reference MWF maps and the acquired relaxometry maps should be investigated in the future.

Finally, the proposed modeling could be easily adapted to learn MWF features estimated from different sequences if considered as reference, such as multi-echo GRASE [84, 85], T_2 prep [89], multi-echo GRE [91, 96], among many others [36]. In addition, complementary quantitative maps that have shown to be good indicators of brain myelin content, e.g., proton density, T_2^* [91], quantitative MT [155] and diffusion tensor imaging [297], may serve as additional input channels to improve the overall estimation of MWF maps. MR fingerprinting approaches may be a valuable resource in this direction as they allow to simultaneously estimate multiple physical parameters [25, 298], especially as several efforts have been and are currently made to reach whole-brain coverage in short acquisition times [299, 300]. Of notice, approaches have been also developed to perform the multi-component decomposition of the acquired MR fingerprinting signals to estimate the proportion of water compartments and thus MWF maps [259, 260, 301]. Moreover, by including fast sequences to the currently employed protocol to map additional physical parameters, the proposed approach could also be easily scaled to infer other properties of the tissue microstructure such as iron concentration [128], axonal g-ratio [302, 303], and conductivity [304], given the availability of training data and that information about the target parameter is reflected in the source parameters. Unraveling the relation between measurable physical properties and the microstructural features of brain tissues will promote and increase the value of qMRI acquisitions, paving the way towards in vivo histology using MRI [284, 285].

5.5 Conclusion

Different modeling approaches were investigated to derive MWF maps from relaxometry data. The tested cGAN provided maps with the best trade-off between agreement with the reference MESE data and detailed anatomical boundaries. The employed protocol for fast and whole brain relaxometry in combination with machine learning may thus have the potential to provide multi-contrast data in clinical settings without the need for long scan times.

6 Quantitative brain relaxation atlases for personalized detection and characterization of brain pathology

The content of the following chapter is based on the postprint version of the article: “Quantitative brain relaxation atlases for personalized detection and characterization of brain pathology” published in Magnetic Resonance in Medicine [288]. DOI: [10.1002/mrm.27927](https://doi.org/10.1002/mrm.27927). The article was co-authored by Tom Hilbert, Cristina Granziera, Guillaume Bonnier, Reto Meuli, Filippo Molinari, Jean-Philippe Thiran, and Tobias Kober. All co-authors contributed to the idea and reviewed the manuscript.

Abstract: To exploit the improved comparability and hardware independency of qMRI, databases of MR physical parameters in healthy tissue are required, to which tissue properties of patients can be compared. In this chapter, normative values for longitudinal and transverse relaxation times in the brain were established and tested in single-subject comparisons for detection of abnormal relaxation times. To that end, relaxometry maps of the brain were acquired from 52 healthy volunteers. After spatially normalizing the MRI volumes into a common space, T_1 and T_2 inter-subject variability was modeled voxel-wise within the healthy cohort. A method for single-subject comparison against the atlases was developed by computing z-scores with respect to the established healthy norms. The comparison was applied to two multiple sclerosis and one clinically isolated syndrome cases for a proof of concept. The established atlases exhibit a low variation in WM structures (median RMSE of models equal to 32 ms for T_1 and 4 ms for T_2), indicating that relaxation times are in a narrow range for normal tissues. The proposed method for single-subject comparison detected relaxation time deviations from healthy norms in the example patient datasets. Relaxation times were found to be increased in brain lesions (mean z-scores > 5). Moreover, subtle and confluent differences (z-scores ~ 2 – 4) were observed in clinically plausible regions (e.g., between lesions, corpus callosum). Example patient deviation maps demonstrated good sensitivity of the atlases for detecting relaxation time alterations on a single-subject level.

6.1 Introduction

QMRI techniques allow moving from conventional relative contrast information to a single, absolute measure of one or more separate tissue properties, hence providing the means for tissue characterization and the potential to gain further insight into microstructural changes caused by diseases [284] (see **Section 2.3** in Chapter 2). Moreover, the quantitative nature of the images may potentially overcome problems related to image reproducibility and interpretation, facilitating comparison in longitudinal and multi-centric studies [305, 306]. Of interest, brain relaxometry measures proved to be of value in several neurological diseases as alterations of T_1 and T_2 were related to neuronal cell death, axonal loss, and demyelination processes (see **Section 2.3.5** in Chapter 2). Despite these advantages, the long acquisition times required to obtain parametric maps hindered the introduction of qMRI in clinical routine. To overcome this limitation, various fast quantitative mapping techniques were developed over the past years. Among those, the MP2RAGE sequence for T_1 mapping [16] (see **Section 2.3.1** in Chapter 2) and GRAPPATINI for T_2 mapping [54] (see **Section 2.4.3** in Chapter 2) are of particular interest to this work.

Although quantitative maps are better comparable across scanners and sites, they only have limited direct clinical value. To fully exploit the information provided by T_1 and T_2 maps, normative values for relaxometry in healthy tissue are required, enabling the comparison of tissue properties from a single patient to normal values [43, 44]. Furthermore, the quantification of changes in T_1 and T_2 with respect to normal values promotes the definition of imaging biomarkers for characterization of pathologies, potentially improving diagnosis and follow-up assessments by correlating T_1 and T_2 variations with microstructural changes.

Following this rationale, the work in this chapter aims at building normative atlases for T_1 and T_2 relaxation in the human brain with the goal of a voxel-wise single-subject comparison.

6.2 Methods

6.2.1 Study population

Fifty-two healthy subjects were enrolled in this study (24 male, 21–48 y/o, 27.5 y median age) and written informed consent was obtained from each subject before the exam. Two subjects with a benign cyst in the pineal gland and an enlarged perivascular space (EPVS) in the parietal lobe of WM, assessed by a radiologist according to local guidelines, were excluded from the generation of the atlases but were used for validation, as the cysts and especially the EPVS would alter the normative T_1 and T_2 values in the corresponding voxels. A radiological assessment was not performed on the other participants. On visual inspection (G.F.P., MR physicist, 2 years of experience), however, neither macroscopic brain abnormalities (e.g., atrophy) nor focal damages (e.g., focal WM abnormalities) were found.

In addition, three age-matched patients (a male of 31 y/o diagnosed with progressive-relapsing

Table 6.1 – Relevant parameters of the acquired LPM protocol.

Parameter	T ₁ mapping (MP2RAGE)	T ₂ mapping (GRAPPATINI)
Acquisition type	3D	2D
Resolution	0.7×0.7×3 mm ³	
Field of View	230×215×132 mm ³	
TI ₁ /TI ₂	700/2500 ms	–
ΔTE/N-Echoes	–	10 ms / 16
Flip angles	4-5°	180°
TR	5 s	4 s
Undersampling	2× GRAPPA	2× GRAPPA and 5× MARTINI
Undersampling direction	R > L phase encoding	
Slice partial Fourier	6/8	–
Phase resolution	80%	
Bandwidth	240 Hz/Px	220 Hz/Px
TA	3:02 min	3:22 min

MS (PRMS); a female of 44 y/o with relapsing-remitting MS (RRMS); a male of 31 y/o with clinically isolated syndrome (CIS)) were scanned with the same protocol in agreement with the institutional regulations.

6.2.2 MR protocol

All subjects were scanned at 3 T (MAGNETOM Skyra, Siemens Healthcare, Erlangen, Germany) using a standard 20-channel head/neck coil. The synchronized whole brain protocol, hereafter referred to as the *Lausanne Parametric Mapping* (LPM) protocol, consisted of MP2RAGE for T₁ relaxometry and GRAPPATINI for quantitative T₂ mapping, with aligned FOVs and a total acquisition time of 6:24 min. Relevant sequence parameters of the LPM protocol are reported in Table 6.1.

6.2.3 Image processing

The processing steps applied to the acquired volumes before the computation of the normative atlases are summarized in Figure 6.1.

First, images were linearly interpolated to 0.7×0.7×1 mm³. Head motion that might have occurred between the acquisition of the T₁ and T₂ map was compensated by a rigid registration of the T₂ map onto the T₁ map using Elastix [64] (similarity metric: normalized mutual information; optimizer: adaptive stochastic gradient descent; interpolation: linear). Consequently, all subsequent steps are performed in the MP2RAGE space for each subject.

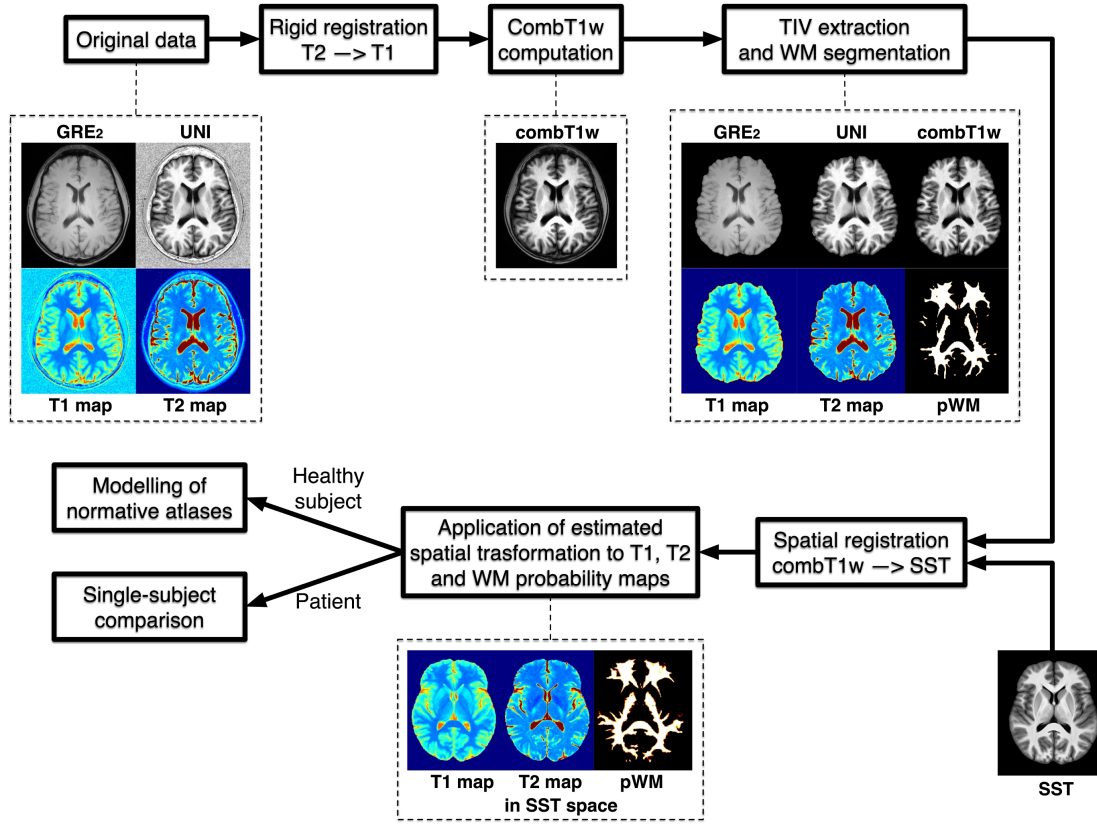


Figure 6.1 – Pre-processing pipeline. First, for each data set, the T_2 map is rigidly registered to the T_1 map to correct for possible head motion between the two acquisitions. The total intracranial volume (TIV) is subsequently extracted based on the combined T_1 -weighted (comb T_1w) image and the probability of each voxel to belong to the WM tissue (pWM) is estimated. Finally, the skull-stripped comb T_1w volumes are aligned with the study-specific template (SST) via a non-linear spatial registration; the estimated transformation is then applied to T_1 , T_2 , and pWM maps.

The total intracranial volume (TIV) was extracted to improve the robustness of the inter-subject spatial normalization to a common space [307]. More specifically, the TIV extraction was performed using the in-house prototype software MorphoBox by matching a template onto a combined T_1 -weighted (comb T_1w) image computed by multiplying the MP2RAGE GRE₂ and UNI volumes [58, 59] (see **Section 2.5.1** in Chapter 2).

Given that the T_2 maps were previously aligned with T_1 maps, the same TIV mask was used to extract the brain in both T_1 and T_2 maps. Furthermore, the probability of belonging to one of the three main brain tissues (WM, GM, and CSF) was estimated for each voxel using MorphoBox.

A study-specific template (SST) was built from 20 randomly selected subjects as it was previously shown [308–310] that the use of a SST instead of already existing templates (e.g., N27 or MNI) improves the accuracy of the registration before the computation of the voxel-wise atlases. The Advanced Normalization Tools (ANTs) [66] was used for this task as it provides an adapted feature set for atlas creation (see **Section 2.5.2** in Chapter 2). The computation of the

template required ~ 12 h on a desktop computer (Intel Core i7 CPU 3.06 GHz CPU and 24.0 GB of RAM).

T_1 and T_2 maps from all subjects were then spatially normalized onto the SST using Elastix [64]. First, the $\text{comb}T_1w$ image of every subject was registered to the SST by the subsequent computation of an affine and non-rigid registration (similarity metric: advanced Mattes mutual information; optimizer: stochastic gradient descent; interpolation: linear). Subsequently, the estimated transformation from the native space to the SST was applied to T_1 , T_2 , and WM probability maps.

6.2.4 Population-derived norms

T_1 and T_2 brain normative atlases were estimated by modeling the relaxation time variability within the healthy cohort (HC) using a linear regression model in each voxel. The impact of the subjects' sex and age on the physical properties was accounted for by using them as predictive variables. The models for each voxel position (\mathbf{r}) were:

$$\mathbb{E}\{T_1(\mathbf{r})\} = \beta_{0,T_1}(\mathbf{r}) + \beta_{sex,T_1}(\mathbf{r}) \cdot sex + \beta_{age,T_1}(\mathbf{r}) \cdot age, \quad (6.1)$$

$$\mathbb{E}\{T_2(\mathbf{r})\} = \beta_{0,T_2}(\mathbf{r}) + \beta_{sex,T_2}(\mathbf{r}) \cdot sex + \beta_{age,T_2}(\mathbf{r}) \cdot age, \quad (6.2)$$

with β_0 being the model intercept, sex a categorical variable equal to 1 if the subject is male or 0 if female and age in years (as a whole number) centered at the mean age of our HC (29 y). β_{sex} and β_{age} are the predictive variables, respectively. For each model, the RMSE was evaluated as an estimation of the SD of the residuals error across the linear model. Established atlases (i.e., model coefficients and RMSE for each voxel) were made available online along with the anatomical template (Supporting Information at onlinelibrary.wiley.com/doi/abs/10.1002/mrm.27927). Although models were evaluated in the whole brain, it should be noted that coefficients are not meaningful in CSF regions, because the T_1 and T_2 values found there exceed the range of reliably measurable relaxation times of both relaxometry methods.

In addition, an analysis of variance was carried out through an F -test to evaluate the goodness of fit in comparison to an intercept-only model. P -values < 0.05 were considered as significant after a false discovery rate correction for multiple comparisons was applied at a cluster level (defined by $P < 0.005$ at voxel level) [311]. In addition, the inter-subject variation of relaxation maps was compared with the intra-subject spatial variability by computing the SD of T_1 and T_2 values in WM tissues for each subject in the HC.

6.2.5 Method of single-subject comparison

A method for performing a single-subject comparison against the derived linear regression models was established. To that end, z-scores are computed for each voxel-position (\mathbf{r}):

$$z_{T_1}(\mathbf{r}) = \frac{T_1(\mathbf{r}) - \mathbb{E}\{T_1(\mathbf{r})\}}{RMSE_{T_1}(\mathbf{r})}, \quad (6.3)$$

$$z_{T_2}(\mathbf{r}) = \frac{T_2(\mathbf{r}) - \mathbb{E}\{T_2(\mathbf{r})\}}{RMSE_{T_2}(\mathbf{r})}, \quad (6.4)$$

The expected normative T_1 and T_2 values, usually computed only as an average of the tissue properties across a group of healthy subjects, will therefore vary for each tested subject depending on gender and age. To avoid false positives in the cortex resulting from much more pronounced anatomic variation, the analysis was restricted to WM voxels by multiplying the resulting z-score map with a WM prior in the template space. This WM prior is the average of the spatially normalized WM probability maps of each healthy subject. The inverse registration into native space of the subject is applied to the z-score maps to overlay them with the originally acquired weighted images.

6.2.6 Norms validation

Because the z-score calculation assumes a normal distribution, relaxation times were first tested to be normally distributed in each WM voxel over all HC with the Kolmogorov-Smirnov test. $P < 0.05$ were considered as significant after a false discovery rate correction for multiple comparisons was applied at a cluster level (defined by $P < 0.005$ at voxel level).

Furthermore, the generated atlases were validated inside the HC to assess their robustness with respect to the detection of false positives when used for a binary detection of brain voxels being normal or abnormal. To that end, a model prediction interval at 95% level of confidence was considered as the normative range for fitted relaxation times $\mathbb{E}\{T\}$ at each voxel position \mathbf{r} and computed as

$$\mathbb{E}\{T(\mathbf{r})\} \pm t_{\alpha/2, n-p} RMSE, \quad (6.5)$$

where t is the Student's t-statistics evaluated for a level of significance $\alpha = 0.05$ and $n-p$ degrees of freedom, with n being the number of observations used to build the model (50 healthy subjects) and $p = 3$ the number of estimated coefficients (intercept, age, and sex). Because in this case $t_{\alpha/2, n-p} = 2.01$, voxels exceeding an absolute z-score of 2.01 were considered as false positives. The false positive rate (FPR) of detection at each voxel was evaluated by partitioning the available data set in $k = 10$ subsets and performing a k-fold cross-validation. The predictive model was trained with $k-1$ subgroups and its performance was validated on the remaining subset by computing the FPR for each voxel. The procedure was iteratively repeated k times, so that each subset was used as a test sample once. The outcomes of each repetition were averaged.

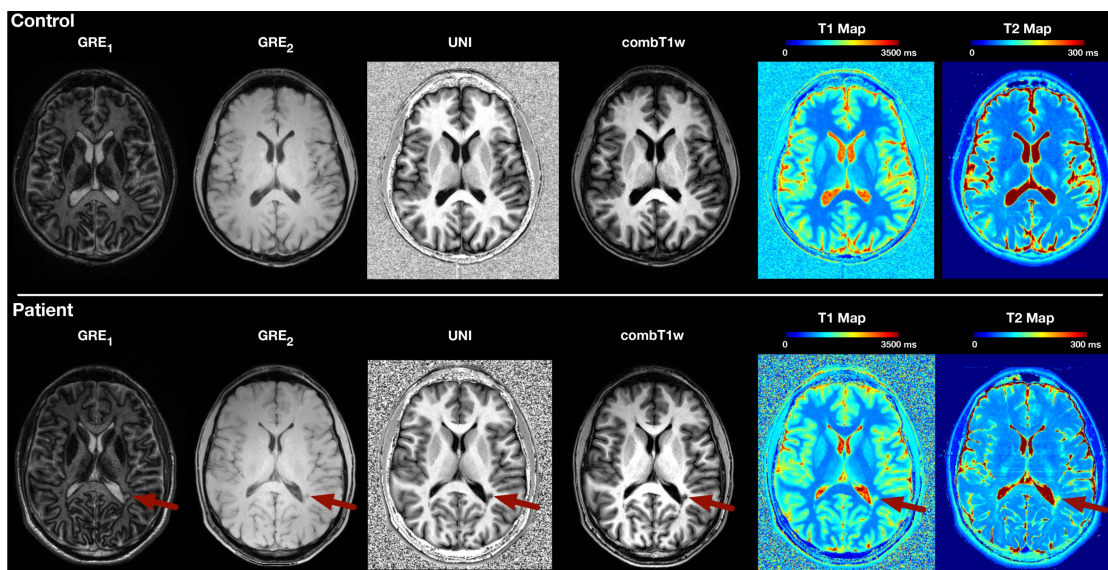


Figure 6.2 – Example GRE_1 , GRE_2 , UNI , T_1 map and T_2 map acquired with the LPM protocol and the combined T_1 -weighted ($combT_1w$) image obtained as multiplication of GRE_2 and UNI for a healthy subject and a patient. An example lesion is indicated by a red arrow in the patient's volumes. Stripes in patient's T_2 map are likely due to either blood flow or patient motion that violate the model in the model-based reconstruction leading to artifacts along the phase encoding direction.

6.2.7 Detection of relaxometry alterations in example patient's cases

The single-subject comparison method was applied on three case report patients to demonstrate its feasibility and the good sensitivity of the atlases in the detection of tissue alterations.

6.3 Results

Example brain volumes acquired with the LPM protocol are shown in Figure 6.2 for one healthy volunteer and one MS patient.

The $combT_1w$ SST built with ANTs is shown in Figure 6.3 along with the WM prior computed in the common space.

A representative slice of the established atlases accounting for normal T_1 and T_2 variation in the brain is reported in Figure 6.4. The spatial maps of the intercept coefficients resemble the average T_1 and T_2 maps at the mean age of the HC (29 y). As example for expected relaxation times, T_1 and T_2 values in a voxel of the WM frontal lobe for the mean age of the HC were found to be: $\mathbb{E}\{T_1\} \pm \text{RMSE} = 791 \text{ ms} \pm 27 \text{ ms}$, $\mathbb{E}\{T_2\} \pm \text{RMSE} = 69 \text{ ms} \pm 3 \text{ ms}$. The atlases exhibit a low RMSE in brain WM ($\Delta T_1 = 18\text{--}60 \text{ ms}$, median = 32 ms; $\Delta T_2 = 2\text{--}19 \text{ ms}$, median $T_2 = 4 \text{ ms}$), but higher RMSE in the cortex ($\Delta T_1 = 30\text{--}600 \text{ ms}$, median = 138 ms; $\Delta T_2 = 5\text{--}80 \text{ ms}$, median = 12 ms). The intra-subject variations of T_1 and T_2 evaluated as the SD of relaxation times in WM tissue was found to be: $\Delta T_1 = 57\text{--}72 \text{ ms}$ (median 64 ms); $\Delta T_2 = 6.1\text{--}7.7 \text{ ms}$ (median 7 ms), which is higher than the inter-subject variation expressed in the RMSE of the established

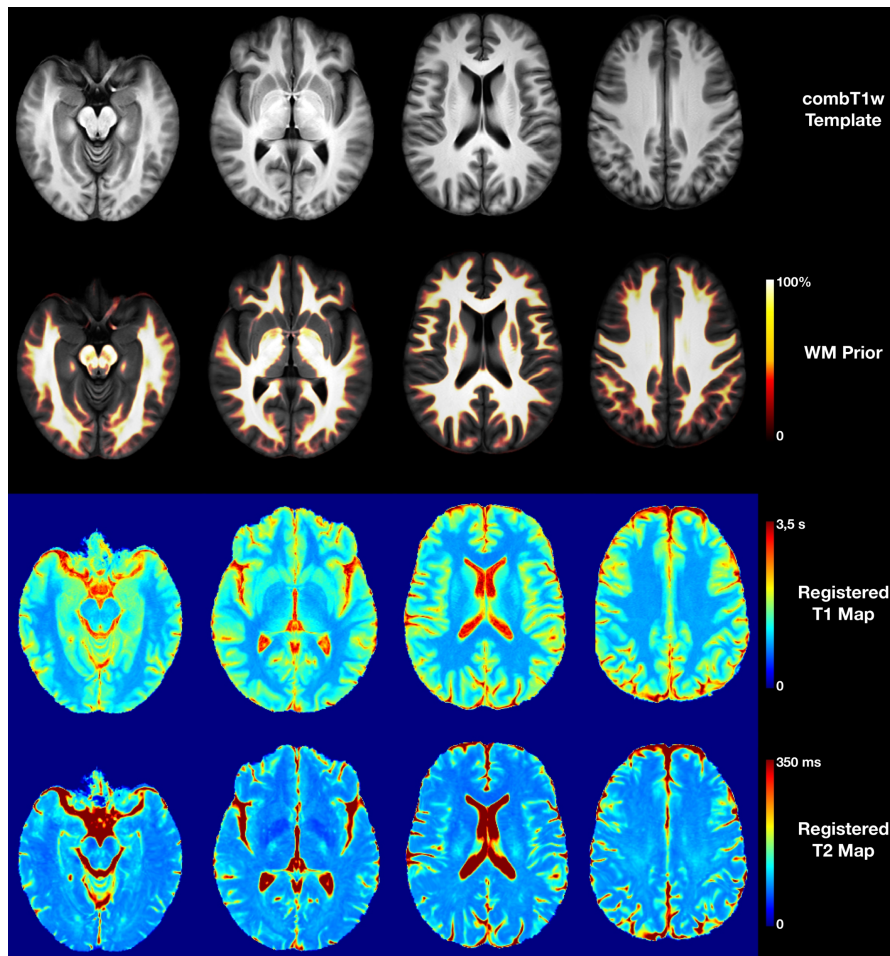


Figure 6.3 – Axial slices of the study-specific template are shown in the first row. Representative axial slices of white matter (WM) prior are overlaid on the combined T_1 -weighted (comb T_1w) template. An outcome of spatial registration after skull-stripping is also shown for a healthy volunteer as an example that derived contrasts from MP2RAGE represent a reliable input for automatic brain image processing tools.

models.

After correction for multiple comparisons, sex and age were found to have a significant impact on relaxation times only in some clusters located in the caudate for T_1 and in the putamen and pallidum for T_2 (Figure 6.5). In voxels with significant results, both T_1 and T_2 were found to decrease within the age range of the HC, whereas male subjects generally exhibited slightly higher T_2 values but shorter T_1 than female subjects (Figure 6.5).

Relaxation times across the HC were tested for being normally distributed. T_1 and T_2 values were found to satisfy the condition in almost all voxels within the WM (92.64% of the voxels for T_1 and 95.02% for T_2). Most of the voxels where T_1 and T_2 were not normally distributed can be found at the boundaries between WM and GM tissues (see Figure 6.6).

Figure 6.7 illustrates cross-validation results for some brain slices. Overall, obtained val-

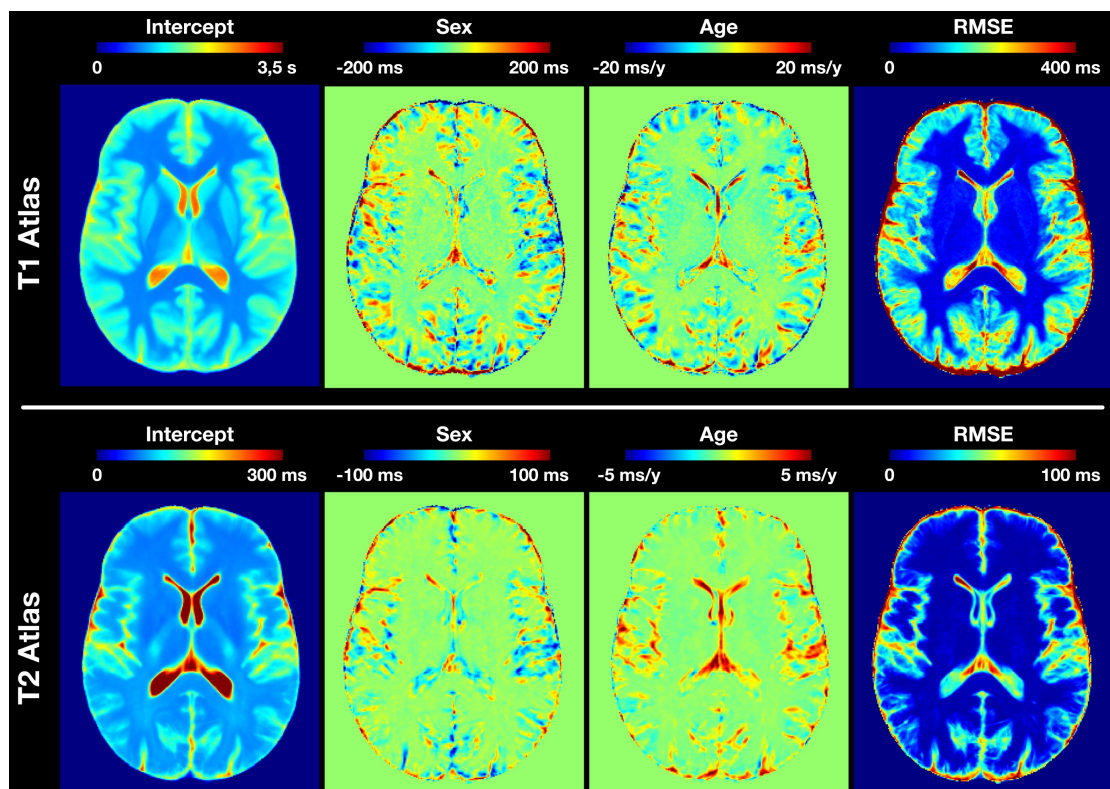


Figure 6.4 – Representative slice of the normative T_1 and T_2 atlases. The intercept, sex and age maps are intended as the β_0 , β_{sex} and β_{age} coefficients of Eq. 6.1 and 6.2. The age coefficient was centered at the mean age of 29 y to ensure that the intercept corresponds to the average relaxation times. It should be noted that the apparent “age effect” in the CSF should be ignored as both the T_1 and T_2 mapping methods cannot measure such long times reliably.

ues were $FPR(T_1)$: median = 2.13%, range = [0–34.04]%; $FPR(T_2)$: median = 2.13%, range = [0–29.79]%. The highest FPRs were found at the interface between WM and deep or cortical GM structures.

T_1 and T_2 z-score deviation maps for a healthy subject (included in HC), a healthy volunteer with an EPVS (not included in HC), and two MS patients are shown in Figure 6.8. The z-score map of the healthy control shows low z-scores (mean $|z_{T_1}| = 0.04$ and mean $|z_{T_2}| = 0.06$) and only few voxels with significant T_1 and T_2 alterations ($|z\text{-score}| > 2$ in 0.3% of WM voxels). Similarly, the z-score map of one of the healthy subjects with an EPVS does not reveal any alteration in T_1 and T_2 , except for the EPVS itself. High z-scores are observed within the EPVS because of different tissue properties compared to WM. By drawing a region of interest, a mean z_{T_1} of 8.77 ± 2.19 , range = [4.82–12.53] and a mean z_{T_2} of 27.34 ± 9.39 , range = [9.25–43.26] were assessed inside the EPVS. Furthermore, in the T_1 and T_2 maps of the MS patients, the method showed increased z-scores in lesion tissue. In the RRMS patient, a lesion close to the ventricle was found to have a mean z_{T_1} of 14.22 ± 7.74 , range = [3.78–33.74] and a mean z_{T_2} of 12.04 ± 6.72 , range = [1.71–27.54], exhibiting a clear deviation from the population-derived norm.

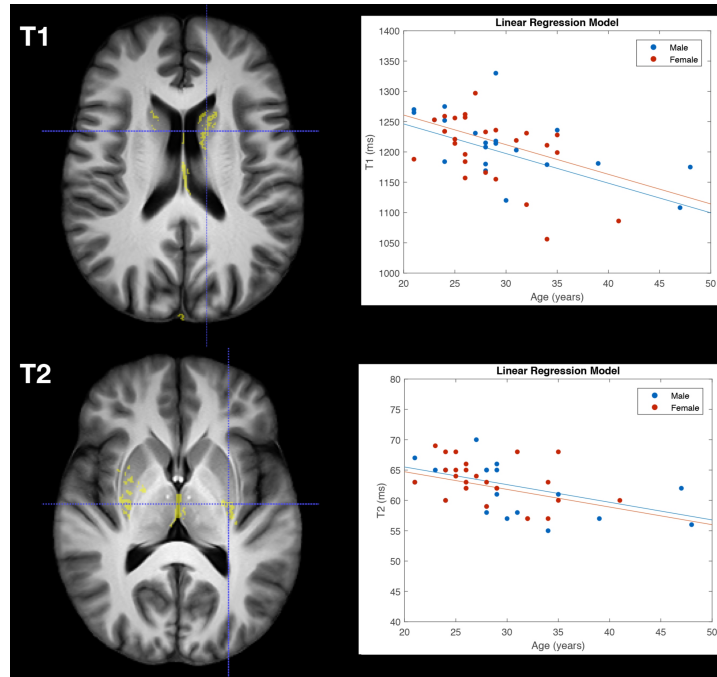


Figure 6.5 – The left column shows voxels with significant correlation between age and sex with T_1 or T_2 (highlighted in yellow). The right column shows linear regression models versus age in an example voxel in the caudate for T_1 and in the putamen for T_2 .

Regarding the CIS patient, representative slices with T_1 and T_2 deviations are shown in Figure 6.9. T_1 and T_2 were found to deviate in lesions also in this case. For illustration, in two example plaques pointed out in Figure 6.9 (green arrows), the following deviation values were found: (1) mean $z_{T_1} = 15.81 \pm 4.19$, range = [8.43–22.48]; mean $z_{T_2} = 11.59 \pm 2.75$, range = [7.21–16.92]; and (2) mean $z_{T_1} = 10.73 \pm 3.34$, range = [4.32–16.61]; mean $z_{T_2} = 7.61 \pm 2.31$, range = [1.94–11.86]. In addition, this case showed more spread deviations of MR relaxation signals between lesions and in the corpus callosum for T_2 (z-score deviations between 2–4). Notably, these subtle changes are not visible in conventional contrasts.

Despite using a WM prior in the SST space to restrict the analysis to WM, false positives occurred because of registration imprecisions. Conversely, the restriction to the WM may cause false negatives, especially for lesions close to the ventricles. Some false-positives and false-negatives are shown in Figure 6.9 (red arrows), where significant z-scores are seen in cortical GM structures, and lesioned tissue shows low z-scores close to the ventricle.

6.4 Discussion

The present chapter introduces a method for personalized detection and characterization of brain abnormalities causing alterations of relaxation times. Voxel-wise population-derived norms were established by modeling T_1 and T_2 distributions within a HC and proved valuable in revealing tissue deviations from the normative atlases in single-subject comparisons. The

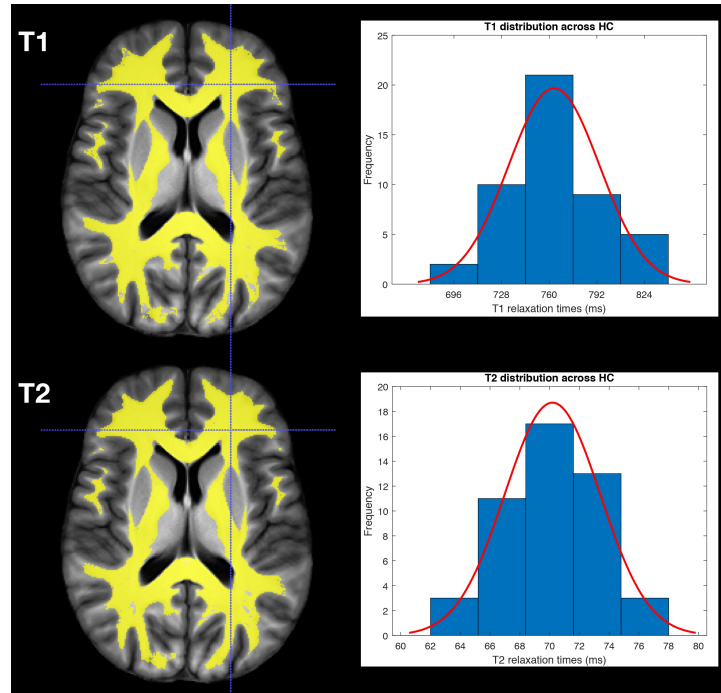


Figure 6.6 – Voxels with a normal distribution of T_1 and T_2 values across the healthy subjects are highlighted in yellow in the left column. The two histograms in the right column show a normal distribution of T_1 and T_2 values for an example voxel.

possibility of detecting subtle alterations that are not visible in conventional MRI, presented here in the proof-of-concept patient datasets, shows the methodology clinical potential.

The capability of the proposed method to detect tissue alterations with respect to population-derived norms is based on the low inter-subject variability of T_1 and T_2 relaxation times, reflected by a RMSE < 40 ms for T_1 and < 4 ms for T_2 in WM. These results show that relaxation parameters of normal tissue obtained with the applied MR sequences fall within a narrow range. In addition, the spatial inhomogeneity of T_1 and T_2 was found to be more pronounced than the inter-subject variation in WM tissues, reinforcing the idea that relaxation atlases at a voxel-by-voxel level are necessary to detect abnormalities locally on a voxel basis. However, higher RMSE was observed in cortical GM structures, which is mostly because of large anatomic inter-subject variation of the cortices leading to their imperfect spatial normalization. This slightly flawed matching of cortices across subjects results in a mixed distribution of WM and GM in these voxels and renders the interpretation of results problematic in single-subject analyses [312]. Consequently, a SST was built to have an optimal common space and a WM prior was applied to restrict the analysis only to subcortical areas. Future work should focus on improving the spatial normalization of the cortex while ideally avoiding the commonly used spatial smoothing that causes loss in resolution and difficulties in detecting focal changes [313]. Elastix was used for performance reasons because pair-wise registrations with ANTs typically require a computational time ranging from 30 min to 1 h [63], whereas Elastix requires around 3 min. Novel methods based on deep learning approaches [314] may

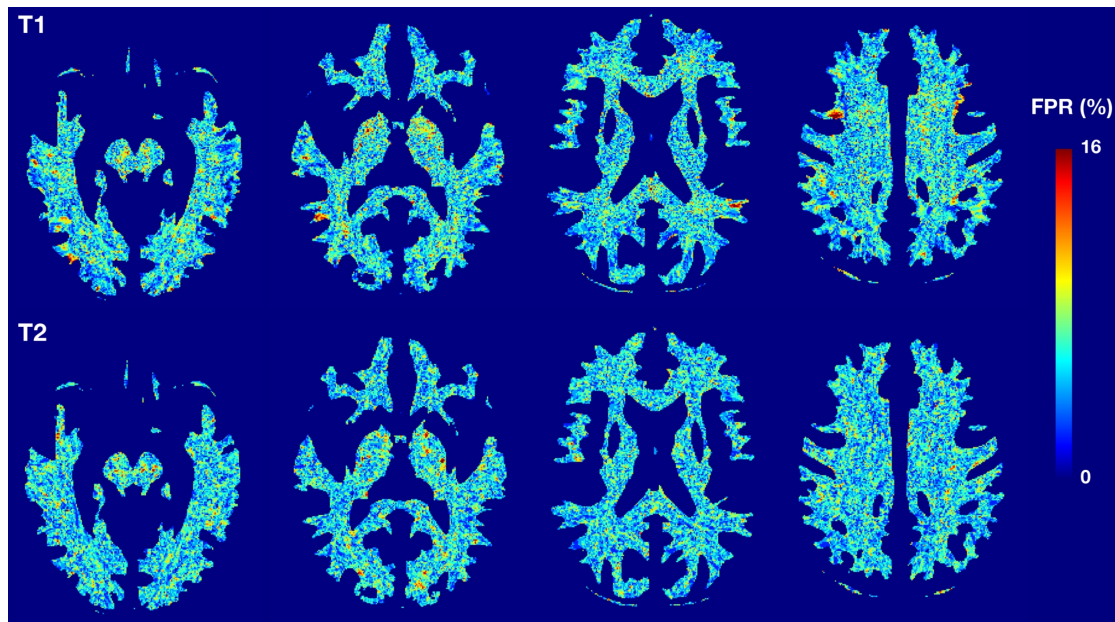


Figure 6.7 – Representative axial slices reporting the results of the 10-fold cross-validation as false-positive detection rate (FPR) of the established normative models for T_1 (upper row) and T_2 (lower row).

be investigated in the future to replace the current registration tools.

This study moves away from conventional group comparisons (often used to improve statistical power) and provides information about relaxation alterations on a single-subject basis. The robustness of the proposed method was confirmed by the low false-positive rate assessed in the healthy controls with a 10-fold cross validation, which resulted in a low median FPR of 2.13% for both T_1 and T_2 . As expected, the highest FPRs were found at WM/GM and WM/deep GM boundaries, where inaccurate alignment of subjects' cortices leads to partial volume effects as described above. In patient data, the z-score deviation maps showed strong deviations in lesion tissue in the WM. In agreement with previous studies [37, 38], T_1 alterations appeared to be more pronounced in focal lesions than T_2 , reflecting the higher sensitivity of T_1 to changes of structural tissue organization. Additional and more confluent differences were observed between lesions or in the splenium of the corpus callosum, especially for T_2 deviations [315]. Notably, these types of differences cannot be seen with the naked eye; we speculate that they could be of clinical significance (e.g., they may be helpful in the early detection of tissue inflammation, micro-edema formation, or neurodegeneration) [37]. This hypothesis needs, however, further clinical validation. In the results, undetected lesion tissue was observed especially at tissue boundaries; an accurate true negative rate was however not estimated because no ground truth (i.e., manual lesion segmentation) was available. Moreover, despite using a WM prior in the SST space, a false-positive cluster in a cortical region close to the WM was detected because of a slight mismatch between the WM prior and the GM of the registered patient's data set. A patient-specific WM mask could be used to ensure the perfect restriction of the single-subject comparison in WM tissues. However, the tissue classification

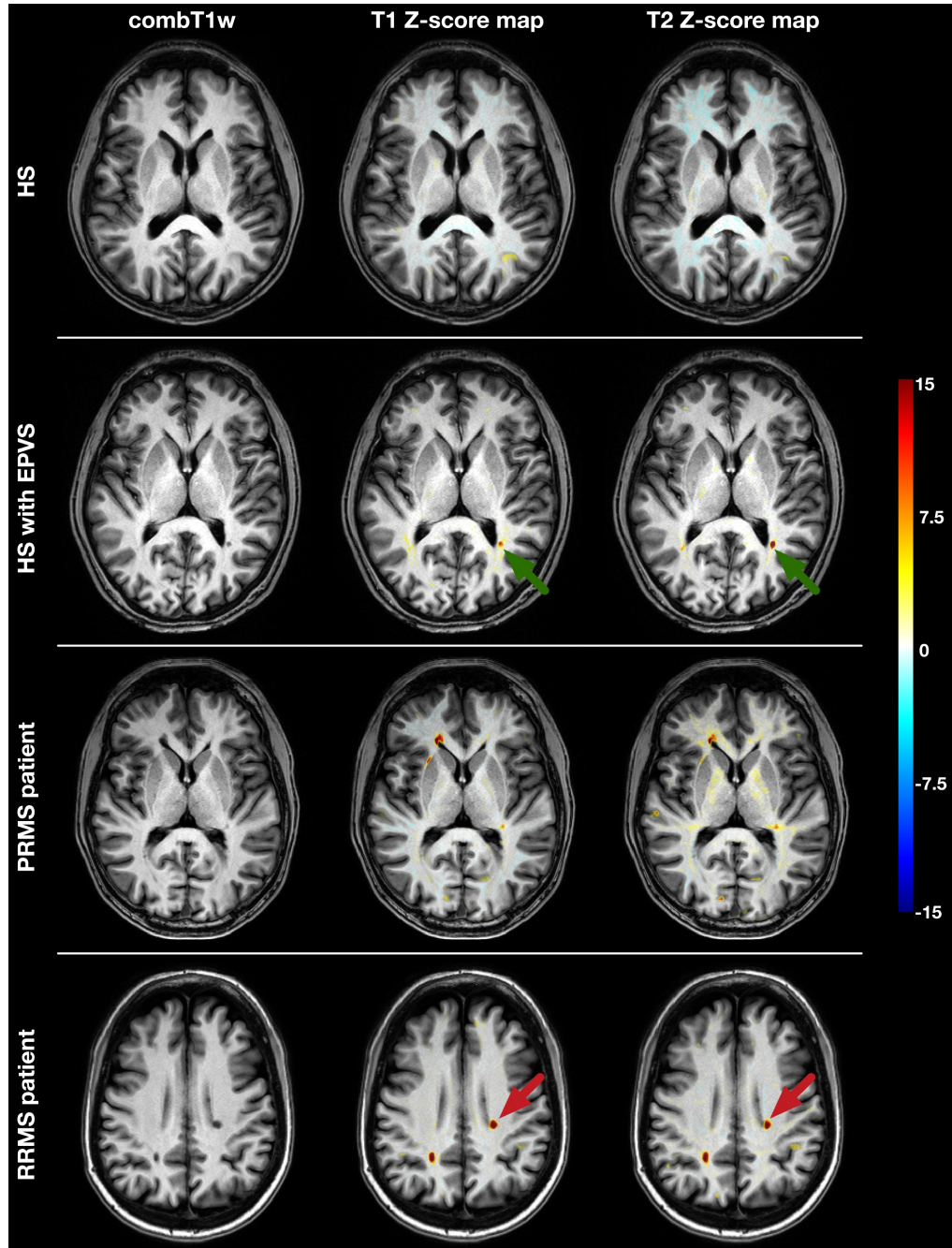


Figure 6.8 – Z-score deviation maps resulting from a single subject comparison against voxel based population derived norms for a healthy subject (HS, male, 28 y/o), a HS with an enlarged perivascular space (EPVS) (male, 27 y/o) and two multiple sclerosis patients (progressive relapsing: PRMS, male, 31 y/o; relapsing remitting: RRMS, female, 44 y/o) are overlaid on a representative combined T_1 -weighted ($combT_1w$) axial slice. By drawing a region of interest around the HS EPVS (green arrows), a mean T_1 z-score of 8.77 ± 2.19 , range = [4.82-12.53] and a mean T_2 z-score of 27.34 ± 9.39 , range = [9.25-43.26] were assessed. In the lesion close to the ventricles of the RRMS patient (red arrows), a mean T_1 z-score of 14.22 ± 7.74 , range = [3.78-33.74], and a mean T_2 z-score of 12.04 ± 6.72 , range = [1.71-27.54] were found.

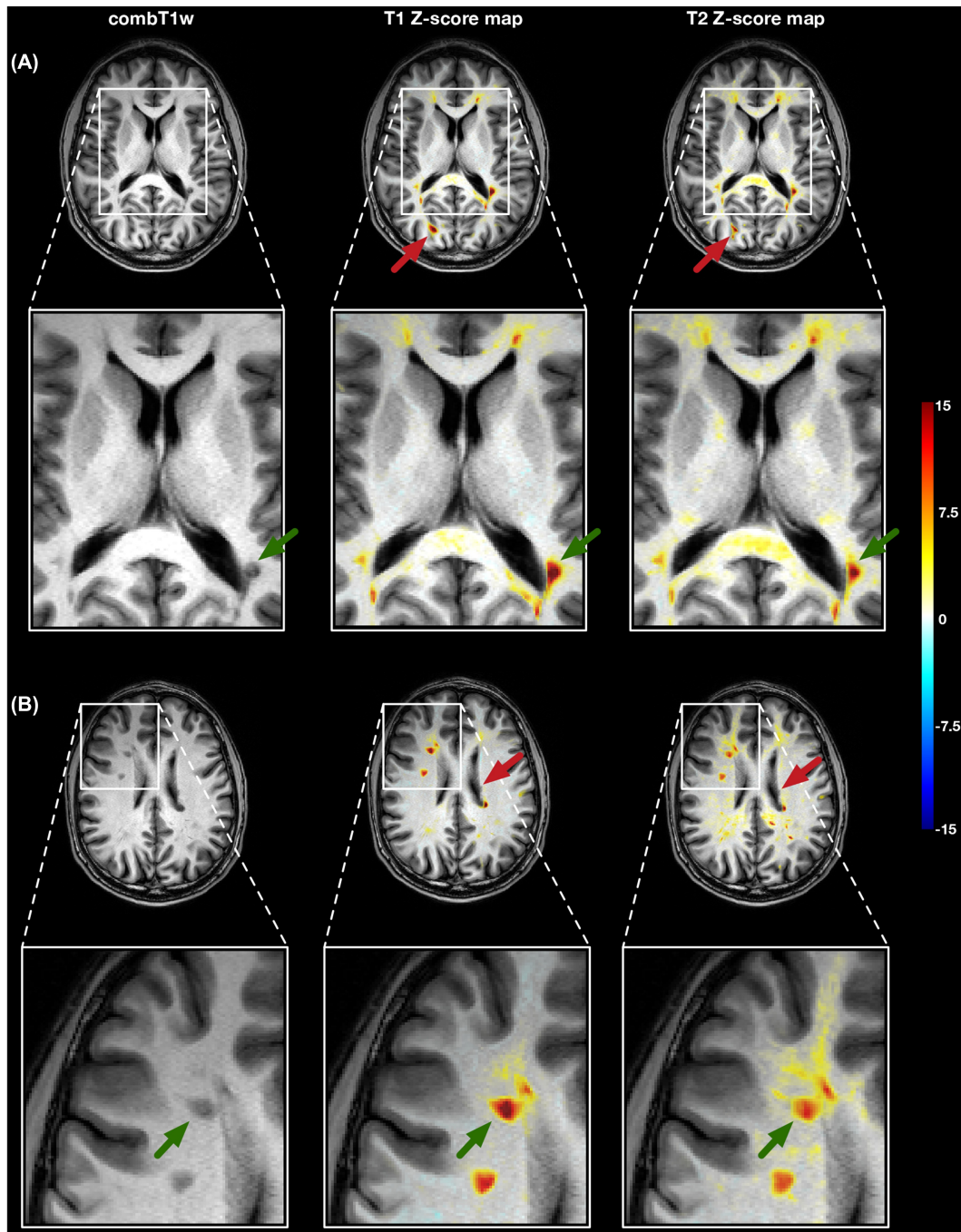


Figure 6.9 – Z-score maps resulting from a single subject comparison against voxel based population derived norms overlaid on a representative combined T_1 -weighted ($combT_1w$) axial slice for a patient diagnosed with clinically isolated syndrome (CIS, male, 31 y/o). In the pointed lesions (green arrows), it was found: (A) mean $z_{T_1} = 15.81 \pm 4.19$, range = [8.43-22.48]; mean $z_{T_2} = 11.59 \pm 2.75$, range = [7.21-16.92]; (B) mean $z_{T_1} = 10.73 \pm 3.34$, range = [4.32-16.61]; mean $z_{T_2} = 7.61 \pm 2.31$, range = [1.94-11.86]. In addition, more spread and subtle deviations of MR relaxation signal in tracks between lesions and in corpus callosum for T_2 (z-score deviations between 2-4) were found. A cluster of false positive voxels in the cortex is pointed out in (A) and a false negative can be seen in (B) (red arrows).

performed by the used tool is based on image intensities and would identify tissue alterations, such as MS lesions, as GM or CSF, hence excluding them from the analysis.

Contrary to the deviations shown in focal MS lesions, the cerebrospinal and interstitial fluids inside the EPVS revealed a higher T_2 deviation (mean $z_{T_2} = 27.34$) than T_1 (mean $z_{T_1} = 8.77$). This exemplifies that the use of z-scores as deviation measures allows relating the amplitude of the changes in T_1 and T_2 to each other; combining these “abnormality” metrics may therefore enable their use as biomarkers to classify different kinds of brain tissue alterations. For instance, previous attempts in the differentiation of active and non-active lesion by the means of relaxation times difference were only partially successful [38]. The quality of the quantitative maps and the coherence of the dataset built in this study may be of help in fulfilling this goal.

Previously established norms for brain relaxation times pooled values from different brain regions, missing the spatial specificity of a voxel-by-voxel atlases as established here, or were not further explored for single-subject comparisons [311, 316–318]. Moreover, in previously reported single-subject comparison studies based on relaxometry data, reference values were derived by averaging the respective tissue property across the entire HC [43, 44], as well as in other imaging studies based on diffusion [319] or MWI [320]. Conversely, our proposed method allows including confounding factors in the normative atlases such as sex and age of the subjects. Although quantitative MR aims at providing absolute measures, hardware differences across scanners and centers may result in small deviations in the acquired maps. An additional advantage of the proposed method is the possibility of easily extend the regression models to account for this additional variability. Whereas, in this study, all volumes were acquired with same scanner to reduce this potential influence, future work is focused on building such an extended atlas including data from other sites and validating that the added variability does not eclipse the effect of pathologies on relaxation times. Previous work indicates, however, that the used quantitative mapping sequences show low sensitivity to the hardware that was used [54, 255].

Notably, the T_1 and T_2 mapping protocol proposed in this work has a clinically acceptable acquisition time of 6:24 min that allows inclusion in clinical studies, potentially also in a clinical protocol. Furthermore, the maps and derived contrasts proved to be a reliable input for automatic brain image processing tools (e.g., TIV extraction, brain segmentation), therefore avoiding the need of an additional T_1 w image for this purpose. The used anisotropic resolution renders the images more prone to partial volume effects and corresponding post-processing steps more challenging, which prompted us to introduce an upsampling of the acquired volumes. The 2D (i.e., slice-selective) nature of the GRAPPATINI sequence impeded the acquisition of maps with isotropic resolution because a slice profile below 3 mm would induce strong stimulated echoes, prolong the acquisition time and lower the SNR. Therefore, the 3D MP2RAGE was matched in terms of brain coverage and resolution instead. Nevertheless, the short acquisition time and the high in-plane resolution ($0.7 \times 0.7 \text{ mm}^2$) constitutes a good compromise between whole brain coverage and an acquisition time compatible with clinical routine in this proof-of-concept work. Future work focuses on the development of a 3D version

of the LPM protocol that will be able to provide a 1 mm^3 isotropic resolution. Furthermore, the assumption behind the GRAPPATINI sequence of mono-exponentiality of the T_2 decays is simplistic as numerous studies have shown the multi-exponential nature of T_2 decays in brain tissues. However, the proposed T_2 mapping strategy has been proved to deliver maps in agreement with conventional techniques and with excellent reproducibility [54], as well as good sensitivity toward T_2 alterations caused by pathologies [305, 321, 322].

The main limitation of our current HC is the narrow age range of healthy subjects included in the study and restricts the use of the method to patients whose ages fall into this very range. Therefore, ongoing work aims at expanding the size and age range of the HC data set by including paediatric and elderly subjects. This will improve the modeling of T_1 and T_2 variability among healthy subjects, because previous studies showed that both sex and normal aging affect T_1 and T_2 values [311, 316–318]. Although sex and age were both used as predictors, the model was found to be significantly better than an intercept-only model only in a few clusters (in the caudate for T_1 , in pallidum and putamen for T_2) – notably within the limited age range of our HC. In clusters where relaxation times were found to be significantly affected by sex and age, T_1 and T_2 appear to decrease within the age range of the HC. This is in agreement with previous studies [311, 318], where it was demonstrated that the myelination process, in combination with iron deposition, shortens T_1 before the age of 40–50 y [323]. Furthermore, the decrease in free water with age due to the accumulation of macromolecules causes shorter T_2 .

Future work should also focus on a clinical validation including a microstructural interpretation of the observed alterations. The knowledge of the relationship between microstructural changes and quantitative values will add tremendous value to qMRI, leading toward the possibility of achieving what was coined in vivo histology using MRI [284]. To that end, additional quantitative measures sensitive to the microstructural integrity of WM that provide complementary information to relaxometry maps, such as MWF or MPF maps, may be considered for the method proposed here in the future.

6.5 Conclusion

Voxel-wise population-derived norms were established by modeling T_1 and T_2 distributions within a cohort of healthy subjects. The feasibility of single-subject comparisons in example case studies was examined, demonstrating the potential of the normative atlases in the detection and characterization of tissue alterations. Notably, the proposed method may allow the assessment of NAWM using qMRI acquisition protocols with clinically acceptable scan times. Therefore, the single-subject comparison to a quantitative atlas in combination with fast acquisition methods may increase the usefulness and facilitate the integration of qMRI techniques into the clinical realm.

7 Normal volumetric and T_1 relaxation time values at 1.5 T in segmented pediatric brain MRI using a MP2RAGE acquisition

The content of the following chapter is based on the postprint version of the article: “Normal volumetric and T_1 relaxation time values at 1.5 T in segmented pediatric brain MRI using a MP2RAGE acquisition” published in European Radiology [324]. DOI: [10.1007/s00330-020-07194-w](https://doi.org/10.1007/s00330-020-07194-w). The article was co-authored by Baptiste Morel, Jean-Philippe Cottier, Clovis Tauber, Christophe Destrieux, Tom Hilbert, Dominique Sirinelli, Jean-Philippe Thiran, Bénédicte Maréchal and Tobias Kober. Gian Franco Piredda and Baptiste Morel contributed equally to this work. The remaining co-authors contributed to the idea and reviewed the manuscript.

Abstract: This study introduced a tailored MP2RAGE-based brain acquisition for a comprehensive assessment of the normal maturing brain. Seventy normal patients (35 girls and 35 boys) from 1 to 16 years of age were recruited within a prospective monocentric study. Brain MRI examinations were performed at 1.5 T and an optimized 3D MP2RAGE sequence with a total acquisition time of 6:36 min. The automated segmentation of 38 brain regions was performed using the prototype software MorphoBox, which underwent a major adaptation of its T_1 -weighted anatomical template. Age-dependent models of normal brain maturation with respect to changes in volume and T_1 relaxometry were established using a logarithmic and a modified Gompertz growth model, respectively. After an initial rapid increase until 24 months of life, the total intracranial volume was found to converge towards 1400 mL during adolescence. The expected volumes of WM and cortical GM showed a similar trend with age. After an initial major decrease, T_1 relaxation times were observed to decrease progressively in all brain structures. The T_1 drop in the second year of life was more pronounced in WM (from 1000–1100 ms to 650–700 ms) than in GM structures. In conclusion, the 3D MP2RAGE sequence allowed establishing normative ranges of brain volumes and T_1 relaxation times in pediatrics, which will help to further identify, describe, and understand neurodevelopmental disorders in children.

7.1 Introduction

Maturation of the human central nervous system begins in utero and continues through adolescence, with the most dramatic changes occurring in the first few years of life. Similar patterns of brain development among individuals have been identified, which involve – among others – the myelination of WM and GM tissues, axonal pruning, gyrification of the brain cortex, and an increase in brain size [325]. Developmental delay and other neurological disorders have been associated with an atypical spatiotemporal maturation of brain tissues [326]. Although being a key component in the interpretation of pediatric brain MRI studies, the estimation of WM and GM volumes remains mainly subjective and qualitative in clinical practice, with moderate performance [327]. In addition, the interpretation of signal intensities is still challenging, as shown, for example, in the WM of neonatal brain MRI scans [328]. A quantitative characterization of normal brain maturation in children using MRI is thus of major interest.

Methods developed in adults for automated volumetric brain segmentation need to be adapted to work on younger subjects due to, for instance, the “inverted” different brain parenchyma contrasts before 2 years of age [329] and anatomical differences, which in turn required the establishment of new anatomical templates [330]. Nowadays, several methods exist to study quantitative volumetric data for various brain structures, mainly in adults [58, 331, 332], in pediatrics [333–335], or in neonates [336]. Brain structure parcellation in children relies on morphological [335], statistical [337], or qMRI-based [331, 338, 339] approaches. However, limited sample sizes of patients were employed during the first few years of life. With regards to relaxometry, previous studies measured relaxation times for several specific brain structures (basal ganglia, GM, WM, hippocampus, among others), yet only recruiting cohorts with limited age ranges and never for the entire childhood [255, 338, 340–344]. In addition, sequences with long acquisition times are often needed, rendering them impractical for daily clinical practice.

In view of that, this chapter aimed at automatically assessing brain volumetry and T_1 relaxometry during development with the MP2RAGE sequence [16] (see **Section 2.3.1** in Chapter 2), which provides a clinically compatible acquisition. The MP2RAGE sequence proved to result in a high repeatability for the segmentation of brain regions, particularly for subcortical structures [345], and for the quantification of T_1 relaxation times [346]. The MP2RAGE sequence may thus constitute a promising imaging technique to help analyze brain maturation in a pediatric population, yet the rapid morphological and microstructural tissue changes occurring during development necessitate the adaptation of the MR sequence parameters as well as dedicated post-processing to reduce potential errors and minimize bias.

In this work, three age-group templates were adapted for the pediatric brain segmentation to obtain detailed anatomy, morphometry, and T_1 relaxometry information of main structures. As an application, we determined the normal ranges of brain volumes and T_1 relaxation times in vivo depending on age.

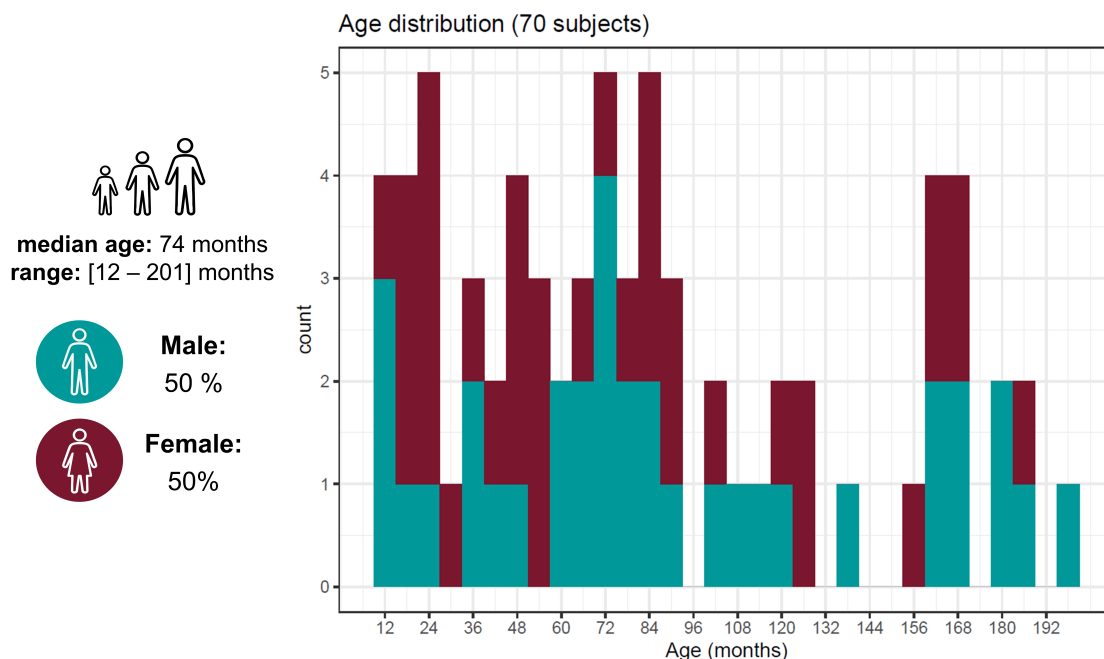


Figure 7.1 – Demographics of the healthy subjects considered in this study for modeling the evolution with age of regional brain volumes and T_1 values.

7.2 Material and methods

7.2.1 Study population

A prospective monocentric study was conducted recruiting 70 children with an original indication of an isolated headache without neurological symptoms that showed a spontaneously favourable evolution. Normal clinical follow-up was conducted at least for one year. The study population was composed of 35 males and 35 females (see detailed demographics in Figure 7.1). Three age groups were defined: from 1 to 2 years (10 subjects), 2 to 8 years (37 subjects), and 8 to 16 years (23 subjects). Approval was received by the local Ethics Committee in Human research (RNI-2017-093). All the children's parents gave informed consent.

Clinical exclusion criteria for this study were identified pathologies in the brain, prior intracranial operation, known developmental delay in language or motor domains, autism spectrum disorder, chronic epilepsy, significant prematurity (younger than 34 weeks GA at delivery), significant macrocephaly (head circumference > 97th percentile), significant microcephaly (head circumference < 3rd percentile), hydrocephalus, suspected or proven genetic abnormalities, and genetic dispositions known to be involved in abnormal brain development. Imaging exclusion criteria were the presence of motion and/or susceptibility artifacts in the MP2RAGE UNI contrast. Artifacts were ruled out independently by two observers.

7.2.2 Image acquisition

All patients were scanned at 1.5 T (MAGNETOM Aera, Siemens Healthcare, Erlangen, Germany) using a 20-channel head coil without general anaesthesia. Intrarectal pentobarbital (5 mg/kg) has been delivered in children requiring sedation. Whole brain imaging was achieved with the MP2RAGE sequence using acquisition parameters tailored to pediatric applications (resolution = $1.33 \times 1.33 \times 1.25 \text{ mm}^3$, FOV = $256 \times 240 \text{ mm}^2$, TI1/TI2 = 600/2000 ms, flip angles = $5\text{--}6^\circ$, TR = 5000 ms, TA = 6:36 min).

7.2.3 Image processing

Automated brain segmentation was performed using the MorphoBox prototype [58] which underwent a major adaptation of its T_1 -weighted template. Three age-appropriate T_1 -weighted templates were generated for each age group including 10 subjects aged 1–2 years, 37 subjects aged 2–8 years, and 23 subjects aged 8–16 years. The considered T_1 -weighted contrast was obtained by multiplying the MP2RAGE GRE₂ and UNI images to remove the salt-and-pepper noise outside the head and in proximity of cortical GM structures [59]. Templates were built using an iterative method, requiring N non-linear registrations [64, 347] to be performed at each iteration, where N is the number of normal subjects. A voxel-wise average across subjects was used as an initial reference target volume. This target volume was updated after each iteration by a voxel-wise average across the N registered volumes. A total of 38 anatomical classes were drawn by a pediatric neuroradiologist on the three resulting templates and consensus was obtained with two other neuroradiologists according to the standard anatomical nomenclature. These templates were included in the MorphoBox pipeline, substituting the adult template. Apart from this change, the MorphoBox pipeline was used in its original form to segment the 70 pediatric datasets automatically. Regional volumes and average T_1 relaxation values were then calculated from each segmentation mask.

7.2.4 Qualitative segmentation validation assessment

A qualitative assessment of the segmentation quality was performed independently by two experts (7 and 8 years of experience). The validation procedure consisted in verifying the following criteria:

- assessment of image quality;
- assessment of movement artifact;
- assessment of errors in intracranial volume segmentation: checking whether the intracranial volume is correctly segmented, i.e., no skull is included, and no brain parenchyma is excluded from the segmented brain region;
- assessment of appropriate anatomic coverage: the tissue segmentation was overlaid onto the MP2RAGE image to verify that the boundaries between WM, GM, and CSF corresponded to actual tissue boundaries in the image contrast.

The parcellation of the brain was verified by visually comparing the subjects' individual brain parcellation to the parcellation of the template.

7.2.5 Normative data modeling

Reference ranges accounting for the normal evolution of brain volumes (V) with age were established for each region (\mathbf{r}) using a logarithmic model:

$$\mathbb{E}\{V(\mathbf{r})\} = \beta_0(\mathbf{r}) + \beta_1(\mathbf{r}) \cdot \log(\text{age}) , \quad (7.1)$$

with β_0 being the model intercept and β_1 the coefficient pertaining to the age effect.

A modified Gompertz growth model was used to establish reference ranges for T_1 values:

$$\mathbb{E}\{T_1(\mathbf{r})\} = \beta_0(\mathbf{r}) e^{e^{-\beta_1(\mathbf{r}) \cdot \text{age}} - \beta_2(\mathbf{r}) \cdot \text{age}} , \quad (7.2)$$

with β_0 corresponding to the T_1 at the transition between the two different growth states, β_1 the growth rate during the fast development in the first years of life, and β_2 the growth rate during the following slower development. A Shapiro-Wilk test was employed in both cases to investigate whether fitting residuals were normally distributed. Resulting P -values smaller than 0.05 were considered to reject normality after Bonferroni's correction for multiple comparisons.

7.3 Results

7.3.1 Image processing

A reduction of blurriness and enhanced definition of tissue boundaries were observed after each iteration during the template creation in each age group (Figure 7.2).

Using these age-appropriate templates, brain segmentation was successfully achieved in all 70 normal subjects according to the quality assessment defined in the "Material and methods" section. Axial slices of the acquired MP2RAGE T_1 -weighted images and T_1 maps, along with the corresponding segmentation masks are shown in Figure 7.3 for five subjects of different age.

7.3.2 Development of brain volumes

Normal evolutions during development of various brain structure volumes are reported in Figure 7.4, Figure 7.5, Figure 7.6 and Figure 7.7.

The total intracranial volume was found to rapidly increase between 12 and 24 months, then with a slower and progressively smaller rate, reaching a value of approximately 1400 mL in

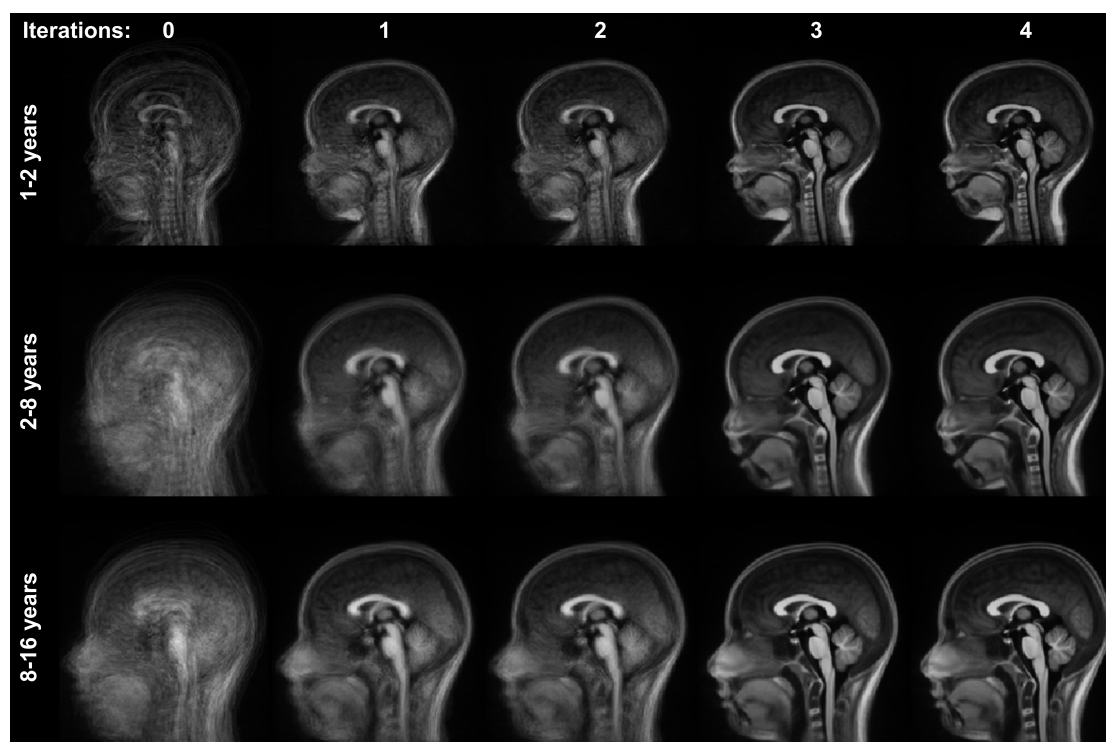


Figure 7.2 – T_1 -weighted anatomical template building process over four iterations (left-right) and for the considered three age groups (top-bottom).

early adolescence (Figure 7.4). A continuous increase throughout the age range of the study population was observed also for the WM volume, reaching a value of 400 mL in adolescence (Figure 7.4). Lobe-wise, a slightly more accentuated increase of frontal lobe WM volume was observed with respect to other lobes (Figure 7.5). The GM volume (including deep and cortical GM) increased rapidly during the first 24–48 months of life as well, yet with an overall change that is less evident than that of WM and mostly driven by the expansion of the temporal lobe GM (Figure 7.5). A maximum absolute volume of cortical GM of 600 mL is reached between 4 and 5 years of age.

Basal ganglia volumes were estimated to vary from 35 mL at 1 year of life to around 60 mL at 16 years. Thalami volume was found to change from 10 mL to 19 mL. Hippocampus volume was estimated to vary from 3.5 mL to 7 mL. Cerebellum GM volumes were from 80 mL to 140 mL and WM from 10 mL to 25 mL. Corpus callosum volume undergoes a slow increase from 1 mL to 2.5 mL. Brainstem volumes were estimated to enlarge from 15 mL to 40 mL (Figure 7.6).

Values of intraventricular CSF volume demonstrated relative stability throughout childhood. Lateral ventricle volumes were estimated to vary between 5 mL and 30 mL, the third ventricle between 2 mL and 5 mL, and the fourth ventricle from 1 mL to 4mL (Figure 7.7).

Residuals of the established models were found to be distributed normally for all brain regions.

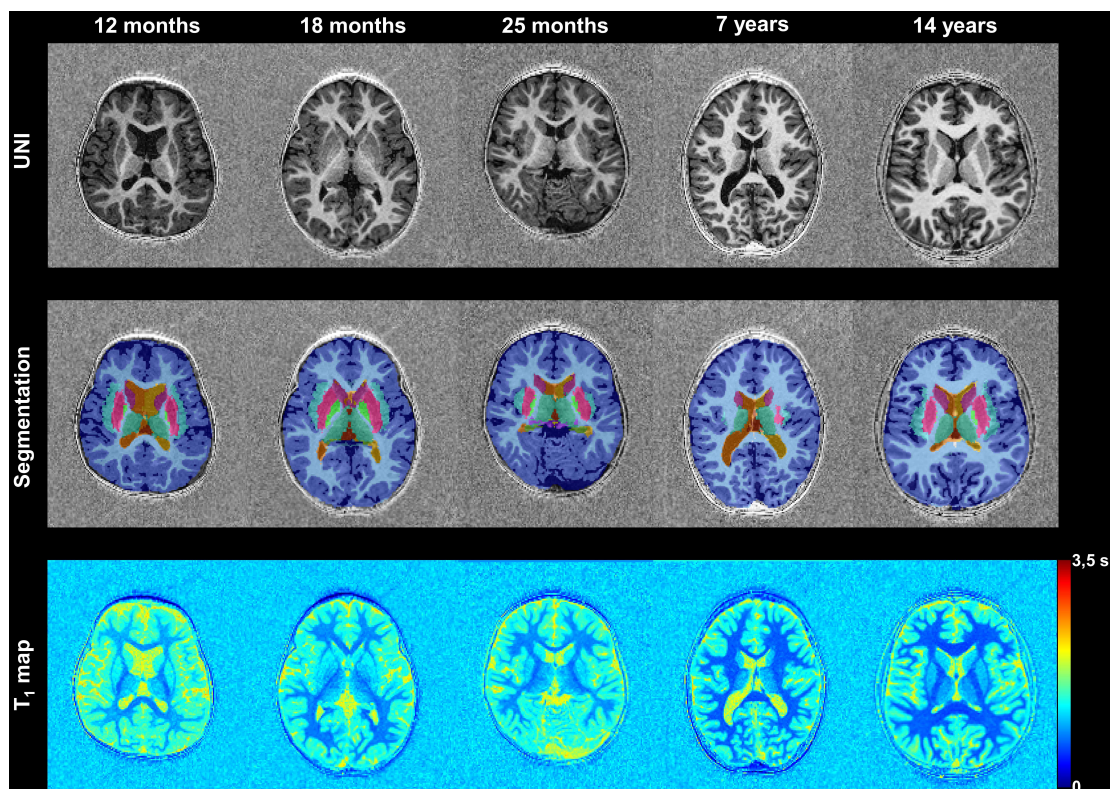


Figure 7.3 – Representative axial slices of MP2RAGE uniform (UNI) T_1 -weighted contrast (top), corresponding segmentation masks (middle) and T_1 maps (bottom) of five randomly picked male subjects with increasing age (left to right).

7.3.3 Evolution of relaxation times

The normal evolution of T_1 relaxation times for the segmented structures with development is reported in Figure 7.8 and Figure 7.9.

After an initial major decrease of T_1 between 12 and 24 months of life, a steady and less rapid decrease was observed in all brain structures. The T_1 drop in the first year of life was more pronounced in WM than in GM structures (Figure 7.8), most likely due to the myelination of WM. Throughout the development of brain tissues with age, T_1 values were found to decrease from 1400–1500 to 1100–1200 ms in cortical GM structures and from 1000–1100 to 650–700 ms in WM structures (Figure 7.9). In other subcortical structures, T_1 values were found to decrease from 1200 to 900 ms in the basal ganglia and from 1100 to 850 in the brainstem.

Residuals of the established models were found to be normally distributed for all brain regions except for occipital WM, cerebellum, amygdala, and brainstem.

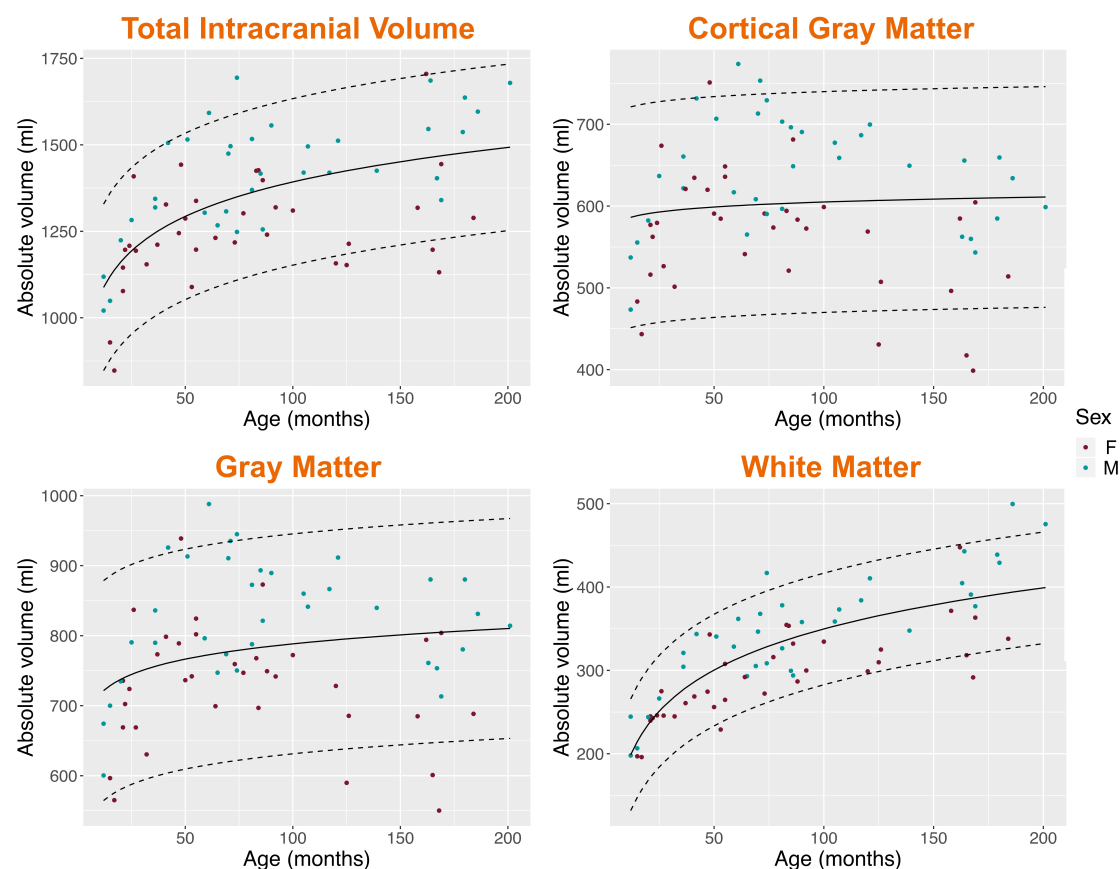


Figure 7.4 – Normal evolution from 1 to 16 years of age of the total intracranial volume, cortical gray matter, whole gray matter, and white matter volumes.

7.4 Discussion

This study introduced a framework of an optimized MR sequence and subsequent image processing to automatically measure regional volumes and T_1 relaxation times in 38 brain structures in children. Reference courses of these quantitative measurements in the 1-to-16-year age range were established and found to be similar to trends observed in previous studies.

An automated quantitative brain segmentation that enables longitudinal tracking and comparison with normative reference ranges of brain volumes is of major interest [338]. As many diseases lead to focal parenchymal abnormalities that would not be detected by whole brain volumetric analysis alone, the possibility to analyze brain structures both in their entirety and region-wise is desirable. To that end, the findings of this study will be most advantageous in the assessment of diffuse and focal disease processes.

Considering the main brain structures, the volumes obtained with the automated segmentation in this study were in full accordance to previously reported data [331, 337, 339, 348], especially with the study conducted by Courchesne et al. [339] and the NIH MRI study of nor-

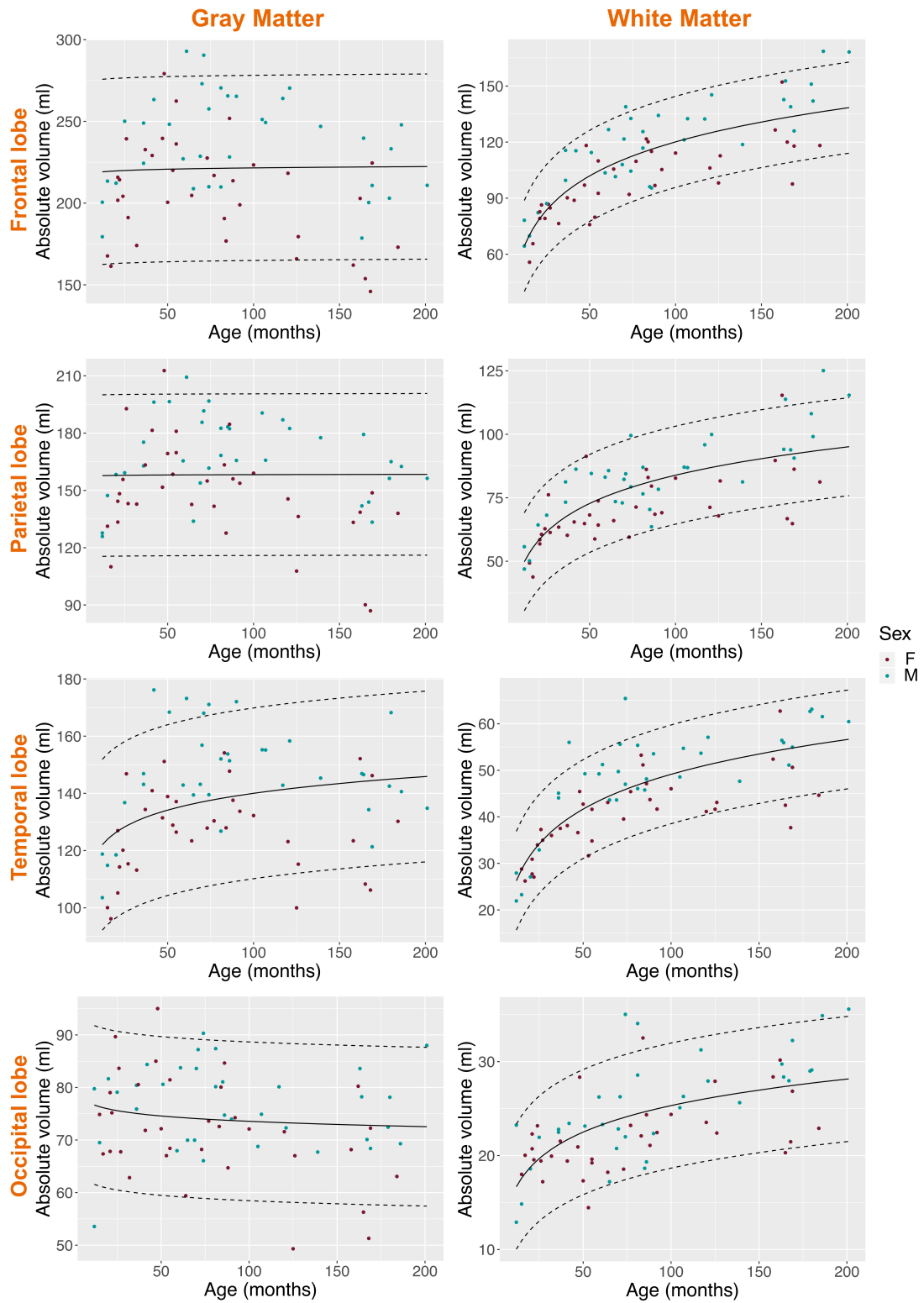


Figure 7.5 – Normal evolution from 1 to 16 years of age of the cortical gray matter and white matter volumes with respect to brain lobes.

Chapter 7. Normal volumetric and T_1 relaxation time values at 1.5 T in segmented pediatric brain MRI using a MP2RAGE acquisition

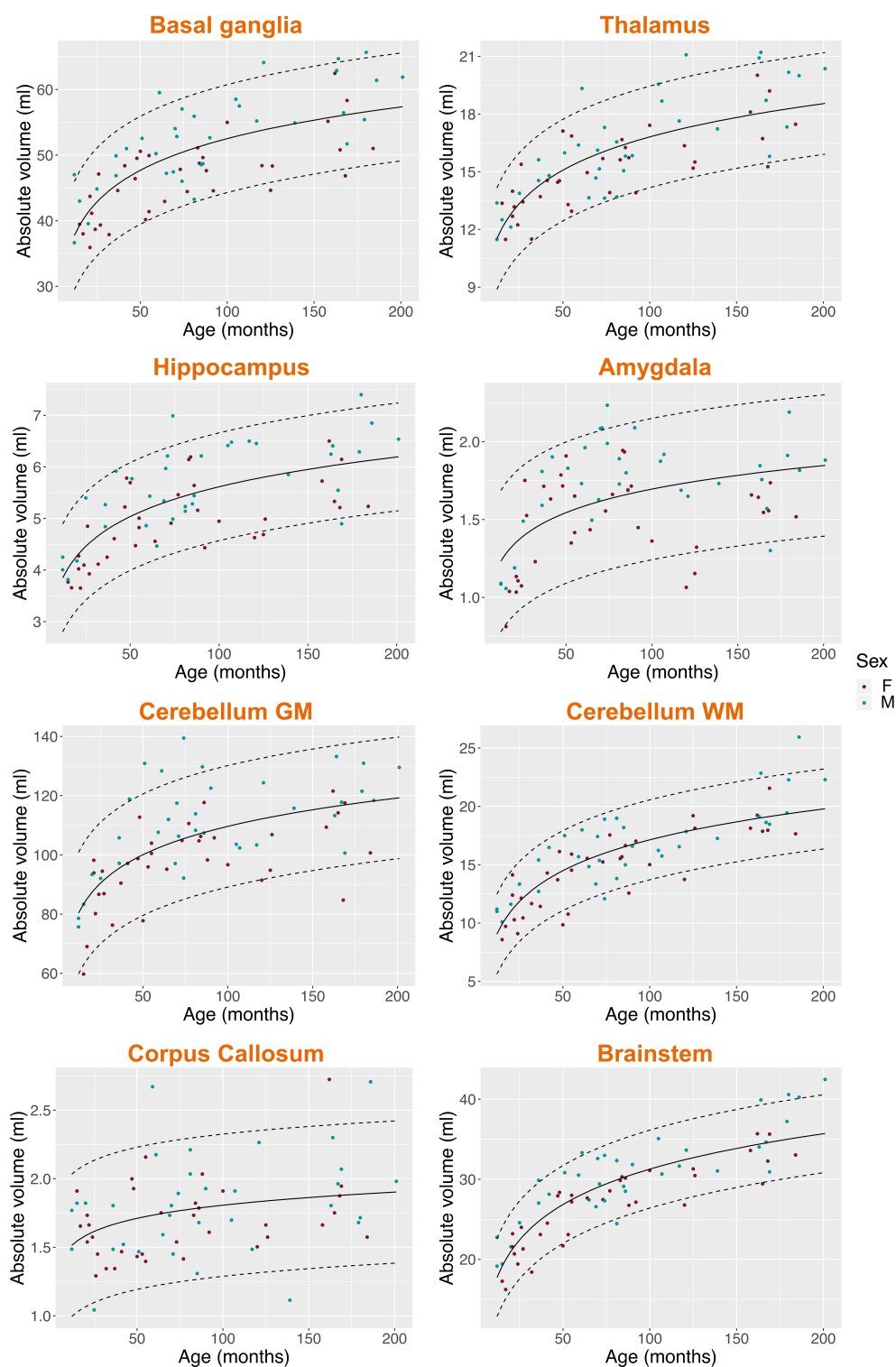


Figure 7.6 – Normal evolution from 1 to 16 years of age of the basal ganglia, thalamus, hippocampus, amygdala, cerebellum gray matter (GM) and white matter (WM), corpus callosum, and brainstem volumes.

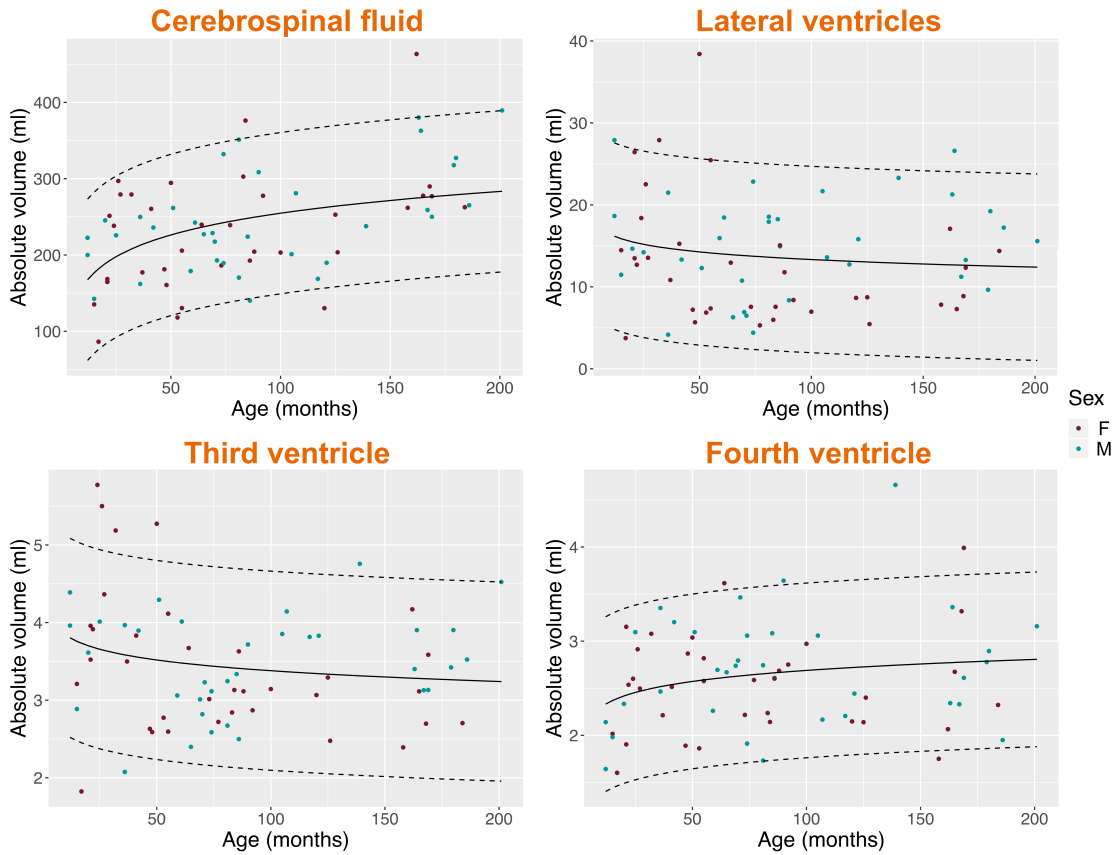


Figure 7.7 – Normal evolution from 1 to 16 years of age of the cerebrospinal fluid, lateral ventricle, third ventricle, and fourth ventricle volumes.

mal brain development [348]. The latter reported a rapid increase in the first 24 months, then with a progressively smaller and slower rate, reaching a value of 1400 mL in early adolescence, which was also found here. Similarly, the WM converged to a volume value of 400 mL in early adolescence, comparing well with the 475 mL reported in the NIH cohort [348].

A maximum absolute GM volume of 800 mL was found to be reached between 4 and 5 years of age, much earlier than in the study conducted by McAllister et al. [338], yet similar to what was shown by Serai et al. [337] and to the value of 787 mL reported in the NIH cohort [348]. Of note, a gradual decline throughout the teenage years was not observed as previously shown [338]. These discrepancies could be explained by the employed model for volumetry (see Eq. 7.2) and partially by differences in the employed segmentation algorithms. Future work should focus on studying the evolution of brain volumes by using different models depending on the brain structure under investigation.

Further analysis focused on more detailed parcellation of subcortical structures (basal ganglia, thalami, corpus callosum, and cerebellum, among others) whose volumes were confirmed to increase during childhood. When comparing these specific brain structures, volumes obtained in our study were found very similar to those reported in the NIH cohort [348].

Chapter 7. Normal volumetric and T_1 relaxation time values at 1.5 T in segmented pediatric brain MRI using a MP2RAGE acquisition

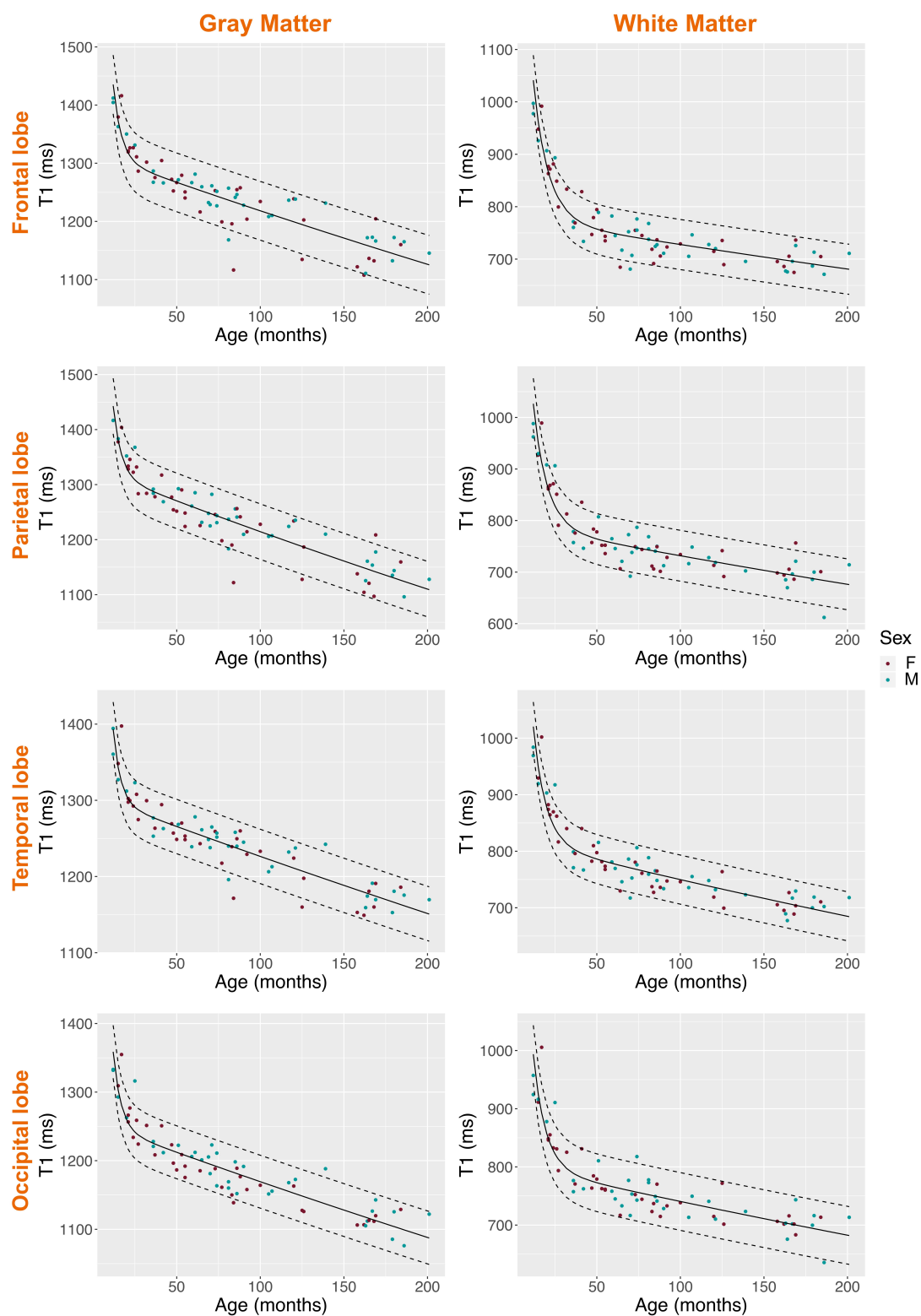


Figure 7.8 – Normal evolution from 1 to 16 years of age of the cortical gray matter and white matter T_1 relaxation times depending on brain lobes.

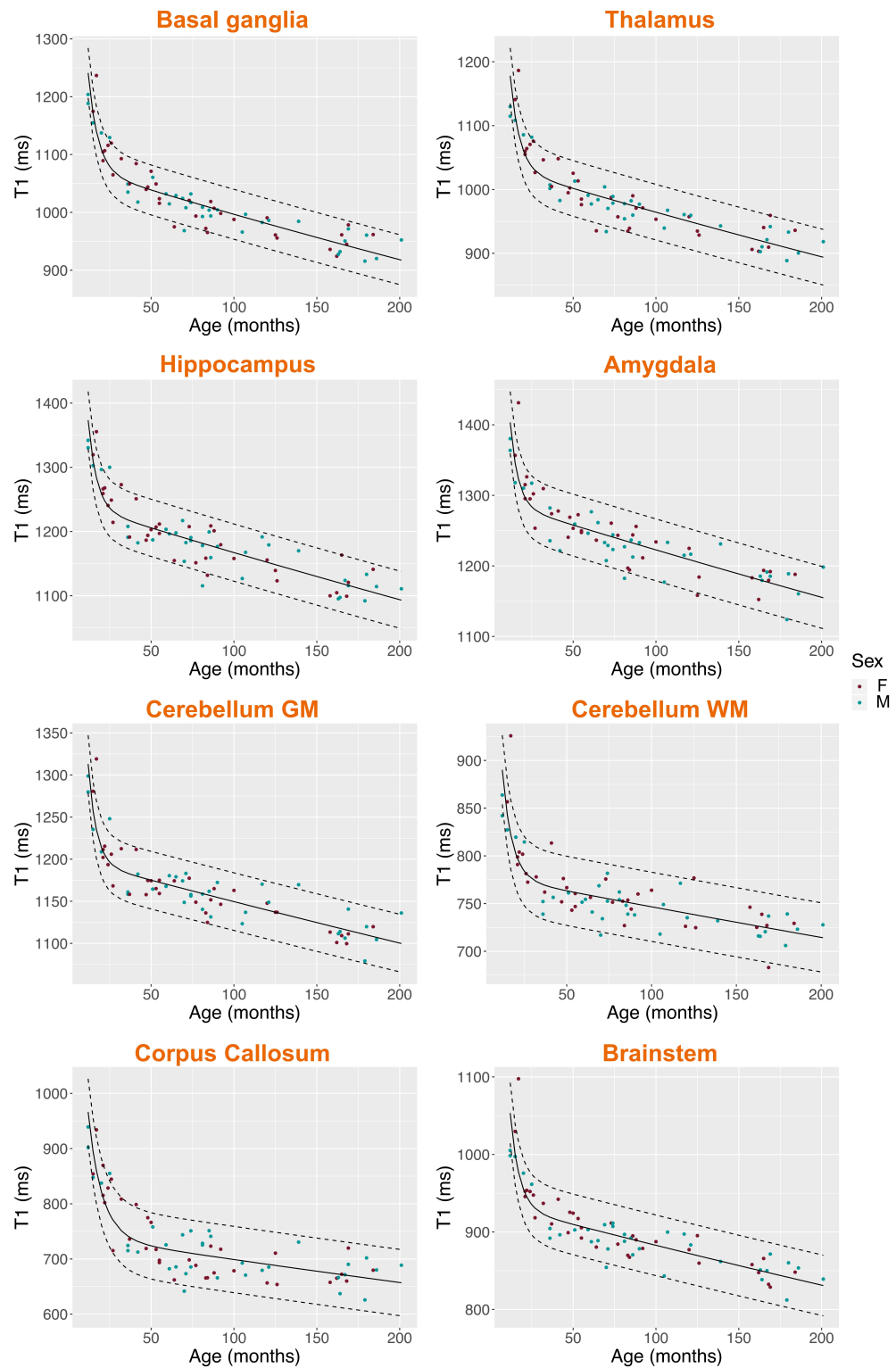


Figure 7.9 – Normal evolution from 1 to 16 years of age of the basal ganglia, thalamus, hippocampus, amygdala, cerebellum gray matter (GM) and white matter (WM), corpus callosum, and brainstem T₁ relaxation times.

Chapter 7. Normal volumetric and T_1 relaxation time values at 1.5 T in segmented pediatric brain MRI using a MP2RAGE acquisition

The normative range values might be relevant to explore the volumetric data further in patients with microcephaly and macrocephaly and distinguish the affected brain structures better. Obtaining these data in pediatric patients with focal epilepsy in context of focal cortical dysplasia might help in screening and determining the pathological area and its impact on the total or lobar brain volumes, as it has been studied in adults [349, 350]. Volumetric data would also be helpful in the follow-up of patients with hydrocephaly.

The employed MP2RAGE sequence has the additional advantage of providing T_1 relaxometry maps for the assessment of microstructural changes related to brain maturation. A rapid decrease of T_1 values was observed between 12 and 24 months of life, with a subsequent steady yet less rapid progression in all lobes and the supra- and infratentorial brain structures. This drop in T_1 was more pronounced in WM than in GM structures, most likely due to myelination processes occurring in WM tissues [359]. The initial high water content of the brain is indeed progressively replaced by myelin. The reported expected T_1 values of GM and WM were found to be in the same range as previously reported. For example, T_1 values in the parietal WM were between 700 ms and 1000 ms, in accordance with values estimated in previous studies, 833 ms in the study conducted by Chen et al. [259] and between 800 ms and 1000 ms in the study by Eminian et al. [340].

The characterization of healthy brain maturation that has been derived in this chapter would be helpful for further assessment of a variety of neurodevelopmental disorders as deviations from normal growth trajectories [288]. Age-related changes in T_1 relaxation time have been described by location in GM and WM in healthy adults [346]. Additionally, it would be useful during the interpretation of “morphologically normal” brain MRI images during exploration of focal epilepsy or mental retardation [327]. The fact that two metrics (volumetry and T_1 relaxometry) can be combined to characterize a given brain region should give additional specificity to the comparison: volumetry thereby measuring brain growth and T_1 relaxometry probing the tissue microstructure at the same time. T_1 relaxation may help to better identify biomarkers related to a retard in myelination or to depict metabolic pathologies. The determination of volume and T_1 relaxation times of brain structures only reflected a partial aspect of the MR-based brain tissue characterization. More advanced techniques as MR fingerprinting are currently being developed to quantify multiple tissue properties simultaneously (T_1 , T_2 , MT, among others) [25, 261]. However, even though the recent integration of parallel imaging and deep learning-based reconstruction techniques can reduce acquisition time (~7 min in adults), MR fingerprinting acquisitions are not yet established in pediatric clinical use [300].

The proposed approach has the advantage of being fast, accurate, and reproducible, but may possibly give slightly less accurate results than a careful manual delineation of the structures of interest. The same subjects were used for both building the templates and getting the regional values, which could have led to improve our segmentation results. It also has influenced the building of the template with a heterogeneity of the number of subjects in each age group. Although respectable, the sample size of 70 normal subjects was smaller in comparison with those used for the development of the CDC growth charts or in head circumference [351].

Larger sample sizes may well define percentiles with appropriate precision particularly for the outlying percentiles [352]. Moreover, our normal subjects were only representative of a sample of our regional population of mainly Caucasian people. So, the established normative ranges will probably have to be adapted to a population with different genetic traits and/or environmental/epigenetic exposures [353,354].

It should be noted that we have not performed a repeatability study on a pediatric cohort to characterize the stability of the proposed analyses. This was considered prohibitive as MRI exams are considerably more stressful for children than for adults [355]. Nonetheless, the employed morphometric algorithm with the adult template has been used in multiple research studies and is well characterized in terms of performance and quality metrics. A complementary test-retest reproducibility study has shown a high reliability for every region [345]. Brain volumetry repeatability has shown a high reproducibility and MP2RAGE was the most reliable for sub-cortical structures [345]. Finally, results must be confirmed by a larger prospective multi-centric study to validate the possibility of extending the use of the established norms to different centers. Corresponding norms at higher field strengths (e.g., 3 T MRI) should also be established as T_1 values naturally differ with field strength.

WM changes were observed to be fast during the first 2 years of life. This phenomenon suggests that the anatomical templates used for segmentation should probably be split by semester or trimester to adapt to this fast development better. This especially concerns the segmentation and determination of T_1 values of the termination areas of myelination.

A clinical evaluation to assess the performance of the established framework for the detection and characterization of different brain pathologies is currently ongoing. For instance, in patients with suspected focal epilepsy of unknown cause, the presence of volumetric and T_1 relaxometry deviations from the normal cohort may allow describing brain abnormalities undetected in conventional MRI [356].

7.5 Conclusion

A 3D MP2RAGE acquisition tailored for pediatric applications was here proposed and investigated to establish a fully automated processing pipeline to evaluate volumetric and T_1 changes between 1 and 16 years of age based on a large pediatric cohort of normal subjects. This objective assessment of brain evolution during childhood provided by this framework might help to further identify, describe, and understand neurodevelopmental disorders in children.

8 Conclusions, scientific and clinical impact

The main goal of this thesis was to advance the field of relaxometry and myelin water imaging in order to bring qMRI closer to the clinical application. To that end, novel techniques were developed addressing scientific questions spanning from the very image acquisition to analysis and application of the acquired data. Additionally, some of the developed methods were further investigated and validated with scientific and clinical partners by exploiting the interconnected environment in which this thesis was realized. This chapter summarizes the main contributions and additional projects conducted together with these collaboration partners. The thesis concludes with possible future research directions.

8.1 Main contributions

8.1.1 Myelin water imaging

A multi-echo GRASE sequence for sampling T_2 decays was accelerated by combining it with CAIPIRINHA undersampling [85] (see **Chapter 4**). In vivo experiments showed that the proposed sequence yields MWF maps comparable with those derived from a reference MESE sequence ($r = 0.83$, mean bias = -0.20%), while providing increased brain coverage (multi-echo GRASE: $1.6 \times 1.6 \times 1.6 \text{ mm}^3$, 84 slices; MESE: $1 \times 1 \times 3 \text{ mm}^3$, single slice) in an acquisition time of 10:30 min. Compared to the state-of-art 3D multi-echo GRASE acquisition for MWI [80] ($1 \times 1 \times 5 \text{ mm}^3$, 20 slices, TA = 14.4 min), we demonstrated the feasibility of obtaining MWF with higher resolution and brain coverage but reduced acquisition time when employing a $3 \times 2^{(1)}$ CAIPIRINHA undersampling pattern. The increased resolution and shortened scan time may help to facilitate the wide-spread use of MWI in clinical research to validate the proposed sequence as a practical alternative to time-consuming MESE acquisitions. To that end, the implemented sequence has been made available as a prototype on Siemens Healthineers scanners and was distributed to 14 research sites.

8.1.2 Learning tissue microstructure from relaxometry

In search of alternative and less conventional methods to further accelerate MWI, a data-driven estimation of brain myelin water content from single-compartment relaxometry measurements was proposed in this thesis (see **Chapter 5**). More specifically, the direct estimation of MWF maps derived from a reference MESE sequence was investigated from T_1 and T_2 relaxometry measurements. To that end, three different modeling strategies were explored, which proved the feasibility of estimating MWF maps from relaxometry and confirmed the hypothesis at the basis of this study that brain myelin water content information is engrained in relaxometry measurements. Among the different modeling strategies, the cGAN produced MWF maps with the best agreement to reference values (bias 0.01%, LoA = [-3.13; 3.16]%). The data suggested that fast relaxometry like the 6:24 minutes whole brain protocol used in this work in conjunction with machine learning may thus have the potential to replace time-consuming MESE acquisitions. Furthermore, MWF may be calculated retrospectively for studies that only acquired T_1 and T_2 maps.

8.1.3 Characterization of abnormal tissues

This thesis introduced a method for personalized detection and characterization of brain abnormalities causing alterations of relaxation times [288] (see **Chapter 6**). Voxel-wise population-derived norms were established by modeling T_1 and T_2 inter-subject variability within a healthy cohort and proved valuable in revealing tissue deviations from the normative atlases in single-subject comparisons. The possibility of detecting subtle alterations that are not visible in conventional MRI showed the method clinical potential. Therefore, the proposed comparison to a quantitative atlas on a single-subject basis in combination with fast acquisition methods may increase the usefulness and facilitate the integration of qMRI techniques into the clinical realm.

8.2 Scientific and clinical collaborations

To further leverage the impact and usefulness of the developed methods, multiple research collaborations were conducted during the course of this thesis. Together with the respective collaboration partner, this opened up different lines of research, both advancing the methods and validating the proposed techniques in the clinics. The following subsections briefly describe the larger projects in that direction.

8.2.1 Myelin water imaging

In collaboration with the UPHUMMEL laboratory of the École Polytechnique Fédérale de Lausanne, a repeatability and reproducibility study has been designed to further validate the MWF maps derived from the developed multi-GRASE sequence. Twenty healthy subjects were

scanned twice (at least two weeks apart) in two different locations using the same 3 T scanners (MAGNETOM Prisma, Siemens Healthcare, Erlangen, Germany) at the Clinique Romande de Réadaptation in Sion and at the Campus Biotech in Geneva. For each time point, a scan-rescan session was held, yielding a total of eight acquisitions per subject. The repeatability of the MWF maps will be tested by comparing the scan-rescan datasets acquired during the same time point; the reproducibility will be tested by comparing the acquisitions of the different time points and in the two different centers.

In addition to the development of the multi-echo GRASE sequence, technical improvements have been proposed to enhance the reconstruction of the MWF maps from the acquired T_2 decays. First, in the study by Canales-Rodríguez et al. [273], to which the author of this thesis contributed, a comprehensive comparison of different methods used to retrieve MWF maps from T_2 relaxometry was conducted. In fact, several approaches can be found in the literature to solve this inverse problem, comprising well-established methods such as NNLS optimization with first- and second-order Tikhonov regularizations in addition to several criteria to select the regularization weight (e.g., L-curve, Generalized Cross-Validation, Chi-square residual fitting, among others). However, a quantitative comparison among the different approaches was missing. Based on our results, a list of recommendations was provided to help deciding which method is most suitable for a specific clinical application. All the evaluated algorithms are also available at <https://github.com/ejcanalesr/multicomponent-T2-toolbox> to foster the use of MWF in clinical practice and reproducible results in open science. Additionally, the author of this thesis contributed to the work by Yu et al. [357], where a model-informed machine learning (MIML) approach was proposed for multicomponent T_2 relaxometry in brain tissues by using a multi-layer perceptron. Compared to more established methods, MIML provided more accurate and noise-robust distributions in synthetic data, showed the highest correlation to a histological map of myelin volume and a better contrast between lesions and normal appearing tissues in MS patients. Furthermore, MIML reconstructions proved to be 22 to 4980 times faster than those performed with non-parametric and parametric methods, respectively.

The developed sequence and reconstruction are now distributed and acquired in patients in several imaging centers. In one of the first clinical applications, multicomponent T_2 relaxometry from the multi-echo GRASE data and multicompartiment diffusion were combined to perform the classification of abnormal tissues in MS patients [358]. Results showed that multi-modal features allow to characterize and classify abnormal tissue otherwise considered as non-lesional in MS patients.

8.2.2 Characterization of abnormal tissues

The narrow age range of our cohort represents the main limitation of the established atlases and restricts the use of the method to patients whose ages fall into this very range (21-48 years). Therefore, additional studies have been carried out aiming at expanding the size and

Chapter 8. Conclusions, scientific and clinical impact

age range of the dataset with two main collaborations.

Within the China 2020 project, 997 subjects were scanned in eleven different centers in China using the LPM protocol, but with a 1 mm³ isotropic resolution MP2RAGE. Normative atlases of relaxation times in the brain were established and validated from – to the best of the authors' knowledge – the largest healthy T₁ and T₂ relaxometry cohort today, covering a comprehensive age range (19-72 years) [359]. Additionally, the reproducibility of the employed relaxometry techniques across the enrolled sites was validated by comparing maps acquired from three subjects that were scanned in nine participating centers. The intraclass correlation coefficients ICC(2,1) among average T₁ and T₂ values within brain regions of interest were found to be higher than 0.99 for T₁, and above 0.90 for T₂, demonstrating the good reproducibility of the employed techniques for relaxometry [359].

In collaboration with the Paediatric Radiology Department of the Clocheville Hospital (CHRU Tours, France), age-dependent models of normal brain maturation in the 1-to-16-year age range were established with respect to changes in volume and T₁ relaxometry [324] (see **Chapter 7**). This study introduced a framework that, based on an optimized MP2RAGE acquisition for pediatric cohorts, automatically assesses regional volumes and T₁ relaxation times in 38 brain structures. To that end, automated brain morphometry was adapted to comply with the different brain sizes during development. Of interest, a rapid decrease of T₁ values was observed between 12 and 24 months of life, with a subsequent steady yet less rapid progression in all brain structures. This drop in T₁ was more pronounced in WM than in GM structures, most likely due to myelination processes occurring in WM tissues. This objective assessment of brain evolution during childhood will help to further identify, describe, and understand neurodevelopmental disorders in children.

First clinical applications of the developed method are currently being explored. For example, we are investigating the usefulness of T₁ z-scores in explaining clinical outcomes of MS patients in collaboration with the Department of Radiology of the Charles University and General University Hospital (Prague, Poland) [360–364]. To that end, a normative atlas of T₁ values was built from 92 healthy controls (60 females, age = [21-59] y/o) and T₁ z-scores were computed in two cohorts of 47 early (i.e., on disease onset) MS patients (35 females, age = [19-50] y/o, median Expanded Disability Status Scale (EDSS) = 2.0 [0-4]) and 52 progressive MS patients (43 females, age = [35-64] y/o, median EDSS = 5.5 [3.5-6.5]). We then compared the correlation between the EDSS and more conventional MRI-based radiological measures, i.e. lesion volume and count, against correlations with T₁ z-score derived metrics in lesions and NAWM, namely the volume of voxels exceeding a given z-score threshold [361]. Spearman's ρ correlations between EDSS, lesion volume and lesion count were found to be 0.23 and 0.18, respectively. Higher correlations were found between EDSS and z-score derived metrics, with the highest correlation found when considering absolute z-scores in the NAWM of the occipital lobe ($\rho = 0.47$). Additionally, we extended the method by evaluating tract-specific T₁ z-scores, with values in the NAWM of brainstem and cerebellar tracts showing the highest correlations (up to $\rho = 0.48$ and $\rho = 0.47$, respectively) [363]. Finally, we investigated whether

previously reported periventricular gradients of NAWM damage [365–369] could be detected and characterized by quantitative T_1 z-scores in the two patient cohorts. Of notice, a clear periventricular gradient of abnormal T_1 values in NAWM was found to occur in early phases of MS and to increase in the progressive stage of the disease, suggesting that this type of analyses may have clinical relevance [364].

In children, we conducted a first prospective monocentric study on 13 patients with suspected focal epilepsy of unknown cause aiming at comparing brain volumes and T_1 values to the normal cohort and investigating correlation with their electro-clinical presentations. The presence of volumetric and T_1 relaxometry abnormalities in children with focal epilepsy allowed describing brain abnormalities undetected in conventional brain MRI in more than 80% of the cases [356].

8.3 Future research directions

8.3.1 Myelin water imaging

Future work should focus on exploring different sampling and reconstruction strategies to further accelerate the multi-echo GRASE acquisition. In a preliminary study [370], we proposed to combine the CAIPIRINHA sampling with complementary encoding across echoes in a joint-CAIPI (J-CAIPI) reconstruction to improve image quality and further reduce the acquisition time following recent advances in the reconstruction of MR acquisitions with multiple echoes/phase-cycles/contrasts [279, 371]. While preserving comparable MWF values, J-CAIPI reconstructed data were found to be free from aliasing artifacts, allowing to further reduce the acquisition time from 10:30 minutes to 6:18 minutes for a 1.6 mm^3 isotropic whole brain scan. A more thorough validation in a larger dataset of subjects is however needed. The current acquisition scheme based on CAIPIRINHA could be also improved by employing sinusoidal gradients in the phase-encoding directions during the readout, which would result in evenly spread acquired samples in all three directions. This strategy, typically referred to as wave-CAIPI [50] (see **Section 2.4.1** in Chapter 2), proved to reduce undersampling artifacts in parallel imaging and would allow to increase the acceleration factor. Additionally, the random sampling of the outer k-space could be investigated to incorporate compressed sensing priors into the J-CAIPI reconstruction, which showed good promise in single-echo GRASE imaging [281].

Finally, since the reconstruction of the MWF maps is not available at the scanner yet, the reconstruction algorithm should be implemented for an online reconstruction on the scanner hardware. This will offer the possibility to gain more experience within real clinical settings.

8.3.2 Learning tissue microstructure from relaxometry

The proposed approach for the direct estimation of MWF maps from relaxometry might be further improved in several ways. The GLM and RFRM were trained considering average MWF values in selected brain regions and subsequently employed to estimate MWF for each brain voxels. The pooling of values only from specific brain regions that share similar characteristics is expected to improve the fitting of the data. The use of three different models restricted to specific tissue classes – WM, GM, and deep GM – should be thus explored, as well as the training of separate models for each single region. Image-to-image translation using deep learning networks was never investigated on quantitative MR data, to the best of the authors' knowledge. So far, these approaches have been used in studies with weighted imaging [286, 290, 293]. The amount of training data is one of the crucial concerns while training deep neural networks. While the results presented are promising especially given the small amount of data, future work should focus on expanding the training set size. Of notice, the capability of dealing with unpaired data would enlarge the spectrum of suitable images for the training. To that end, cycle GANs have been developed to cope with unregistered data and should be investigated in this context [294, 295]. Additionally, the generalizability of the employed models in the presence of demyelinated tissue should be tested in patient datasets.

Additionally, complementary quantitative maps that have shown to be good indicators of brain myelin content, e.g. T_2^* [91], quantitative MT [155] and DTI [297], may serve as additional input channels to improve the overall estimation of MWF maps. By adding fast sequences to the currently employed clinical protocol to map these physical parameters, the proposed approach could be easily scaled to infer other properties of the tissue microstructure such as iron concentration [128], axonal g-ratio [302, 303], and conductivity [304].

8.3.3 Characterization of abnormal tissues

To address one of the main limitations of the proposed LPM protocol, i.e., current resolution, future work should focus on the development of a 3D version of the protocol that will be able to provide 1 mm^3 isotropic maps. In fact, the 2D nature of the GRAPPATINI sequence impeded the acquisition of maps with isotropic resolution as a slice profile below 3 mm would induce strong stimulated echoes, prolong the acquisition time, and lower the SNR. Preliminary work in this direction has been already performed, replacing the GRAPPATINI sequence with a 3D T_2 -prep acquisition accelerated with compressed sensing [296, 372]. Additional validation of this newly developed sequence is, however, still needed to make it suitable for clinical applications.

Another main limitation of the proposed framework is the restriction to WM tissues due to difficulties in spatially registering the variable cortical GM gyrification structures between different subjects. Current ongoing work aims at extending the developed method to the cortex by exploiting the surface reconstruction framework provided by FreeSurfer [332]. Preliminary results demonstrated that, using this framework, it may be possible to establish a T_1 atlas and

perform a T_1 z-score calculation in the different cortical GM layers on a single-subject level (unpublished results).

At the moment, the developed method is also limited to 1.5 T acquisitions in children and 3 T in adults. As relaxation times vary across field strengths, additional data would be required to build new atlases and extend the developed framework to different field strengths. Additionally, the quantitative nature of the acquired maps also facilitates the comparison of the measured physical parameters in longitudinal studies. A longitudinal pipeline for qMRI acquisition comparison should be thus developed, aiming at deriving personalized deviation maps over time.

8.4 Final consideration

This thesis was centered around increasing the value and promoting the practical utility of qMRI in clinical settings with a focus on brain relaxometry and MWI. The problem at hand was tackled from different angles. It was shown that accelerating the image acquisition may facilitate the use of qMRI in a fast clinical workflow in the first place. Furthermore, maps specific to the tissue microstructure may be derived from qMRI data that fit into the requirements of routine use, thus replacing time consuming acquisitions while providing additional clinical value. Finally, this thesis has aimed at further improving the clinical value of qMRI by developing tools to compute normative ranges of physical parameters and visualize deviations from such norms in accordance with requirements of the clinical workflow. The different developed methods yielded various prototype packages, which were shared with scientific collaborators and resulted in methodological spin-off research and clinical validation projects. Despite these new insights, further efforts need to be undertaken to eventually attain the aim of this thesis. Nonetheless, there are promising grounds to think that a paradigm shift may happen in the future, turning “qualitative” MRI into an instrument for personalized precision medicine.

Bibliography

- [1] W. Gerlach and O. Stern. Der experimentelle nachweis der richtungsquantelung im magnetfeld. *Zeitschrift für Physik*, 9(1):349–352, 1922.
- [2] E.M. Purcell, H.C. Torrey, and V.R. Pound. Resonance absorption by nuclear magnetic moments in a solid. *Physical review*, 69(1-2):37, 1946.
- [3] F. Bloch. Nuclear induction. *Physical Review*, 1946.
- [4] P.C. Lauterbur. Image Formation by Induced Local Interactions: Examples Employing Nuclear Magnetic Resonance. *Nature*, 242(5394):190–191, 1973.
- [5] P. Mansfield and P.K. Grannell. NMR 'diffraction' in solids? *Journal of Physics C: Solid State Physics*, 6(22):L422–L426, 1973.
- [6] P. Tofts. *Quantitative MRI of the Brain: Measuring Changes Caused by Disease*. John Wiley & Sons, 2005.
- [7] O. Jahn, S. Tenzer, and H.B. Werner. Myelin proteomics: Molecular anatomy of an insulating sheath. *Molecular Neurobiology*, 40(1):55–72, 2009.
- [8] A. Mackay, K. Whittall, J. Adler, D. Li, D. Paty, and D. Graeb. In vivo visualization of myelin water in brain by magnetic resonance. *Magnetic Resonance in Medicine*, 31(6):673–677, 1994.
- [9] S.C.L. Deoni. Quantitative Relaxometry of the Brain. *Topics in Magnetic Resonance Imaging*, 21(2):101–113, 2010.
- [10] R.W. Brown, Y.-C.N. Cheng, E.M. Haacke, M.R. Thompson, and R. Venkatesan. *Magnetic resonance imaging: physical principles and sequence design*. John Wiley & Sons, 2014.
- [11] D.W. McRobbie, E.A. Moore, M.J. Graves, and M.R. Prince. *MRI: from picture to proton*. Cambridge University Press, 2017.
- [12] M.A. Bernstein, K.F. King, and X.J. Zhou. *Handbook of MRI pulse sequences*. Elsevier, 2004.
- [13] J.P. Mugler and J.R. Brookeman. Three-dimensional magnetization prepared rapid gradient-echo imaging (3D MPRAGE). *Magnetic Resonance in Medicine*, 15(1):152–157, 1990.
- [14] V.J. Hajnal, D.J. Bryant, L. Kasuboski, P.M. Pattany, B. De Coene, P.D. Lewis, J.M. Pennock, A. Oatridge, I.R. Young, and G.M. Bydder. Use of fluid attenuated inversion recovery (FLAIR) pulse sequences in MRI of the brain. *Journal of computer assisted tomography*, 16:841, 1992.
- [15] D.C. Look and D.R. Locker. Time saving in measurement of NMR and EPR relaxation times. *Review of Scientific Instruments*, 41(2):250–251, 1970.

Bibliography

- [16] J.P. Marques, T. Kober, G. Krueger, W. van der Zwaag, P-F. Van de Moortele, and R. Gruetter. MP2RAGE, a self bias-field corrected sequence for improved segmentation and T1-mapping at high field. *NeuroImage*, 49(2):1271–1281, 2010.
- [17] H.Y. Carr and E.M. Purcell. Effects of Diffusion on Free Precession in Nuclear Magnetic Resonance Experiments. *Physical Review*, 94(3):630–638, 1954.
- [18] M.D. Does and J.C. Gore. Rapid Acquisition Transverse Relaxometric Imaging. *Journal of Magnetic Resonance*, 147(1):116–120, 2000.
- [19] K. Oshio and D.A. Feinberg. GRASE (Gradient-and Spin-Echo) imaging: A novel fast MRI technique. *Magnetic resonance in medicine*, 20(2):34–349, 1991.
- [20] P. Mansfield. Multi-planar image formation using NMR spin echoes. *Journal of Physics C: Solid State Physics*, 10(3):L55–L58, 1977.
- [21] S.C.L. Deoni, B.K. Rutt, and T.M. Peters. Rapid combined T1 and T2 mapping using gradient recalled acquisition in the steady state. *Magnetic Resonance in Medicine*, 49(3):515–526, 2003.
- [22] K.A. Christensen, D.M. Grant, E.M. Schulman, and C. Walling. Optimal determination of relaxation times of Fourier transform nuclear magnetic resonance. Determination of spin-lattice relaxation times in chemically polarized species. *The Journal of Physical Chemistry*, 78(19):1971–1977, 1974.
- [23] H.Y. Carr. Steady-State Free Precession in Nuclear Magnetic Resonance. *Physical Review*, 112(5):1693–1701, 1958.
- [24] J.B.M. Warntjes, O. Dahlqvist Leinhard, J. West, and P. Lundberg. Rapid magnetic resonance quantification on the brain: Optimization for clinical usage. *Magnetic Resonance in Medicine*, 60(2):320–329, 2008.
- [25] D. Ma, V. Gulani, N. Seiberlich, K. Liu, J.L. Sunshine, J.L. Duerk, and M.A. Griswold. Magnetic resonance fingerprinting. *Nature*, 495(7440):187–192, 2013.
- [26] K.A. Williams, C.M. Deber, and O.A. Klrshner. The structure and function of central nervous system myelin. *Critical Reviews in Clinica Laboratory Sciences*, 30(1):29–64, 1993.
- [27] Y. Min, K. Kristiansen, J.M. Boggs, C. Husted, J.A. Zasadzinski, and J. Israelachvili. Interaction forces and adhesion of supported myelin lipid bilayers modulated by myelin basic protein. *Proceedings of the National Academy of Sciences of the United States of America*, 106(9):3154–3159, 2009.
- [28] S. Poliak and E. Peles. The local differentiation of myelinated axons at nodes of ranvier. *Nature Reviews Neuroscience*, 4(12):968–980, 2003.
- [29] R.D. Fields. White matter in learning, cognition and psychiatric disorders. *Trends in Neurosciences*, 31(7):361–370, 2008.
- [30] M. Bouhrara, D.A. Reiter, C.M. Bergeron, L.M. Zukley, L. Ferrucci, S.M. Resnick, and R.G. Spencer. Evidence of demyelination in mild cognitive impairment and dementia using a direct and specific magnetic resonance imaging measure of myelin content. *Alzheimer's & Dementia*, 14(8):998–1004, 2018.
- [31] S. Xie, J.X. Xiao, G.L. Gong, Y.F. Zang, Y.H. Wang, H.K. Wu, and X.X. Jiang. Voxel-based detection of white matter abnormalities in mild Alzheimer disease. *Neurology*, 66(12):1845–189, 2006.

-
- [32] D.C. Dean, J. Sojkova, S. Hurley, S. Kecskemeti, O. Okonkwo, B.B. Bendlin, F. Theisen, S.C. Johnson, A.L. Alexander, and C.L. Gallagher. Alterations of Myelin Content in Parkinson's Disease: A Cross-Sectional Neuroimaging Study. *PLOS ONE*, 11(10):e0163774, 2016.
 - [33] Y. Hakak, J.R. Walker, C. Li, W.H. Wong, K.L. Davis, J.D. Buxbaum, V. Haroutunian, and A.A. Fienberg. Genome-wide expression analysis reveals dysregulation of myelination-related genes in chronic schizophrenia. *Proceedings of the National Academy of Sciences*, 98(8):4746–4751, 2001.
 - [34] D. Reich, C.F. Lucchinetti, and P.A. Calabresi. Multiple Sclerosis. *New England Journal of Medicine*, 378(2):169–180, 2018. doi: 10.1056/NEJMra1401483.
 - [35] C. Laule, I.M. Vavasour, S.H. Kolind, D.K.B. Li, T.L. Traboulsee, G.R.W. Moore, and A.L. MacKay. Magnetic Resonance Imaging of Myelin. *Neurotherapeutics*, 4(3):460–484, 2007.
 - [36] G.F. Piredda, T. Hilbert, J.-P. Thiran, and T. Kober. Probing myelin content of the human brain with MRI: A review. *Magnetic Resonance in Medicine*, 85(2):627–652, 2021.
 - [37] G. Bonnier, A. Roche, D. Romascano, S. Simioni, D. Meskaldji, D. Rotzinger, Y.-C. Lin, G. Menegaz, M. Schluep, R. Du Pasquier, T.J. Sumpf, J. Frahm, J.-P. Thiran, G. Krueger, and C. Granziera. Advanced MRI unravels the nature of tissue alterations in early multiple sclerosis. *Annals of Clinical and Translational Neurology*, 1(6), 2014.
 - [38] I. Blystad, I. Håkansson, A. Tisell, J. Ernerudh, Ö. Smedby, P. Lundberg, and E.-M. Larsson. Quantitative MRI for Analysis of Active Multiple Sclerosis Lesions without Gadolinium-Based Contrast Agent. *American Journal of Neuroradiology*, 37(1):94–100, 2016.
 - [39] S. Baudrexel, L. Nürnberger, U. Rüb, C. Seifried, J.C. Klein, T. Deller, H. Steinmetz, R. Deichmann, and R. Hilker. Quantitative mapping of T1 and T2* discloses nigral and brainstem pathology in early Parkinson's disease. *Neuroimage*, 51(2):512–520, 2010.
 - [40] M.J. House, T.G.S. Pierre, J.K. Foster, R.N. Martins, and R. Clarnette. Quantitative MR imaging R2 relaxometry in elderly participants reporting memory loss. *American Journal of Neuroradiology*, 27(2):430–439, 2006.
 - [41] B.C. Bernhardt, F. Fadaie, R. Vos de Wael, S.-J. Hong, M. Liu, M.C. Guiot, D.A. Rudko, A. Bernasconi, and N. Bernasconi. Preferential susceptibility of limbic cortices to microstructural damage in temporal lobe epilepsy: A quantitative T1 mapping study. *NeuroImage*, 182:294–303, 2018.
 - [42] T.N. Townsend, N. Bernasconi, G.B. Pike, and A. Bernasconi. Quantitative analysis of temporal lobe white matter T2 relaxation time in temporal lobe epilepsy. *NeuroImage*, 23(1):318–324, 2004.
 - [43] J.B.M. Warntjes, M. Engström, A. Tisell, and P. Lundberg. Brain Characterization Using Normalized Quantitative Magnetic Resonance Imaging. *PLoS ONE*, 2013.
 - [44] G. Bonnier, E. Fischi-Gomez, A. Roche, T. Hilbert, T. Kober, G. Krueger, and C. Granziera. Personalized pathology maps to quantify diffuse and focal brain damage. *NeuroImage: Clinical*, 21:101607, 2019.
 - [45] J. Hamilton, D. Franson, and N. Seiberlich. Recent advances in parallel imaging for MRI. *Progress in Nuclear Magnetic Resonance Spectroscopy*, 101:71–95, 2017.
 - [46] K.P. Pruessmann, M. Weiger, M.B. Scheidegger, and P. Boesiger. SENSE: Sensitivity encoding for fast MRI. *Magnetic Resonance in Medicine*, 42(5):952–962, 1999.

Bibliography

- [47] M.A. Griswold, P.M. Jakob, R.M. Heidemann, M. Nittka, V. Jellus, J. Wang, B. Kiefer, and A. Haase. Generalized autocalibrating partially parallel acquisitions (GRAPPA). *Magnetic Resonance in Medicine*, 47(6):1202–1210, 2002.
- [48] K.P. Pruessmann, M. Weiger, P. Börnert, and P. Boesiger. Advances in sensitivity encoding with arbitrary k-space trajectories. *Magnetic Resonance in Medicine: An Official Journal of the International Society for Magnetic Resonance in Medicine*, 46(4):638–651, 2001.
- [49] F.A. Breuer, M. Blaimer, M.F. Mueller, N. Seiberlich, R.M. Heidemann, M.A. Griswold, and P.M. Jakob. Controlled aliasing in volumetric parallel imaging (2D CAIPIRINHA). *Magnetic Resonance in Medicine*, 55(3):549–556, 2006.
- [50] B. Bilgic, B.A. Gagoski, S.F. Cauley, A.P. Fan, J.R. Polimeni, P.E. Grant, L.L. Wald, and K. Setsompop. Wave-CAIPI for highly accelerated 3D imaging. *Magnetic Resonance in Medicine*, 73(6):2152–2162, 2015.
- [51] M. Lustig, D. Donoho, and J.M. Pauly. Sparse MRI: The application of compressed sensing for rapid MR imaging. *Magnetic Resonance in Medicine*, 58(6):1182–1195, 2007.
- [52] K.T. Block, M. Uecker, and J. Frahm. Model-based iterative reconstruction for radial fast spin-echo MRI. *IEEE Transactions on Medical Imaging*, 28(11):1759–1769, 2009.
- [53] T.J. Sumpf, M. Uecker, S. Boretius, and J. Frahm. Model-based nonlinear inverse reconstruction for T2 mapping using highly undersampled spin-echo MRI. *Journal of Magnetic Resonance Imaging*, 34(2):420–428, 2011.
- [54] T. Hilbert, Sumpf T.J., E. Weiland, J. Frahm, J.-P. Thiran, R. Meuli, T. Kober, and G. Krueger. Accelerated T2 mapping combining parallel MRI and model-based reconstruction: GRAPPATINI. *Journal of Magnetic Resonance Imaging*, 48(2):359–368, 2018.
- [55] A. Makropoulos, S.J. Counsell, and D. Rueckert. A review on automatic fetal and neonatal brain MRI segmentation. *NeuroImage*, 170:231–248, 2018.
- [56] Z. Akkus, A. Galimzianova, A. Hoogi, D.L. Rubin, and B.J. Erickson. Deep Learning for Brain MRI Segmentation: State of the Art and Future Directions. *Journal of Digital Imaging*, 30(4):449–459, 2017.
- [57] I. Despotović, B. Goossens, and W. Philips. MRI segmentation of the human brain: Challenges, methods, and applications. *Computational and Mathematical Methods in Medicine*, 2015, 2015.
- [58] D. Schmitter, A. Roche, B. Maréchal, D. Ribes, A. Abdulkadir, M. Bach-Cuadra, A. Daducci, C. Granziera, S. Klöppel, P. Maeder, R. Meuli, and G. Krueger. An evaluation of volume-based morphometry for prediction of mild cognitive impairment and Alzheimer’s disease. *NeuroImage: Clinical*, 7:7–17, 2015.
- [59] K. Fujimoto, J.R. Polimeni, A.J.W. van der Kouwe, M. Reuter, T. Kober, T. Benner, B. Fischl, and L.L. Wald. Quantitative comparison of cortical surface reconstructions from MP2RAGE and multi-echo MPRAGE data at 3T and 7T. *NeuroImage*, 90:60–73, 2014.
- [60] A. Gholipour, N. Kehtarnavaz, R. Briggs, M. Devous, and K. Gopinath. Brain functional localization: A survey of image registration techniques. *IEEE Transactions on Medical Imaging*, 26(4):427–451, 2007.
- [61] A. Sotiras, C. Davatzikos, and N. Paragios. Deformable medical image registration: A survey. *IEEE Transactions on Medical Imaging*, 32(7):1153–1190, 2013.

- [62] F.P.M. Oliveira and J.M.R.S. Tavares. Medical image registration: A review. *Computer Methods in Biomechanics and Biomedical Engineering*, 17(2):73–93, 2014.
- [63] Y. Ou, H. Akbari, M. Bilello, X. Da, and C. Davatzikos. Comparative evaluation of registration algorithms in different brain databases with varying difficulty: Results and insights. *IEEE Transactions on Medical Imaging*, 33(10):2039–2065, 2014.
- [64] S. Klein, M. Staring, K. Murphy, M.A. Viergever, and J. Pluim. Elastix: A Toolbox for Intensity-Based Medical Image Registration. *IEEE Transactions on Medical Imaging*, 29(1):196–205, 2010.
- [65] B.B. Avants, N.J. Tustison, and G. Song. Advanced normalization tools (ANTS). *Insight j*, 2:1–35, 2009.
- [66] B.B. Avants, N.J. Tustison, G. Song, P.A. Cook, A. Klein, and J.C. Gee. A reproducible evaluation of ANTs similarity metric performance in brain image registration. *NeuroImage*, 54(3):2033–2044, 2011.
- [67] B.B. Avants, C.L. Epstein, M. Grossman, and J.C. Gee. Symmetric diffeomorphic image registration with cross-correlation: Evaluating automated labeling of elderly and neurodegenerative brain. *Medical Image Analysis*, 12(1):26–41, 2008.
- [68] B.B. Avants, P. Yushkevich, J. Pluta, D. Minkoff, M. Korczykowski, J. Detre, and J.C. Gee. The optimal template effect in hippocampus studies of diseased populations. *NeuroImage*, 49(3):2457–2466, 2010.
- [69] E. Alonso-Ortiz, I.R. Levesque, and G.B. Pike. MRI-based myelin water imaging: A technical review. *Magnetic Resonance in Medicine*, 73(1):70–81, 2015.
- [70] R.M. Henkelman, G.J. Stanisz, and S.J. Graham. Magnetization transfer in MRI: A review. *NMR in Biomedicine*, 14(2):57–64, 2001.
- [71] R.A. Horch, J.C. Gore, and M.D. Does. Origins of the ultrashort-T2 1H NMR signals in myelinated nerve: A direct measure of myelin content? *Magnetic Resonance in Medicine*, 66(1):24–31, 2011.
- [72] V. Vasilescu, E. Katona, V. Simplăceanu, and D. Demco. Water compartments in the myelinated nerve. III. Pulsed NMR result. *Experientia*, 34(11):1443–1444, 1978.
- [73] R.S. Menon and P.S. Allen. Application of continuous relaxation time distributions to the fitting of data from model systems and excised tissue. *Magnetic Resonance in Medicine*, 20(2):214–227, 1991. doi: 10.1002/mrm.1910200205.
- [74] R.S. Menon, M.S. Rusinko, and P.S. Allen. Proton Relaxation Studies of Water Compartmentalization in a Model Neurological System. *Magnetic Resonance in Medicine*, 28(2):264–27, 1992. doi: 10.1002/mrm.1910280208.
- [75] K.P. Whittall and A.L. MacKay. Quantitative interpretation of NMR relaxation data. *Journal of Magnetic Resonance (1969)*, 84(1):134–152, 1989.
- [76] A.A. Istratov and O.F. Vyvenko. Exponential analysis in physical phenomena. *Review of Scientific Instruments*, 70(2):1233–1257, 1999.
- [77] C. Laule, E. Leung, D.K.B. Li, A.L. Traboulsee, D.W. Paty, A.L. MacKay, and G.R.W. Moore. Myelin water imaging in multiple sclerosis: quantitative correlations with histopathology. *Multiple Sclerosis Journal*, 12(6):747–753, 2006.

Bibliography

- [78] C. Laule, P. Kozlowski, E. Leung, D.K.B. Li, A.L. MacKay, and G.R.W. Moore. Myelin water imaging of multiple sclerosis at 7 T: Correlations with histopathology. *NeuroImage*, 40(4):1575–1580, 2008.
- [79] C. Laule, I.M. Vavasour, G.R.W. Moore, J. Oger, D.K.B. Li, D.W. Paty, and A.L. MacKay. Water content and myelin water fraction in multiple sclerosis: A T2 relaxation study. *Journal of Neurology*, 251(3):284–293, 2004.
- [80] T. Prasloski, A. Rauscher, A.L. MacKay, M. Hodgson, I.M. Vavasour, C. Laule, and B. Mädler. Rapid whole cerebrum myelin water imaging using a 3D GRASE sequence. *NeuroImage*, 63(1):533–539, 2012.
- [81] J. Hennig. Multiecho imaging sequences with low refocusing flip angles. *Journal of Magnetic Resonance (1969)*, 78(3):397–407, 1988.
- [82] T. Prasloski, B. Mädler, Q.S. Xiang, A. MacKay, and C. Jones. Applications of stimulated echo correction to multicomponent T2 analysis. *Magnetic Resonance in Medicine*, 67(6):1803–1814, 2012.
- [83] V.A. Dvorak, E. Ljungberg, I.M. Vavasour, H. Liu, P. Johnson, A. Rauscher, J.L.K. Kramer, R. Tam, D.K.B. Li, C. Laule, L. Barlow, H. Briemberg, A.L. MacKay, A. Traboulsee, P. Kozlowski, N. Cashman, and S.H. Kolind. Rapid myelin water imaging for the assessment of cervical spinal cord myelin damage. *NeuroImage: Clinical*, 23:101896, 2019.
- [84] G.S. Drenthen, W.H. Backes, A.P. Aldenkamp, and J.F.A. Jansen. Applicability and reproducibility of 2D multi-slice GRASE myelin water fraction with varying acquisition acceleration. *NeuroImage*, 195:333–339, 2019.
- [85] G.F. Piredda, T. Hilbert, E.J. Canales-Rodríguez, M. Pizzolato, C. Deuster, R. Meuli, J. Pfeuffer, A. Daducci, J.-P. Thiran, and T. Kober. Fast and high-resolution myelin water imaging: Accelerating multi-echo GRASE with CAIPIRINHA. *Magnetic Resonance in Medicine*, 85(1):209–222, 2021.
- [86] W.D. Foltz, O. Al-Kwafi, M.S. Sussman, J.A. Stainsby, and G.A. Wright. Optimized spiral imaging for measurement of myocardial T2 relaxation. *Magnetic Resonance in Medicine*, 49(6):1089–1097, 2003.
- [87] J. Oh, E.T. Han, D. Pelletier, and S.J. Nelson. Measurement of in vivo multi-component T2 relaxation times for brain tissue using multi-slice T2 prep at 1.5 and 3 T. *Magnetic Resonance Imaging*, 24(1):33–43, 2006.
- [88] T.D. Nguyen, C. Wisnieff, M.A. Cooper, D. Kumar, A. Raj, P. Spincemaille, Y. Wang, T. Vartanian, and S.A. Gauthier. T2prep three-dimensional spiral imaging with efficient whole brain coverage for myelin water quantification at 1.5 T. *Magnetic Resonance in Medicine*, 67(3):614–621, 2012.
- [89] T.D. Nguyen, K. Deh, E. Monohan, S. Pandya, P. Spincemaille, A. Raj, Y. Wang, and S.A. Gauthier. Feasibility and reproducibility of whole brain myelin water mapping in 4 minutes using fast acquisition with spiral trajectory and adiabatic T2prep (FAST-T2) at 3T. *Magnetic Resonance in Medicine*, 76(2):456–465, 2016.
- [90] J. O’Muircheartaigh, I. Vavasour, E. Ljungberg, D.K.B. Li, A. Rauscher, V. Levesque, H. Garren, D. Clayto, R. Tam, A. Traboulsee, and S. Kolind. Quantitative neuroimaging measures of myelin in the healthy brain and in multiple sclerosis. *Human Brain Mapping*, 40(7):2104–2116, 2019.

- [91] Y.P. Du, R. Chu, D. Hwang, M.S. Brown, B.K. Kleinschmidt-DeMasters, D. Singel, and J.H. Simon. Fast multislice mapping of the myelin water fraction using multicompartment analysis of T2* decay at 3T: A preliminary postmortem study. *Magnetic Resonance in Medicine*, 58(5):865–870, 2007.
- [92] P.E. Gill and W. Murray. Quasi-Newton Methods for Unconstrained Optimization. *IMA Journal of Applied Mathematics*, 9(1):91–108, 2007.
- [93] D. Hwang, D.H. Kim, and Y.P. Du. In vivo multi-slice mapping of myelin water content using T2* decay. *NeuroImage*, 52(1):198–204, 2010.
- [94] P. Van Gelderen, J.A. De Zwart, J. Lee, P. Sati, D.S. Reich, and J.H. Duyn. Nonexponential T2* decay in white matter. *Magnetic Resonance in Medicine*, 67(1):110–117, 2012.
- [95] P. Sati, P. van Gelderen, A.C. Siva, D.S. Reich, H. Merkle, J.A. de Zwart, and J.H. Duyn. Micro-compartment specific T2* relaxation in the brain. *NeuroImage*, 77:268–278, 2013.
- [96] Y. Nam, J. Lee, D. Hwang, and D.H. Kim. Improved estimation of myelin water fraction using complex model fitting. *NeuroImage*, 116:214–221, 2015.
- [97] Z. Wu, B. Bilgic, H. He, Q. Tong, Y. Sun, Y. Du, K. Setsompop, and J. Zhong. Wave-CAIPI ViSta: highly accelerated whole-brain direct myelin water imaging with zero-padding reconstruction. *Magnetic Resonance in Medicine*, 80(3):1061–1073, 2018.
- [98] S.H. Oh, M. Bilello, M. Schindler, C.E. Markowitz, J.A. Detre, and J. Lee. Direct visualization of short transverse relaxation time component (ViSta). *NeuroImage*, 83:485–492, 2013.
- [99] T.A. Bjarnason, I.M. Vavasour, C.L.L. Chia, and A.L. MacKay. Characterization of the NMR behavior of white matter in bovine brain. *Magnetic Resonance in Medicine*, 54(5):1072–1081, 2005.
- [100] R. Kreis, C. Fusch, and C. Boesch. In vivo characterization of three water compartments in human white matter using a single voxel technique with short TE. *Proceedings of the 11th annual meeting of SMRM, Berlin, Germany*, page 1963, 1992.
- [101] S.C.L. Deoni, B.K. Rutt, T. Arun, C. Pierpaoli, and D.K. Jones. Gleaning multicomponent T1 and T2 information from steady-state imaging data. *Magnetic Resonance in Medicine*, 60(6):137–1387, 2008.
- [102] J.H. Duijn, G.B. Matson, A.A. Maudsley, J.W. Hugg, and M.W. Weiner. Human brain infarction: proton MR spectroscopy. *Radiology*, 18(3):711–718, 1992. doi: 10.1148/radiology.183.3.1584925.
- [103] J.H. Duyn, C.X. Tan, P. Van Gelderen, and M.N. Yongbi. High-Sensitivity Single-Shot Perfusion-Weighted fMRI. *Magnetic Resonance in Medicine*, 46:88–94, 2001.
- [104] C. Labadie, J.H. Lee, W.D. Rooney, S. Jarchow, M. Aubert-Frécon, C.S. Springer, and H.E. Möller. Myelin water mapping by spatially regularized longitudinal relaxographic imaging at high magnetic fields. *Magnetic Resonance in Medicine*, 71(1):375–387, 2014.
- [105] C.L. Tardif, A. Schäfer, M. Waehnert, J. Dinse, R. Turner, and P.L. Bazin. Multi-contrast multi-scale surface registration for improved alignment of cortical areas. *NeuroImage*, 111:107–122, 2015.
- [106] R. Barta, S. Kalantari, C. Laule, I.M. Vavasour, A.L. MacKay, and C.A. Michal. Modeling T1 and T2 relaxation in bovine white matter. *Journal of Magnetic Resonance*, 259:56–67, 2015.
- [107] D.F. Gochberg and J.C. Gore. Quantitative imaging of magnetization transfer using an inversion recovery sequence. *Magnetic Resonance in Medicine*, 49(3):501–505, 2003.

Bibliography

- [108] R.M. Henkelman, X. Huang, Q.-S. Xiang, G.J. Stanisz, S.D. Swanson, and M.J. Bronskill. Quantitative Interpretation of Magnetization Transfer. *Magnetic resonance in medicine*, 29(6):759–766, 1993.
- [109] A. Lutti, F. Dick, M.I. Sereno, and N. Weiskopf. Using high-resolution quantitative mapping of R1 as an index of cortical myelination. *NeuroImage*, 93:176–188, 2014.
- [110] S.H. Koenig. Cholesterol of myelin is the determinant of gray-white contrast in MRI of brain. *Magnetic Resonance in Medicine*, 20(2):285–291, 1991.
- [111] W. Kucharczyk, P.M. Macdonald, G.J. Stanisz, and R.M. Henkelman. Relaxivity and magnetization transfer of white matter lipids at MR imaging: importance of cerebroside and pH. *Radiology*, 192(2):521–529, 1994.
- [112] J.D. Yeatman, B.A. Wandell, and A.A. Mezer. Lifespan maturation and degeneration of human brain white matter. *Nature Communications*, 5(1):4932, 2014.
- [113] D.A. Slater, L. Melie-Garcia, M. Preisig, F. Kherif, A. Lutti, and B. Draganski. Evolution of white matter tract microstructure across the life span. *Human Brain Mapping*, 40(7):2252–2268, 2019.
- [114] F. Dick, A. Taylor Tierney, A. Lutti, O. Josephs, M.I. Sereno, and N. Weiskopf. In Vivo Functional and Myeloarchitectonic Mapping of Human Primary Auditory Areas. *Journal of Neuroscience*, 32:16095–16105, 2012.
- [115] M.I. Sereno, A. Lutti, N. Weiskopf, and F. Dick. Mapping the human cortical surface by combining quantitative T1 with retinotopy. *Cerebral Cortex*, 23(9):2261–2268, 2013.
- [116] Hong Zhang and Masumi Ishikawa. An Extended Hybrid Genetic Algorithm for Exploring a Large Search Space. *2nd International Conference on Autonomous Robots and Agents*, pages 244–248, 2004.
- [117] S.C.L. Deoni, L. Matthews, and S.H. Kolind. One component? Two components? Three? The effect of including a nonexchanging “free” water component in multicomponent driven equilibrium single pulse observation of T1 and T2. *Magnetic Resonance in Medicine*, 70(1):147–154, 2013.
- [118] M. Warntjes, Engström M., A. Tisell, and P. Lundberg. Modeling the presence of myelin and edema in the brain based on multi-parametric quantitative MRI. *Frontiers in Neurology*, 7:16, 2016.
- [119] R. Ouellette, G. Mangeat, I. Polyak, M. Warntjes, Y. Forslin, A. Bergendal, M. Plattén, M. Uppman, C.A. Treba, J. Cohen-Adad, F. Piehl, M. Kristoffersen Wiberg, S. Fredrikson, C. Mainero, and T. Granberg. Validation of Rapid Magnetic Resonance Myelin Imaging in Multiple Sclerosis. *Annals of Neurology*, 87(5):710–724, 2020.
- [120] S. Fujita, A. Hagiwara, N. Takei, K.-P. Hwang, I. Fukunaga, S. Kato, C. Andica, K. Kamagata, K. Yokoyama, N. Hattori, O. Abe, and S. Aoki. Accelerated Isotropic Multiparametric Imaging by High Spatial Resolution 3D-QALAS With Compressed Sensing. *Investigative Radiology*, Publish Ah, 2020.
- [121] G.E. Santyr. Magnetization transfer effects in multislice MR imaging. *Magnetic Resonance Imaging*, 11(4):521–532, 1993.
- [122] B. Mädler and A.L. Mackay. In-vivo 3D Multi-component T2-Relaxation Measurements for Quantitative Myelin Imaging at 3T. *Proceedings of the International Society of Magnetic Resonance in Medicine*, page 2112, 2006.

- [123] H.-G. Shin, S.-H. Oh, M. Fukunaga, Y. Nam, D. Lee, W. Jung, M. Jo, S. Ji, J.Y. Choi, and J. Lee. Advances in gradient echo myelin water imaging at 3T and 7T. *NeuroImage*, 188:835–844, 2019.
- [124] E. Alonso-Ortiz, I.R. Levesque, and G.B. Pike. Multi-gradient-echo myelin water fraction imaging: Comparison to the multi-echo-spin-echo technique. *Magnetic Resonance in Medicine*, 79(3):1439–1446, 2018.
- [125] C. Laule, I.M. Vavasour, B. Mädler, S.H. Kolind, S.M. Sirrs, E.E. Brief, A.L. Traboulsee, G.R.W. Moore, D.K.B. Li, and A.L. MacKay. MR evidence of long T2 water in pathological white matter. *Journal of Magnetic Resonance Imaging*, 26(4):1117–1121, 2007.
- [126] S.M. Sirrs, C. Laule, B. Mädler, E.E. Brief, S.A. Tahir, C. Bishop, and A.L. MacKay. Normal-appearing White Matter in Patients with Phenylketonuria: Water Content, Myelin Water Fraction, and Metabolite Concentrations. *Radiology*, 242(1):236–243, 2007. doi: 10.1148/radiol.2421051758.
- [127] N. Stikov, M. Boudreau, I.R. Levesque, C.L. Tardif, J.K. Barral, and G.B. Pike. On the accuracy of T1 mapping: Searching for common ground. *Magnetic Resonance in Medicine*, 73(2):514–522, 2015.
- [128] C. Stüber, M. Morawski, A. Schäfer, C. Labadie, M. Wähnert, C. Leuze, M. Streicher, N. Barapatre, K. Reimann, S. Geyer, D. Spemann, and R. Turner. Myelin and iron concentration in the human brain: A quantitative study of MRI contrast. *NeuroImage*, 93(P1):95–106, 2014.
- [129] M.F. Callaghan, G. Helms, A. Lutti, S. Mohammadi, and N. Weiskopf. A general linear relaxometry model of R1 using imaging data. *Magnetic Resonance in Medicine*, 73(3):1309–1314, 2015.
- [130] R. Metere and H.E. Möller. Quantifying the Myelin and Iron Contents of the Brain in vivo using a Linear Model of Relaxation. *Proceedings of the International Society of Magnetic Resonance in Medicine, Paris, France*, page 5505, 2018.
- [131] J Zhang, S.H. Kolind, C. Laule, and A.L. Mackay. Comparison of myelin water fraction from multiecho T2 decay curve and steady-state methods. *Magnetic Resonance in Medicine*, 73(1):22–232, 2015.
- [132] C.L. Lankford and M.D. Does. On the inherent precision of mcDESPOT. *Magnetic Resonance in Medicine*, 69(1):127–136, 2013.
- [133] D.J. West, R.P.A.G. Teixeira, T.C. Wood, V.J. Hajnal, J.-D. Tournier, and S.J. Malik. Inherent and unpredictable bias in multi-component DESPOT myelin water fraction estimation. *NeuroImage*, 195:78–88, 2019.
- [134] M. Bouhrara and R.G. Spencer. Improved determination of the myelin water fraction in human brain using magnetic resonance imaging through Bayesian analysis of mcDESPOT. *NeuroImage*, 127:456–471, 2016.
- [135] M. Bouhrara and R.G. Spencer. Rapid simultaneous high-resolution mapping of myelin water fraction and relaxation times in human brain usingBMC-mcDESPOT. *NeuroImage*, 147:800–811, 2017.
- [136] J.G. Sled. Modelling and interpretation of magnetization transfer imaging in the brain. *NeuroImage*, 182:128–135, 2018.
- [137] S.D. Wolff and R.S. Balaban. Magnetization transfer contrast (MTC) and tissue water proton relaxation in vivo. *Magnetic Resonance in Medicine*, 10(1):135–144, 1989. doi: 10.1002/mrm.1910100113.

Bibliography

- [138] G. Bonanno, T. Hilbert, A. Joseph, E. Mussard, C. Forman, G.F. Piredda, and T. Kober. High-resolution magnetization transfer ratio maps using spiral-phyllotaxis Cartesian FLASH and compressed sensing in under five minutes. *Proceedings of the International Society of Magnetic Resonance in Medicine, Sydney, Australia*, page 3138, 2020.
- [139] Clare Morrison and R Mark Henkelman. A model for magnetization transfer in tissues. *Magnetic resonance in medicine*, 33(4):475–482, 1995.
- [140] B.N. Provotorov. MAGNETIC RESONANCE SATURATION IN CRYSTALS. *J. Exptl. Theoret. Phys. (U.S.S.R.)*, 14(5):1582–1591, 1962.
- [141] M. Goldman. Spin Temperature and Nuclear Magnetic Resonance in Solids. *Oxford University Press*, 1970.
- [142] H.N. Yeung, R.S. Adler, and S.D. Swanson. Transient Decay of Longitudinal Magnetization in Heterogeneous Spin Systems under Selective Saturation. IV. Reformulation of the SpinBath-Model Equations by the Redfield-Provotorov Theory. *Journal of Magnetic Resonance, Series A*, 106(1):37–45, 1994.
- [143] C. Morrison, G. Stanisiz, and R.M. Henkelman. Modeling Magnetization Transfer for Biological-like Systems Using a Semi-solid Pool with a Super-Lorentzian Lineshape and Dipolar Reservoir. *Journal of Magnetic Resonance, Series B*, 108(2):103–113, 1995.
- [144] A. Gass, G.J. Barker, D. Kidd, J.W. Thorpe, D. MacManus, A. Brennan, PS. Tofts, A.J. Thompson, W.I. McDonald, and D.H. Miller. Correlation of magnetization transfer ration with clinical disability in multiple sclerosis. *Annals of Neurology*, 36(1):62–67, 1994.
- [145] M. Filippi, M.A. Rocca, G. Martino, M.A. Horsfield, and G. Comi. Magnetization transfer changes in the normal appearing white matter precede the appearance of enhancing lesions in patients with multiple sclerosis. *Annals of Neurology*, 43(6):809–814, 1998.
- [146] K. Schmierer, F. Scaravilli, D.R. Altmann, G.J. Barker, and D.H. Miller. Magnetization transfer ratio and myelin in postmortem multiple sclerosis brain. *Annals of Neurology*, 56(3):407–415, 2004.
- [147] G. Helms, H. Dathe, K. Kallenberg, and P. Dechent. High-resolution maps of magnetization transfer with inherent correction for RF inhomogeneity and T1 relaxation obtained from 3D FLASH MRI. *Magnetic Resonance in Medicine*, 60(6):1396–1407, 2008.
- [148] A. Lema, C. Bishop, O. Malik, M. Mattosio, R. Ali, R. Nicholas, P.A. Muraro, P.M. Matthews, A.D. Waldman, and R.D. Newbould. A Comparison of Magnetization Transfer Methods to Assess Brain and Cervical Cord Microstructure in Multiple Sclerosis. *Journal of Neuroimaging*, 27(2):221–226, 2017.
- [149] J.G. Sled and G.B. Pike. Quantitative Interpretation of Magnetization Transfer in Spoiled Gradient Echo MRI Sequences. *Journal of Magnetic Resonance*, 145(1):24–36, 2000.
- [150] J.G. Sled and G.B. Pike. Quantitative imaging of magnetization transfer exchange and relaxation properties in vivo using MR. *Magnetic Resonance in Medicine*, 46(5):923–931, 2001.
- [151] A. Ramani, C. Dalton, D.. Miller, PS. Tofts, and G.J. Barker. Precise estimate of fundamental in-vivo MT parameters in human brain in clinically feasible times. *Magnetic Resonance Imaging*, 20(10):721–731, 2002.
- [152] V.L. Yarnykh. Pulsed Z-spectroscopic imaging of cross-relaxation parameters in tissues for human MRI: Theory and clinical applications. *Magnetic Resonance in Medicine*, 47(5):929–939, 2002.

- [153] S. Portnoy and G.J. Stanisz. Modeling pulsed magnetization transfer. *Magnetic Resonance in Medicine*, 58(1):144–155, 2007.
- [154] H.R. Underhill, R.C. Rostomily, A.M. Mikheev, C. Yuan, and V.L. Yarnykh. Fast bound pool fraction imaging of the in vivo rat brain: Association with myelin content and validation in the C6 glioma model. *NeuroImage*, 54(3):2052–2065, 2011.
- [155] K. Schmierer, D.J. Tozer, F. Scaravilli, D.R. Altmann, G.J. Barker, P.S. Tofts, and D.H. Millr. Quantitative magnetization transfer imaging in postmortem multiple sclerosis brain. *Journal of Magnetic Resonance Imaging*, 26(1):41–51, 2007.
- [156] V.L. Yarnykh. Fast macromolecular proton fraction mapping from a single off-resonance magnetization transfer measurement. *Magnetic Resonance in Medicine*, 68(1):166–178, 2012.
- [157] G. Varma, G. Duhamel, C. De Bazelaire, and D.C. Alsop. Magnetization transfer from inhomogeneously broadened lines: A potential marker for myelin. *Magnetic Resonance in Medicine*, 73(2):614–622, 2015.
- [158] G. Varma, O.M. Girard, V.H. Prevost, A.K. Grant, G. Duhamel, and D.C. Alsop. Interpretation of magnetization transfer from inhomogeneously broadened lines (ihMT) in tissues as a dipolar order effect within motion restricted molecules. *Journal of Magnetic Resonance*, 260:67–76, 2015.
- [159] A.P. Manning, K.L. Chang, A.L. MacKay, and C.A. Michal. The physical mechanism of “inhomogeneous” magnetization transfer MRI. *Journal of Magnetic Resonance*, 74:125–136, 2017.
- [160] D.F. Bocian and S.I. Chan. NMR Studies of Membrane Structure and Dynamics. *Annual Review of Physical Chemistry*, 29(1):307–335, 1978.
- [161] J.S. Lee, A.K. Khitrin, R.R. Regatte, and A. Jerschow. Uniform saturation of a strongly coupled spin system by two-frequency irradiation. *Journal of Chemical Physics*, 134(23), 2011.
- [162] G. Duhamel, V.H. Prevost, M. Cayre, A. Hertau, S. Mchinda, V.N. Carvalho, G. Varma, P. Durbec, D.C. Alsop, and O.M. Girard. Validating the sensitivity of inhomogeneous magnetization transfer (ihMT) MRI to myelin with fluorescence microscopy. *NeuroImage*, 199:289–303, 2019.
- [163] G. Varma, O.M. Girard, S. Mchinda, V.H. Prevost, A.K. Grant, G. Duhamel, and D.C. Alsop. Low duty-cycle pulsed irradiation reduces magnetization transfer and increases the inhomogeneous magnetization transfer effect. *Journal of Magnetic Resonance*, 296:60–71, 2018.
- [164] V.H. Prevost, O.M. Girard, S. Mchinda, G. Varma, D.C. Alsop, and G. Duhamel. Optimization of inhomogeneous magnetization transfer (ihMT) MRI contrast for preclinical studies using dipolar relaxation time (T1D) filtering. *NMR in Biomedicine*, 30(6):e3706, 2017.
- [165] S. Mchinda, G. Varma, V.H. Prevost, A. Le Troter, S. Rapacchi, M. Guye, J. Pelletier, J.P. Ranjeva, D.C. Alsop, G. Duhamel, and O.M. Girard. Whole brain inhomogeneous magnetization transfer (ihMT) imaging: Sensitivity enhancement within a steady-state gradient echo sequence. *Magnetic Resonance in Medicine*, 79(5):2607–2619, 2018.
- [166] M.D. Robson, P.D. Gatehouse, M. Bydder, and G.M. Bydder. Magnetic Resonance: An Introduction to Ultrashort. *Components*, 27(6):825–846, 2003.
- [167] D.J. Tyler, M.D. Robson, R.M. Henkelman, I.R. Young, and G.M. Bydder. Magnetic resonance imaging with ultrashort TE (UTE) PULSE sequences: Technical considerations. *Journal of Magnetic Resonance Imaging*, 25(2):279–289, 2007.

Bibliography

- [168] P.E.Z. Larson, P.T. Gurney, K. Naya, G.E. Gold, J.M. Pauly, and D.G. Nishimura. Designing long-T2 suppression pulses for ultrashort echo time imaging. *Magnetic Resonance in Medicine*, 56(1):94–103, 2006.
- [169] L. Soustelle, J. Lamy, F. Rousseau, J.P. Armspach, and P. Loreiro de Sousa. A diffusion-based method for long-T 2 suppression in steady state sequences: Validation and application for 3D-UTE imaging. *Magnetic Resonance in Medicine*, 80(2):548–559, 2018.
- [170] J. Du, G. Ma, S. Li, M. Carl, N.M. Szevenenyi, S. VandenBerg, J. Corey-Bloom, and G.M. Bydder. Ultrashort echo time (UTE) magnetic resonance imaging of the short 2 components in white matter of the brain using a clinical 3T scanner. *NeuroImage*, 87:32–41, 2014.
- [171] V. Sheth, H. Shao, J. Chen, S. Vandenberg, J. Corey-Bloom, G.M. Bydder, and J. Du. Magnetic resonance imaging of myelin using ultrashort Echo time (UTE) pulse sequences: Phantom, specimen, volunteer and multiple sclerosis patient studies. *NeuroImage*, 136:37–44, 2016.
- [172] T. Boucneau, P. Cao, S. Tang, M. Han, D. Xu, R.G. Henry, and P.E.Z. Larson. In vivo characterization of brain ultrashort-T2 components. *Magnetic Resonance in Medicine*, 80(2):726–735, 2018.
- [173] S.J. Fan, Y. Ma, Y. Zhu, A. Searleman, N.M. Szevenenyi, G.M. Bydder, and J. Du. Yet more evidence that myelin protons can be directly imaged with UTE sequences on a clinical 3T scanner: Bicomponent T2* analysis of native and deuterated bovine brain specimens. *Magnetic Resonance in Medicine*, 80(2):538–547, 2018.
- [174] A. Mezer, J.D. Yeatman, N. Stikov, K.N. Kay, Cho N.J., R.F. Dougherty, M.L. Perry, J. Parvizi, L.H. Hua, K. Butts-Pauly, and B.A. Wandell. Quantifying the local tissue volume and composition in individual brains with magnetic resonance imaging. *Nature Medicine*, 19(12):1667–1672, 2013.
- [175] E.K. Fram, R.J. Herfkens, G.A. Johnson, G.H. Glove, J.P. Karis, A. Shimakawa, T.G. Perkins, and N.J. Pelc. Rapid calculation of T1 using variable flip angle gradient refocused imaging. *Magnetic Resonance Imaging*, 5(3):201–208, 1987.
- [176] P.J. Gareau, B.K. Rutt, J.R. Mitchellb, and S.J. Karlikb. Magnetization Transfer Measurements in NAWM with Eistopathologic Correlation in an Experimental Model of Multiple Sclerosis. *J. Magn. Reson. Imaging*, 11:1998, 1998.
- [177] L.L. Cook, P.J. Foster, J.R. Mitchell, and S.J. Karlik. In vivo 4.0-T magnetic resonance investigation of spinal cord inflammation, demyelination, and axonal damage in chronic-progressive experimental allergic encephalomyelitis. *Journal of Magnetic Resonance Imaging*, 20(4):563–571, 2004.
- [178] I.M. Vavasour, C. Laule, D.K.B. Li, A.L. Traboulsee, and A.L. MacKay. Is the magnetization transfer ratio a marker for myelin in multiple sclerosis? *Journal of Magnetic Resonance Imaging*, 33(3):713–718, 2011.
- [179] B.L. Geeraert, R.M. Lebel, A.C. Mah, S.C. Deoni, D.C. Alsop, G. Varma, and C. Lebel. A comparison of inhomogeneous magnetization transfer, myelin volume fraction, and diffusion tensor imaging measures in healthy children. *NeuroImage*, 182:343–350, 2018.
- [180] H. Rasoanandrianina, A.-M. Grapperon, M. Taso, O.M. Girard, G. Duhamel, M. Guye, J.-P. Ranjeva, S. Attarian, A. Verschueren, and V. Callot. Region-specific impairment of the cervical spinal cord (SC) in amyotrophic lateral sclerosis: A preliminary study using SC templates and quantitative MRI (diffusion tensor imaging/inhomogeneous magnetization transfer). *NMR in Biomedicine*, 30(12):e3801, 2017.

- [181] E. Van Obberghen, S. Mchinda, A. Le Troter, V.H. Prevost, P. Viout, M. Guye, G. Varma, D.C. Alsop, J.P. Ranjeva, J. Pelletier, O. Girard, and G. Duhamel. Evaluation of the sensitivity of inhomogeneous magnetization transfer (ihMT) MRI for multiple sclerosis. *American Journal of Neuroradiology*, 39(4):634–641, 2018.
- [182] A. Hertanu, O.M. Girard, V.N.D. Carvalho, L. Soustelle, G. Varma, D.C. Alsop, and G. Duhamel. Toward quantitative inhomogeneous magnetization transfer (qihMT) using a general Matrix Exponential Model. *Proceedings of the International Society of Magnetic Resonance in Medicine, Montreal, Canada*, page 0428, 2019.
- [183] V.N.D. Carvalho, A. Hertanu, A. Grélard, S. Mchinda, L. Soustelle, A. Loquet, E.J. Dufourc, G. Varma, D.C. Alsop, P. Thureau, O.M. Girard, and G. Duhamel. MRI assessment of multiple dipolar relaxation time (T1D) components in biological tissues interpreted with a generalized inhomogeneous magnetization transfer (ihMT) model. *Journal of Magnetic Resonance*, 311, 2020.
- [184] R.A. Horch, K. Wilkens, D.F. Gochberg, and M.D. Does. RF coil considerations for short-T2 MRI. *Magnetic Resonance in Medicine*, 64(6):1652–1657, 2010.
- [185] K.D. Harkins and M.D. Does. Myelin UTE imaging, to be or not to be? *Proceedings of the International Society of Magnetic Resonance in Medicine*, page 4895, 2019.
- [186] R. Brown. On the particles contained in the pollen of plants; and on the general existence of active molecules in organic and inorganic bodies. *Edinburgh New Philosophical Journal*, 5:358–371, 1828.
- [187] A. Einstein. *Investigations on the Theory of the Brownian Movement*. Courier Corporation, 1956.
- [188] C. Thomsen, O. Henriksen, and P. Ring. In Vivo Measurement of Water Self Diffusion in the Human Brain by Magnetic Resonance Imaging. *Acta Radiologica*, 28(3):353–361, 1987.
- [189] L. Minati and W.P. Weglarz. Physical foundations, models, and methods of diffusion magnetic resonance imaging of the brain: A review. *Concepts in Magnetic Resonance Part A: Bridging Education and Research*, 30(5):278–307, 2007.
- [190] K.J. Van Everdingen, J. Van Der Grond, L.J. Kappelle, L.M.P. Ramos, and W.P.T.M. Mali. Diffusion-weighted magnetic resonance imaging in acute stroke. *Stroke*, 29(9):1783–1790, 1998.
- [191] A.R. Padhani, G. Liu, D. Mu-Koh, T.L. Chenevert, H.C. Thoeny, T. Takahara, A. Dzik-Juas, B.D. Ross, M. Van Cauteren, D. Collins, D.A. Hammoud, G.J.S. Rustin, B. Taouli, and P.L. Choyke. Diffusion-weighted magnetic resonance imaging as a cancer biomarker: Consensus and recommendations. *Neoplasia*, 11:102–125, 2009.
- [192] E.O. Stejskal and J.E. Tanner. Spin diffusion measurements: Spin echoes in the presence of a time-dependent field gradient. *The Journal of Chemical Physics*, 42(1):288–292, 1965.
- [193] D. Le Bihan, E. Breton, D. Lallemand, P. Grenier, E. Cbanis, and M. Laval-Jeantet. MR imaging of intravoxel incoherent motions: Application to diffusion and perfusion in neurological disorders. *Radiology*, 161(2):401–407, 1986.
- [194] P. Mukherjee, S.W. Chung, J.I. Berman, C.P. Hess, and R. Henry. Diffusion tensor MR imaging and fiber tractography: Technical considerations. *American Journal of Neuroradiology*, 29(5):843–852, 2008.
- [195] P. Mukherjee, J. Berman, S. Chung, C. Hess, and R. Henry. Diffusion tensor mr imaging and fiber tractography: theoretic underpinnings. *American journal of neuroradiology*, 29:632–641, 2008.

Bibliography

- [196] S.W. Sun, H.F. Liang, K. Trinkaus, A.H. Cross, R.C. Armstrong, and S.K. Song. Noninvasive detection of cuprizone induced axonal damage and demyelination in the mouse corpus callosum. *Magnetic Resonance in Medicine*, 55(2), 2006.
- [197] S.K. Song, S.W. Sun, M.J. Ramsbottom, C. Chang, J. Russell, and A.H. Cross. Dysmyelination revealed through MRI as increased radial (but unchanged axial) diffusion of water. *NeuroImage*, 17(3):1429–1436, 2002.
- [198] K. Schmierer, C.A.M. Wheeler-Kingshott, Boulby P.A., F. Scaravilli, D. Altmann, G.J. Barker, P.S. Tofts, and D.H. Miller. Diffusion tensor imaging of post mortem multiple sclerosis brain. *NeuroImage*, 35(2):467–477, 2007.
- [199] M. Filippi, M. Cercignani, M. Inglese, M.A. Horsfield, and G. Comi. Diffusion tensor magnetic resonance imaging in multiple sclerosis. *Neurology*, 56(3):304–311, 2001.
- [200] S.D. Roosendaal, J.J.G. Geurts, H. Vrenken, H.E. Hulst, K.S. Cover, J.A. Castelijns, P.J.W. Pouwels, and F. Barkhof. Regional DTI differences in multiple sclerosis patients. *NeuroImage*, 44(4):1397–1403, 2009.
- [201] L. Testaverde, L. Caporali, E. Venditti, G. Grillea, and C. Colonnese. Diffusion tensor imaging applications in multiple sclerosis patients using 3T magnetic resonance: A preliminary study. *European Radiology*, 22(5):990–997, 2012.
- [202] S.N. Jespersen, C.R. Bjarkam, J.R. Nyengaard, M.M. Chakravarty, B. Hansen, T. Vosegaard, L. Østergaard, D. Yablonskiy, N.C. Nielse, and P. Vestergaard-Poulsen. Neurite density from magnetic resonance diffusion measurements at ultrahigh field: Comparison with light microscopy and electron microscopy. *NeuroImage*, 49(1):205–216, 2010.
- [203] Y. Assaf and P.J. Basser. Composite hindered and restricted model of diffusion (CHARMED) MR imaging of the human brain. *NeuroImage*, 27(1):48–58, 2005.
- [204] M. Cercignani and C. Gadin. From micro- to macro-structures in multiple sclerosis: what is the added value of diffusion imaging. *NMR in Biomedicine*, 32(4), 2019.
- [205] D.C. Alexander, T.B. Dyrby, M. Nilsson, and H. Zhang. Imaging brain microstructure with diffusion MRI: practicality and applications. *NMR in Biomedicine*, 32(4), 2019.
- [206] E.M. Haacke, Y. Xu, Y.C.N. Cheng, and J.R. Reichenbach. Susceptibility weighted imaging (SWI). *Magnetic Resonance in Medicine*, 52(3):612–618, 2004.
- [207] S. Liu, S. Buch, Y. Chen, H.S. Choi, Y. Dai, C. Habib, J. Hu, J.Y. Jung, Y. Luo, D. Utriainen, M. Wang, D. Wu, S. Xia, and E.M. Haacke. Susceptibility-weighted imaging: current status and future directions. *NMR in Biomedicine*, 30(4), 2017.
- [208] E.M. Haacke, N.Y.C. Cheng, M.J. House, Q. Liu, J. Neelavalli, R.J. Ogg, A. Khan, M. Ayaz, W. Kirsch, and A. Obenaus. Imaging iron stores in the brain using magnetic resonance imaging. *Magnetic Resonance Imaging*, 23(1):1–25, 2005.
- [209] B. Yao, T.Q. Li, v.P. Gelderen, K. Shmueli, J.A. de Zwart, and J.H. Duyn. Susceptibility contrast in high field MRI of human brain as a function of tissue iron content. *NeuroImage*, 44(4):1259–1266, 2009.
- [210] W. Li, B. Wu, and C. Liu. Quantitative susceptibility mapping of human brain reflects spatial variation in tissue composition. *NeuroImage*, 55(4):1645–1656, 2011.

- [211] J. Lee, K. Shmueli, B.T. Kang, B. Yao, M. Fukunaga, P. Van Gelderen, S. Palumbo, F. Bosetti, A.C. Silva, and J.H. Duyn. The contribution of myelin to magnetic susceptibility-weighted contrasts in high-field MRI of the brain. *NeuroImage*, 59(4):3967–3975, 2012.
- [212] S. Hametner, V. Endmayr, A. Deistung, P. Palmrich, M. Prihoda, E. Haimburger, C. Menard, X. Feng, T. Haider, M. Leisser, U. Köck, A. Kaider, R. Höftberger, S. Rbinson, J.R. Reichenbach, H. Lassmann, H. Traxler, S. Trattnig, and G. Grabner. The influence of brain iron and myelin on magnetic susceptibility and effective transverse relaxation - A biochemical and histological validation study. *NeuroImage*, 179:117–133, 2018.
- [213] E.M. Haacke, Liu S., S. Buch, W. Zheng, D. Wu, and Y. Ye. Quantitative susceptibility mapping: Current status and future directions. *Magnetic Resonance Imaging*, 33(1):1–25, 2015.
- [214] A. Deistung, F. Schweser, and J.R. Reichenbach. Overview of quantitative susceptibility mapping. *NMR in Biomedicine*, 30(4), 2017.
- [215] C. Liu, W. Li, G.A. Johnson, and B. Wu. High-field (9.4T) MRI of brain dysmyelination by quantitative mapping of magnetic susceptibility. *NeuroImage*, 56(3):930–938, 2011.
- [216] G.A. Lodygensky, J.P. Marques, R. Maddage, E. Perroud, V.S. Sizonenko, P.S. Hüppi, and R. Gruetter. In vivo assessment of myelination by phase imaging at high magnetic field. *NeuroImage*, 59(3):1979–1987, 2012.
- [217] K. Deh, G.D. Ponath, Z. Molvi, G.C.T. Parel, K.M. Gillen, S. Zhang, T.D. Nguyen, P. Spincemaille, Y. Ma, A. Gupta, S.A. Gauthier, D. Pitt, and Y. Wang. Magnetic susceptibility increases as diamagnetic molecules breakdown: Myelin digestion during multiple sclerosis lesion formation contributes to increase on QSM. *Journal of Magnetic Resonance Imaging*, 48(5):1281–1287, 2018.
- [218] R. Muthupillai, D.J. Lomas, P.J. Rossan, J.F. Greenleaf, A. Manduca, and R.L. Ehman. Magnetic resonance elastography by direct visualization of propagating acoustic strain waves. *Science*, 269(5232):1854–1857, 1995.
- [219] M.C. Murphy, J. Huston, and R.L. Ehman. MR elastography of the brain and its application in neurological diseases. *NeuroImage*, 187:176–183, 2019.
- [220] M.C. Murphy, J. Huston, C.R. Jack, K.J. Glaser, A. Manduca, J.P. Felmlee, and R.L. Ehman. Decreased brain stiffness in Alzheimer’s disease determined by magnetic resonance elastography. *Journal of Magnetic Resonance Imaging*, 34(3):494–498, 2011.
- [221] C.L. Johnson, J.L. Holtrop, M.D.J. McGarry, J.B. Weaver, K.D. Paulsen, J.G. Georgiadis, and B.P. Sutton. 3D multislabs, multishot acquisition for fast, whole-brain MR elastography with high signal-to-noise efficiency. *Magnetic Resonance in Medicine*, 71(2):477–485, 2014.
- [222] S. Hirsch, J. Guo, R. Reiter, S. Papazoglou, T. Kroencke, J. Braun, and I. Sck. MR Elastography of the Liver and the Spleen Using a Piezoelectric Driver, Single-Shot Wave-Field Acquisition, and Multifrequency Dual Parameter Reconstruction. *Magnetic Resonance in Medicine*, 71(1):267–277, 2014.
- [223] M.D.J. McGarry, E.E.W. Van Houten, C.L. Johnson, J.G. Georgiadis, B.P. Sutton, J.B. Weaver, and K.D. Paulsen. Multiresolution MR elastography using nonlinear inversion. *Medical Physics*, 39(10):6388–6396, 2012.
- [224] F.B. Freimann, S. Müller, K.J. Streitberger, J. Guo, S. Rot, A. Ghorri, P. Vajoczy, R. Reiter, I. Sack, and J. Braun. MR elastography in a murine stroke model reveals correlation of macroscopic viscoelastic properties of the brain with neuronal density. *NMR in Biomedicine*, 26(11):1534–1539, 2013.

Bibliography

- [225] C. Klein, E.G. Hain, J. Braun, K. Riek, S. Mueller, B. Steiner, and I. Sack. Enhanced adult neurogenesis increases brain stiffness: In vivo magnetic resonance elastography in a mouse model of dopamine depletion. *PLoS ONE*, 9(3), 2014.
- [226] E.G. Hain, C. Klein, T. Munder, J. Baun, K. Riek, S. Mueller, I. Sack, and B. Steiner. Dopaminergic neurodegeneration in the mouse is associated with decrease of viscoelasticity of substantia nigra tissue. *PLoS ONE*, 11(8), 2016.
- [227] K. Schregel, E.W. Née Tysiak, P. Garteiser, I. Gemeinhardt, T. Prozorowski, O. Aktas, H. Merz, D. Petersen, J. Wuerfel, and R. Sinkus. Demyelination reduces brain parenchymal stiffness quantified in vivo by magnetic resonance elastography. *Proceedings of the National Academy of Sciences of the United States of America*, 109(17):6650–6655, 2012.
- [228] J.M. Millwad, J. Guo, D. Berndt, J. Braun, I. Sack, and C. Infante-Duarte. Tissue structure and inflammatory processes shape viscoelastic properties of the mouse brain. *NMR in Biomedicine*, 28(7):831–839, 2015.
- [229] J. Wuerfel, F. Paul, B. Beierbach, U. Hamhaber, D. Klitt, S. Papazoglou, F. Zipp, P. Martus, J. Braun, and I. Sack. MR-elastography reveals degradation of tissue integrity in multiple sclerosis. *NeuroImage*, 49(3):2520–2525, 2010.
- [230] K.J. Streitberger, I. Sack, D. Krefting, C. Pfüller, J. Braun, F. Paul, and J. Wuerfel. Brain viscoelasticity alteration in chronic-progressive multiple sclerosis. *PLoS ONE*, 7(1), 2012.
- [231] T. Yoshiura, S. Higano, A. Rubio, D.A. Shrier, W.E. Kwok, S. Iwanaga, and Y. Numaguchi. Heschl and Superior Temporal Gyri: Low Signal Intensity of the Cortex on T2-weighted MR Images of the Normal Brain. *Radiology*, 214(1):217–221, 2000. doi: 10.1148/radiology.214.1.r00ja17217.
- [232] I.S. Sigalovsky, B. Fischl, and J.R. Melcher. Mapping an intrinsic MR property of gray matter in auditory cortex of living humans: A possible marker for primary cortex and hemispheric differences. *NeuroImage*, 32(4):1524–1537, 2006.
- [233] M.F. Glasser and D.C. Van Essen. Mapping Human Cortical Areas In Vivo Based on Myelin content as Revealed by T1- and T2-Weighted MRI. *Journal of Neuroscience*, 31(32):11597–11616, 2011.
- [234] M. Ganzetti, N. Wenderoth, and D. Mantini. Whole brain myelin mapping using T1- and T2-weighted MR imaging data. *Frontiers in Human Neuroscience*, 8, 2014.
- [235] M.N. Uddin, T.D. Figley, R.A. Marrie, and C.R. Figley. Can T1w/T2w ratio be used as a myelin-specific measure in subcortical structures? Comparisons between FSE-based T1w/T2w ratios, GRASE-based T1w/T2w ratios and multi-echo GRASE-based myelin water fractions. *NMR in Biomedicine*, 31(3):e3868, 2018.
- [236] Y. Sui, P. Storey, A. Samsonov, and M. Lazar. Comparison between quantitative magnetization transfer imaging and ratio of T1w/T2w approach in myelin mapping. *Proc. Joint Annual Meeting ISMRM-ESMRMB, Paris, France*, page 1867, 2018.
- [237] H. Grydeland, K.B. Walhovd, C.K. Tamnes, L.T. Westlye, and A.M. Fjell. Intracortical Myelin Links with Performance Variability across the Human Lifespan: Results from T1- and T2-Weighted MR Myelin Mapping and Diffusion Tensor Imaging. *Journal of Neuroscience*, 33(47):18618–18630, 2013.

- [238] A. Beer, V. Biberacher, P. Schmidt, R. Righart, D. Buck, A. Berthele, J. Kirschke, C. Zimmer, B. Hemmer, and M. Mühlau. Tissue damage within normal appearing white matter in early multiple sclerosis: assessment by the ratio of T1- and T2-weighted MR image intensity. *Journal of Neurology*, 263(8):1495–1502, 2016.
- [239] C. Beaulieu. The Biological Basis of Diffusion Anisotropy. In *Diffusion MRI*, pages 155–183. Elsevier, 2014.
- [240] S.D. Robinson, K. Bredies, D. Khabipova, B. Dymerska, J.P. Marques, and F. Schweser. An illustrated comparison of processing methods for MR phase imaging and QSM: combining array coil signals and phase unwrapping. *NMR in Biomedicine*, 30(4), 2017.
- [241] F. Schweser, S.D. Robinson, L. de Rochefort, W. Li, and K. Bredies. An illustrated comparison of processing methods for phase MRI and QSM: removal of background field contributions from sources outside the region of interest. *NMR in Biomedicine*, 30(4):e3604, 2017.
- [242] A. Hagiwara, M. Hori, K. Kamagata, M. Warntjes, D. Matsuyoshi, M. Nakazawa, R. Ueda, C. Andica, S. Koshino, T. Maekawa, R. Irie, T. Takamura, K.K. Kumamaru, O. Abe, and S. Aoki. Myelin Measurement: Comparison Between Simultaneous Tissue Relaxometry, Magnetization Transfer Saturation Index, and T1w/T2w Ratio Methods. *Scientific Reports*, 8(1):10554, 2018.
- [243] N.C. Silver, E. Hughes, K. Birnie, P.D. Molyneux, D.G. MacManus, G.J. Barker, P.S. Tofts, and D.H. Miller. Magnetization transfer imaging provides a highly reproducible quantitative measure of brain tissue structural integrity. *Proceedings of the International Society of Magnetic Resonance in Medicine*, page 1430, 1997.
- [244] I.R. Levesque, J.G. Sled, S. Narayanan, Giacomini P.S., L.T. Ribeiro, D.L. Arnold, and G.B. Pike. Reproducibility of quantitative magnetization-transfer imaging parameters from repeated measurements. *Magnetic Resonance in Medicine*, 64(2):391–400, 2010.
- [245] L. Zhang, T. Chen, H. Tian, H. Xue, H. Ren, L. Li, Q. Fan, B. Wen, and Z. Ren. Reproducibility of inhomogeneous magnetization transfer (ihMT): A test-retest, multi-site study. *Magnetic Resonance Imaging*, 57:243–249, 2019.
- [246] T. Duval, V. Smith, N. Stikov, E.C. Klawiter, and J. Cohen-Adad. Scan-rescan of axcaliber, macro-molecular tissue volume, and g-ratio in the spinal cord. *Magnetic Resonance in Medicine*, 79(5):2759–2765, 2018.
- [247] C. Vollmar, J. O’Muircheartaigh, G.J. Barker, M.R. Symms, P. Thompson, V. Kumari, J.S. Duncan, M.P. Richardson, and M.J. Koepp. Identical, but not the same: Intra-site and inter-site reproducibility of fractional anisotropy measures on two 3.0T scanners. *NeuroImage*, 51(4):1384–1394, 2010.
- [248] X. Feng, A. Deistung, and J.R. Reichenbach. Quantitative susceptibility mapping (QSM) and R2* in the human brain at 3 T: Evaluation of intra-scanner repeatability. *Zeitschrift für Medizinische Physik*, 28(1):36–48, 2018.
- [249] X. Huang, H. Chafi, K.L. Mathews, O. Carmichael, T. Li, Q. Miao, S. Wang, and G. Jia. Magnetic resonance elastography of the brain: A study of feasibility and reproducibility using an ergonomic pillow-like passive driver. *Magnetic Resonance Imaging*, 59:68–76, 2019.
- [250] M. Arshad, J.A. Stanley, and N. Raz. Test-retest reliability and concurrent validity of in vivo myelin content indices: Myelin water fraction and calibrated T1w/T2w image ratio. *Human Brain Mapping*, 38(4):1780–1790, 2017.

Bibliography

- [251] S.M. Meyers, I.M. Vavasour, B. Mädler, T. Harris, E. Fu, D.K.B. Li, A.L. Traboulsee, A.L. Mackay, and C. Laule. Multicenter measurements of myelin water fraction and geometric mean T2: Intra- and inter-site reproducibility. *Journal of Magnetic Resonance Imaging*, 38(6):1445–1453, 2013.
- [252] B. Lakhani, M.R. Borich, J.N. Jackson, K.P. Wadden, S. Peters, A. Villamayor, A.L. MacKay, I.M. Vavasour, A. Rauscher, and L.A. Boyd. Motor Skill Acquisition Promotes Human Brain Myelin Plasticity. *Neural Plasticity*, 2016:1–7, 2016.
- [253] L.E. Lee, E. Ljungberg, D. Shin, C.R. Figley, I.M. Vavasour, A. Rauscher, J. Cohen-Adad, D.K.B. Li, A.L. Traboulsee, A.L. MacKay, J. Lee, and S.H. Kolind. Inter-Vendor Reproducibility of Myelin Water Imaging Using a 3D Gradient and Spin Echo Sequence. *Frontiers in Neuroscience*, 12(NOV), 2018.
- [254] Y. Nam, D.H. Kim, and J. Lee. Physiological noise compensation in gradient-echo myelin water imaging. *NeuroImage*, 120:345–349, 2015.
- [255] G. Okubo, T. Okada, A. Yamamoto, M. Kanagaki, Y. Fushimi, T. Okada, K. Murata, and K. Togashi. MP2RAGE for deep gray matter measurement of the brain: A comparative study with MP-RAGE. *Journal of Magnetic Resonance Imaging*, 43(1):55–62, 2016.
- [256] S.C. Deoni, R. Samson, and C.A. Wheeler-Kingshot. Intra and inter-site reproducibility of myelin water volume fraction value derived using mcDESPOT. *Proceedings of the 17th Annual Meeting of the International Society of Magnetic Resonance in Medicine*, page 4530, 2009.
- [257] A. Hagiwara, M. Hori, J. Cohen-Adad, M. Nakazawa, Y. Suzuki, A. Kasahara, M. Horita, T. Haruyama, C. Andica, T. Maekawa, K. Kamagata, K.K. Kumamaru, O. Abe, and S. Aoki. Linearity, Bias, Intrascanner Repeatability, and interscanner Reproducibility of Quantitative Multidynamic Multiecho Sequence for Rapid Simultaneous Relaxometry at 3 T: A Validation Study with a Standardized Phantom and Healthy Controls. *Investigative Radiology*, 54(1):39–47, 2019.
- [258] K.L. West, N.D. Kelm, R.P. Carson, D.F. Gochberg, K.C. Ess, and M.D. Does. Myelin volume fraction imaging with MRI. *NeuroImage*, 182:511–521, 2018.
- [259] Y. Chen, M.-H. Chen, K.R. Baluyot, T.M. Potts, J. Jimenez, and W. Lin. MR fingerprinting enables quantitative measures of brain tissue relaxation times and myelin water fraction in the first five years of life. *NeuroImage*, 186:782–793, 2019.
- [260] M. Nagtegaal, P. Koken, T. Amthor, and M. Donev. Fast multi-component analysis using a joint sparsity constraint for MR fingerprinting. *Magnetic Resonance in Medicine*, 83(2):521–534, 2020.
- [261] T. Hilbert, D. Xia, K.T. Block, Z. Yu, R. Lattanzi, D.K. Sodickson, T. Kober, and M.A. Cloos. Magnetization transfer in magnetic resonance fingerprinting. *Magnetic Resonance in Medicine*, 84(1):128–141, 2020.
- [262] G. Nataraj, J.-F. Nielsen, M. Gao, and J.A. Fessler. Fast, Precise Myelin Water Quantification using DESS MRI and Kernel Learning. *arXiv preprint arXiv:1809.08908*, 2018.
- [263] G.F. Piredda, T. Hilbert, J. Richiardi, E.J. Canales-Rodríguez, M. Pizzolato, R. Meuli, J.-P. Thiran, and T. Kober. Deriving Brain Myelin Water Fraction Maps from Relaxometry: a Data-Driven Approach. *Proceedings of the International Society of Magnetic Resonance in Medicine, Montreal, Canada*, page 668, 2019.
- [264] Y. Tachibana, A. Hagiwara, M. Hori, J. Kershaw, M. Nakazawa, T. Omatsu, R. Kishimoto, K. Yokoyama, N. Hattori, S. Aoki, T. Higashi, and T. Obata. The utility of a convolutional neural network for generating a myelin volume index map from rapid simultaneous relaxometry imaging. *Magnetic Resonance in Medical Sciences*, 19(4), 2019.

-
- [265] K.D. Harkins, M.D. Does, and W.A. Grissom. Iterative method for predistortion of MRI gradient waveforms. *IEEE Transactions on Medical Imaging*, 33(8):1641–1647, 2014.
 - [266] D.A. Feinberg and K. Oshio. Phase errors in multi-shot echo planar imaging. *Magnetic Resonance in Medicine*, 32(4):535–539, 1994.
 - [267] D.A. Feinberg and K. Oshio. Gradient-echo shifting in fast MRI techniques (GRASE imaging) for correction of field inhomogeneity errors and chemical shift. *Journal of Magnetic Resonance (1969)*, 97(1):177–183, 1992.
 - [268] R.M. Lebel and A.H. Wilman. Transverse relaxometry with stimulated echo compensation. *Magnetic Resonance in Medicine*, 64(4), 2010.
 - [269] D. Kumar, S. Siemonsen, C. Heesen, J. Fiehler, and J. Sedlacik. Noise robust spatially regularized myelin water fraction mapping with the intrinsic B1-error correction based on the linearized version of the extended phase graph model. *Journal of Magnetic Resonance Imaging*, 43(4):800–817, 2016.
 - [270] F.A. Breuer, S.A.R. Kannengiesser, M. Blaimer, N. Seiberlich, P.M. Jakob, and M.A. Griswold. General formulation for quantitative G-factor calculation in GRAPPA reconstructions. *Magnetic Resonance in Medicine*, 62(3):739–746, 2009.
 - [271] V.J. Manjón, P. Coupé, L. Concha, A. Bades, D.L. Collins, and M. Robles. Diffusion Weighted Image Denoising Using Overcomplete Local PCA. *PLoS ONE*, 8(9), 2013.
 - [272] E.J. Canales-Rodríguez, M. Pizzolato, G.F. Piredda, T. Hilbert, K. Nicolas, T. Kober, J.-P. Thiran, C. Pot, and A. Daducci. Robust Myelin Water Imaging from multi-echo T2 data using second-order Tikhonov regularization with control points. *Proceedings of the International Society of Magnetic Resonance in Medicine, Montreal, Canada*, 2019.
 - [273] E.J. Canales-Rodríguez, M. Pizzolato, G.F. Piredda, T. Hilbert, N. Kunz, C. Pot, T. Yu, R. Salvador, E. Pomarol-Clotet, T. Kober, J.-P. Thiran, and A. Daducci. Comparison of non-parametric T2 relaxometry methods for myelin water quantification. *Medical Image Analysis*, page 101959, 2021.
 - [274] A. MacKay, C. Laule, I. Vavasour, T. Bjarnason, S. Kolind, and B. Mädler. Insights into brain microstructure from the T distribution. *Magnetic Resonance Imaging*, 24(4):515–525, 2006.
 - [275] T. Hilbert, J. Schulz, J.P. Marques, J.-P. Thiran, G. Krueger, D.G. Norris, and T. Kober. Fast model-based T2 mapping using SAR-reduced simultaneous multislice excitation. *Magnetic Resonance in Medicine*, 82(6):2090–2103, 2019.
 - [276] A.M. Sprinkart, J.A. Luetkens, F. Träber, J. Doerner, J. Gieseke, B. Schnackenburg, G. Schitz, D. Thomas, R. Homs, W. Block, H. Schild, and C.P. Naehle. Gradient Spin Echo (GraSE) imaging for fast myocardial T2 mapping. *Journal of Cardiovascular Magnetic Resonance*, 17(1):12, 2015.
 - [277] V.F. Megen, A. Knowles, E. Vrijhof, J.H. Wondergem, and V.D.H. Bosch. Application of a GRASE multi-echo sequence for rapid high resolution T2 mapping of the prostate. *Proceedings of the International Society of Magnetic Resonance in Medicine*, 2003.
 - [278] S. Sabouri, S.D. Chang, R. Savdie, J. Zhang, E.C. Jones, S.L. Goldenberg, P.C. Black, and P. Kozlowski. Luminal water imaging: A new MR imaging T2 mapping technique for prostate cancer diagnosis. *Radiology*, 284(2):451–459, 2017.

Bibliography

- [279] B. Bilgic, T.H. Kim, C. Liao, M.K. Manhard, L.L. Wald, J.P. Haldar, and K. Setsompop. Improving parallel imaging by jointly reconstructing multi-contrast data. *Magnetic Resonance in Medicine*, 80(2):619–632, 2018.
- [280] H. Szu, M. Chen, E. Ljungberg, A.L. Mackay, and P. Kozlowski. Compressed Sensing 3D GRASE with Group-Sparse Reconstruction for Brain Myelin Water Imaging. *Proceedings of the International Society of Magnetic Resonance Imaging*, 2017.
- [281] A. Cristobal-Huerta, Poot D.H.J., M.W. Vogel, G.P. Krestin, and J.A. Hernandez-Tamames. Compressed Sensing 3D-GRASE for faster High-Resolution MRI. *Magnetic Resonance in Medicine*, 82(3):984–999, 2019.
- [282] C. Laule and G.R.W. Moore. Myelin water imaging to detect demyelination and remyelination and its validation in pathology. *Brain Pathology*, 28(5):750–764, 2018.
- [283] M.D. Does. Inferring brain tissue composition and microstructure via MR relaxometry. *NeuroImage*, 182:136–148, 2018.
- [284] N. Weiskopf, S. Mohammadi, A. Lutti, and M.F. Callaghan. Advances in MRI-based computational neuroanatomy: from morphometry to in-vivo histology. *Current Opinion in Neurology*, 28(4):313–322, 2015.
- [285] K. Tabelow, E.e Balteau, J. Ashburner, M.F. Callaghan, B. Draganski, G. elms, F. Kherif, T. Leutritz, A. Lutti, C. Phillips, E. Reimer, L. Ruthotto, M. Seif, N. Weiskopf, G. Ziegler, and S. Mohammadi. hMRI - A toolbox for quantitative MRI in neuroscience and clinical research. *NeuroImage*, 194:191–210, 2019.
- [286] G.S. Drenthen, W.H. Backes, and J.F.A. Jansen. Estimating myelin-water content from anatomical and diffusion images using spatially undersampled myelin-water imaging through machine learning. *NeuroImage*, 226:117626, 2021.
- [287] N. Khattar, Z. Gong, M. Kiely, C. Triebswetter, M.H. Alsameen, and M. Bouhrara. Myelin water fraction determination from relaxation times and proton density through deep learning neural network. *Proceedings of the International Society of Magnetic Resonance in Medicine, Vancouver, Canada*, page 2171, 2021.
- [288] G.F. Piredda, T. Hilbert, C. Granziera, G. Bonnier, R. Meuli, F. Molinari, J.-P. Thiran, and T. Kober. Quantitative brain relaxation atlases for personalized detection and characterization of brain pathology. *Magnetic Resonance in Medicine*, 83(1):337–351, 2020.
- [289] P. Isola, J.Y. Zhu, T. Zhou, and A.A. Efros. Image-to-image translation with conditional adversarial networks. *Proceedings - 30th IEEE Conference on Computer Vision and Pattern Recognition, CVPR 2017*, January:5967–5976, 2017.
- [290] S.U.H. Dar, M. Yurt, L. Karacan, A. Erde, E. Erdem, and T. Cukur. Image Synthesis in Multi-Contrast MRI With Conditional Generative Adversarial Networks. *IEEE Transactions on Medical Imaging*, 38(10):2375–2388, 2019.
- [291] O. Ronneberger, P. Fischer, and T. Brox. U-net: Convolutional networks for biomedical image segmentation. *Lecture Notes in Computer Science*, 9351:234–241, 2015.
- [292] M. Mirza and S. Osindero. Conditional Generative Adversarial Nets. *arXiv preprint arXiv:1411.1784*, 2014.
- [293] A. Chartsias, T. Joyce, M.V. Giuffrida, and S.A. Tsaftaris. Multimodal MR Synthesis via Modality-Invariant Latent Representation. *IEEE Transactions on Medical Imaging*, 37(3):803–814, 2018.

-
- [294] J.-Y. Zhu, T. Park, P. Isola, and A.A. Efros. Unpaired Image-to-Image Translation Using Cycle-Consistent Adversarial Networks. *2017 IEEE International Conference on Computer Vision (ICCV)*, pages 2242–2251, 2017.
 - [295] Per Welader, Simon Karlsson, and Anders Eklund. Generative Adversarial Networks for Image-to-Image Translation on Multi-Contrast MR Images - A Comparison of CycleGAN and UNIT. *arXiv preprint arXiv:1806.07777*, 2018.
 - [296] E. Mussard, T. Hilbert, C. Forman, R. Meuli, J.-P. Thiran, and T. Kober. High-resolution 3D T1 and T2 Mapping in the Brain Using Compressed Sensing and Dictionary Fitting. *Proceedings of the International Society of Magnetic Resonance in Medicine, Montreal, Canada*, 2019.
 - [297] M. Bellani, F. Boschello, G. Devecchio, N. Dusi, C.A. Altamura, M. Ruggeri, and P. Brambilla. DTI and myelin plasticity in bipolar disorder: Integrating Neuroimaging and Neuropathological Findings. *Frontiers in Psychiatry*, 7(MAR), 2016.
 - [298] A. Panda, B.B. Mehta, S. Coppo, Y. Jiang, D. Ma, N. Seiberlich, M.A. Griswold, and V. Gulani. Magnetic resonance fingerprinting—an overview. *Current opinion in biomedical engineering*, 3:56–66, 2017.
 - [299] B. Rieger, M. Akçakaya, J.C. Pariente, S. Llufríu, E. Martínez-Heras, S. Weingärtner, and L.R. Schad. Time efficient whole-brain coverage with mr fingerprinting using slice-interleaved echo-planar-imaging. *Scientific reports*, 8(1):1–12, 2018.
 - [300] Y. Chen, Z. Fang, S. Che Hung, W.T. Chang, D. Shen, and W. Lin. High-resolution 3D MR Fingerprinting using parallel imaging and deep learning. *NeuroImage*, 06:116329, 2020.
 - [301] S. Tang, C. Fernandez-Granda, S. Lannuzel, B. Bernstein, R. Lattanzi, M. Cloos, F. Knoll, and J. Assländer. Multicompartment magnetic resonance fingerprinting. *Inverse problems*, 34(9):094005, 2018.
 - [302] S. Mohammadi, D. Carey, F. Dick, J. Diedrichsen, M.I. Sereno, M. Reiser, M.F. Callaghan, and N. Weiskopf. Whole-brain in-vivo measurements of the axonal G-ratio in a group of 37 healthy volunteers. *Frontiers in Neuroscience*, 9(NOV), 2015.
 - [303] M. Bouhrara, A.C. Rejimon, D.Y. Lee, and R.G. Spencer. Myelin water fraction, diffusion tensor imaging and g-ratio measurements characterize myelin changes in normative aging, mild cognitive impairment and dementia. *Proc. Joint Annual Meeting ISMRM-ESMRMB, Paris, France*, page 931, 2018.
 - [304] D.H. Kim, N. Choi, S.M. Gho, J. Shin, and C. Liu. Simultaneous imaging of in vivo conductivity and susceptibility. *Magnetic Resonance in Medicine*, 71(3):1144–1150, 2014.
 - [305] G. Bonnier, B. Maréchal, M.J. Fartaria, P. Falkowski, J.P. Marques, S. Simioni, M. Schluep, R. Du Pasquier, J.-P. Thiran, G. Krueger, and C. Granziera. The Combined Quantification and Interpretation of Multiple Quantitative Magnetic Resonance Imaging Metrics Enlightens Longitudinal Changes Compatible with Brain Repair in Relapsing-Remitting Multiple Sclerosis Patients. *Frontiers in Neurology*, 8:506, 2017.
 - [306] T. Chitnis, C.R. Guttmann, A. Zaitsev, A. Musallam, B. Weinstock-Guttman, A. Yeh, M. Rodriguez, J. Ness, M.P. Gorman, and B.C. Healy. Quantitative MRI analysis in children with multiple sclerosis: a multicenter feasibility pilot study. *BMC neurology*, 13:173, 2013.
 - [307] EPh.S. Fischmeister, I. Höllinger, N. Klinger, A. Geissler, M.C. Wurnig, E. Matt, J. Rath, S.D. Robinson, S. Trattnig, and R. Beisteiner. The benefits of skull stripping in the normalization of clinical fMRI data. *NeuroImage: Clinical*, 3:369–380, 2013.

Bibliography

- [308] C.-M. Huang, S.-H. Lee, I.-T. Hsiao, W.-C. Kuan, Y.-Y. Wai, H.-J. Ko, Y.-L. Wan, Y.-Y. Hsu, and H.-L. Liu. Study-specific EPI template improves group analysis in functional MRI of young and older adults. *Journal of Neuroscience Methods*, 189(2):257–266, 2010.
- [309] S. hang and K. Arfanakis. Role of standardized and study-specific human brain diffusion tensor templates in inter-subject spatial normalization. *Journal of Magnetic Resonance Imaging*, 37(2):372–381, 2013.
- [310] A.R. Ridwan, S. Zhang, X. Qi, D.A. Benntt, Y. Yang, and K. Arfanakis. Evaluation of standardized as well as study-specific and age-specific structural T1-weighted brain templates for use in studies on older adults. *Proceedings of the International Society of Magnetic Resonance in Medicine, Montreal, Canada*, page 334, 2019.
- [311] G. Okubo, T. Okada, A. Yamamoto, Y. Fushimi, T. Okada, and K. Togashi. Age-related change of the whole brain T1 relaxation time: voxel-wise study with MP2RAGE. *Proceedings of the Annual Meeting of ISMRM*, page 2338, 2017.
- [312] C. Scarpazza, G. Sartori, M.S. De Simone, and A. Mechelli. When the single matters more than the group: Very high false positive rates in single case Voxel Based Morphometry. *NeuroImage*, 70:175–188, 2013.
- [313] G. Grabner, B.A. Poser, K. Fujimoto, J.R. Polimeni, L.L. Wal, S. Trattng, I. Toni, and M. Barth. A study-specific fMRI normalization approach that operates directly on high resolution functional EPI data at 7 Tesla. *NeuroImage*, 100:710–714, 2014.
- [314] G. Balakrishnan, A. Zhao, M.R. Sabuncu, J. Guttag, and V.A. Dalca. VoxelMorph: A Learning Framework for Deformable Medical Image Registration. *IEEE Transactions on Medical Imaging*, pages 1–1, 2019.
- [315] M. Neema, D. Goldberg-Zimring, Z.D. Guss, B.C. Healy, C.R.G. Guttman, M.K. Houtchens, H.L. Weiner, M.A. Horsfield, D.B. Hackney, D.C. Alsop, and R. Bakshi. 3 T MRI relaxometry detects T2 prolongation in the cerebral normal-appearing white matter in multiple sclerosis. *NeuroImage*, 46(3):633–641, 2009.
- [316] K.M. Hasan, I.S. Walimuni, L.A. Kramer, and R.E. Frye. Human brain atlas-based volumetry and relaxometry: Application to healthy development and natural aging. *Magnetic Resonance in Medicine*, 64(5):1382–1389, 2010.
- [317] C. Badve, A. Yu, M. Rogers, D. Ma, Y. Liu, M. Schluchter, J. Sunshine, M. Griswold, and V. Gulani. Simultaneous T1 and T2 brain relaxometry in asymptomatic volunteers using magnetic resonance fingerprinting. *Tomography: a journal for imaging research*, 1(2):136, 2015.
- [318] R. Kumar, S. Delsha, M.A. Woo, P.M. Macey, and R.M. Harper. Age-related regional brain T2-relaxation changes in healthy adults. *Journal of Magnetic Resonance Imaging*, 35(2):300–308, 2012.
- [319] V.A. Faria, A. Hoon, E. Stashinko, X. Li, H. Jiang, A. Mashayekh, K. Akhter, J. Hsu, K. Oishi, J. Zhang, M.I. Miller, P.C.M. van Zijl, and S. Mori Susumu. Quantitative analysis of brain pathology based on MRI and brain atlases-Applications for cerebral palsy. *NeuroImage*, 54(3), 2011.
- [320] S. Kolind, L. Matthews, H. Johansen-erg, M.I. Leite, S.C.R. Williams, S. Deoni, and J. Palace. Myelin water imaging reflects clinical variability in multiple sclerosis. *NeuroImage*, 60(1):263–270, 2012.
- [321] J. Mai, M. Abubrig, T. Lehmann, T. Hilbert, E. Weiland, M.O. Grimm, U. Teichgräber, and T. Franiel. T2 Mapping in Prostate Cancer. *Investigative Radiology*, 54(3):146–152, 2019.

- [322] N. Vietti Violi, T. Hilbert, J.A.M. Bastiaansen, J.-F. Knebel, J.-B. Ledoux, A. Stemmer, R. Meuli, T. Kober, and S. Schmidt. Patient respiratory-triggered quantitative T2 mapping in the pancreas. *Journal of Magnetic Resonance Imaging*, 50(2):410–416, 2019.
- [323] R.J. Ogg and R.G. Steen. Age-related changes in BrainT1 are correlated with iron concentration. *Magnetic Resonance in Medicine*, 40(5):749–753, 1998.
- [324] B. Morel, G.F. Piredda, J.-P. Cottier, C. Tauber, C. Destrieux, T. Hilbert, D. Sirinelli, J.-P. Thiran, B. Maréchal, and T. Kober. Normal volumetric and T1 relaxation time values at 1.5 T in segmented pediatric brain MRI using a MP2RAGE acquisition. *European Radiology*, 31(3):1505–1516, 2021.
- [325] A.W. Toga, P.M. Thompson, and E.R. Sowell. Mapping brain maturation. *Trends in Neurosciences*, 29(3):148–159, 2006.
- [326] J. Pujol, A. López-Sala, N. Sebastián-Gallés, J. Deus, N. Cardoner, C. Soriano-Mas, A. Moreno, and A. Sans. Delayed myelination in children with developmental delay detected by volumetric MRI. *NeuroImage*, 22:897–903, 2004.
- [327] M. Serru, B. Maréchal, T. Kober, L. Ribier, C. Sembely Taveau, D. Sirinelli, J.-P. Cottier, and B. Morel. Improving diagnosis accuracy of brain volume abnormalities during childhood with an automated MP2RAGE-based MRI brain segmentation. *Journal of Neuroradiology*, 2019.
- [328] B. Morel, G. Antoni, J.P. Teglas, I. Bloch, and C. Adamsbaum. Neonatal brain MRI: how reliable is the radiologist’s eye? *Neuroradiology*, 58(2):189–193, 2016.
- [329] S. Guleria and T.G. Kelly. Myelin, myelination, and corresponding magnetic resonance imaging changes. *Radiologic clinics of North America*, 52(2):227–239, 2014.
- [330] M. Wilke, V.J. Schmithorst, and S.K. Holland. Normative pediatric brain data for spatial normalization and segmentation differs from standard adult data. *Magnetic Resonance in Medicine*, 50(4):749–757, 2003. <https://doi.org/10.1002/mrm.10606>.
- [331] J. West, J.B.M. Warntjes, and P. Lundberg. Novel whole brain segmentation and volume estimation using quantitative MRI. *European Radiology*, 22(5):998–1007, 2012.
- [332] B. Fischl. FreeSurfer. *NeuroImage*, 62(2):774–781, 2012.
- [333] C. Andica, A. Hagiwara, M. Hori, M. Nakazawa, M. Goto, S. Koshino, K. Kamagata, K.K. Kumamaru, and S. Aoki. Automated brain tissue and myelin volumetry based on quantitative MR imaging with various in-plane resolutions. *Journal of Neuroradiology*, 45(3):164–168, 2018.
- [334] K. Ambarki, A. Wåhlin, R. Birgander, A. Eklund, and J. Malm. MR Imaging of Brain Volumes: Evaluation of a Fully Automatic Software. *American Journal of Neuroradiology*, 32(2):408 LP – 412, 2011.
- [335] M. Wilke, I. Krägeloh-Mann, and S.K. Holland. Global and local development of gray and white matter volume in normal children and adolescents. *Experimental Brain Research*, 178(3):296–307, 2007.
- [336] Y. Xu, B. Morel, S. Dahdouh, É. Puybureau, A. Virzì, H. Urien, T. Géraud, C. Adamsbaum, and I. Bloch. The challenge of cerebral magnetic resonance imaging in neonates: A new method using mathematical morphology for the segmentation of structures including diffuse excessive high signal intensities. *Medical Image Analysis*, 48:75–94, 2018.
- [337] S.D. Serai, J. Dudley, and J.L. Leach. Comparison of whole brain segmentation and volume estimation in children and young adults using SPM and SyMRI. *Clinical Imaging*, 57:77–82, 2019.

Bibliography

- [338] A. McAllister, J. Leach, H. West, B. Jones, B. Zhang, and S. Serai. Quantitative synthetic MRI in children: Normative intracranial tissue segmentation values during development. *American Journal of Neuroradiology*, 38(12):2364–2372, 2017.
- [339] E. Courchesne, H.J. Chisum, J. Townsend, A. Cowles, J. Covington, B. Egaas, M. Harwood, S. Hinds, and G.A. Press. Normal Brain Development and Aging: Quantitative Analysis at in Vivo MR Imaging in Healthy Volunteers. *Radiology*, 216(3):672–682, 2000. doi: 10.1148/radiology.216.3.r00au37672.
- [340] S. Eminian, S.D. Hajdu, R. Meuli, P. Maeder, and P. Hagmann. Rapid high resolution T1 mapping as a marker of brain development: Normative ranges in key regions of interest. *PLoS ONE*, 13(6), 2018.
- [341] S. Cho, D. Jones, W.E. Reddick, R.J. Ogg, and R.G. Steen. Establishing norms for age-related changes in proton T1 of human brain tissue in vivo. *Magnetic resonance imaging*, 15(10):1133–1143, 1997.
- [342] R.G. Steen, R.J. Ogg, W.E. Reddick, and P.B. Kingsley. Age-related changes in the pediatric brain: quantitative MR evidence of maturational changes during adolescence. *American Journal of Neuroradiology*, 18(5):819 LP – 828, 1997.
- [343] P. Galluzzi, M.C. de Jong, S. Sirin, P. Maeder, P. Piu, A. Cerase, L. Monti, H.J. Brisse, J.A. Castelijns, P. de Graaf, S.L. Goericke, and On behalf of the European Retinoblastoma Imaging Collaboration (ERIC). MRI-based assessment of the pineal gland in a large population of children aged 0–5 years and comparison with pineoblastoma: part I, the solid gland. *Neuroradiology*, 58(7):705–712, 2016.
- [344] R. Tutunji, M. El Homsy, S. Saaybi, N. AL Arab, H. Tamim, M. Makki, M. Hourani, and R. Hourani. Thalamic volume and dimensions on MRI in the pediatric population: Normative values and correlations: (A cross sectional study). *European Journal of Radiology*, 109:27–32, 2018. doi: 10.1016/j.ejrad.2018.10.018.
- [345] S. Ya, T. Qian, B. Maréchal, T. Kober, X. Zhang, J. Zhu, J. Lei, M. Li, and Z. Jin. Test-retest variability of brain morphometry analysis: an investigation of sequence and coil effects. *Annals of Translational Medicine*, 8(1):12–12, 2020.
- [346] G. Okubo, T. Okada, A. Yamamoto, Y. Fushimi, T. Okada, K. Murata, and K. Togashi. Relationship between aging and T1 relaxation time in deep gray matter: A voxel-based analysis. *Journal of Magnetic Resonance Imaging*, 46(3):724–731, 2017. <https://doi.org/10.1002/jmri.25590>.
- [347] D.P. Shamonin, E.E. Bron, B.P.F. Lelieveldt, M. Smits, S. Klein, and M. Staring. Fast parallel image registration on CPU and GPU for diagnostic classification of Alzheimer’s disease. *Frontiers in neuroinformatics*, 7:50, 2013.
- [348] Brain Development Cooperative Group. Total and Regional Brain Volumes in a Population-Based Normative Sample from 4 to 18 Years: The NIH MRI Study of Normal Brain Development. *Cerebral Cortex*, 22(1):1–12, 2012.
- [349] X. Chen, T. Qian, B. Maréchal, G. Zhang, T. Yu, Z. Ren, D. Ni, C. Liu, Y. Fu, N. Chen, and K. Li. Quantitative volume-based morphometry in focal cortical dysplasia: A pilot study for lesion localization at the individual level. *European Journal of Radiology*, 105:240–245, 2018. doi: 10.1016/j.ejrad.2018.06.019.

- [350] R. Kotikalapudi, P. Martin, M. Erb, K. Scheffler, J. Marquetand, B. Bender, and N.K. Focke. MP2RAGE multispectral voxel-based morphometry in focal epilepsy. *Human Brain Mapping*, 40(17):5042–5055, 2019. <https://doi.org/10.1002/hbm.24756>.
- [351] World Health Organization. Child Growth Standards: methods and development. WHO, 2007.
- [352] S.S. Guo, A.F. Roche, W.M.C. Chumlea, C. Johnson, R.J. Kuczmarski, and R. Curtin. Statistical effects of varying sample sizes on the precision of percentile estimates. *American Journal of Human Biology*, 1(1):64–74, 2000. [https://doi.org/10.1002/\(SICI\)1520-6300\(200001/02\)12:13.0.CO;2-N](https://doi.org/10.1002/(SICI)1520-6300(200001/02)12:13.0.CO;2-N).
- [353] L.H. Tan, J.A. Spinks, C.-M. Feng, W.T. Siok, C.A. Perfetti, J. Xiong, P.T. Fox, and J.-H. Gao. Neural systems of second language reading are shaped by native language. *Human Brain Mapping*, 18(3):158–166, 2003. <https://doi.org/10.1002/hbm.10089>.
- [354] Y. Tang, C. Hojatkashani, I.D. Dinov, B. Sun, L. Fan, X. Lin, H. Qi, X. Hua, S. Liu, and A.W. Toga. The construction of a Chinese MRI brain atlas: A morphometric comparison study between Chinese and Caucasian cohorts. *NeuroImage*, 51(1):33–41, 2010.
- [355] B. Morel, F. Andersson, M. Samalbidé, G. Binninger, E. Carpentier, D. Sirinelli, and J.-P. Cottier. Impact on child and parent anxiety level of a teddy bear-scale mock magnetic resonance scanner. *Pediatric Radiology*, 50(1):116–120, 2020.
- [356] B. Morel, A. Piegay, M. Perivier, S. Obry, B. Maréchal, G.F. Piredda, T. Hilbert, T. Kober, C. Tauber, P. Castelnau, and J.P. Cottier. Automated brain MRI volumetry and T1 relaxometry in children with focal epilepsy of unknown cause. *Proceedings of the International Society of Magnetic Resonance in Medicine, Vancouver, Canada*, page 1048, 2021.
- [357] T. Yu, E.J. Canales-Rodríguez, M. Pizzolato, G.F. Piredda, T. Hilbert, E. Fisch-Gomez, M. Weigel, M. Barakovic, M. Bach Cuadra, C. Granziere, T. Kober, and J.-P. Thiran. Model-informed machine learning for multi-component T2 relaxometry. *Medical Image Analysis*, 69:101940, 2021.
- [358] E. Fisch-Gomez, J. Rafael-Patino, M. Pizzolato, G.F. Piredda, T. Hilbert, T. Kober, E.J. Canales-Rodriguez, and J.-P. Thiran. Multi-Compartment Diffusion Mri, T2 Relaxometry And Myelin Water Imaging As Neuroimaging Descriptors For Anomalous Tissue Detection. *2021 IEEE 18th International Symposium on Biomedical Imaging (ISBI)*, pages 307–311, 2021.
- [359] G.F. Piredda, P. Liang, T. Hilbert, H. He, J.-P. Thiran, Y. Sun, J. Zhong, K. Li, and T. Kober. Large-scale quantitative atlases over the whole adult age range. *Proceedings of the International Society of Magnetic Resonance in Medicine, Sydney, Australia*, page 1011, 2020.
- [360] M. Andelova, G.F. Piredda, K. Vodehnalova, J. Krasensky, T. Hrnčiarova, B. Šrpova, T. Uher, I. Menkyova, D. Stastná, D. Horakova, V. Ravano, B. Maréchal, M.J. Fartaria, T. Hilbert, T. Kober, and M. Vaneckova. Quantitative T1 changes relate to infratentorial pathology in early multiple sclerosis. *MULTIPLE SCLEROSIS JOURNAL*, 26:417–418, 2020.
- [361] G.F. Piredda, T. Hilbert, M. Vaneckova, J. Krasensky, T. Uher, B. Šrpova, E. Havrdova, M. Andelova, K. Vodehnalova, D. Horakova, V. Ravano, M.J. Fartaria, B. Maréchal, J.-P. Thiran, and T. Kober. Quantitative T1 deviations in brain lesions and NAWM improve the clinico-radiological correlation in early MS. *MULTIPLE SCLEROSIS JOURNAL*, 26:418, 2020.
- [362] M. Vaneckova, J. Krasensky, T. Uher, B. Šrpova, E.K. Havrdova, M. Andelova, K. Vodehnalova, D. Horakova, B. Maréchal, M.J. Fartaria, V. Ravano, G.F. Piredda, and T. Kober. A promising biomarker based on T1 relaxation time mapping for early MS. *MULTIPLE SCLEROSIS JOURNAL*, 26:371–372, 2020.

Bibliography

- [363] V. Ravano, G.F. Piredda, M. Vaneckova, J. Krasensky, M. Andelova, T. Uher, B. Srpova, E.K. Havrdova, K. Vodehnalova, D. Horakova, T. Hilbert, B. Maréchal, R. Meuli, J.-P. Thiran, T. Kober, and J. Richiardi. T1 abnormalities in atlas-based white matter tracts: reducing the clinico-radiological paradox in multiple sclerosis using qMRI. *Proceedings of the International Society of Magnetic Resonance in Medicine*, page 2796, 2021.
- [364] G.F. Piredda, T. Hilbert, M. Vaneckova, J. Krasensky, M. Andelova, T. Uher, B. Srpova, E.K. Havrdova, K. Vodehnalova, D. Horakova, V. Ravano, B. Maréchal, J.-P. Thiran, and T. Kober. Periventricular gradients of brain pathology in early and progressive MS revealed by qMRI. *Proceedings of the International Society of Magnetic Resonance in Medicine*, page 2795, 2021.
- [365] Z. Liu, M. Pardini, O. Yaldizli, V. Sethi, N. Muhlert, C.A.M. Gandini Wheeler-Kingshott, R.S. Samson, D.H. Miller, and Chard D.T. Magnetization transfer ratio measures in normal-appearing white matter show periventricular gradient abnormalities in multiple sclerosis. *Brain*, 138(5):1239–1246, 2015.
- [366] M. Pardini, C.H. Sudre, F. Prados, O. Yaldizli, V. Sethi, N. Muhlert, R.S. Samson, S. Van De Pavert, M.J. Cardoso, S. Ourselin, C.A.M. Gandini Wheeler-Kingshott, D.H. Miller, and D.T. Chard. Relationship of grey and white matter abnormalities with distance from the surface of the brain in multiple sclerosis. *Journal of Neurology, Neurosurgery and Psychiatry*, 87(11):1212–1217, 2016.
- [367] J.W.L. Brown, M. Pardini, W.J. Brownlee, K. Fernando, R.S. Samson, F.P. Carrasco, S. Ourselin, C.A.M. Gandini Wheeler-Kingshott, D.H. Miller, and D.T. Chard. An abnormal periventricular magnetization transfer ratio gradient occurs early in multiple sclerosis. *Brain*, 140(2):387–398, 2017.
- [368] M. Pardini, M. Petracca, A. Harel, L. Fleysher, N. Oesingmann, G. Bommarito, M. Fabian, D. Chard, F. Lublin, and M. Inglese. The relationship between cortical lesions and periventricular NAWM abnormalities suggests a shared mechanism of injury in primary-progressive MS. *NeuroImage: Clinical*, 16:111–115, 2017.
- [369] J.W.L. Brown, F. Prados Carrasco, A. Eshaghi, C.H. Sudre, T. Button, M. Pardini, R.S. Samson, S. Ourselin, C.A.M.G. Wheeler-Kingshott, J.L. Jones, A.J. Coles, and D.T. Chard. Periventricular magnetisation transfer ratio abnormalities in multiple sclerosis improve after alemtuzumab. *Multiple Sclerosis Journal*, 26(9):1093–1101, 2020.
- [370] G.F. Piredda, T. Hilbert, B. Bilgic, E.J. Canales-Rodríguez, M. Pizzolato, R. Meuli, J.-P. Thiran, and T. Kober. Joint-CAIPI reconstruction of multi-echo GRASE data for fast, high-resolution myelin water imaging. *Proceedings of the International Society of Magnetic Resonance in Medicine, Vancouver, Canada*, page 3078, 2021.
- [371] B. Bilgic, I. Chatnuntawch, M.K. Manhard, Q. Tian, C. Liao, S.S. Iyer, S.F. Cauley, S.Y. Huang, J.R. Polimeni, L.L. Wald, and K. Setsompop. Highly accelerated multishot echo planar imaging through synergistic machine learning and joint reconstruction. *Magnetic Resonance in Medicine*, 82(4):1343–1358, 2019.
- [372] E. Mussard, T. Hilbert, C. Forman, R.B. Van Heeswijk, R. Meuli, J.-P. Thiran, and T. Kober. Optimised T2 Preparation for Brain Imaging: Application to Compressed Sensing 3D T2 Mapping. *Proceedings of the International Society of Magnetic Resonance in Medicine, Montreal, Canada*, page 4536, 2019.

Curriculum Vitae

Gian Franco Piredda

Nationality	Italian	Date of Birth	26 th February 1993
Address	Avenue de Jurigoz 5, 1006 Lausanne, Switzerland	Mobile Phone	+41 77 997 12 59
		Email	gianfranco.piredda93@gmail.com
		Linkedin	linkedin/gianfrancopiredda

Education

- Apr. 2018 - **PhD in Electrical Engineering (Magnetic Resonance Imaging)**
Present *École Polytechnique Fédérale de Lausanne, Lausanne, Switzerland.*
In collaboration with Siemens Healthcare AG and CHUV.
Thesis: "Quantitative Microstructural Imaging for Clinical Use".
Publications: 8 journal articles, 1 conference article, 30 conference abstracts.
Supervision of 1 Master Student.
- Sept. 2015 - **M.Sc. in Biomedical Engineering**
Oct. 2015 *Politecnico di Torino, Turin, Italy.*
Thesis: "Brain Disease Detection Using Quantitative Magnetic Resonance Imaging".
Final Grade: 110/110 cum laude.
- Sept. 2015 - **Alta Scuola Politecnica**
Oct. 2017 *Politecnico di Torino - Politecnico di Milano, Italy.*
Advanced double-degree program restricted to 150 talented students, selected solely on the basis of merit, among the applicants to a Master of Science at *Politecnico di Torino* and *Politecnico di Milano* (asp-poli.it).
Final project: "AFCam - Contact-less system for the detection of Atrial Fibrillation using Camera face recordings". Team members: 8 students.
- Sept. 2016 - **Exchange student**
Feb. 2017 *École Polytechnique Fédérale de Lausanne, Lausanne, Switzerland.*
- Sept. 2012 - **B.Sc. in Biomedical Engineering**
July 2015 *Politecnico di Torino, Turin, Italy.*
Thesis: "Registration, Color Deconvolution and Segmentation of cellular images of Cardiospheres".
Final Grade: 110/110 cum laude.

Experiences

Nov. 2017 - **MR Research Engineer**

Present *Advanced Clinical Imaging Technology, Siemens Healthcare AG, Switzerland.*

- Design, conduct and report validation results of proof-concept MRI research projects.
- Involved in international research collaborations with hospitals worldwide.
- Design work-in-progress packages (MR sequences) for Siemens scanners.
- Involved in Intellectual Property writing (1 patent granted, 1 filed).

Feb. 2017 - **Master Thesis Student**

Aug. 2017 *Advanced Clinical Imaging Technology, Siemens Healthcare AG, Switzerland.*

Project: “Brain Disease Detection Using Quantitative Magnetic Resonance Imaging”.

Oct. 2016 - **Semester Project Student**

Jan. 2017 *Medical Image Processing Lab (MIP), Campus Biotech, Geneva, Switzerland.*

Project: “Deep learning network for predicting lesions in stroke.”.

Mar. 2015 - **Intern**

May 2015 *DET, Politecnico di Torino, Turin, Italy.*

Internship devolved to developing the B.Sc. thesis entitled “Registration, Color Deconvolution and Segmentation of cellular images of Cardiospheres”.

Volunteer Experiences

Nov. 2018 - **Treasurer & Swiss IMAGINE IF! Director**

Jan. 2021 *Innovation Forum Lausanne (IFL), Lausanne, Switzerland.*

IFL is a PhD-led non-profit association within a global network that aims at fostering the next generation of scientist entrepreneurs (inno-forum.org).

IMAGINE IF! is the first truly global competition and pre-accelerator program for sciences ventures in the healthcare and clean-tech area (inno-forum.org/accelerator).

Feb. 2018 - **Associate**

Oct. 2018 *Innovation Forum Lausanne (IFL), Lausanne, Switzerland.*

Skills and Competences

■ Programming

MATLAB, Python, R, C/C++, Java, Assembly.

■ Software / Libraries

Elastix, ANTs, FSL, FreeSurfer, SPM, TensorFlow, Keras, Pytorch, Microsoft Office Suite, \LaTeX .

■ Languages

Italian: Native. *English:* Full professional proficiency. *French:* Basic proficiency.

Hobbies and Interests

Sports Swimming and skiing.

Others Reading, cooking, and travelling.

Publications

Articles in peer-reviewed journals

1. **Piredda GF**, Hilbert T, Granziera C, Bonnier G, Meuli R, Molinari F, Thiran JP, Kober T.
Quantitative brain relaxation atlases for personalized detection and characterization of brain pathology. *Magn Reson Med*. 2020;83(1):337-351. doi: [10.1002/mrm.27927](https://doi.org/10.1002/mrm.27927).
2. **Piredda GF**, Hilbert T, Canales-Rodríguez EJ, Pizzolato M, von Deuster C, Meuli R, Pfeuffer J, Daducci A, Thiran JP, Kober T.
Fast and high-resolution myelin water imaging: Accelerating multi-echo GRASE with CAIPIRINHA. *Magn Reson Med*. 2021;85(1):209-222. doi: [10.1002/mrm.28427](https://doi.org/10.1002/mrm.28427)
3. **Piredda GF**, Hilbert T, Thiran JP, Kober T.
Probing myelin content of the human brain with MRI: A review. *Magn Reson Med*. 2021;85(2):627-652. doi: [10.1002/mrm.28509](https://doi.org/10.1002/mrm.28509).
4. Morel B*, **Piredda GF***, Cottier JP, Tauber C, Destrieux C, Hilbert T, Sirinelli D, Thiran JP, Maréchal B, Kober T.
Normal volumetric and T₁ relaxation time values at 1.5 T in segmented pediatric brain MRI using a MP2RAGE acquisition. *Eur Radiol*. 2021;31(3):1505–1516. doi: [10.1007/s00330-020-07194-w](https://doi.org/10.1007/s00330-020-07194-w).
* Morel and Piredda contributed equally to this work.
5. Bano W, **Piredda GF**, Davies M, Marshall I, Golbabaee M, Meuli R, Kober T, Thiran JP, Hilbert T.
Model-based super-resolution reconstruction of T₂ maps. *Magn Reson Med*. 2020;83(3):906-919. doi: [10.1002/mrm.27981](https://doi.org/10.1002/mrm.27981)
Note: **MRM Editor's pick of the month** (March 2020)
6. Yu T, Canales-Rodríguez EJ, Pizzolato M, **Piredda GF**, Hilbert T, Fisch-Gomez E, Weigel M, Barakovic M, Bach Cuadra M, Granziera C, Kober T, Thiran JP.
Model-Informed Machine Learning for Multicomponent T₂ Relaxometry. *Med Image Anal*. 2021;101940. doi: [10.1016/j.media.2020.101940](https://doi.org/10.1016/j.media.2020.101940).
7. Canales-Rodríguez EJ, Pizzolato M, **Piredda GF**, Hilbert T, Kunz N, Pot C, Yu T, Salvador R, Pomarol-Clotet E, Kober T, Thiran JP, Daducci A.

Comparison of non-parametric T_2 relaxometry methods for myelin water quantification. *Med Image Anal.* 2021;101959. doi: [10.1016/j.media.2021.101959](https://doi.org/10.1016/j.media.2021.101959).

8. Canales-Rodríguez EJ, Pizzolato M, Yu T, **Piredda GF**, Hilbert T, Radua J, Kober T, Thiran JP. Revisiting the T_2 spectrum imaging inverse problem: Bayesian regularized non-negative least squares. *NeuroImage*. 2021;244:118582. doi: [10.1016/j.neuroimage.2021.118582](https://doi.org/10.1016/j.neuroimage.2021.118582).

The complete list of articles published in peer-reviewed journals can be also found at the following link: [scholar.google.pireddagianfranco](https://scholar.google.com/citations?user=pireddagianfranco)

Articles currently under revision in peer-reviewed journals

1. **Piredda GF**, Hilbert T, Ravano V, Canales-Rodríguez EJ, Pizzolato M, Meuli R, Thiran JP, Jonas R, Kober T.
Data-driven myelin water imaging based on T_1 and T_2 relaxometry.
Currently under revision in *NMR in Biomedicine*.

Articles in proceedings of international conferences

IEEE ISBI 2021

IEEE International Symposium on Biomedical Imaging, Virtual Event

1. Fischi-Gomez E, Rafael-Patino J, Pizzolato M, **Piredda GF**, Hilbert T, Kober T, Canales-Rodríguez EJ, Thiran JP.
Multicompartment diffusion MRI, T_2 relaxometry and myelin water imaging as neuroimaging descriptors for anomalous tissue detection. doi: [10.1109/ISBI48211.2021.9433856](https://doi.org/10.1109/ISBI48211.2021.9433856).

Abstracts in proceedings of international conferences

ISMRM 2018

Joint Annual Meeting ISMRM-ESMRMB, Paris, France

1. **Piredda GF**, Hilbert T, Granziera C, Bonnier G, Meuli R, Molinari F, Thiran JP, Kober T.
Quantitative T_1 and T_2 Brain Atlases for the Detection of Abnormal Relaxation Times.
Abstract number: 0793.
ISMRM Merit Award Summa Cum Laude 2018.

ISMRM 2019

Annual Meeting ISMRM, Montréal, QC, Canada

2. **Piredda GF**, Hilbert T, Richiardi J, Canales-Rodríguez EJ, Pizzolato M, Meuli R, Thiran JP, Kober T.

Deriving Brain Myelin Water Fraction Maps from Relaxometry: a Data-Driven Approach.
Abstract number: 0668.

ISMRM Merit Award Magna Cum Laude 2019.

3. **Piredda GF**, Hilbert T, Canales-Rodríguez EJ, Pizzolato M, Meuli R, Pfeuffer J, Thiran JP, Kober T.

Accelerating Multi-Echo GRASE with CAIPIRINHA for Fast and High-Resolution Myelin Water Imaging. Abstract number: 4400.

4. **Piredda GF**, Hilbert T, Meuli R, Pfeuffer J, Thiran J-P, Kober T.

Combining Parallel Imaging and Model-based Reconstruction for Isotropic 3D T₂ mapping with Multi-Echo GRASE. Abstract number: 4561.

5. Bano W, **Piredda GF**, Davies M, Marshall I, Golbabaee M, Meuli R, Kober T, Thiran JP, Hilbert T.

High-resolution Isotropic Whole Brain T₂ Mapping with Model-based Super-resolution Reconstruction. Abstract number: 1256.

ISMRM Merit Award Magna Cum Laude 2019.

6. Hilbert T, **Piredda GF**, Egger K, Yang S, Kober T.

Age-specific Quantitative Brain Atlas Modelling Brain Shape and T₁ Changes. Abstract number: 0340.

7. Canales-Rodríguez EJ, Pizzolato M, **Piredda GF**, Hilbert T, Nicolas K, Kober T, Thiran JP, Pot C, Daducci A.

Robust Myelin Water Imaging from multi-echo T₂ data using second-order Tikhonov regularization with control points. Abstract number: 4901.

ECR 2020

European Congress of Radiology, Vienna, Austria

8. Morel B, **Piredda GF**, Hilbert T, Tauber C, Cottier JP, Maréchal B, Kober T.

Quantitative paediatric MRI going clinical: comprehensive brain assessment from a single sequence based on quantitative brain maturation atlases.

ECMRN 2020

European Congress of Magnetic Resonance in Neuropediatrics, Marseille, France

9. Maréchal B, **Piredda GF**, Hilbert T, Le Bars E, Leboucq N, Kober T.

Normative brain volume growth: pooling data across magnetic resonance field strengths.

10. Morel B, **Piredda GF**, Hilbert T, Tauber C, Cottier JP, Maréchal B, Kober T.

Volumetric, anatomical and relaxometry evaluation with a single MR sequence for brain maturation assessment.

ISMRM 2020

Annual Meeting ISMRM, Virtual Event

11. **Piredda GF**, Liang P, Hilbert T, He H, Thiran JP, Maréchal B, Zhong J, Li K, Kober T.
Large-scale quantitative atlases over the whole adult age range. Abstract number: 1011.
12. **Piredda GF**, Liang P, Hilbert T, Egger K, Yang S, Thiran JP, Maréchal B, Sun Y, Li K, Kober T.
Brain T₁ relaxometry changes across the life span: a comparison between two populations.
Abstract number: 3792.
13. **Piredda GF**, Piskin V, Dunet V, Manasseh G, Fartaria MJ, Huelnhagen T, Thiran JP, Kober T, Corredor-Jerez R.
A practical application of generative models for MR image synthesis: from post- to pre-contrast imaging. Abstract number: 1297.
14. **Piredda GF**, Hilbert T, Morel B, Tauber C, Cottier JP, Lars L, Thiran JP, Maréchal B, Kober T.
Measuring brain maturation with quantitative MRI. Abstract number: 0079.
15. **Piredda GF**, Perivier M, Morel B, Tauber C, Cottier JP, Thiran JP, Maréchal B, Hilbert T, Kober T.
Detecting and characterizing abnormal brain lateralization using quantitative MRI in clinical practice. Abstract number: 4638.
16. Maréchal B, **Piredda GF**, Hilbert T, Tauber C, Cottier JP, Thiran JP, Kober T, Morel B.
Simultaneous micro- and macrostructural assessment of normal brain development. Abstract number: 4626.
17. Bonanno G, Hilbert T, Joseph A, Mussard E, Forman C, **Piredda GF**, Kober T.
High-resolution magnetization transfer ratio maps using spiral-phyllotaxis Cartesian FLASH and compressed sensing in under five minutes. Abstract number: 3138.
18. Huelnhagen T, Fartaria MJ, Corredor-Jerez R, Mahdi MFA, **Piredda GF**, Maréchal B, Richiardi J, Kober T.
Don't Lose Your Face - Refacing for Improved Morphometry. Abstract number: 0546.

MSVirtual2020

Joint ACTRIMS-ECTRIMS Meeting, Virtual Event

19. **Piredda GF**, Hilbert T, Vaneckova M, Krasensky J, Uher T, Srpova B, Havrdova EV, Andelova M, Vodehnalova K, Horakova D, Ravano V, Fartaria MJ, Maréchal B, Thiran JP, Kober T.
Quantitative T₁ deviations in brain lesions and NAWM improves the clinico-radiological correlation in early MS.
20. Andelova M, **Piredda GF**, Vodehnalova K, Krasensky J, Hrnciarova T, Srpova B, Uher T, Menkyova I, Stastna D, Horakova D, Ravano V, Maréchal B, Fartaria MJ, Hilbert T, Tobias K,

Vaneckova M.

Quantitative T_1 time changes relate to infratentorial pathology in early multiple sclerosis.

21. Vaneckova M, Krasensky J, Uher T, Srpova B, Havrdova EK, Andelova M, Vodehnalova K, Horakova D, Maréchal B, Fartaria MJ, Ravano V, **Piredda GF**, Kober T.
A Promising Biomarker Based on T_1 Relaxation Time Mapping for Early MS.

ISMRM 2021

Annual Meeting ISMRM, Virtual Event

22. **Piredda GF**, Hilbert T, Bilgic B, Canales-Rodríguez EJ, Pizzolato M, Meuli R, Thiran JP, Kober T.
Joint-CAIPI reconstruction of multi-echo GRASE data for fast, high-resolution myelin water imaging. Abstract number: 3072.
23. **Piredda GF**, Hilbert T, Vaneckova M, Krasensky J, Andelova M, Uher T, Srpova B, Havrdova EV, Vodehnalova K, Horakova D, Ravano V, Maréchal B, Thiran JP, Kober T.
Periventricular gradients of brain pathology in early and progressive MS revealed by qMRI. Abstract number: 2795.
24. Ravano V, **Piredda GF**, Vaneckova M, Krasensky J, Andelova M, Uher T, Srpova B, Havrdova EV, Vodehnalova K, Horakova D, Hilbert T, Maréchal B, Meuli R, Thiran JP, Kober T, Richiardi J.
 T_1 abnormalities in atlas-based white matter tracts: reducing the clinico-radiological paradox in multiple sclerosis using qMRI. Abstract number: 2796.
Awarded by the ISMRM qMR Study Group in the “Clinical Translation” category.
25. Ravano V, **Piredda GF**, Hilbert T, Maréchal B, Meuli R, Thiran JP, Kober T, Richiardi J.
The sensitivity of classical and deep image similarity metrics to MR acquisition parameters. Abstract number: 2181.
ISMRM Merit Award Magna Cum Laude 2021.
26. Hilbert T, Soustelle L, **Piredda GF**, Troalen T, Sommer S, Joseph A, Meuli R, Thiran JP, Duhamel G, Girard O, Kober T.
On Comparability and Reproducibility of Myelin Sensitive Imaging Techniques. Abstract number: 0094.
ISMRM Merit Award Magna Cum Laude 2021.
27. Bapst B, Massire A, Kober T, **Piredda GF**, Maréchal B, Brugières P.
Volume-based brain morphometry and T_1 mapping: comparison between MP2RAGE accelerated by parallel imaging and compressed sensing at 3 Tesla. Abstract number: 2148.
28. Morel B, Piegay AS, Perivier M, Obry S, Maréchal B, **Piredda GF**, Hilbert T, Kober T, Tauber C, Castelnau P, Cottier JP.
Automated brain MRI volumetry and T_1 relaxometry in children with focal epilepsy of unknown cause. Abstract number: 1048.

ECTRIMS 2021

Congress of the European Committee for Treatment and Research in Multiple Sclerosis, Virtual Event

29. Ravano V, **Piredda GF**, Vaneckova M, Krasensky J, Andelova M, Uher T, Srpova B, Havrdova EV, Vodehnalova K, Horakova D, Hilbert T, Maréchal B, Thiran JP, Kober T, Richiardi J.
T₁ relaxometry abnormalities in white matter tracts predict functional systems scores in MS.
30. Vaneckova M, **Piredda GF**, Andelova M, Krasensky J, Uher T, Srpova B, Havrdova EK, Vodehnalova K, Horakova D, Hilbert T, Maréchal B, Fartaria MJ, Ravano V, Kober T.
Periventricular gradients of T₁ z-scores correlate with disability in early multiple sclerosis.

Patent applications

1. Hilbert T, Kober T, **Piredda GF**.
Method and system for abnormal tissue detection using z-scores in a joint histogram.
US10657410B2; granted on May 19, 2020.
2. **Piredda GF**, Hilbert T, Kober T, Lauer L.
Measurement of maturation stage using quantitative MRI.
2020P05839US; filed on March 22, 2021.

Work-in-progress packages (MR sequences)

1. **Piredda GF**, Hilbert T, Kober T.
Multi-echo GRASE sequence:
 - N4 (VE11C, VE11E) – Siemens WIP No. 989.
 - NX (VA20A) – Siemens WIP No. 062.